Engineering 3D microenvironments for the generation of functional, pre-vascularized human beige adipose tissue: from ex vivo organoid model to transplantable micro-tissue

Mélanie Escudero

Université Fédérale
Toulouse Midi-Pyrénées

THÈSE

En vue de l'obtention du
DOCTORAT DE L'UNIVERSITÉ DE TOULOUSE

Délivré par l'Université Toulouse 3 - Paul Sabatier

Présentée et soutenue par

Mélanie ESCUDERO

Le 21 décembre 2023

Ingénierie de micro-environnements 3D pour la génération de tissus adipeux beiges humains fonctionnels et pré-vascularisés : Du modèle organoïde ex vivo au micro-tissu transplantable

Ecole doctorale : **BSB - Biologie, Santé, Biotechnologies**

Spécialité : **MALADIES METABOLIQUES ET CARDIOVASCULAIRES**

Unité de recherche :
RESTORE

Thèse dirigée par
Louis CASTEILLA et Laurent MALAQUIN

Jury

Mme Joelle AMéDéE VILAMITJANA, Rapporteure
Mme Julie DAM, Rapporteure
M. Maxime MAHé, Examinateur
Mme Nathalie VERGNOLLE, Examinatrice
M. Louis CASTEILLA, Directeur de thèse
M. Laurent MALAQUIN, Co-directeur de thèse
Mme Laurence VAYSSE, Co-encadrante de thèse

Table of contents

Table of contents

Table of contents **1**

Résumé **7**

Summary **10**

Table of figures and tables **13**

List of abbreviations **17**

Bibliographic introduction **21**

I. Scientific context **23**

II. How to drive *in vitro* 3D tissue development to obtain complex physiology? **25**

1. Insight about cellular processes of tissue development, regeneration and homeostasis **27**

1.1. Influence of cell microenvironment on cell fate specification, proliferation and survival 27

1.2. Stochasticity of gene expression supporting cell-to-cell decisions variability 34

1.3. Tissue shaping and cell migration 38

2. Two main conceptual approaches for *in vitro* generation of complex tissues **42**

2.1. Organoids: nature-driven engineering of tissue 42

2.2. Tissue engineering: structure-driven engineering of tissue 46

3. Driving self-organization of cells through 3D engineered microenvironment **50**

3.1. Ensuring cell-matrix interactions: Engineering extracellular matrix 50

3.2. Providing soluble factors: nature, supply and distribution 55

3.3. Ensuring cell-cell interactions: Cell density and cellular assemblies 60

III. How to engineer tissue architecture to generate functional large-scale tissue constructs? **63**

1. Pioneer top-down engineering: Cell seeding onto organ-shaped scaffold **64**

2. Hydrogel-based bioprinting for the precise deposition of cells into predefined spatial arrangements **66**

3. Organ building blocks for modular tissue engineering **70**

4. Toward hybrid methods of tissue engineering: Cell injection of organoid-forming cells **74**

5. Engineering vascular-based perfusion systems for long term cell culture and function **75**

5.1. Nature-driven: self-assembly of vascular formation 76

5.2. Engineering-driven: Generation of “endothelialized” perfusable channels 78

IV. Thermogenic adipose tissues as promising therapeutic targets to restore energy balance in metabolic disorders **81**

1. Adipose tissues: key regulators of energy homeostasis **82**

1.1. Specialized metabolic function and distribution of adipose tissues 82

1.2. Secretory function of adipose tissues 85
2. Pathological dysregulation of adipose tissues metabolic functions 88
2.1. Limits of white adipose tissue expandability and development of obesity and related-metabolic disorders 88
2.2. Dysregulations of thermogenic adipocytes function in pathological conditions 90
3. Thermogenic adipocytes-based therapies for metabolic disorders 91
4. Adipose tissue architecture and cell composition 93
4.1. Extra-cellular matrix 94
4.2. Innervation 95
4.3. Vascularization 95
4.4. Adipocytes 96
4.5. Adipocytes progenitors: adipose derived mesenchymal stem cells 99
4.6. Immune cells 100
5. Understanding thermogenic adipose tissue development and activation 102
5.1. Adipocytes development: common process and specificity to thermogenic fat 102
5.2. Thermogenesis activation and transcriptional regulation of UCP1 107
5.3. Interplay between adipocyte and vascularization development in adipose tissue 110
6. *In vitro* generation of human brown and beige adipose tissue 112
6.1. Human cell sources for *in vitro* generation of thermogenic adipocytes 112
6.2. Current 3D models of thermogenic AT 115
6.3. Current strategies of human thermogenic adipocytes transplantation 117
Thesis objectives and hypotheses 121
Results and discussion 125
I. Engineering 3D microenvironment for the generation of physiological human beige adipose tissue constructs 125
1. Article: Scalable generation of generation of pre-vascularized and functional human beige adipose tissue organoids 125
2. Discussion and perspectives 127
2.1 Engineered organoids as physiological mimicking of human beige adipose tissue 127
2.2 Generalization of the 3D microenvironment engineering approach to other tissues and systems 130
II. Preliminary development of cell culture system to study spheroid cell rearrangement in response to mass transport and matrix compositions 134
1. Objectives and hypotheses: 134
2. Device design and first development steps 138
III. Tissue therapy for the treatment of metabolic disorders: Preliminary transplantation assays 145

1. Introduction 145
2. Material and methods 147
3. Results 150
4. Discussion 154
General conclusion and perspectives 159
Annexes 165
I. Scientific contributions: 167
Remerciements 169
References 174

Résumé

Résumé

Au sein des tissus, les cellules s'organisent dans des microenvironnements 3D complexes, composés de leurs cellules voisines, de contraintes physiques en grande partie générées par la matrice extracellulaire et de gradients chimiques dynamiques. Développer des modèles 3D fonctionnels de tissus adultes humains représente un défi important dans le domaine des biosciences en tant que modèles ex vivo pertinents permettant le progrès de la recherche fondamentale et le criblage de molécules mais aussi en tant qu'objet thérapeutique transplantable pour de futures biothérapies.

L'objectif de cette thèse s'inscrit dans ce contexte et a eu pour premier objectif de définir un microenvironnement 3D permettant la génération de modèles 3D polyvalents de tissus adipeux (TA) beiges humains. En effet, l'augmentation de leur activité par pharmacothérapie ou greffes cellulaires représente une approche thérapeutique prometteuse pour faire face à la montée de l'obésité et du diabète. Cependant, les modèles *in vitro* de TA beige humain sont rares, ce qui entrave la recherche sur ces tissus et le développement de biothérapies. Au cours de cette thèse, nous avons développé une approche d'ingénierie innovante qui permet la génération d'organoïdes adipeux beiges fonctionnels et vascularisés dérivés de la fraction vasculaire stromale humaine (SVF) de tissu adipeux blanc. Nous avons défini un environnement chimique et biomécanique précis, applicable à différentes échelles, pour guider l'auto-organisation de sphéroïdes vers l'émergence d'organoïde fonctionnel. L'encapsulation des sphéroïdes dans un hydrogel dérivé de gélatine, le GelMA, a été utilisée pour favoriser le maintien et l'organisation cellulaire. Le volume et le pourcentage de GelMA ont été optimisés pour favoriser la colonisation et la viabilité des cellules. L'inhibition de la voie TGFβ s'est avérée essentielle dans les cultures 3D afin de favoriser l'abiogenèse beige et la formation vasculaire. La combinaison de l'environnement biomécanique de GelMA et biochimique du milieu de différentiation a permis la génération d'organoïdes adipeux beiges vascularisés mimant l'architecture des tissus natifs à partir de cellules de SVF amplifiées ou fraîchement isolées. Ces organoïdes présentent des caractéristiques clés des TA beiges natifs, notamment l'expression inductible d'UCP1, une augmentation de la respiration mitochondriale découplée et la sécrétion de batokines. La transposition de l'environnement spécifié au niveau d'un sphéroïde à un contexte multi-sphéroïdes a conduit à la génération de micro-tissus adipeux beige vascularisé sans modifier la viabilité cellulaire et la différentiation adipocytaire. Des premiers essais de transplantation de ces micro-tissus dans des souris NSG saines ont montré une intégration efficace des vaisseaux humains néoformés dans la vascularisation murine associée à un maintien prometteur de la viabilité des cellules humaines. Par ailleurs, nous avons commencé à explorer des solutions technologiques pouvant permettre d'examiner

plus précisément l'influence des paramètres du microenvironnement sur l'organisation cellulaire au sein de matrices 3D.

Notre approche constitue une avancée majeure dans la création de modèles 3D de tissu adipeux beige humain in vitro qui n'existait pas à l'heure actuelle, permettant une variété d'applications allant de la recherche fondamentale aux biothérapies. Compte tenu de la multipotence des ASC et du caractère modulable des hydrogels de GelMA, cette méthode d'ingénierie pourrait être transposée à d'autres tissus, démontrant le potentiel de ce système pour aborder des aspects essentiels de la génération de tissus au-delà du tissu adipeux.

Summary

Cells in tissues and organs are organized within complex 3D environments surrounded by neighboring cells, extracellular matrices, and dynamic chemical gradients. Advancing methods to develop relevant 3D models of functional human adult tissue represents a pivotal challenge in Biosciences. These tissue constructs serve as enhanced models to advance basic science or to screen therapeutic targets as well as advanced therapy medicinal products to favor tissue regeneration or to support organ with defective function.

In this thesis, we aimed to engineer defined 3D microenvironment to generate multi-purposes 3D adult tissue models. We specifically focused on human beige adipose tissues (AT). Due to their unique properties in energy dissipation, increasing beige AT activity by pharmacotherapy or cell-based transplantations holds therapeutic promises to face obesity and diabetes pandemics. However, *in vitro* 3D relevant models of human beige AT are currently lacking which hinder research into these tissues and biotherapy development. During this thesis, we developed an innovative method to generate functional and vascularized beige adipose organoids using human stromal vascular fraction (SVF) of white adipose tissue as a source of adipose derived stromal cells (ASC) and endothelial progenitors. We engineered defined chemical and biomechanical environment, applicable at multiple tissue scales, to drive self-organization of spheroids. Embedding of spheroids in GelMA hydrogel was used to promote cell viability and cell organization. GelMA volume and GelMA percentage were optimized to favor cell colonization and cell viability. Translating from 2D to 3D culture, inhibition of TGFβ pathway was also key to promote beige adipogenesis while maintain vascular formation from amplified SVF cells-spheroids. Combination of GelMA environment and beige adipogenic medium promoted generation of beige adipose organoids containing beige adipocyte and vascular compartment mirroring native tissue architecture from both amplified and fresh SVF cells. These organoids display

key features of native beige AT including inducible UCP1 expression, increased uncoupled mitochondrial respiration and batokines secretion.

To scale up beige adipose organoid generation toward micro-tissue, we developed GelMA molding and spheroid patterning to replicate environment specified at the individual spheroid level within a multi-spheroid setting. This led to the generation of beige adipose micro-tissue containing embedded vasculature without hindering beige adipocyte differentiation level and cell viability. Preliminary transplantation assays of these microtissue in healthy NSG mice showed efficient integration of human vessels in host vasculature with promising maintenance of human cell viability.

Finally, we also explored technological approaches to generate cell culture system allowing for a better examination of how microenvironment parameters drive cell organization in 3D matrices.

Our approach represents significant advances in developing *in vitro* human beige AT models and facilitates broad applications ranging from basic research to biotherapies. Given multipotency of ASC and tunability of GelMA hydrogels, this engineering method could be transposable to other tissues highlighting the potential of this system to address essential aspects of tissue generation beyond adipose tissue.

Table of figures and tables

Table of figures

Figure 1. Principles of extrinsic cues sensing and cell signaling in developmental processes. 29
Figure 2. Historical concept of tissue patterning Induction by morphogens. 31
Figure 3. Regulation of adult stem cells renewal and differentiation is coordinated by interacting extrinsic signals. 32
Figure 4. Regulation of YAP/TAZ activity by extrinsic factors. 33
Figure 5. Principle of extrinsic and intrinsic noise in cell-to-cell variability of gene expression. 35
Figure 6. Stochasticity of cell fate specification: exploitation and compensating mechanisms in development. 36
Figure 7. Collective migration in tissue structuration involves chemotactic cues, cell-cell coupling and ECM remodeling. 39
Figure 8. Components of organoid culture generation. ESC, embryonic stem cells; iPSC, induced pluripotent stem cells. 43
Figure 9. Variety of organ specific organoids can be derived from pluripotent and adult stem cells. 44
Figure 10. Components of classical tissue engineering approaches. 47
Figure 11. Schematic concepts of driving in vitro tissue development through 3D engineered microenvironment for the production of physiologically relevant tissue constructs. 51
Figure 12. Chemical and biophysical parameters of biomaterial contributing to tissue development. 53
Figure 13. Chemical modifications of hydrogels for controlling growth factors retention and release. 57
Figure 14. Perfusion systems for soluble factors delivery in 3D culture. 59
Figure 15. Aggregation of cells promotes cell interconnectivity and cell organization within 3D culture. 61
Figure 16. Pioneers tissue engineering approach based on organ shaped scaffold. 66
Figure 17. Principle of hydrogel-based bioprinting. 67
Figure 18. Schematics of tissue-engineered-construct fabrication via modular assembly methodologies. 71
Figure 19. Requirements for in vitro self-assembly and self-organization of vascular networks. 77
Figure 20. Principle of microfluidic chip “endothelialization” for in vitro vascular development. 79
Figure 21. Coordinated regulation of energy homeostasis. 81
Figure 22. Adipose tissue subtypes distribution and metabolic functions in humans. 83
Figure 23. Limit of white adipose tissue expansion in obesity and related dysfunctions. 89
Figure 24. Adipose tissue lobular architecture and cellular microenvironment composition. 93
Figure 25. Characteristics of white, beige and brown adipocytes. 97

Figure 26. Principles of UCP1-dependent non-shivering thermogenesis in thermogenic adipocytes. 99
Figure 27: Effect of TGFβ/BMP subfamilies and related microenvironment factors on differentiation potential of multipotent adipose-derived mesenchymal stromal cells (ASCs). _____ 103
Figure 28. Common adipocyte differentiation program. _____ 105
Figure 29. Developmental origins of white, brown and beige adipocytes._____ 107
Figure 30. Thermogenesis activation mechanisms in brown and beige adipocytes. _____ 108
Figure 31. Functional and developmental cross-talks between adipose tissue vasculature and adipocytes. _____ 111
Figure 32. Within 3D matrix migration of spheroid cells are influenced by asymmetric distribution of driving forces including cell-cell, cell-matrix interactions and soluble biochemical factors availability. _____ 135
Figure 33. Design of cell culture chip and principle of GelMA patterning to study impact of mass transport, matrix composition and hydrogel interfaces on spheroid cell colonization._____ 139
Figure 34. Mold generation and preliminary molding assays. _____ 140
Figure 35. Preliminary assessment of cell culture feasibility in patterned GelMA. _____ 142
Figure 36. Preliminary transplantation assays protocols. _____ 146
Figure 37. Evaluation of transplanted micro-tissue survival and vascular engraftment. _____ 151
Figure 38. Evaluation of UCP1 induction within human beige micro-tissue after transplantation. _ 153

Table of Tables

Table 1. Key signaling pathways implicated in development orchestration_____ 26
Table 2. Organoid culture characteristics._____ 46
Table 3 Summary of classical tissue engineering approaches characteristics. _____ 49
Table 4. Advantages, disadvantages, and main clinical uses of different kinds of biomaterials. ____ 55
Table 5. Endocrine functions of selected adipokines._____ 85
Table 6. Roles of selected human batokines in thermogenesis._____ 87
Table 7. Cell sources to generate human thermogenic adipocytes in vitro _____ 113
Table 8. Current 3D models of human thermogenic adipose tissue. _____ 115
Table 9. Existing strategies for human thermogenic adipocytes transplantations. _____ 117
Table 10. List of antibodies and dyes used for immunofluorescence and immunochemistry cell characterization_____ 148
Table 11. List of primer used for qRT-PCR analyses _____ 149

List of abbreviations

List of abbreviations

2D: two-dimensional

3D: three-dimensional

ADIPOQ: adiponectin

β-AR : β-adrenergic receptor

ASC: adipose derived stromal cell

AT: adipose tissue

ATM: adipose tissue macrophages

ATMP: advanced therapy medicinal product

BAP: brown adipose progenitor

BAT: brown adipose tissue

BMP: bone morphogenetic protein

cAMP: cyclic AMP

Col. : collagen CVD: cardiovascular disease.

CXCL14: C-X-C motif chemokine ligand-14

EC: endothelial cells

ECM: extracellular matrix

EGF: epidermal growth factor

FABP4: Fatty-acid-binding protein 4

FDG: ^{18}F-fluorodeoxyglucose

FFA: free fatty acids

FGF: fibroblast growth factor

FRESH: freeform reversible embedding of suspended hydrogels

GelMA: gelatin methacryloyl

GDF15: growth-and-differentiation factor-15

GF: growth factor

GRN: gene regulatory network

(h)ESC: (human) embryonic stem cells

(h)iPSC: (human) induced pluripotent stem cells

(h)PSC: (human) pluripotent stem cells

HSL: hormone-sensitive lipase

IL-6: interleukin-6

JNK: JUN kinase

LT: lymphocytes

MMP: matrix metalloproteinase

MPS: microphysiological systems

MSC: mesenchymal stromal cells

MVF: microvascular fragments

Myf5: Myogenic factor 5

NAFLD: non-alcoholic fatty liver disease

NE: norepinephrine

NF-κB: nuclear factor-kappa

NGF: nerve growth factor

Pax7: Paired box 7

PET/CT: positron emission tomography/ computed tomography

PDGF(R): platelet derived growth factor (receptor)

PDMS: poly(dimethyl siloxane)

PGC1α: PPARγ coactivator 1α

PKA: Protein Kinase A

PPARγ: Peroxisome Proliferator-Activated Receptor-γ

PPRE: peroxisome-proliferator-responsive element

PDRM16: PRD1-BF-1-RIZ1 homologous domain-containing protein 16

RA: retinoic acid

RAR: retinoic acid receptor

αSMA: α smooth muscle actin

SNS: sympathetic nervous system

SVF: stromal vascular fraction

T2D: type 2 diabetes

T3: 3,5,3'-triiodothyronine

T4: thyroxine

TF: transcription factor

TG: triglycerides

TGFβ: transforming growth factor β

TH: thyroid hormone

TIMPs: tissue inhibitors of MMP

TNF-α: tumor necrosis factor-α

TRE: thyroid hormone response element

UCP1: uncoupling protein 1

VEGF: vascular endothelial growth factor

WAT: white adipose tissue

zfp423: multi-C2H2 zinc finger transcriptional coregulator

Bibliographic introduction

I. Scientific context

In the realm of scientific advancement, the creation of three-dimensional (3D) tissue constructs *in vitro* stands as a pivotal breakthrough with far-reaching implications. These tissue constructs serve as invaluable tools for advancing basic science as well as biomedical sciences, offering enhanced models for studying physiological and pathophysiological development, identifying putative therapeutic targets, while holding the potential to revolutionize regenerative medicine as future advanced therapy medicinal products (ATMP).

To advance medical science, scientists traditionally utilized two-dimensional (2D) cell cultures and animal testing. While these methods have expanded our knowledge, they have significant limitations. Cells in tissues and organs exist in complex 3D environments surrounded by neighboring cells, extracellular matrices (ECM), and dynamic chemical gradients, which 2D cultures fail to replicate [1]. In 2D cultures, cells interact with each other in a planar configuration, are homogeneously exposed to chemical factors and are grown on unnaturally stiff substrates [1]. Moreover, 2D cultures often lack cellular diversity, limiting their ability to mimic native tissues [1]. This leads to incomplete replication of native tissue conditions, impacting disease modeling and drug screening accuracy. As a result, complex diseases like cancer or metabolic syndromes are inadequately represented, and over 90% of drugs that pass preclinical tests fail in clinical trials [2]. Animal testing, while longstanding, raises ethical concerns and may yield species-specific results, causing inaccuracies in disease research and therapy development [3]. These collective limitations emphasize the necessity to create innovative 3D tissue models with the potential to transform biomedical research and drug development.

In the field of regenerative medicine, in vitro-generated tissue constructs represent a vital step in creating functional and transplantable replacement tissues, potentially alleviating organ shortages and enhancing transplant outcomes [4]. Tissue regeneration is mediated by tissue specific stem cells which are characterized by their self-renewal and differentiation potential able to drive *de novo* tissue morphogenesis [5,6]. However, adult mammals and especially humans exhibit low innate capacity for self-regeneration of tissues and organs [7]. These limitations have prompted the development of the tissue engineering concept in the late 1980s aiming to generate *in vitro* transplantable substitutes to replace failing organs [8–10]. While it has become apparent that whole organ generation *in vitro* is far from reachable, new methods in regenerative medicines aim to generate engineered tissue constructs capable of replacing damaged areas or supporting endogenous regeneration.

Generation of engineered-tissue constructs for both transplantation or 3D *ex vivo* models of organs and disease development lay on the same engineering objective which is understanding how to drive

cellular processes in vitro toward self-organization of complex tissues. The remarkable progress in our understanding of stem cell biology and organ development has revealed that tissue emergence lies on interactions between intrinsic self-organization capacity of cells and extrinsic factors of their microenvironment [11,12]. Hence, *in vitro* tissue development requires both careful choice of cell sources and mimicking of cell environment components such as biochemical factors, cell-extracellular matrix (ECM) and cell-cell interactions [13,14]. Various approaches have been described to generate 3D cell culture systems such as spheroids, organoids or scaffold-based engineering approaches with their own advantages, limits and applications [1,15]. Increasing progresses in the field of biomaterials, bioprinting and microfabrication fuel the field toward the generation of tissue constructs with clinically relevant size, micro-structuration and function [16,17], the major challenging being concomitant generation of embedded vasculature [18,19].

This thesis is situated within this general scientific context and endeavors to create versatile 3D tissue models and investigate how biochemical and biophysical factors influence their development. As a target tissue, we focus on human beige and brown thermogenic adipose tissues (AT) which have emerged as therapeutic opportunities to tackle the increasing global prevalence of obesity and diabetes thanks to their unique properties in energy dissipation [20,21]. Two primary therapeutic approaches for targeting human thermogenic adipocytes include *in situ* increase of thermogenic mass and activity through pharmacological approaches or *ex vivo* generation of transplantable thermogenic adipocytes [20,21]. Developing relevant ex vivo models for thermogenic AT is crucial for understanding tissue physiology, creating *in vitro* drug screening assays, and providing a source for transplantable thermogenic adipocytes. Unlike white adipose tissue engineering, which mainly addresses soft tissue defects and metabolic disorders, only few protocols have been described for functional human thermogenic AT generation [22–25]. Additionally, these protocols often overlook the critical vascular component that impacts AT physiology [22,23,25] and transplant survival. Throughout this study, we have introduced innovative engineering strategies for creating 3D microenvironments that facilitate the production of functional, pre-vascularized human beige adipose tissue organoids. Our broader goal was to derive fundamental principles of in vitro tissue development from this work.

To gain a thorough grasp of in vitro tissue development complexities, we will initially explore fundamental concepts of human tissue development (See II.1). Next, we will delve into the diverse principles that have been proposed to facilitate the creation of 3D *ex vivo* models across tissue scales (see II.2-3, III). Lastly, we will provide an overview of the present understanding of human thermogenic adipose tissues and how to generate them *in vitro* (see IV). This overview will emphasize their functions, architectures and the cellular mechanisms that drive their *in vivo* development.

II. How to drive *in vitro* 3D tissue development to obtain complex physiology?

Any organ is composed of several intricated tissues. Tissue which conduct the specific function of the organ is referred to as the parenchyma while the stroma also called mesenchyme encompass connective tissue, blood vessels and innervation [26]. Connective tissues especially provide nutritional and mechanical support for other cell compartments [26]. Each tissue is characterized by distinct cellular and ECM compositions that are organized into a tissue-specific architecture supporting tissue functions [26]. Tissue are composed of several interconnected group of cells, also called cell compartment, each of them being characterized by a specific cell organization and performing one or more specific functions. This cell organization importantly rely on the ECM compartment which is composed of fibrillar proteins (e.g collagen, elastin, fibronectin and laminin) and polysaccharides proteins (e.g. glycoasminoglycan) as well as entrapped water and soluble factors. The proportion of ECM components and their spatial distribution are tissue specific and strongly associated with specific functions [27].

Recreating tissue with complex physiology requires methods to recapitulate these complex tissue compositions but also understand how to drive them to assemble and organize in space within appropriate local environments.

Organ and tissue development lies on multiple multicellular processes driven both by the intrinsic genetic programs of cells and their complex extrinsic environment [28]. During the last decades, great advances in 3D imaging and omics analysis from tissue to single cell level have given us unrivaled insights on the spatial and temporal instructions leading to tissue emergence (see II.1). One of the main challenges in the *in vitro* generation of complex tissues is therefore to translate this understanding into bio-fabrication processes. Two primary research communities have devoted their efforts to addressing this challenge: the organoids community and the field of tissue engineering (see II.2). While the organoids community initially placed its emphasis on harnessing and initiating the intrinsic capabilities of stem cells to engage in cascades of developmental events to give rise to self-organized macro-structures [29], the tissue engineering community focused on replicating the defining characteristics of native tissues [30]. Both fields have seen a shift in their conceptual approaches to converge toward a common principle of guiding self-organized cellular development through the engineering of controlled 3D microenvironments [31,32] (see II.3).

1. Insight about cellular processes of tissue development, regeneration and homeostasis

Understanding the cellular processes responsible for tissue development in vivo and their homeostasis throughout adult life should be the fundamental focus of our consideration. The goal is to extract from the intricate nature of tissue emergence and maintenance a set of parameters and principles that can be fine-tuned and replicated in laboratories to facilitate *in vitro* tissue development.

Organ and tissue development result from complex interactions of developmental processes conserved across species. These processes involve cell fate determination [33], cell proliferation and survival [34] which collectively oversee the growth of tissues and the development of their characteristics [28]. Additionally, they encompass cell motility and interactions between cells, which play a crucial role in shaping cellular and structural organizations of tissues [35]. In adult organs, tissue homeostasis, repair and regeneration are ensured by resident adult stem cells that reside in specialized environments called niches [12]. Over the past decades, numerous research endeavors have been directed towards gaining a deeper insight into the coordination of these cell processes in the context of tissue development, regeneration and homeostasis [28,34,36]. These studies have unveiled, for each of them, a strong dependence on cell microenvironment components which include extrinsic chemical cues, cell-ECM and cell-cell interactions. Nevertheless, far from the classical view of organ development as an unvarying sequence of events, single cell level analyses have revealed high cell heterogeneity and development stochasticity that should be considered to grasp cell complexity and dynamic within tissues [37–39].

The next section will aim to give some insights into the importance of the cell microenvironment on stem cell fate specification, proliferation and survival (see II.1.1) as well as how gene stochasticity can influence these cell fate (see II.1.2). Finally, acquisition of tissue structuration through cell migration and rearrangement will be discussed (see II.1.3).

1.1. Influence of cell microenvironment on cell fate specification, proliferation and survival

Multicellular organism development and tissue regeneration involve spatiotemporal regulation of stem cell fate determination, differentiation, proliferation, survival and migration. These processes operate at the single-cell level and collectively lead to significant morphological transformations and functional specialization at the cell population level. Embryonic stem cells are pluripotent meaning that they have the capacity to initiate all lineages of the mature organism in a flexible manner directed

by signals in the embryo. During embryonic development, stem cells proliferate and differentiate into mature cells through successive generation of daughter cells characterized by progressive restriction in potentiality associated with cell specification toward specific cell lineages [34]. Spatiotemporal regulation of cell proliferation is also a fundamental aspect regulating tissue growth and size determination [34]. Tissue and organ size are well defined and emerge during development whereas their size is maintained after formation by replenishment of cells from resident adult stem cells characterized by restricted lineage commitment [5,40].

Before the revolution of single cell-based study, historical biochemical and cell genetic approaches led to the systematic characterization of seemingly static gene regulatory networks (GRN) overseeing spatiotemporal regulation of cell fate specification, proliferation and survival. Surprisingly, these approaches have revealed that few signaling pathways are key in their regulation (Table 1). These pathways are typically distributed into main classes based on their ligand or transduction mechanism [41]. Examples include transforming growth factor β/bone morphogenetic proteins family (TGF-β/BMP), fibroblast growth factor (FGF), epidermal growth factor (EGF), Wnt, retinoic acid receptor (RAR), Hippo or Notch [41].

Table 1. Key signaling pathways implicated in development orchestration (adapted from *[41]*)

Signaling pathway	Development processes
TGF-β/BMP	Patterning, growth
Wnt	Patterning, growth, cell polarity
Notch	Patterning, cell fate specification through lateral cell inhibition
Hedgehog	Patterning, growth
EGF	Patterning, morphogenesis
FGF	Patterning, morphogenesis, cell migration
PDGF/VEGF	Morphogenesis, cell migration
Hippo	Growth, cell polarity
NF-κB	Patterning, innate immunity
JNK	Patterning, cell migration, innate immunity

Abbreviations: TGF, transforming growth factor; BMP, bone morphogenetic proteins; EGFR, epidermal growth factor; FGF, fibroblast growth factor; PDGF, platelet derived growth factor; VEGF, vascular endothelial growth factor; NF-κB, nuclear factor-kappa B ; JNK, JUN kinase

Developmental signaling pathways are activated through the interaction of receptors, mostly located at the membrane surface, with specific ligands (Figure 1). These ligands can be soluble diffusible factors, transmembrane ligands from neighboring cells or ECM components. Cell receptors act as sensors of the biochemical and mechanical cell environment. Hence, induction of each developmental process in each cell does not rely on unique signals. Instead, cell response depends on multiple signal expositions varying in their individual amplitude and duration. Cell response strongly relies on these extrinsic cues in interaction with cell intrinsic competency to sense and respond to them as well as the structure of the GRN which will translate fine-tuned inhibition and activation of interacting pathways into single cell outcome [28,41] (Figure 1). The following paragraphs will only focus on extrinsic signals contributing to development processes.

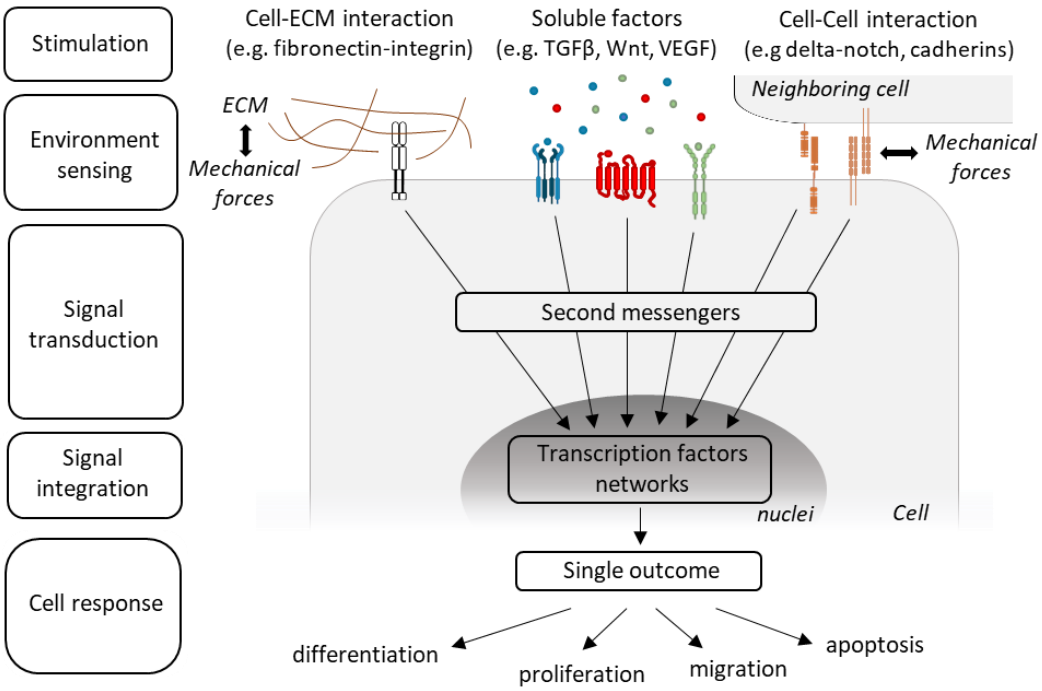

Figure 1. Principles of extrinsic cues sensing and cell signaling in developmental processes. Transcription factors play a pivotal role in orchestrating developmental processes to external perturbations via signaling pathways. Cells engage with their microenvironment using a variety of receptors. When stimulated by signaling molecules such as matrix proteins, soluble factors, or other cell membrane proteins, these receptors initiate intracellular signaling cascades. These cascades transduce and amplify signals through second messengers to activate effectors proteins including transcription factors. The integration and coordination of multiple signaling pathways involve cross-talk at each step, ultimately resulting in the modulation of a specific set of transcription factors. Therefore, the combination of extrinsic signaling is translated into a combination of gene regulations, leading to a unique cellular response.

In early stages of embryo development, cell processes are mostly driven by intrinsic cell determinants and their asymmetric distributions into daughter cells. Throughout embryonic development, extrinsic factors gain increasing significance in the regulation of cell processes, with the establishment of paracrine secretion and the emergence of developmental signaling centers corresponding to clusters of inducer cells secreting diffusible molecules. Spatially restricted lineages associated with tissue patterning are often correlated with the generation of morphogen gradients referring to signaling molecules dictating cell fate in a concentration-dependent manner (Figure 2A) [41]. Information position perceived by a cell is often the result of interacting axial and orthogonal morphogen gradients [41]. This is well exemplified by mesoderm induction which relies on the establishment of nodal gradient, a member of TGF-β family in vertebrates [42,43]. In xenopopus, generation of this gradient result from the interaction of Wnt-family β-catenin and maternal TGF-family growth factor Vg1 gradients [43] (Figure 2B). Low expression of nodal-related molecule induces specification of ventral mesoderm while their high expression induces the gastrula organizer, Spemman center. As for cell fate restrictions, secreted signaling molecules and their distribution as morphogen gradients control hierarchically cell division of progenitor cells [44]. Several growth factors have been described to promote cell proliferation and cell survival in a concentration-dependent manner such as VEGF or platelet-derived growth factors (PDGF) [45–47]. The ECM can regulate the spatial presentation of these factors through their binding to the ECM components mediated by specific protein-binding domains such as heparin-binding domains [48]. Hence, combination of chemical factors and their spatial distribution is a key parameter in driving cellular development.

On the other hand, during early development, cell-cell contact predominates but as embryonic development progresses, differentiated cells secreting ECM emerge [48]. Hence, cells become mechanically coupled to the ECM through the interaction of matrix proteins such as fibronectin to integrin cell surface receptors. Thus, cells are able to sense exerted extrinsic forces but also ECM rigidity associated with distinct tissues types or cell compartments. Cell-ECM interactions enable the coupling of mechanical and biochemical factors to ensure morphogenesis and tissue patterning in a growing organism or organ, thus connecting macro-scale physical inputs to nanoscale chemical signaling [36,48].

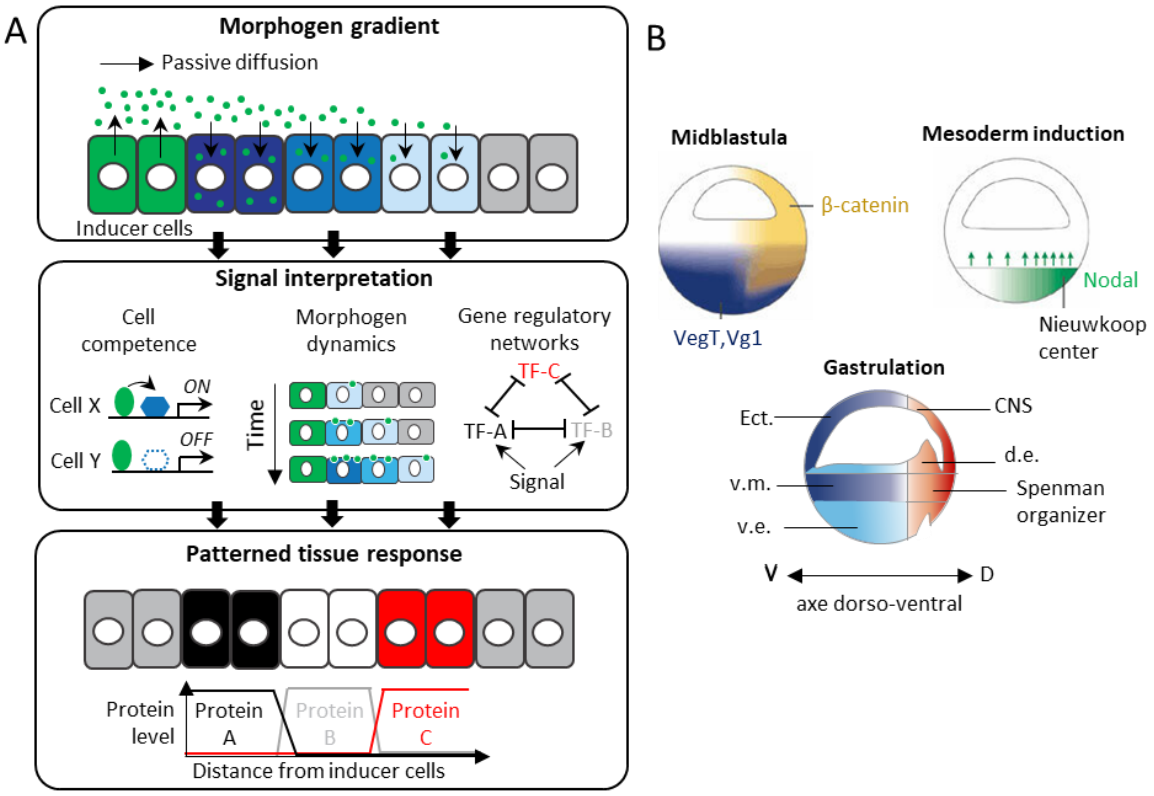

Figure 2. Historical concept of tissue patterning Induction by morphogens. A) Principles of morphogen gradient interpretation. Adapted from [49]. Morphogen dictate patterned tissue response (e.g. lineage specification, cell proliferation or cell survival) in a concentration-dependent manner. Interpretation of inductive signals by receiving cells depends on cell-intrinsic competence to induce specific target, duration of inductive cues exposure and cell signaling through gene regulatory network. TF-X: transcription factor X. B) Model of mesoderm specification in xenopopus embryo. Adapted from [43]. At the midblastula stage, higher -Catenin levels on the dorsal side of the embryo, together with the vegetally located transcription factor VegT and the maternal TGF-family growth factor Vg1, generate a gradient of Nodal-related molecules expressed in the endoderm. In turn, this gradient induces the formation of overlying mesoderm: low doses of Nodal-related molecules lead to the formation of ventral mesoderm, whereas high doses lead to the establishment of Spemann's organizer. Ect, Ectoderm; v.m., ventral mesoderm, v.e, ventral endoderm; d.e, dorsal endoderm.

During postnatal life, tissue homeostasis and tissue regeneration upon injury is ensured by tissue resident progenitors and adult stem cells. Upon activation, stem cells proliferate and differentiate into functional cells. Maintenance of tissue homeostasis thus relies on the capacity to maintain a pool of stem cells throughout life which depend both on self-renewal ability of these cells and the maintenance of their stemness [6,14]. Adult stem cells can either exist in a proliferating stage or non-proliferative quiescent stage [40]. Highly cycling adult stem cells can be found in tissues undergoing continuous loss of cell mass such as epithelium (e.g skin, intestine) [5]. By contrast, quiescent stem cells such as in the liver only proliferate in response to injury and cease dividing once the tissue is restored [50]. Adult stem cells reside in specific locations called “niches” which correspond to a specific

microenvironment protecting them from damaging stimuli, pro-proliferative and pro-differentiating instructive cues (Figure 3) [51]. Stem cells can undergo symmetric or asymmetric division [51]. Symmetric divisions generate two daughter cells that remain in the same niche environment and which are mostly identical. Conversely, asymmetric division generates a daughter cell that remains inside the niche and inherits stem cell characteristics while the other cell is further located from the protective niche and starts to differentiate into a committed progenitor [51]. These committed progenitors are highly proliferating cells that are able to differentiate into specific cells. Both progenitors and mature cells reside also into specific microenvironments that maintain their identities (Figure 3). The reliance of stemness on environmental cues raise the question of whether the understanding of stemness can be abstracted from the microenvironment and be considered as a cell identity rather than a cell state [52].

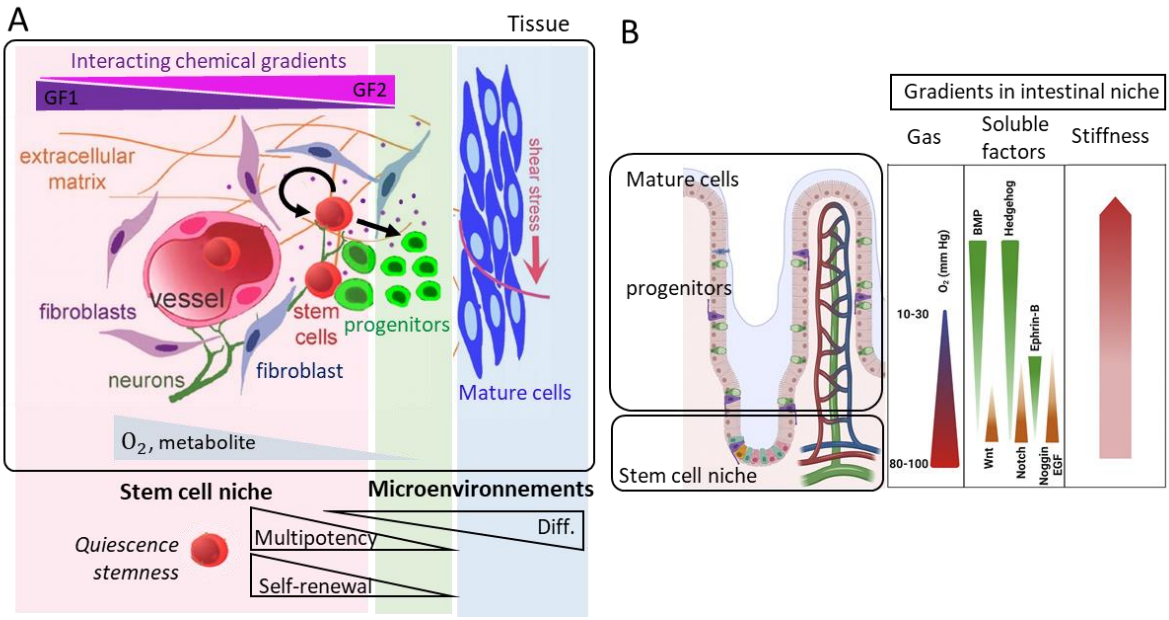

Figure 3. Regulation of adult stem cells renewal and differentiation is coordinated by interacting extrinsic signals. A) Schematic representation of stem cell niche components. Stem cells reside in specific microenvironment that inhibit their proliferation and differentiation. Upon activation, stem cells produce progenitor cells that moved further away from the niche and that are able to differentiate into mature cells. Adapted from [53]. B) Example of intestinal stem cell niche. Gradients of soluble factors, O_2, ECM networks and underlying stromal stiffness along the villus-crypt axis regulate stem cell function and consequent tissue homeostasis. Adapted from [54]. GF, growth factor; Diff., differentiation; BMP, bone morphogenetic protein; EGF, epidermal growth factor.

Within the niche, as for during embryonic development, regulation of adult stem cells proliferation and differentiation is coordinated by interactions of cell-intrinsic factors and extrinsic signals. These extrinsic signals include neighboring supporting cells, regulating stem cells fate through cell-cell interactions and paracrine secretions, the ECM, neural inputs and blood vessels relaying long-range

biochemical signals (Figure 3A). In addition to its role in cell communication, blood vessels ensure supply of oxygen and metabolite critical for cell proliferation [55]. Hence, similarly to embryonic development, gradients of growth factors and variations of ECM rigidity are key regulators of adult stem cell niches and therefore tissue homeostasis [11,56]. A well described example is the intestinal stem cell niche where opposed Wnt/BMP gradients control axial distribution of stem cell, progenitors and differentiated cells compartments along crypt-villi axis [57] (Figure 3B). The Hippo mechano-transduction pathway and its effector protein YAP are key in the coordination of cell mechanical environment and proliferation control [58,59] (Figure 4). Stem cell niche often correlates with soft ECM which reduces cell adhesion and consequently inactivate YAP/TAZ while stem cells moving away from the niche encounter progressive ECM stiffening resulting in YAP/TAZ activation and downstream proliferation activation.

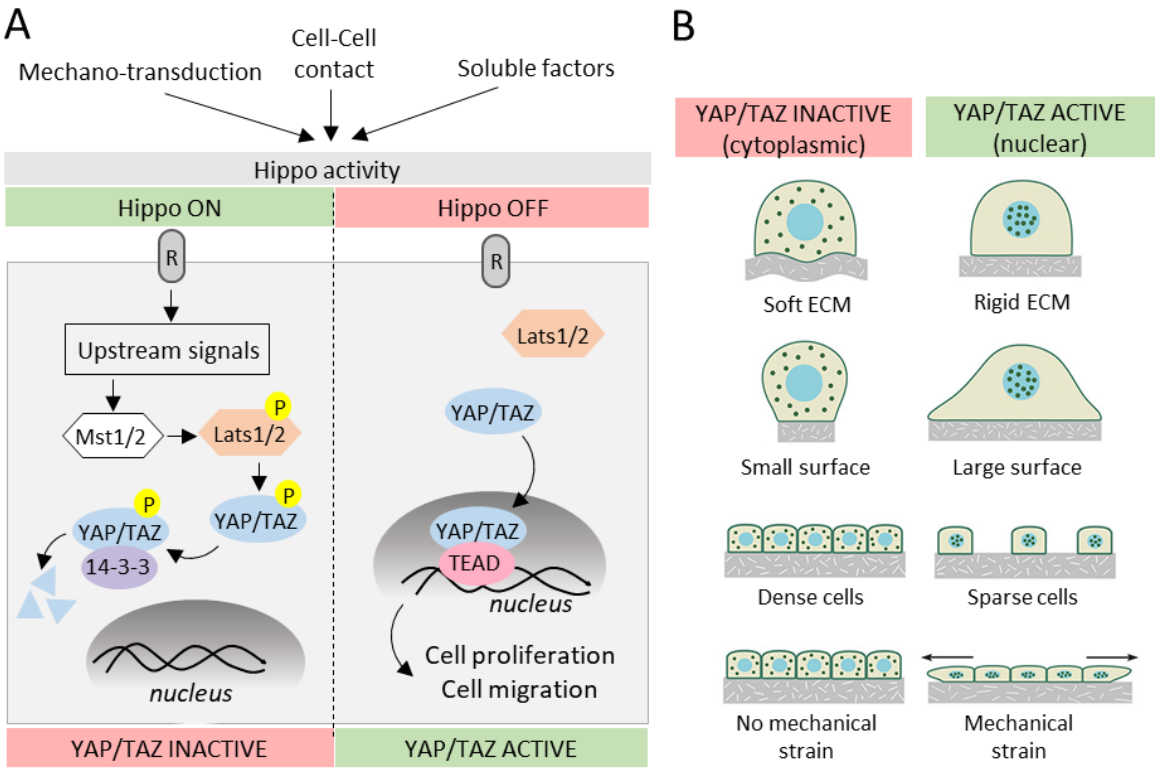

Figure 4. Regulation of YAP/TAZ activity by extrinsic factors. A) The Hippo pathway regulates YAP/TAZ protein localization, co-transcription factors involved in controlling cell proliferation and migration. When the Hippo pathway is active (Left), upstream signals phosphorylate MST1/MST2 and LATS1/LATS2 kinases, leading to YAP/TAZ phosphorylation. This phosphorylation recruits 14-3-3 proteins, either sequestering YAP/TAZ in the cytoplasm or triggering their degradation. Conversely, in an inactive Hippo pathway (Right), unphosphorylated YAP/TAZ translocate to the nucleus and interact with TEADs transcription factors at target gene promoters. B) Regulation of YAP/TAZ activity by mechanical and topological cues. Adapted from https://www.mechanobio.info. YAP/TAZ localization and phosphorylation status is regulated by extracellular matrix (ECM) stiffness, spreading of the cells, cell density and mechanical forces relayed by cell-cell and cell-ECM adhesion.

Therefore, we can understand that the regulation of cell development during both organism development and the lifelong maintenance of tissues shares several common principles. These encompass the dependence of cell responses on the exposure to multiple extrinsic signals including pivotal roles of exposition to spatially distributed chemical factors and to cell-cell and cell-ECM interactions that couples mechanical and biochemical factors. Moving forward, we will explore the importance of stochasticity in cell fate decisions and how it contributes to plasticity of the cells to respond to their microenvironment.

1.2. Stochasticity of gene expression supporting cell-to-cell decisions variability

Classically, the development of multicellular organisms has been viewed as a reproducible and thus determinist course of events. At that time, most of the knowledge was derived from cell population-based endpoint assays that do not reflect spatio-temporal dynamics of gene regulation in stem cells and progenitors during embryonic development and post-natal life. Transcriptional studies at the single cell level have revealed an inherent stochasticity and dynamic of gene expression which can result in stem cell fate variability [37–39]. Apprehending heterogeneity of cells within a given cell population is key to understand cell variability in response to environmental cues. Identifying processes by which multicellular system exploit or compensate these mechanisms are important to understand how to yield reproducible *in vitro* tissue development with physiological relevance.

Gene expression depends on concentrations, state and location of molecules such as transcription factors. Fluctuation in the amount or activity of these molecules between cells lead to fluctuations in the output gene and constitute extrinsic sources of gene expression noise which are global to a single cells [60]. Besides, rate of gene expression varies due to intrinsic randomness of molecular interactions, which applies to each gene [60] (Figure 5).

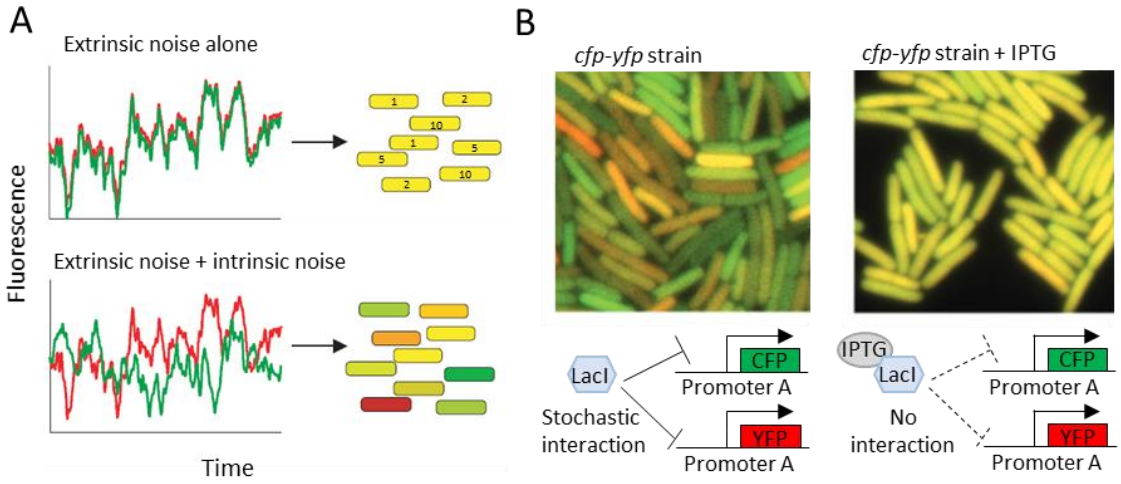

Figure 5. Principle of extrinsic and intrinsic noise in cell-to-cell variability of gene expression. A) Schematic depiction of the temporal behaviors of extrinsic noise (upper) and intrinsic noise (lower). Example of noised gene expression of two fluorescent proteins YFP (red) and CFP (green) identically regulated. Cells expressing equal amount of each protein appear yellow, whereas cells overexpressing one fluorescent protein over the other appear either red or green. Without intrinsic noise, both proteins fluctuate together within cells (upper left), with varying levels among cells due to external noise (upper right). Intrinsic noise can decouple the expression of both genes in individual cells (lower left), causing some cells to favor one fluorescent protein over the other (lower right). B) Demonstration of intrinsic noise in E. coli expressing YFP and CFP under promoter identically repressed by LacI. E. coli exhibit YFP and CFP independent fluctuations in protein expression under LacI repression (Left). Inactivation of LacI by IPTG decreases intrinsic noise (right). Adapted from *[60]*.

Gene expression noise is also regulated by epigenetics modifications, inhibitory epigenetics marks such as DNA methylation correlating with reduced noise conversely to activating epigenetics marks such as acetylations [38]. Stem cells from the "openness" of their chromatin exhibit gene expression noise for most of their genes leading to small expression variations between single stem cells. Heterogeneous gene expression among single cells is an important factor in the generation of plastic identities [37,38]. Single cell RNA sequencing on hematopoietic progenitors has revealed that hematopoietic stem cells are not equivalent but contain various populations of cells exhibiting differentiation bias toward diverse lineages [61]. Hence, gene expression stochasticity can generate primed stem cells able to respond rapidly to extrinsic cues followed by clone selection processes (Figure 6). Besides, the classical view of the existence of few stable cell states corresponding to stem cells, committed progenitors and differentiated cells would have suggested the presence of cell clusters clearly defined with sharp transitions from one stage to another. However, these studies demonstrated smooth transitions from a cluster to another demonstrating that at any given time all cell states coexist within the same tissue.

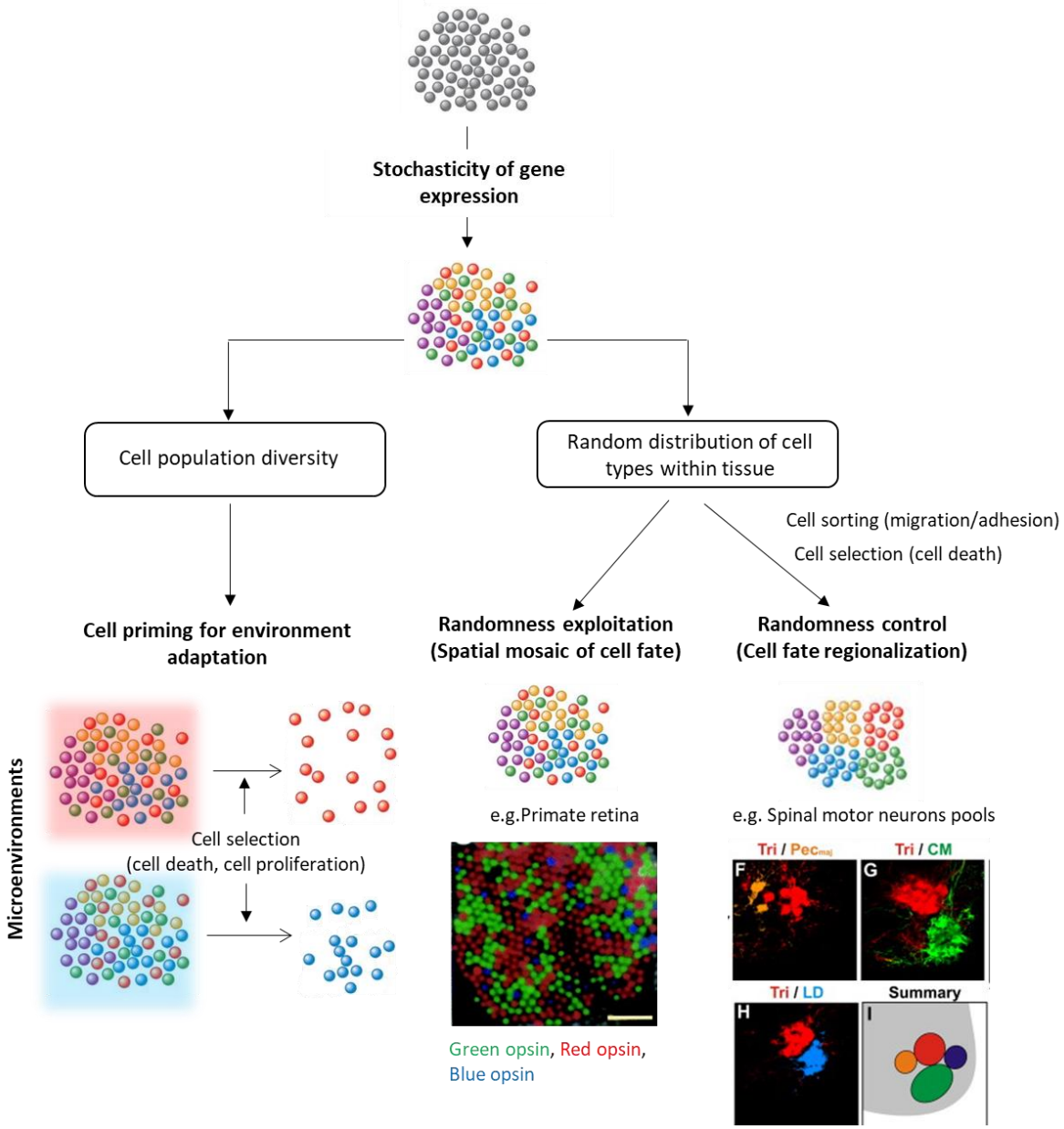

Figure 6. Stochasticity of cell fate specification: exploitation and compensating mechanisms in development. Stochasticity of cell fate specification: exploitation and compensating mechanisms in development. Stochasticity of gene expression induces the generation of a mosaic of cell fate randomly distributed in space. Cell adversity contributes to robust adaptation of populations by cell selection processes (e.g. cell death, clonal cell proliferation) to change in microenvironment. Some systems utilize stochastic mechanisms in specific development programs to generate random patterns of cells such (e.g. photo-receptor selection in primate retina). Other developmental programs compensate for, or direct, stochastic fate specification to yield reproducible and robust outcomes (e.g. specification and regionalization of motor neurons pools). Adapted from (*[37,62,63]*)

As stochastic cell fate specification can generate cellular diversity it can also generate random outcomes during developmental processes [37]. There are examples of systems exploiting developmental randomness to generate mosaics of cell fate across a tissue such as primate photoreceptors across the retina [64] or olfactory sensory neurons across the mouse olfactory system [65] (Figure 6). On the other hand, stochastic fate decisions can impair tissue function when regionalization of cell fate is required. To ensure robust cell compartments, compensating mechanisms exist such as controlled cell deletion through apoptosis or cell sorting [37] (Figure 6). In developing embryos, apoptosis drives morphogenesis and tissue shaping by directing for instance tube hollowing or the removal of interdigital webbing [66]. Apoptosis is also involved in shaping ramified structures such as mature neuron networks [67] or endothelial cell networks [68]. In the context of regeneration, apoptosis also contributes as a late signal regulating tissue patterning [69].

Cell sorting involves both segregation mechanisms by which mixed populations of cells with different fates or properties are redistributed into distinct domains and the maintenance of this segregation delimiting tissue or cell compartment "boundaries". Such cell properties have been exemplified through experiments of cell aggregate dissociation and reassociation [70,71]. When embryonic cells from different cell compartments where mixed together, they first aggregated together to form a cell mass. Then, within the mixed aggregate, cells progressively joined cells from the same origin. This was the first demonstration of autonomous self-assembling and self-organizing abilities of cells. Apart from this artificial illustration of the cell sorting process, the migration of motor neurons during development serves as a tangible instance of cell sorting that facilitates the formation of robust motor neurons pools necessary for electrical coupling [72].

Diverse models have been proposed to explain cell sorting and boundary formation; those details have been reviewed elsewhere [73–75]. Although still not completely understood, data indicate that cell sorting mechanisms strongly rely on cell-cell interactions through mechanical coupling and cell adhesiveness. Boundaries correlate with highly localized signals leading to discontinuities in cell adhesion such as contact inhibition by ephrin/eph signal [76] or such as differential expression of cadherins based on homophilic interactions or overall cadherins expressions [77].

Cell development is intrinsically stochastic. Within living tissues, cells display important cell-to-cell variability in gene expression leading to highly heterogeneous and dynamic cell populations. Stem cell *heterogeneity is an important factor of plastic and rapid adaptation of tissues to microenvironment changes. Driving selection of specific phenotype requires engineering environment that would maintain survival of targeted cells and their progeny. While stochasticity helps to generate cell complexity, cell adhesion and cell migration processes are key sorting processes to allow cell rearrangements and lead*

to regionalized cell compartments. Following section will describe how cell migration participates to tissue shaping through these cellular reorganizations and which parameters intervene in its regulation.

1.3. Tissue shaping and cell migration

Cell migration is a key cellular process which is fundamental both during organism development and tissue regeneration upon injury. Cells are able to migrate individually as single cells or collectively as a group. Collective migration is essential to control the spatial distribution of cells and ensure the morphogenetic movements that shape the complex architecture of tissue and organs during development, i.e. morphogenesis [35]. Examples include collective migration of cell sheets during gastrulation participating in the establishment of three germ layers (Figure 7A). A good example of tissue structuration through cell migration in adult tissue is the branching morphogenesis of vascularization after tissue damage or during tissue expansion [45] (Figure 7B). As the fundamental support for oxygen and nutrients exchanges required cell functioning, vascularization is able to remodel according to cell needs, driven by hypoxic signals.

Cells adopt migratory behavior by modification of their cytoskeleton. Motile cells are polarized with the formation of pseudopods whose stabilization determines the directionality of the movement [78]. The continual extension of pseudopods which ensure cell movement is tightly associated with actin cytoskeletal dynamics and adapts to extrinsic signals through interaction of cells with their extracellular microenvironment. These extrinsic signals include the presence of soluble guidance cues [35] and interactions with the extracellular matrix [48] (Figure 7). To ensure collective cell migration, front and back cells of the group have to be mechanically linked through cell-cell interactions to propagate cell displacement [79–81] (Figure 7). The front cells that undergo protrusion formation and sense environmental cues are referred to as leader or tip cells (Figure 7). In sprouting angiogenesis, the tip cell is in a leading position and actively migrates while follower cells contribute in the elongation of the migrating groups by other mechanisms such as proliferation [35,45] (Figure 7B).

Response to chemotactic cues produced in the surrounding environment is key in the regulation of cell migration directionality. Most migrating cells possess molecular machinery enabling them to sense and move along gradients of soluble attractant and repellents through a process called chemotaxis. These soluble factors include growth factors such as TGF-β, well known to promote fibroblasts and myofibroblast migration [82], or VEGF-A a key chemoattractant in guiding mammalian angiogenesis. Endothelial tip cells sense VEGF-A gradients while overall concentration of VEGF-A promotes cell proliferation of follower cells [45]. Some VEGF molecules contain heparin-binding domains promoting

their binding to ECM components [83]. Hence, the ECM also regulates bioavailability and gradient formation of chemotactic cues.

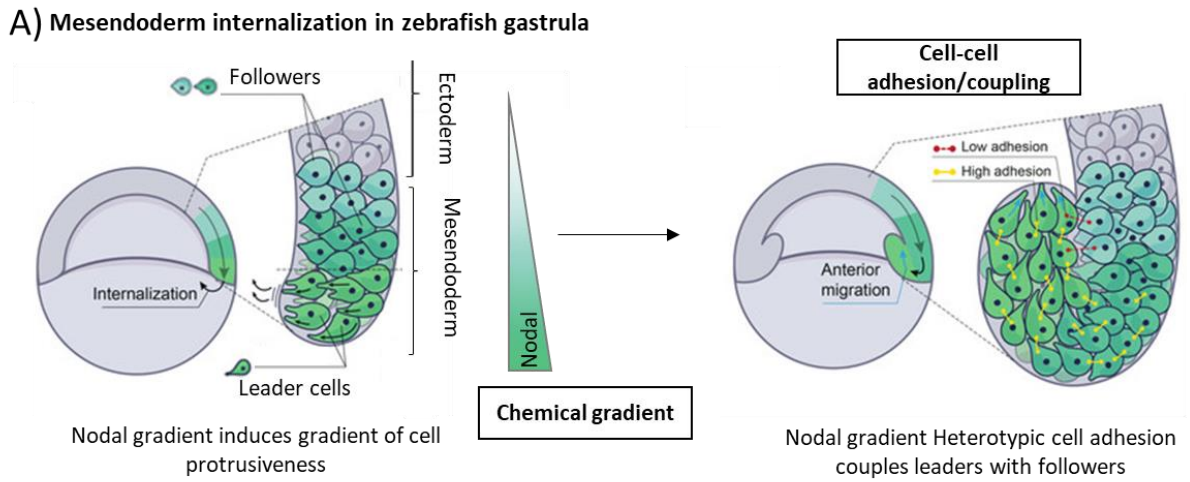

Figure 7. Collective migration in tissue structuration involves chemotactic cues, cell-cell coupling and ECM remodeling. A) Mesendoderm invagination during gastrulation of zebrafish embryo. Chemical nodal gradient induces mesendoderm specification and mechanically subdivides the tissue into leader and follower cells. Nodal signalling gradient further reinforces a system of heterotypic adhesion, connecting leaders to their immediate followers, leading to the collective and organized internalization of mesendoderm. B) Sprouting angiogenesis. Tip lead cell and follower stalk cell are formed in response to angiogenic stimuli such as hypoxia and gradient of proangiogenic growth factor VEGF-A. Following basement membrane and matrix degradation by matrix metalloproteinase (MMP), tip cell starts to form lamellipodia and filopodia to migrate while stalk cells proliferate to elongate the nascent vessel sprout. Tip cell ensures sensing of chemotatic cues driving migration direction.

In addition to its role in the distribution of growth factors, the ECM directly influences cell movement as a physical support for cell migration [48]. Formation of polarized protrusions in migrating cells is mediated by their adhesion and exertion of traction on physical substrates. Control of protrusion polarity and force traction require integrin/fibronectin interaction. Protrusion formation was reported to be promoted in xenopus mesendoderm cells cultivated on fibronectin substrate *in vitro* [84] while there was impaired in response to functional blockade of $\alpha_5\beta_1$ integrin [85]. Moreover, cells are able to sense mechanical properties of the ECM [48]. *In vitro* studies of cell migration assays showed that substrate stiffness affects cell migration with various effect depending on cell types [86–88]. Some studies have reported that fibroblastic cells tend to migrate faster and more efficiently on 2D rigid substrates [89]. Besides, Hadden et al. showed that mesenchymal stem cells tend to migrate toward the stiffer part of the substrate when cultivated onto substrate exhibiting steeper gradients of rigidity [90]. However, *in vivo* cells are almost never confronted to this planar configuration and thus how cross-link density influences cell migration should be considered in 3D substrates. Reduced porosity of 3D matrix is associated with reduced cell migration [86]. In addition, cell migration was shown to be influenced by degradability of the matrix in which they are encapsulated [86]. Localized degradation of the ECM environment is an important parameter controlling branching morphogenesis during vasculature development [45].

To summarize, we have seen that in vivo tissue development and homeostasis result from combination of interacting cell processes including progressive stem cell differentiation, cell proliferation, cell selection through cell survival and cell rearrangement through collective cell migration. All of these cellular processes are under an important control from surrounding cell microenvironment which identify biochemical factors and their distribution, cell-cell and cell-ECM interactions as key parameters to drive cell behaviors. In embryonic development, the system is continuously evolving with successive establishment of temporary local microenvironments that shape and pattern tissue overtime. In adult tissues, specific established microenvironment regulates the maintenance of stem cells and progenitors' populations required for tissue homeostasis. These cell populations are highly heterogeneous due to stochasticity of gene expression which can induce drifts in cell phenotype by cell selection processes upon chronic change in cell microenvironment. This highlights the importance to define conditions in vitro that would allow to recreate and maintain appropriate cell microenvironment for generating complex tissue with long-term maintenance and functionality. Hereafter, we will provide an overview of the primary approaches that have been proposed by organoids and engineering tissues communities to confront this challenge (see II.2).

2. Two main conceptual approaches for *in vitro* generation of complex tissues

Two primary desires have prompted research on the *in vitro* generation of tissue and organ-like constructs: 1) generating *ex vivo* models to better understand and simulate physio-pathological developmental processes 2) creating tissue substitutes for the purposes of replacement therapies and regenerative medicine. Historically, these two intentions have nourished and built two respective research communities, those of organoids and tissue engineering. Following section will provide insights on historical conceptual approaches that have prompted these fields.

2.1. Organoids: nature-driven engineering of tissue

Historically, establishment of organoids culture takes roots in the demonstration of inherent capacity of vertebrate stem cells to self-organize. The term organoid originally emerged in the field of developmental biology and gained in popularity in the years 1965-1985 to describe the organogenesis potency observed within cells during classic experiments of cell dissociation and reaggregation [91,92]. Even after total dissociation these cells were able to rearrange themselves and turn into structure recapitulating the original architecture of the organ (for an overview, see [93]).

Since 2009, the term “organoids” has gained renewed interest with a variation of its definition [91,94]. Most commonly, the term organoids refer to as 3D multi-cellular microtissue derived from stem cells that differentiate and self-organize to generate organ-like tissue when provided with ECM mimicry and growth factors (Figure 8). Organoids recapitulate key processes of organogenesis including cell sorting and spatially restricted lineage commitment [93]. Organoids exhibit multiple organ-specific cell types and should recapitulate some aspect of both complex structuration and functionality of the corresponding *in vivo* organ. Compared to 2D culture, organoids better resemble the native organ regarding transcriptional, proteomic and metabolic as well as regarding microscale tissue architecture [91,95].

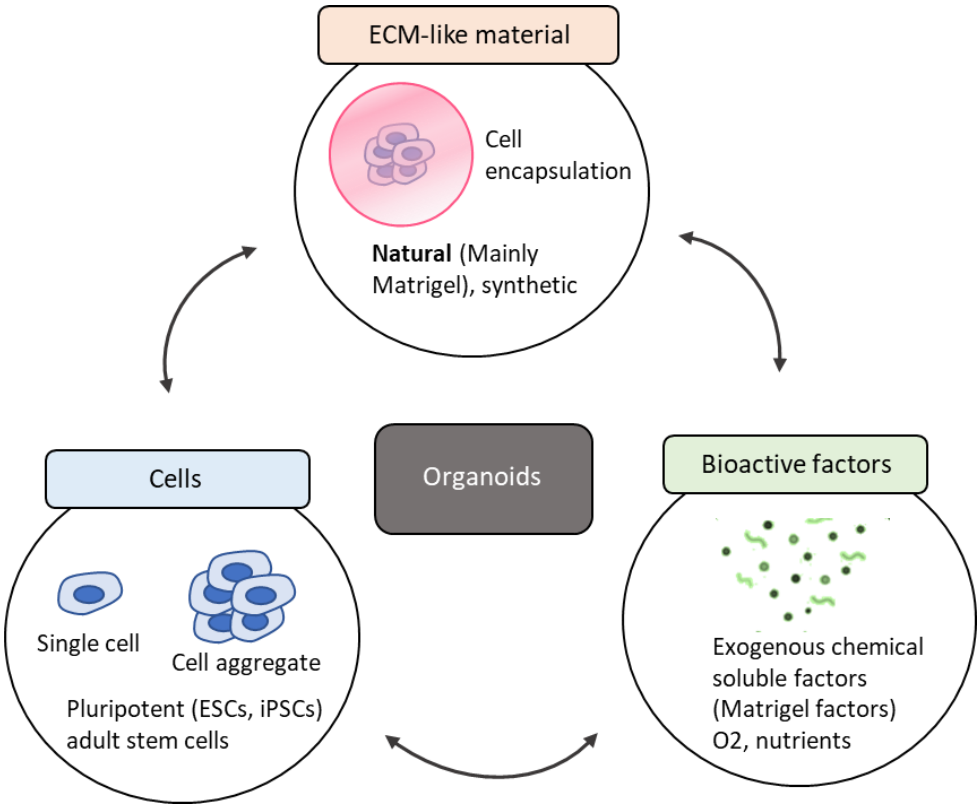

Figure 8. Components of organoid culture generation. ESC, embryonic stem cells; iPSC, induced pluripotent stem cells.

The generation of organoids is based on the use of stem cells. Stem cells possess unique properties that allow them to both self-renew and differentiate into multiple cell types. The balance between self-renewal and progenitor commitment is strictly regulated by the stem cell niche[12], as defined in II.1.1. Archetypal organoid systems aim to recreate this stem cell niche to drive their inherent ability to organize in space and time to recapitulate morphogenesis. First demonstration of such a system was performed by the laboratory of Hans Clevers [94]. They showed that embedding Lgr5+ intestinal stem cells with 3D Matrigel and providing them with soluble niche signals promoted their proliferation but also directed them to follow their innate developmental programs to produce crypt-like projections. Few years later, Lancaster et al. reported the generation of brain organoids from human pluripotent stem cells exhibiting different brain regions [96]. Using patient-derived cells, authors succeeded to generate a model of microcephaly setting organoids as powerful tool to study human development. Since then, numerous organoids have been described from an increasing variety of organs [91,95] (Figure 9). Most of them still rely on the use of Matrigel combined with sequential delivery of soluble niche factors [91,95].

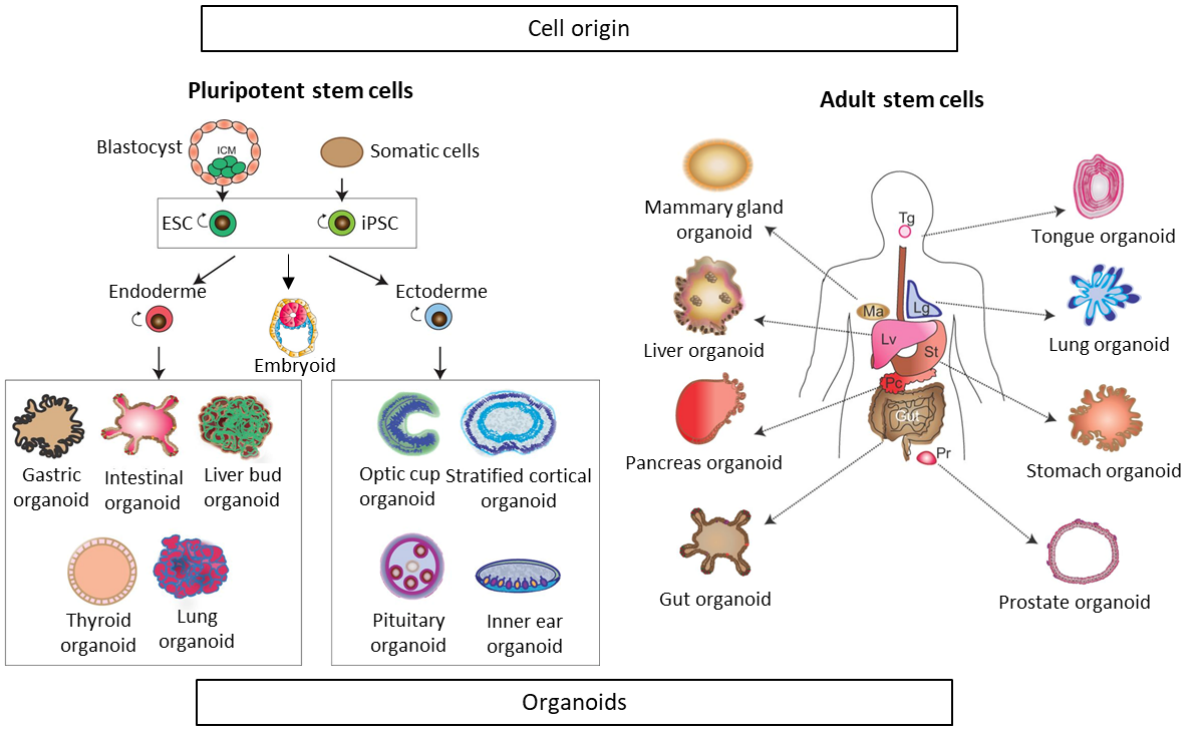

Figure 9. Variety of organ specific organoids can be derived from pluripotent and adult stem cells. Organoids derived from pluripotent stem cells (PSCs) can originate from either embryonic stem cells (ESCs) or induced pluripotent stem cells (iPSCs). These organoids have the capacity to differentiate into various germ layers (endoderm, mesoderm, and ectoderm) in vitro using specific stepwise differentiation protocols. Following the initial specification of germ layers, cells are transferred into 3D systems, where they form organoids that faithfully replicate the developmental processes that occur in vivo. On the other hand, organoids derived from adult stem cells can be generated using adult stem/progenitor cells or tissue fragments from the corresponding organ. Under these conditions, the cells exhibit self-organization in culture while preserving their genetic stability and commitment to their tissue of origin. Adapted from *[97]*.

Organoids can be derived from tissue-resident adult stem cells obtained from biopsies [94,98] or from pluripotent stem cells (PSC) including embryonic stem cells [93,99] and induced pluripotent stem cells (iPSCs) derived from reprogramming of differentiated cells [100,101] (Figure 9). Organoids generated from adult stem cells derived from highly regenerative organs such as intestines benefit from their intrinsic ability to continuously generate progeny to ensure constant replacement of cells. Thanks to the maintenance of stem cells within adult stem cell-derived organoids, these organoids can be expanded almost indefinitely [94]. Generation of organoids from adult stem cells strongly relies on our understanding of instructive cues in a context of tissue repair or regeneration. Conversely, PSC-derived organoids offer an alternative to model organs for which stem cells cannot be easily retrieved such as the brain [93,100]. They also represent a powerful tool to model developmental processes of organogenesis and early life embryogenesis with the emergence of “embryoids” [102,103]. Generally, generation of pluripotent stem cell-derived organoids is a long-lasting process composed of several

steps which aim to provide sequential instructive developmental cues to progressively restrict the differentiation potential of pluripotent stem cells to the required cell lineages.

Currently, organoids exhibit the highest level of *in vitro* organ functionality achieved so far. As a result, they hold great potential in disease modeling for advancing personalized medicine and conducting next-generation drug screening, aiming to reduce the reliance on animal testing. Organoids are also promising platforms for damaged tissue replacement or restoration, provided the possibility to generate large-scale tissue organoids (see III). Nevertheless, several limitations still remain to be overcome before this vision can be realized (Table 2). Firstly, organoid generation is highly dependent on the stochastic nature of development processes which leads to poor reproducibility and important variability in morphology and functions [91,95]. Another explanation for this variability lies in the non-completely defined condition of culture that are currently used in the great majority of organoids. As a raw material extracted from the Engelbreth–Holm–Swarm mouse sarcoma, Matrigel often displays batch to batch variability regarding its composition and its mechanical properties [104]. Reducing this variability for instance by better microenvironment controls through engineering would be crucial for their applications in biomedical sciences. Besides, organoids still show incomplete maturation. Organoids derived from epithelial adult stem cells often fail to recapitulate the whole cellular complexity of native organs mostly due to the restricted differentiation lineages in which these cells can engage. Complete maturation would require the presence of mesenchymal compartments and vascularization. This maturation is also hindered by the lifespans of organoids which is often in disagreement with the duration required for the generation of the whole spectrum of differentiated cell types from stem cells. This is especially true for organoids derived from pluripotent stem cells which fail to mature beyond a fetal stage [91,95]. This limited lifespan of organoids is due to nutrient inaccessibility leading to the development of necrosis areas at the core of the structure. For this same reason, organoids cannot be grown beyond millimetric scale [95]. Organoids progressively grow in size until they reach a critical limit. This is especially true in organoids exhibiting compact structures such as brain organoids (up to 4 mm in diameter) [32,95]. Organoids derived from epithelial cells (e.g. intestinal, pancreas, lung) form hollow structures which progressively accumulate dead cells in their lumen, requiring frequent mechanical fragmentation of organoids to get removed [95]. The necessity of constant organoid fragmentation prevents the generation of large-scale organoids

Table 2. Organoid culture characteristics. ESC, embryonic stem cells; (i)PSC, (induced) pluripotent stem cells

Characteristic type	Organoid culture
Driving concept of in vitro tissue generation	Promoting self-organization of cells by initiating the intrinsic capabilities of stem cells to engage in cascades of developmental events
Cell source	Pluripotent stem cells (ESC, iPSCs), Adult stem cells
Achievements	Multiple organ cell types, organ specific functions and microarchitecture, recapitulation of some morphogenesis processes
Limitations	Low reproducibility, strong reliance on Matrigel, incomplete maturation (PSCs-organoids), size < 1 mm
Uses	Disease and development modeling, drug screening, medicine regenerative, personalized medicine, cryo-banking, phylogenetic studies

2.2. Tissue engineering: structure-driven engineering of tissue

Tissue engineering finds its source in the field of regenerative medicine and many others have used these terms synonymously [105]. Regenerative medicine encompassed all the means allowing the regeneration and remodeling of tissue for the purpose of repairing, replacing or enhancing organ function including cell therapy and tissue engineering [106]. In 1987, the National Science Foundation first defined tissue engineering as “an interdisciplinary field that applies the principles of engineering and the life sciences towards the development of biologic substitutes that restore, maintain, or improve tissue function.” [9,10]. Therefore, therapeutic applications for tissue restoration stands as a central focus in the field of tissue engineering.

Historically, tissue engineering has emerged as the second generation of cell-based therapy [105,107]. First-generation cell therapies use direct injection of isolated cells either using tissue progenitors and expecting them to participate in tissue repair or using mesenchymal stem cells as a source of pro-regenerative factors through their paracrine activities [107,108]. However, a major limitation of cell therapy is the poor retention rate of injected cells. Although beneficial effects of these approaches were reported, most studies concluded that few of them manage to survive post-transplantation. This low cell retention can be explained by their inability to withstand the adverse conditions of the disease environment or to their elimination by the bloodstream. Consequently, tissue engineering approaches have been developed to enhance transplanted cell survival and their integration to the native tissue.

Tissue engineering is based on the use of scaffolds to mimic ECM and provide cells with a 3D supporting structure [105]. These scaffolds are more broadly referred to as biomaterials. These biomaterials could be derived from natural sources or can be synthetically generated [109]. They should be biocompatible with low immunogenicity, biodegradable and bioactive to stimulate tissue responses. Tissue

engineering encompasses both *ex vivo* and *in situ* tissue engineering [105]. *In situ* engineering consists in the use of acellular scaffolds as implants designed to enhance *in situ* capacity of cells to regenerate tissue at injury site *in vivo* [110]. *Ex vivo* tissue engineering aims to generate transplantable living tissue constructs composed of cellularized scaffolds which recapitulate structure and functionality of *in vivo* tissue [9]. Moving forward, our attention will be directed towards *ex vivo* tissue engineering, which we will refer to simply as tissue engineering for the sake of simplicity.

The driving force behind the advancement of tissue engineering methodologies stemmed from the desire to mimic nature. It attempts to maximize cellular functions by recreating tissue composition, architecture and interactions of cells within their local environment [13]. As discussed in 0, cell microenvironment largely influences cell behaviors. Thus, standard tissue engineering approaches combine the use of three factors: cells, biomaterials and signaling molecules (Figure 10). A large variety of biomaterials have been proposed from solid macroporous structure for bone generation to polymeric hydrogel for soft tissue generation [109]. More details will be given in part 3.1. Classical tissue engineering approaches mainly involve one-step seeding and culturing of cells into 3D biomaterial scaffolds that are designed to mimic target tissue architecture [8,9]. Generally, cells are seeded as cell suspension either prior to scaffold generation by mixing cells with the biomaterial [111–113] or on top of pre-formed scaffold requiring cell infiltration [114,115].

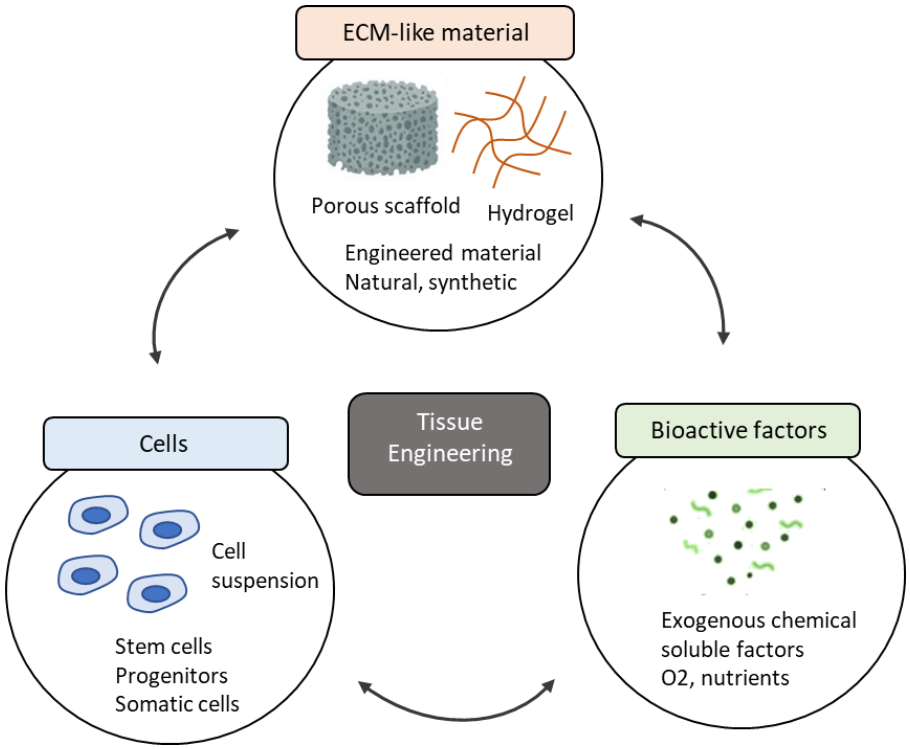

Figure 10. Components of classical tissue engineering approaches.

In opposition to organoids systems which focus on the use of pluripotent and multipotent stem cells, tissue engineering approaches have been described with a broader range of cells. The main consideration is that these cells should have the capacity to express the phenotype of the desired tissue and exist in easily accessible, abundant cell sources. These cell sources can be autologous or allogeneic. Thus, tissue engineering approaches have been obtained using stem cells [116], committed progenitors [117] or even somatic cells such as chondrocytes [113,115]. Regarding stem cells, methods have been described with all types of potency including pluripotent stem cells [118] (e.g. embryonic stem cells, iPSCs), multipotent and unipotent adult stem cells [119] or mesenchymal stromal cells (MSCs) [120] (Figure 10). An important variety of protocols for cell preparation have been reported depending on the cell sources. Most protocols contain steps of cell isolation, cell expansion in 2D cultures, followed or not by cell engagement and/or differentiation steps before harvesting them for assembly with the biomaterial [116,117]. Behind this firstly stands the necessity to produce a high number of cells with homogeneous cell response. This is crucial to ensure sufficient starting material to expect an efficient and reproducible therapeutic effect after transplantation. Secondly, classical tissue engineering approaches rather focus on the co-culture of multiple cell types to mimic tissue cell complexity than driving inner development of stem cells toward all their progenies within the construct.

Tissue engineering holds great promise regarding the development of ATMPs (Table 3). Thanks to the advances in the fields of biomaterials and fabrication technologies, scaffolds can be generated in more and more reproducible and cost-effective manners allowing cells to be seeded in well-defined conditions [121,122]. Some tissue-engineering constructs have already proved their performance in clinical applications such as engineered human skins [123]. However, few successes were reported regarding the generation of fully functional tissues with more complex anatomic structures. Indeed, despite the considerable efforts invested in generating scaffolds that increasingly mimic native tissue, classical tissue engineering approaches often result in limited cellular organization [124,125]. A significant limitation encountered with traditional seeding of single-cell suspension is the achievement of low cell density within tissue constructs [125]. This limitation impedes the cell-cell interactions that underpin collective cellular behaviors and cell tissue functionality. Furthermore, tissue scaffolds are frequently designed beyond the millimetric scale, aiming to replicate the size and morphologies of the target tissue [124,125]. However, nutrient diffusion can be impaired within the scaffold reducing cell viability and functionality.

Table 3 Summary of classical tissue engineering approaches characteristics.

Characteristic type	Engineered tissue constructs
Driving concept of in vitro tissue generation	Biomimicking defining features of native tissues (architecture, cell composition)
Cell source	stem cells, mesenchymal stromal cells, progenitors, differentiated somatic cells
Achievements	Defined biomaterial composition, cell maturation in vivo, reproducible and cost-effective scaffold generation, scaffold can be designed > 1 mm
Limitations	Low functionality, weak cell-cell interactions, low self-organization of cells, long term culture
Uses	Medicine regenerative, personalized medicine, (physiopathology studies, drug screening)

Both organoids and tissue engineering approaches rely on the combination of three main components which are cells, ECM-like material, and signaling molecules. The ultimate objective is to provide cells with a 3D microenvironment to obtain functional tissues in vitro. However conceptual frameworks underlying these approaches were historically different between the two research communities. The organoid community intended to recreate stem cell niche to harness the intrinsic developmental potential of stem cells *and promote emergence of self-organized local microenvironments. Conversely, historical engineering tissue approaches adopted a biomimetic and relatively static perspective of the microenvironment, aiming to provide more committed cells with defining characteristics of native tissues. Doing so, the field of tissue engineering have contributed to the development of biomaterials to tailor cell microenvironment to a given application. However, these approaches led to low cell organization where organoids demonstrated impressive capacity of cells to self-organize, although stochastically, when cultivated in appropriate conditions.*

Self-organization is a phenomenon in which ordered structures arise from local interactions of disordered elements. the spontaneous formation of ordered structures can be explained by the dynamic and non-linear interactions of the distinct elements. Cells constantly adjust their state according to the signals received by the neighboring cells and the environment, leading to cell diversification through events of self-organization. Starting from uniform condition, stochastic fluctuations and cell interactions induce change of sates with a progressive increase of order associated with well-defined conditions. The following section will give some principles on how we can regulate these interacting elements through microenvironment engineering to guide self-organizing of cells toward a specific outcome in vitro (see II.3).

3. Driving self-organization of cells through 3D engineered microenvironment

Past years have seen a change in paradigm in both organoids and tissue engineering fields with the emergence of concepts such as “engineering organoids” [32,95] or “developmental tissue engineering” [125,126]. These terms highlight the mutual intention to enhance the control of organoid system generation through engineering processes and to improve the functionality of engineered-tissue constructs by utilizing developmental pathways. Both perspectives can be reconciled under the principle of driving “self-organization” through 3D engineered microenvironment (Figure 11) [32]. Self-organization relies on the intrinsic ability of cells to perceive their immediate surroundings and to respond accordingly. Just as the cellular microenvironment guides cellular fate, cells reshape their environment. These bidirectional interactions lie at the core of tissue morphogenesis and functionality [13]. Hence, by providing cells with chemically and mechanically permissive environments, it should be possible to better initiate and control multicellular responses toward *in vitro* complex tissue generation.

3.1. Ensuring cell-matrix interactions: Engineering extracellular matrix

As previously mentioned in II.1.1, EMC acts as a physical support for cell adhesion and movement but also functions as a sequestration and storage site for growth factors regulating distribution of signaling molecules to cells 15,42]. Both mechanical and biochemical properties of ECM influence cell behavior. ECM mechanical properties regulate adhesion-related cell functions such as cell proliferation, adhesion, polarity or migration. On the other hand, the biochemical composition of ECM surrounding the cell influences cell fate through interactions with cell-surface receptors and the topology of cell-cell and cell-matrix interactions [48]. ECM composition and reticulation are dynamically regulated by the surrounding cells secreting ECM precursors and ECM enzymatic remodelers [27]. Changes in the ECM properties are detected by cell receptors providing signaling for morphogenesis and cell differentiation [48]. Hence, ECM participates in bidirectional signaling cascades within surrounding cells and ultimately controls their development.

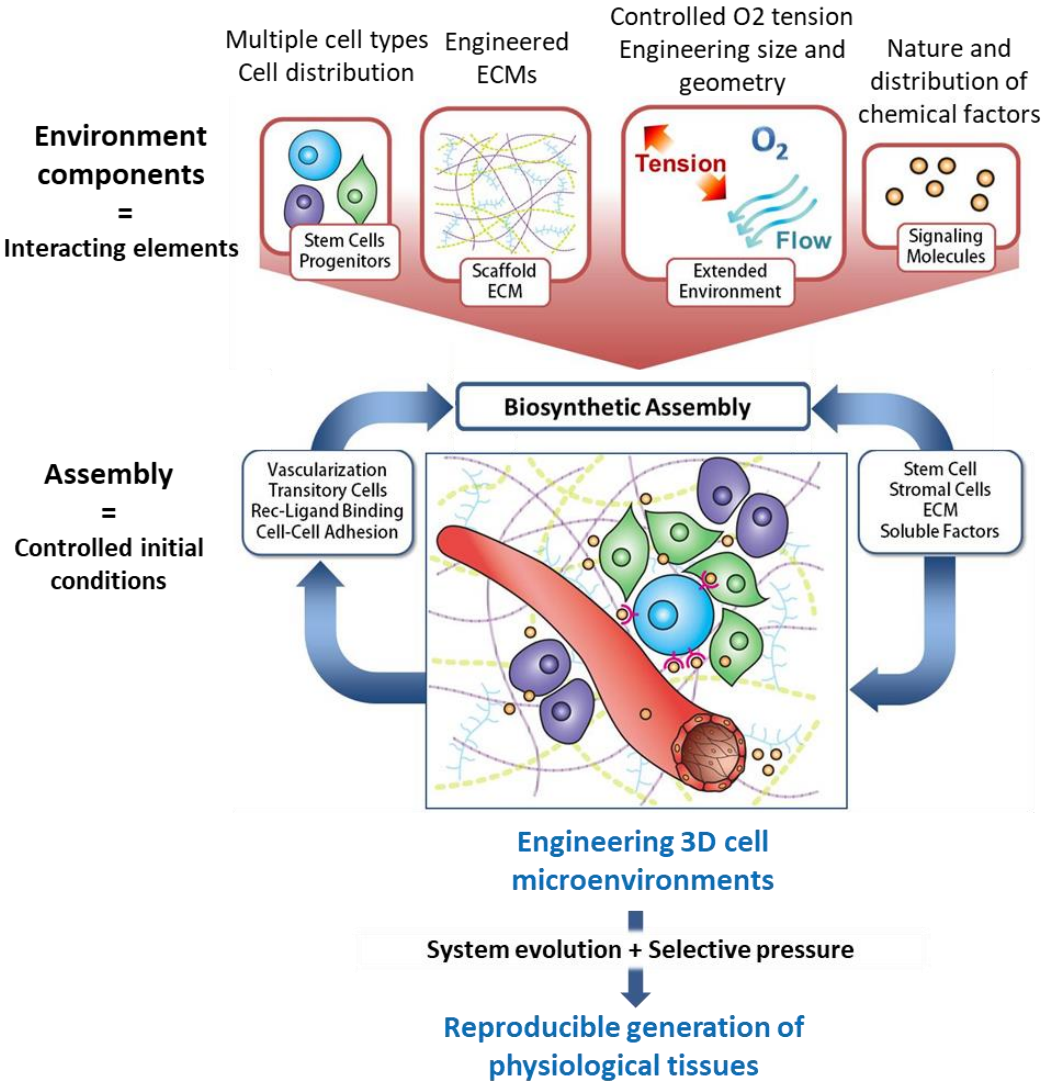

Figure 11. Schematic concepts of driving in vitro tissue development through 3D engineered microenvironment for the production of physiologically relevant tissue constructs. Engineering 3D microenvironment requires careful selections of initial interacting elements to promote self-organization of cells and their controlled assembly defining a set of initial conditions for self-organization process. These components include nature of the cells and their self-organization capacity, engineered extracellular matrix (ECM), controlled of size and shape, as well as soluble chemical factors. Adapted from [127].

Engineering cell microenvironment is partly based on the possibility to provide cells with ECM mimicry using tailor-made biomaterials aiming to reproduce intricate network of interacting macromolecules that constitute the ECM [11,48]. Classical ECM engineering approach either involve bulk synthetic scaffolds or hydrogels. Described scaffolds encompass non-polymeric and polymeric material conversely to hydrogels that are only polymeric in nature [109]. Hydrogel are composed of hydrophilic polymer network allowing them to hold high water content. Thanks to their hydrophilic nature, hydrogels display visco-elastic behavior akin of native ECM [109] making them the most promising engineered material to recapitulate mechanical properties of native ECM properties [109].

In addition to biocompatibility, a number of common parameters should be considered when selecting a biomaterial to ensure its interaction with surrounding cells and its potency to drive multi-cellular processes (Figure 12).

Biomaterials should exhibit good permeability as a basis for cell infiltration and molecules exchange from outside to within the tissue construct [121]. Permeability of biomaterials relies on their porosity with permeability increasing along pore size and density. Biomaterial should possess a macroporous structure composed of interconnected pores allowing for cell seeding, cell motility and nutrient flow. However, pore size should be carefully considered. Studies reported that insufficient pore size trap cells which adopt a round morphology and are unable to migrate [114]. Besides, low pore size limits the distribution of nutrients and removal of waste products leading to the development of necrotic regions within the construct [114]. Conversely, increasing pore size reduces specific surface area and consequently reduces the ligand density available for cells [114]. Decreased cell-matrix interaction hinders cell proliferation, cell migration and influences cell fate. Thus, optimal mean pore size should be defined as a balance between optimal pore size for cell migration and for cell adhesion.

Secondly, mechanical properties of the biomaterials should be considered. Mechanical properties quantify the stress and strain response of material under external forces caused by applying load and displacements. Classically, mechanical properties of a material are measured by standardized rheological tests. ECM stiffness is an essential property by which cells sense external forces and adapt their physiology through mechanotransduction pathways [11,48]. As mentioned above, ECM stiffness drives stem cell fate specifications [28]. Thus, mechanical properties of the chosen biomaterial should be adjusted to mimic those of the native ECM from the tissue of interest. While bulk scaffolds are mostly described for the generation of stiff tissue, hydrogels allow to reach native-like ECM stiffness enabling the engineering of soft tissue [109]. Hydrogel stiffness can be adjusted by monomer concentration and cross-link density [109].

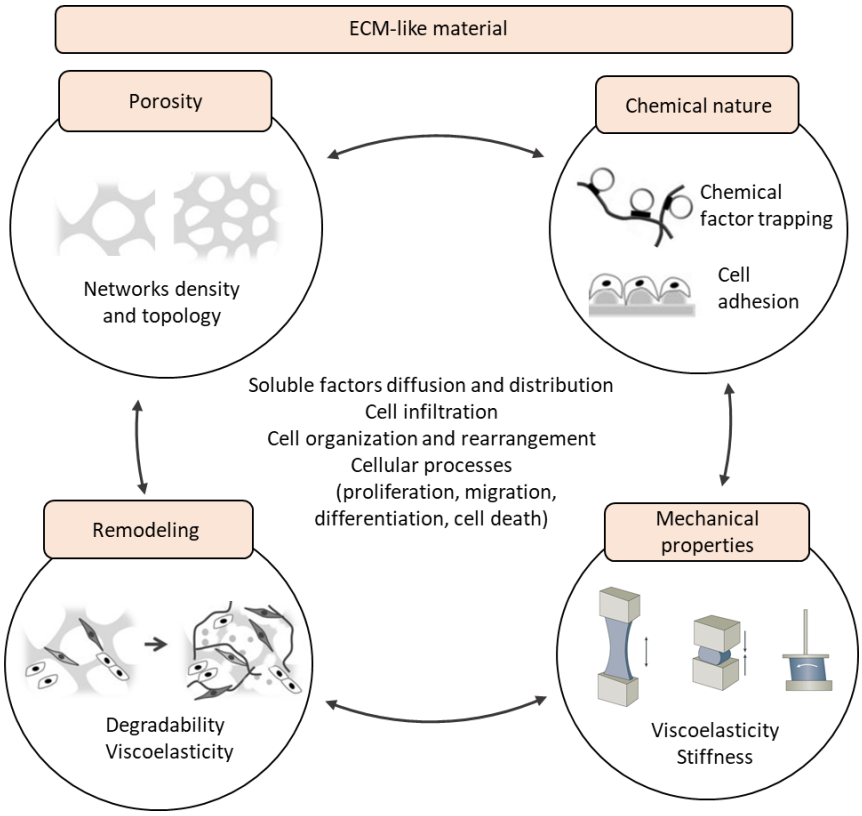

Figure 12. Chemical and biophysical parameters of biomaterial contributing to tissue development. Chemical nature, microarchitecture, remodeling and mechanical properties of a biomaterial are coupled and interact with each other to influence availability of soluble factors, mechanical resistance to cell rearrangements and regulate key cell processes implicated in tissue development. Adapted from [128].

During development, cells need to remodel their environment including the ECM to sustain morphogenetic movements, local cell fate specification and differentiation [35,48]. Non-polymeric material shows low degradability. Conversely, polymeric biomaterials including hydrogels are covalently cross-linked networks of polymers and their degradation by cells is ensured by the presence of enzymatic cleavage sites [109]. As a result of cell-material interactions, degradation of polymeric biomaterials can greatly impact their mechanical properties and how they drive cell behaviors [129]. Ideally, degradation rate of transplantable biomaterials should be synchronized with their replacement by *de novo* deposition of ECM by host and grafted cells to aid tissue regeneration. Same goes for *in vitro* generation of tissue construct as *ex vivo* tissue models. Indeed, given the difficulty to obtain biomaterials meeting all criteria to mimic native ECM [109], one way of circumventing this problem is to use the biomaterial as a temporary physical support, enabling the cells to secrete their own matrix. However, biomaterial degradation is accompanied by deterioration of its mechanical integrity and is influenced by material porosity and stiffness [129]. Conversely, insufficient degradability restricts

extensive matrix displacement required for large-scale morphogenetic processes [130]. Thus, a balance needs to be found between biomaterial degradation rate and ECM deposition rate. Conversely to bulk scaffold, hydrogel can also exist as physically cross-linked polymers that can rearrange themselves by electrostatic interactions. Such hydrogels exhibit more realistic viscoelastic and dynamic properties of native ECMs [32,131].

A final parameter to take into consideration is the chemical nature of biomaterials and how cells interact with them [109] (Table 4). Cell-matrix interactions require the presence of cell adhesion motifs within selected biomaterial. Consequently, non-polymeric biomaterial such as metallic and ceramic bulk scaffold show low cell adhesion capacity [109]. Conversely, polymers present functional groups that dictate adhesion-related cell processes and serve as signaling cues [48,59]. Hydrogels are often divided into naturally derived hydrogel and synthetic hydrogels. Naturally derived hydrogels include chitosan, alginate, hyaluronan, collagen and gelatin-based hydrogels. Natural hydrogels are inherently biocompatible, biodegradable and contain natural extracellular matrix motifs promoting cell attachment and differentiation [132]. However, natural hydrogels often show poor mechanical stability and batch to batch variations. In opposition to natural hydrogels, synthetic hydrogels such as polyethylene glycol (PEG) or polymethacrylamide possess tunable mechanical properties but require incorporation of functional motifs to ensure cell adhesion. Some studies have developed advanced manufacturing processes to enable patterning of RGD cell-adhesive motifs and control for local cell adhesion [121]. However, particular attention must be paid to biosafety of unreacted reagents, surplus monomers and bioproducts of degradation. As an alternative, naturally derived hydrogel functionalized to improve their mechanical stability have emerged. Among them, gelatin methacryloyl hydrogel are photopolymerizable and possess tunable mechanical properties depending on monomer concentration, photo-polymerization duration and light doses [133,134].

Table 4. Advantages, disadvantages, and main clinical uses of different kinds of biomaterials.

Biomaterial (examples)		Advantages	Limitations	Clinical use
Synthetic scaffolds	Metals	Biocompatible Great mechanical properties	Poor biodegradability Oxygation and aggregation issues Potential toxicity of metal ions release	Orthopedic prosthesis
	Ceramics	Osteoconductive and osteoinductive properties Similarity to human bone mineral content	Significant brittleness May display inappropriate degradation/resorption rates	Hip, dental prosthesis Bone, cartilage engineering
	Synthetic Polymers	Tunability of physical properties Low immune response Low production cost High reproducibility Defined composition	Often hydrophobic Lack of cellular recognition patterns Poor biocompatibility Risk of biodegradation side effects (e.g. toxicity, inflammation)	Cardiovascular prosthesis Bone, cartilage, tendon engineering
Hydrogels	Synthetic/ Natural / hybrids	High water content Inexpensive Large selection of materials available	Structural changes over time Limited mechanical strength	Engineering of various tissue types Soft tissue engineering Inductive material for in situ tissue regeneration
	Synthetic (PEG, PLA)	Highly tunable Controlled degradation rate High reproducibility Mechanical stability	Limited cell adhesion Risk of biodegradation side effects (e.g. toxicity, inflammation)	
	Natural (Gelatin, collagen, chitosan)	Highly biocompatible High cell adhesion potential	Gel-to-gel variations Low mechanical stability	
	Hybrids (GelMA, HAMA)	Tunable mechanical properties Highly biocompatible Reproducibility	Potential toxicity of photoiniators and light exposure	

3.2. Providing soluble factors: nature, supply and distribution

Soluble factors are another important component of the cell microenvironment [13]. They generally refer to a wide range of soluble proteins or peptides secreted by cells that can direct cell fate, cell proliferation (e.g. mitogens) and tissue formation (e.g. morphogens) through autocrine, paracrine and endocrine communication [28,44,46]. Such proteins are signaling molecules that include growth factors, cytokines and hormones which can bind to cellular receptors. These soluble factors can more

broadly refer to all soluble chemical cues found surrounding the cells, adding nutrients, metabolites and gases, especially dioxygen, to the definition [34]. Both nutrients and oxygen are key instructors of cell metabolism ensuring tissue homeostasis [55,135] but also acting as instructive cues in directing cell fate and function [136]. Cellular functions are enabled through supply of essential nutrients and the removal of waste products such as toxins. Specifically, the transition of stem cells from a quiescent to an activated state is highly sensitive to nutrients, mainly due to the energy demands associated with cell growth and division. Besides, oxygen serves as both a metabolic substrate and signaling molecule influencing stem cell self-renewal, their differentiation and the function of mature cells.

Mimicking of these soluble factors in vitro is classically done through cell medium composition and its accessibility to the cells [13]. In 2D culture, monolayers of cells are exposed homogeneously to this medium. In contrast, growing cells into 3D multi-layered constructs lead to the development of cell areas with reduced availability in soluble factors due to the reach of diffusion limit [137,138]. Typical growth factors display short-range diffusion through the ECM. Besides, *in vivo* maximum distance between a cell and its nearest capillary is usually more than 100 µm [19]. Hence, cells enclosed within a 3D structure larger than 200 µm in diameter will encounter nutrient and oxygen insufficiency, along with the accumulation of waste products within its central region [95,139]. Such circumstances have prompted the use of systems to better control soluble factors delivery.

Given the importance of growth factor distributions, such as morphogens, and kinetics release on tissue formation (See sections 1.1 and 1.2) two main types of approaches have been developed to increase growth factors retention and their spatial and temporal delivery: biomaterials-based approaches and microfluidic based-approaches.

Biomaterial-based delivery approaches seek to improve the efficiency of biomolecules action on cells by enabling localized administration using biomaterials as a carrier for soluble factors [140,141]. The most straightforward method for the incorporation of biomolecules within the biomaterial is performed by non-covalent binding [140,141]. Such incorporation can either be done through physical absorption of protein after scaffold generation or through physical entrapment by reticulating the biomaterial in presence of the protein. Soluble factors retention in the matrix can be modulated by the physical (e.g. porosity) and chemical properties (e.g. ionic charge) of the biomaterial [140,141]. Nevertheless, non-covalent binding often leads to poor control over temporal delivery of growth factors due to rapid burst release of protein (Figure 13). Covalent-binding of growth factors to the biomaterials has emerged as an alternative (Figure 13). The tethering of growth factors to the biomaterial surface decreases their susceptibility to degradation prolonging their retention and activity [140,141]. Besides, covalent-binding approach allows for precise patterning and spatial organization

of the soluble factors in the biomaterials recapitulating the role of ECM in the emergence of spatial morphogen gradients [140]. Nevertheless, by “supplying” cells with the biomolecules without “delivering” them, classic covalent binding approaches fail to reproduce temporal regulation of growth factors activity [140]. To better recapitulate signaling dynamism, newer systems have emerged based on the use of controllable cleavable linkers to bind growth factors, including enzymatic- and photo-cleavable linkers [141–143] (Figure 13). A very promising aspect of this approach is the development of hydrogel photopatterning for fine tuning both spatial and temporal presentation of signaling molecules to cells [143,144].

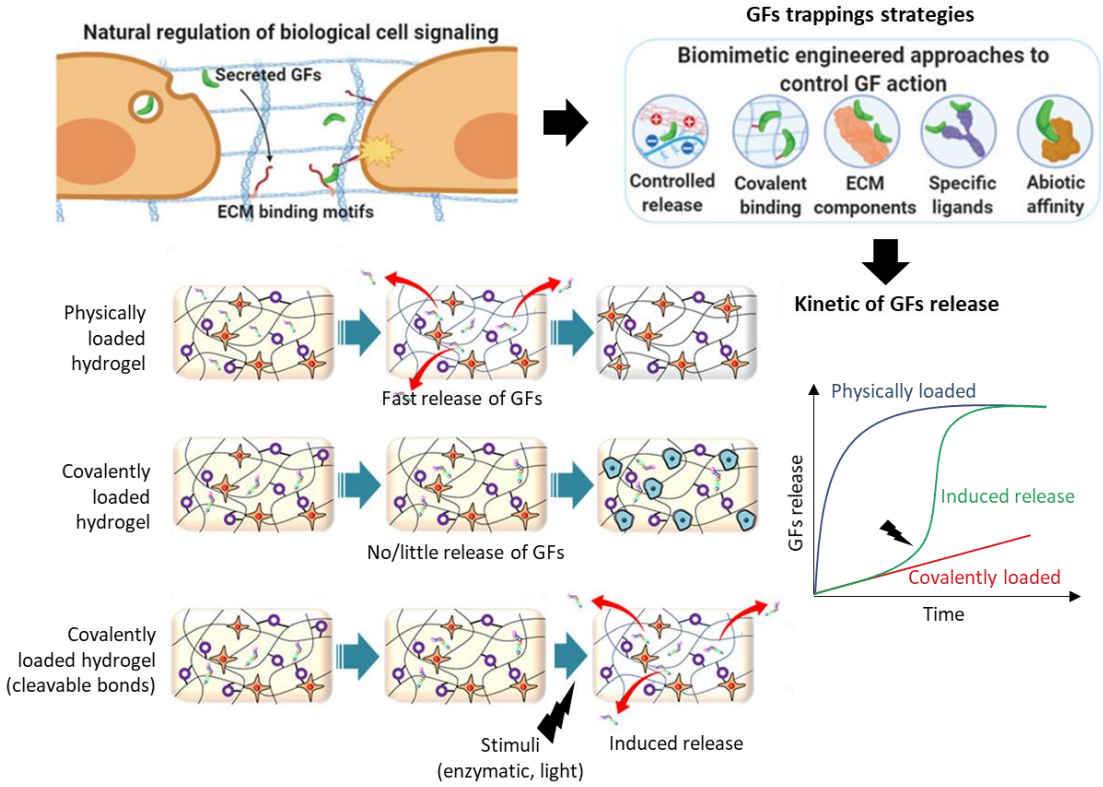

Figure 13. Chemical modifications of hydrogels for controlling growth factors retention and release. Modifications strategies of hydrogel surface for growth factors (GFs) trapping are based on biomimetic regulation of GFs distributions. These strategies include inclusion of ECM components, covalent bonding, selective ligands (e.g. peptides, antibodies, aptamers), or abiotic affinity (e.g. nanoparticles). Covalent bonding of GFs increases growth factors retention compared to fast release of physically loaded hygrogel. Incorporation of cleavable covalent bonds allows for controlled release of growth factors in space and time. Adapted from [140,145].

Another approach to locally control the delivery of growth factors is the use of microfluidic culture systems instead of classic static ones [146] (Figure 14). Microfluidics systems enable high spatiotemporal control of fluid flow. Depending on their complexity microfluidic devices allow the possibility to establish one or several gradients of molecules [146]. Spatially restricted lineages in development are often correlated with orthogonally positioned opposing gradients [44]. Reproducing such orthogonal gradients *in vitro* has enabled spatial differentiation of mouse embryonic stem cells in different contexts [147,148]. Besides, using different channels and microfluidic chambers, it is possible to deliver culture media with distinct composition to different tissue construct areas required to generate and maintain parenchyma and mesenchymal cell compartment of tissue. Such combination of engineered-tissue construct with microfluidic system has emerged as a new trend of tissue engineering referred to as "microphysiological systems" (MPS) or "organ-on-chip" [149].

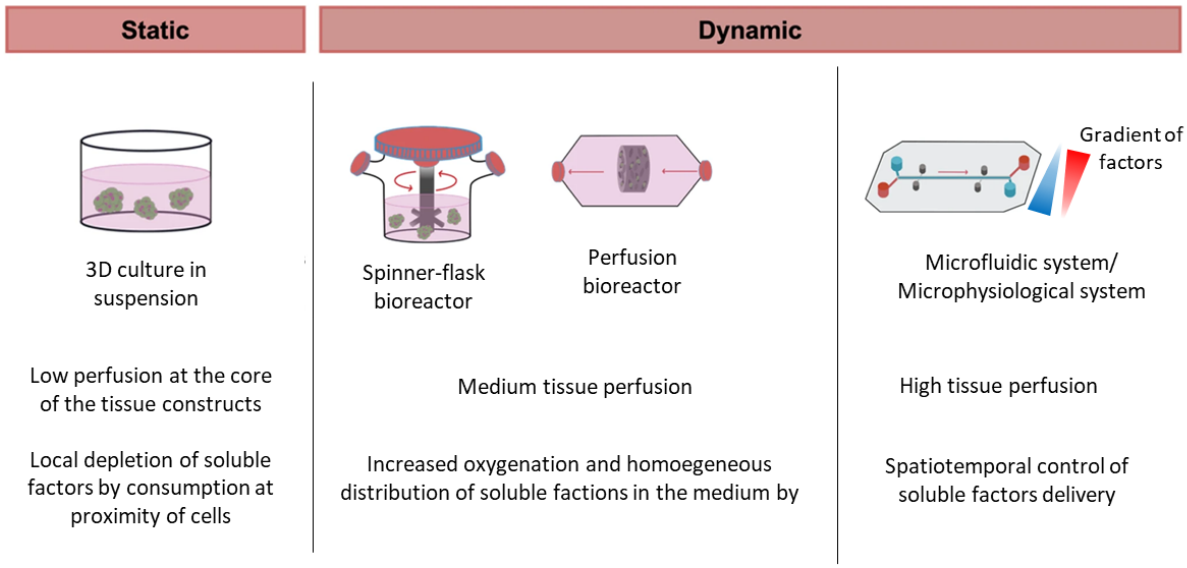

Figure 14. Perfusion systems for soluble factors delivery in 3D culture. 3D culture can be maintained in static or dynamic mode. 3D cultures are grown in suspension either without (static) or with medium agitation (dynamic). In spinner-flask bioreactors, 3D constructs are in contact with a homogeneous medium due to agitation and medium perfusion. Perfusion bioreactor perfuse directly through 3D culture with continuously fresh medium. Microfluidic system allows for spatiotemporal control of medium distribution enabling generation of soluble factor gradients. Adapted from [150].

In addition to growth factor supply and distribution, engineering approaches have focused on the improvement of oxygen and nutrients supply. Major approaches rely on the incorporation of their physiological carrier in tissue construct, meaning tissue vascularization [19]. Various engineering strategies have been described to enhance neo-vascularization within tissue construct and will be the focus of section III.4. Alternative approaches aimed to control for culture media oxygenation to compensate for cell oxygen consumption and limited oxygen diffusion [151]. Perfusion bioreactors

allow for continuous renewal of media ensuring homogeneous oxygen concentration along the culture [151]. Besides, increased in culture media oxygenation can be mediated by addition of oxygen carriers [152]. Advances in biomaterial engineering also lead to the development of oxygen-releasing biomaterials using peroxides or fluorinated compounds that release oxygen through hydrolysis [153].

3.3. Ensuring cell-cell interactions: Cell density and cellular assemblies

Given its importance in the regulation of collective cell behaviors governing tissue shape and tissue patterning, direct cell-cell interaction is an important component of cell microenvironment to take into consideration in *in vitro* models [35,73,80]. As mentioned previously, direct cell-cell interaction depends both on intrinsic expression of adhesion molecules such as cadherin [77] and on extrinsic signals such as cell proximity or cell cortical tension [75].

An approach to manipulate cell-cell interaction would be to directly engineer the cells through genome editing or modifying the cellular membrane to modulate intrinsic adhesive properties of cells. These methods are referred to as chemically programmed assembly and have been reviewed elsewhere [154,155]. Moving forward, we will focus on approaches to modulate cell-cell interaction given any type of adherent cells by extrinsic factors without further cell engineering.

Organoids originate from self-assembled clusters of stem cells which expand through cell proliferation within Matrigel [156]. As a result, organoids exhibit high cell-cell cohesion which enable collective cell rearrangement in space (Figure 15). Alternatively, generation of cohesive aggregates by exploiting intrinsic self-assembling capacity of cells has emerged as a promising approach to control for cell-cell interactions [157]. This intention has led to the development of scaffold-free approaches based on the seeding of cells onto non-adherent substrates to promote binding between neighboring cells [157,158]. Resulting cell aggregates are referred to as spheroids and have been successfully generated from various types of adherent cells in homotypic or heterotypic cultures setting [139,157]. Cells within spheroids demonstrate cell sorting and local spatial rearrangement ability relying on cell-cell interactions such as based on cadherin expression [157]. Besides, when aggregates surpass 200 µm in diameter, diffusion gradients of oxygens and nutrients can be observed within the structure [139,157]. These gradients in oxygen and nutrient availability correlate with the establishment of a stratified concentric structure composed of a proliferating cell population at the periphery and a core of non-dividing and often necrotic cells [139,157]. For this reason, spheroids recapitulate several features of tumor physiology and were shown to better model chemo-resistance compared to classic 2D culture [159,160]. Hence, spheroids have been extensively used for tumor modeling [160]. However, regarding healthy tissue generation multicellular spheroids fail to recapitulate complex *in vivo-like* architecture

of tissue [157]. Although spheroids demonstrate ECM deposition, this non-physiological cell organization may result from the lack of efficient cell-matrix interaction required for long-range spatial cell rearrangements.

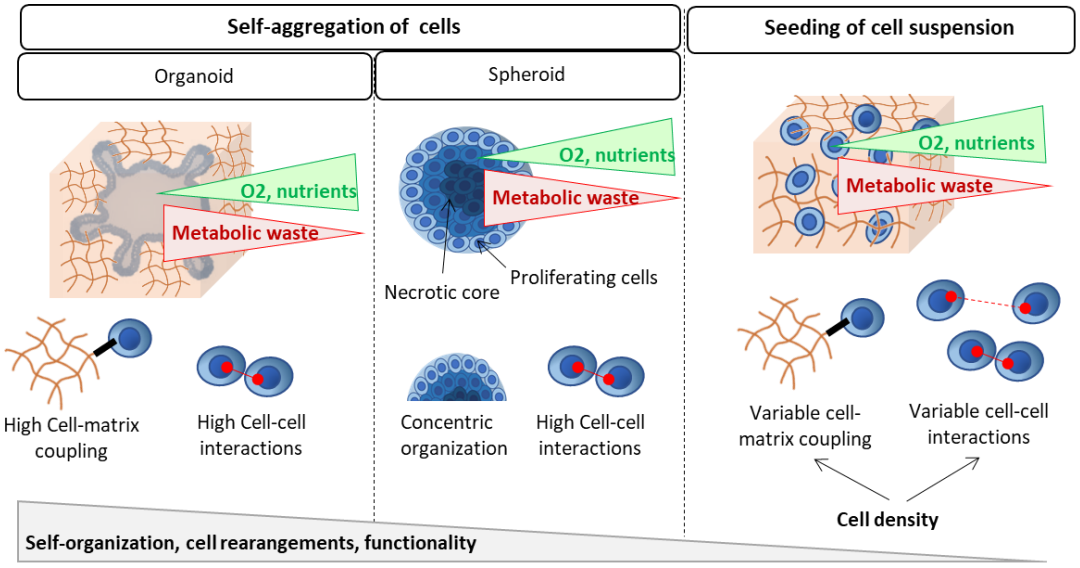

Figure 15. Aggregation of cells promotes cell interconnectivity and cell organization within 3D culture. Details regarding cell-matrix and cell-cell interactions as well as soluble factors distribution (O2, nutrients, metabolic waste) within organoids, spheroid and cell-laden hydrogel. All 3D cultures showed gradients of soluble factors due to diffusion limitations. Organoids display both high cell-cell and cell-matrix interactions supporting long-range cell rearrangements and thus increased self-organization compared to spheroids which exhibit high cell-cell interactions but low cell-matrix interactions. Seeding of cells as cell suspension in hydrogel lead to variable cell-cell vs cell-matrix interactions depending on cell density and is associated with lower cell organization.

Conversely, classic approaches of tissue engineering rely on seeding isolated cells in porous biomaterials. In this configuration, one way to modulate cell interaction is by manipulating the initial cell seeding density, meaning the number of cells per volume unit, in order to influence the spatial proximity of cells. Some studies have explored the influence of cell seeding density on engineered tissue maturation. Increased cell density of human MSCs in agarose or demineralized bone matrix scaffolds led to increased mineralization and bone formation [112]. However, in the context of skeletal muscle and tendon tissue engineering, highest seeding densities correlated respectively with impaired muscle cell contractility and cell death [111]. It has been proposed that impairment of growth factors and nutrient transport mass were responsible for reduced survival rate in the highest seeding condition [111]. Therefore, initial seeding density is a critical variable to consider in functional tissue engineering and should be optimized depending on target tissues. Nevertheless, despite optimizing the seeding density, tissue constructs derived from these approaches intend to correlate with limited cell interconnectivity [125,126]. In absence of engineered vascularization, decreased nutrient availability

in high seeding conditions may hinder acquisition of functional maturity that could have result from increased cell-cell cohesion. A rising alternative to address the limited cell-matrix and cell-cell interactions respectively observed in spheroids and traditional scaffold-based engineered tissues would involve seeding pre-aggregated cells into biomaterials instead of single cells.

To summarize, advancements in biomaterial engineering and microfluidic perfusion systems have provided researchers with invaluable tools to better control cell-ECM interactions and dynamic distribution of chemical factors. Furthermore, the development of non-adherent culture approaches to generate cell-aggregates offer versatility to better promote cohesive cell interactions compared to classical seeding of cell suspension. Therefore, we have seen how we can tune the elements of the microenvironment that are known to drive cell developmental processes to expect more robust self-organization outcome. In III, we will see how these elements can be precisely bring together to generate tissues with relevant architectures and shapes across large tissue scale.

III. How to engineer tissue architecture to generate functional large-scale tissue constructs?

Tissue function is closely associated to tissue architecture [26]. Therefore, engineering functional tissue requires to explore how to arrange cells in space to generate tissue construct that closely mimic the size and geometry of native tissue architecture. This is especially important for the generation of large-scale tissue construct which is limited in spontaneous self-organization of organoids, highest in size being brain organoids (up to 4 mm in diameter) [96]. Hereafter, we will refer to large tissues when their dimensions exceed a diameter of 4 mm. In this section we will provide an overview of the approaches that have been proposed overtime to control shape and size of engineered tissue constructs [161,162].

Pioneering methods, developed as early as the 1980s by Dr. Joseph Vacanti and Dr. Robert Langer, were based on a "top-down" fabrication approach involving seeding cells into scaffolds that mimic the overall size and morphology of tissues. The primary objective of these methods was the engineering of transplantable organ sized tissue construct [9,10] (see III.1). Despite initially promising results, this method yielded few concrete therapeutic applications. Challenges regarding large-scale shaping of biomaterial have led to the development of 3D bioprinting approaches with increased potential to faithfully mimic native tissue architecture [163] (see III.2). On the other hand, fundamental conceptual differences between the "top-down" engineering approach and the natural tissue development led to the emergence of modular tissue engineering approaches, involving tissue generation through component assembly [125,126] (see III.3) and hybrid bioprinting approaches (see III.4). Finally, as tissues grow in size, they are met with diffusion limitations challenges to provide core cells with sufficient supply in nutrients and oxygen. Consequently, to engineer large scale tissue construct it is fundamental to contemplate tissue perfusion strategies to guarantee their viability, which serves as a fundamental requirement for their application in both fundamental and applied sciences. A main focus will be given on engineering embedded vasculature (see III.5).

1. Pioneer top-down engineering: Cell seeding onto organ-shaped scaffold

Top-down construction is one of the earliest approaches of large-scale tissue engineering aiming to generate whole organ architecture. At the early stage of tissue engineering, top-down engineering of large-scale tissue was mostly driven by the macroscopic structure of the target tissue. Hence, the fundamental basis of these strategies to engineer organ sized construct lies in the generation of biomaterial scaffolds relevant in shape and size by the use of either molded biomaterial or decellularized tissues (Figure 16), followed by seeding of cells [113,115].

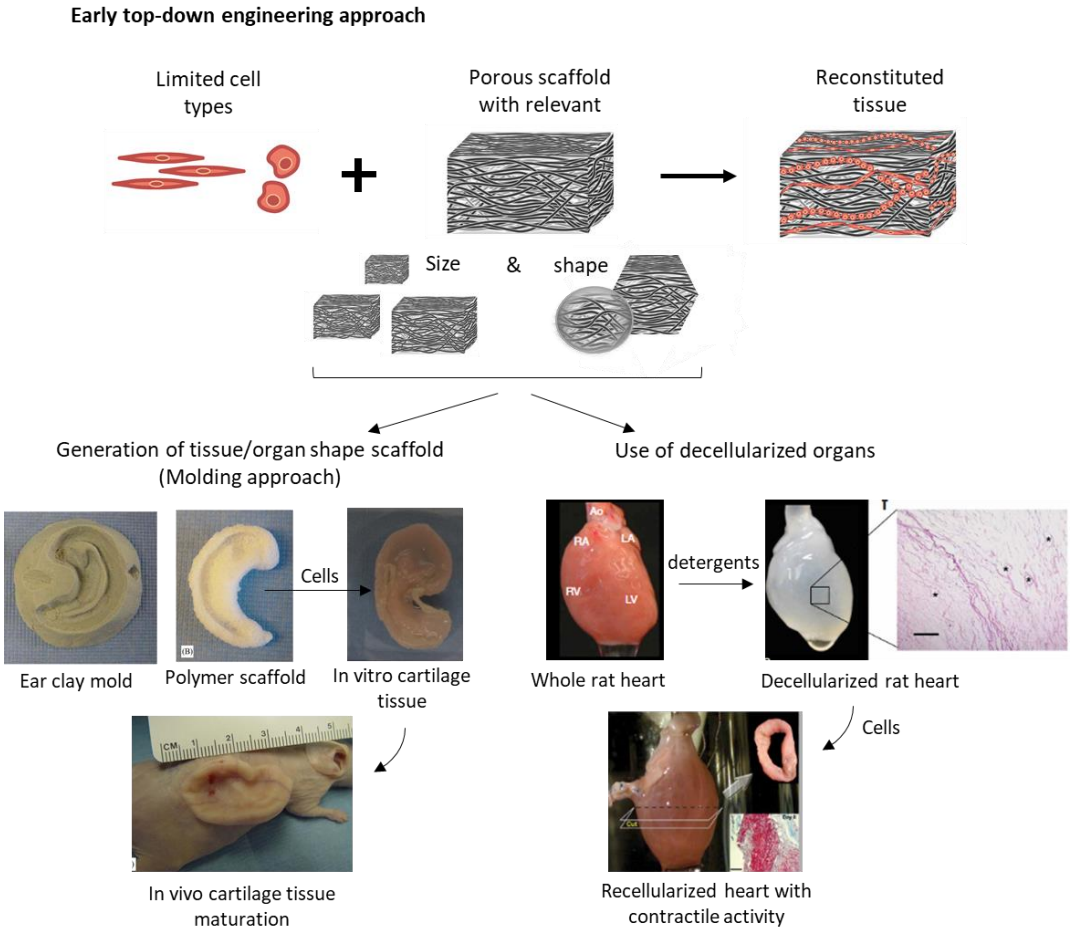

Figure 16. Pioneers tissue engineering approach based on organ shaped scaffold. Early top-down engineering consisted in seeding of cell suspension into porous scaffold for generation of reconstituted tissue. To generate large scale tissue construct relevant in shape and size for transplantation purposes, molding approaches were used for stiff tissue engineering such as cartilage (Bottom left, [113]) while whole organ decellularization was explored for soft tissue engineering (Bottom right, [164]). Adapted from [125].

A pioneer field in the development of these strategies was the engineering of bone and cartilage, characterized by their solid porous structures, for reconstruction surgery [10,113,115]. Engineering of autologous large cartilage pieces such as the ear or nose is a promising technology with potential for

tissue replacement. First observation of neocartilage formation from chondrocyte seeded on top of synthetic scaffold upon transplantation was pivotal in the field [165]. Soon, it was reported that cartilage could be formed from predetermined shapes. After that, scaffold fabrication methods based on molding were used to generate organ-shaped scaffolds [166]. A well-known example is the work of Vacanti and colleagues which generated a scaffold with the shape of an ear using a plaster mold cast from an alginate construct of a human infant [115] (Figure 16, bottom left). The scaffold was populated by chondrocyte cells through cell infiltration and implanted in mice for cartilage maturation. Neo-cartilage formation was observed in all implants after retrieval. However, the shape of the ear was only maintained in presence of stented structures. At that time, these results were exciting news for the perspective of regenerative medicine using tissue engineering.

Conversely, in the early 2000s, achieving the shape and mechanical characteristics of soft organs presented greater difficulties using current material and molding methods. As an alternative, strategies based on the use of decellularized parts of tissue or whole organs have emerged [161]. Decellularized tissue can be obtained from biopsies or cadaveric organs [164,167–169]. Native cells are removed from the tissues using perfusion with surfactant and enzyme solutions. This approach has the advantage of producing a scaffold retaining the native ECM composition and the shape of the targeted tissue. Decellularized dermal and bladder matrices were efficiently generated and used for respective tissue engineering [168,169]. The first instance of whole organ engineering using this approach was reported by Ott et al. in 2008 with the recellularization of a whole rat heart [164] (Figure 16, bottom right). The decellularized heart was seeded with neonatal rat cardiac cells and aortic endothelial cells by intramural injection and perfusion. After eight days of culture in a bioreactor, the heart construct exhibits contractile activity and transcriptional signature of the mature heart. Hence, decellularized scaffolds open opportunities to produce intact 3D templates of native ECM for large scale tissue regeneration.

These impressive works were clear demonstrations of the potential of tissue engineering for regenerative purposes and opened up a new area of tissue engineering. Nevertheless, as previously discussed, these conventional top down approaches of tissue engineering are decorrelated from the intrinsic developmental process enabling organ formation *in vivo*. Random cell seeding or infiltration into organ-shaped material resulted in poor cell organization, limiting their use as ex vivo models [161]. Reproducible artificial organ generation requires better control over cell distribution. Random cell seeding was proved even more difficult in decellularized matrices which showed insufficient porosity for correct cell infiltration [161]. Besides, conventional scaffold fabrication methods fail to replicate tissue microstructure. Altogether, these observations prompted a change of thinking in the field of

large-scale tissue engineering toward the development of approaches allowing a better control over microscale features of engineered-tissue construct.

2. Hydrogel-based bioprinting for the precise deposition of cells into predefined spatial arrangements

Printing of living cells, also known as 3D bioprinting, has emerged as a promising technology in the field of *in vitro* tissue generation for the precise control of cell distribution into ECM-like material. [163,170]. Traditionally, this additive manufacturing process involves printing of individual cells within a hydrogel [163,171]. In past years, its use has evolved toward the printing of multicellular constructs such as cell aggregates, spheroids, or organoids which will be latter discussed in III.3. In this section, we will focus on printing of isolated cells in a supportive material [172].

Hydrogel-based bioprinting involves the use of a single or a mixture of hydrogels, referred to as bioink, to encapsulate the cells. These bioinks can be crosslinked or stabilized during or immediately after printing to establish the architecture of the construct [172]. Conventional bioprinting approaches include extrusion-based bioprinting, inkjet/droplet bioprinting and laser-assisted bioprinting (for details see [172]) which offer a spatial resolution below 50 µm. With its remarkable spatial precision, hydrogel-based bioprinting opens up novel possibilities in the realm of large-scale tissue engineering for the generation of large-scaled cell-containing scaffolds exhibiting biomimetic architectural features.

Compared to conventional scaffold fabrication methods, 3D bioprinting enables the generation of scaffolds with controlled architecture without molding. Advances in medical imaging technology using X-rays, MRI or CT-scans enabled accurate measurements of organs and tissues (Figure 17). These accurate dimensions could be used as blueprints for 3D bioprinting design through advanced CAD tools and software [163]. Combination of medical imaging and spatial resolution of bioprinting offers a viable option for scaffold generation instead of whole organ decellularization. Remarkably, thanks to its unprecedented spatial control of cells and biomaterial deposition, 3D bioprinting strategies allowed to recreate multiscale spatial features of the organs from the general shape of the organ down to half-millimetric topological aspect. Furthermore, a strong suit of bioprinting is the direct deposition of cells along with the biomaterial allowing for even cell distribution compared to limited cell infiltration observed in top-down engineering processes.

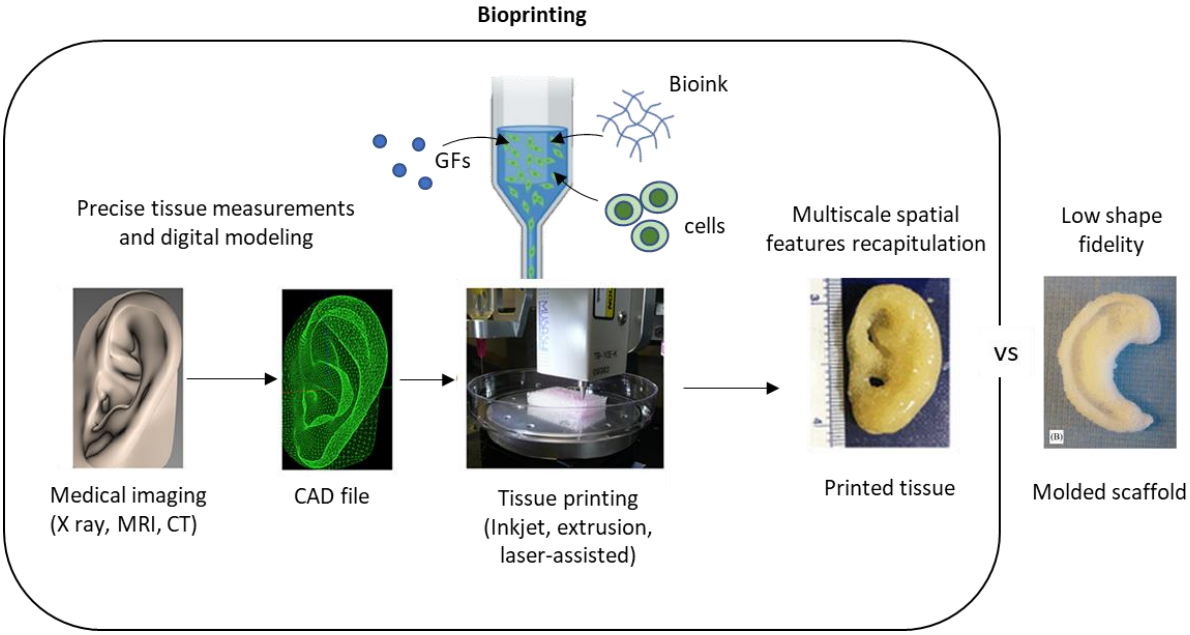

Figure 17. Principle of hydrogel-based bioprinting. Pre-processing involves combination of medical imaging and digital modeling for generation of precise in silico tissue reconstruction. These reconstructions are then provided to 3D bioprinter along with formulated bioink for printing process. 3D bioprinting allow for the generation of printed construct with significant improvement over organ shape fidelity and microstructure compared to previously described molding methods for scaffold fabrication. Adapted from [113,173].

As a first instance, several studies have demonstrated the potential of hydrogel bioprinting for the generation of acellular organ reproduction such as ear with high fidelity and shape stability overtime [173] (Figure 17). Besides, bioprinting of chondrocyte-laden alginate/gellan have enable generation of nose-shaped hydrogel containing cells with high shape fidelity. These constructs showed secretion of cartilage-related matrices during in vitro cultivation showing potential for the perspective of nose reconstruction and more generally cartilage reconstructive surgery [174].

Besides, rapid progress of material printing technology has paved the way for direct printing of living cells into tissue constructs with more physiological composition. The development of multi-head deposition systems (MHDS) has allowed simultaneous or subsequent printing of multiple materials [170]. Therefore, in addition to correct tissue dimension recapitulation, bioprinting of cells have the potential to generate heterogeneous tissue constructs recapitulating various cell compartments of native tissues [170].

3D bioprinting allows for unprecedented spatial and temporal control for cell and biomaterial deposition. Therefore, these biomanufacturing techniques hold great promise to generate large-scale tissue construct by design. However, several limitations still impede the translation of these approaches into high-throughput biomanufacturing processes for clinical purposes. Specific limitations

of 3D bioprinting involve technical aspects of the printing process including printing speed and flow rate and bioinks availability.

Bioprinted chondrocytes showed reduced cell viability inside nose-shaped structures which can be attributed to low nutrient perfusion during the culture or alteration of the cells during printing process. Maintenance of cell viability is a crucial challenge in current 3D bioprinting approaches due to important processing time coupled with relatively low efficiency. As a result, the printing of cells on a large-scale dimension becomes a time-consuming procedure, potentially influencing cell viability, especially when considering the mechanical stress exerted on the cells [162,163].

Another important challenge of 3D bioprinting is the selection of the bioink [171]. An ideal bioink should possess proper mechanical, rheological, chemical and biological properties required for generation of construct with high shape fidelity, tissue-matching mechanics and biocompatibility. Choice of material depends on the cell type and the printing technique employed, such that there is currently no ideal material for a given application [171]. Current approaches aim to use hydrogel which better mimic native ECM compared to conventional synthetic polymer used in 3D printing [163,175]. However, hydrogels often lack sufficient structural integrity and suitable rheological properties for optimal bioprinting. Low mechanical stability is a common limitation observed in extrusion based bioprinting of hydrogels [163,171]. Extrusion-based bioprinting involves dispensing of bioink layer-by-layer and *in situ* cross-linking or gelification during the fabrication process. However, soft material such as hydrogel require proper support to not collapse or deform under their own weight. To remedy this problem, a bioprinting technique termed freeform reversible embedding of suspended hydrogels (FRESH) has been developed [176]. FRESH consists in the use of responsive matrix support bath such as gelatin in which hydrogel can be printed. Complex 3D organ structure can be printed without collapsing and retrieved once formed by melting away the support bath. Based on 3D imagining, several FRESH printed scaffolds of whole heart or heart components were generated. Particularly, a miniaturized replicate of the human heart demonstrating chambered structure and tissue contractility was generated from hiPSC-derived cardiac cells and fibroblasts [177]. While FRESH approach is promising to promote generation of 3D construct with enhanced shape and mechanical fidelity compared to classical hydrogel bioprinting strategies, its use for large scale production remained limited by speed of the printing process. Hence, current single-cell printing processes have inherent scaling limitations.

3. Organ building blocks for modular tissue engineering

Complex organs and tissues can be conceptually decomposed into repeated functional units characterized by their micro-architecture and cell composition, such as lobules of adipose tissue. In this context, modular tissue engineering has gained increasing interest in opposition to one-stage process of cell seeding approaches into bulk biomaterials [162]. Also referred to as “bottom-up” tissue engineering, this approach consists in a two stages process: 1) Generation of multicellular units as organ building-blocks, 2) ultimate assembly of these building blocks. Through the generation of tissue modules emulating the microstructure of native tissues, bottom-up tissue engineering presents novel opportunities to direct the formation of large-scale tissue constructs with increased structure complexity and functionality.

Various types of multicellular construct have been used as tissue modules [126,162,172]. These include compact self-assembly of cells such as cell aggregates, spheroids, embryoid bodies or organoids as well as cell sheets created under conditions that promote ECM secretion of cells. All of these multicellular modules have the advantage to recapitulate some aspects of native tissue organization including enhanced cellularity and cell organization compared to single cells dispersed in biomaterial [91,126,157]. Besides, when generated from stem cells or multiple cell types, they have the potential to mimic native tissue complexity [156,157].

The generation of large-scale tissue construct from preformed building blocks involve two successive processes: building blocks assembly and their fusion to form a cohesive macroscale tissue (Figure 18).

Multiple strategies for building blocks assembly have been described. Detailed principles, advantages and limitations of these techniques can be found elsewhere [126,162,172]. Briefly, while cell sheets are assembled through layer by layer stacking, cell aggregates can be assembled through various methods that can be divided into two main categories, ones based on parallel stacking in confined geometries and ones based on 3D printing with or without carriers [172]. Parallel stacking includes methods such as directed assembly, magnetic assembly, microfluidic assembly or hanging droplets which allows for one-step generation of large structure through spontaneous interactions of numerous building blocks [172]. Although these methods provide simple construction processes, they exhibit insufficient spatial resolution to generate complex arbitrary patterns. Conversely, direct printing of spheroids or organoids through a “pick-and-place” approach allows stacking with complex geometry [178,179]. Using, aspiration-based system for spheroid handling, Ayan et al. generated rings of pyramids of spheroids [179]. Daly et al. used a similar approach to assemble even more complex

structures by benefiting from a self-healing support matrix used as a temporary holder to maintain spheroid suspended in space before complete structure retrieval [178].

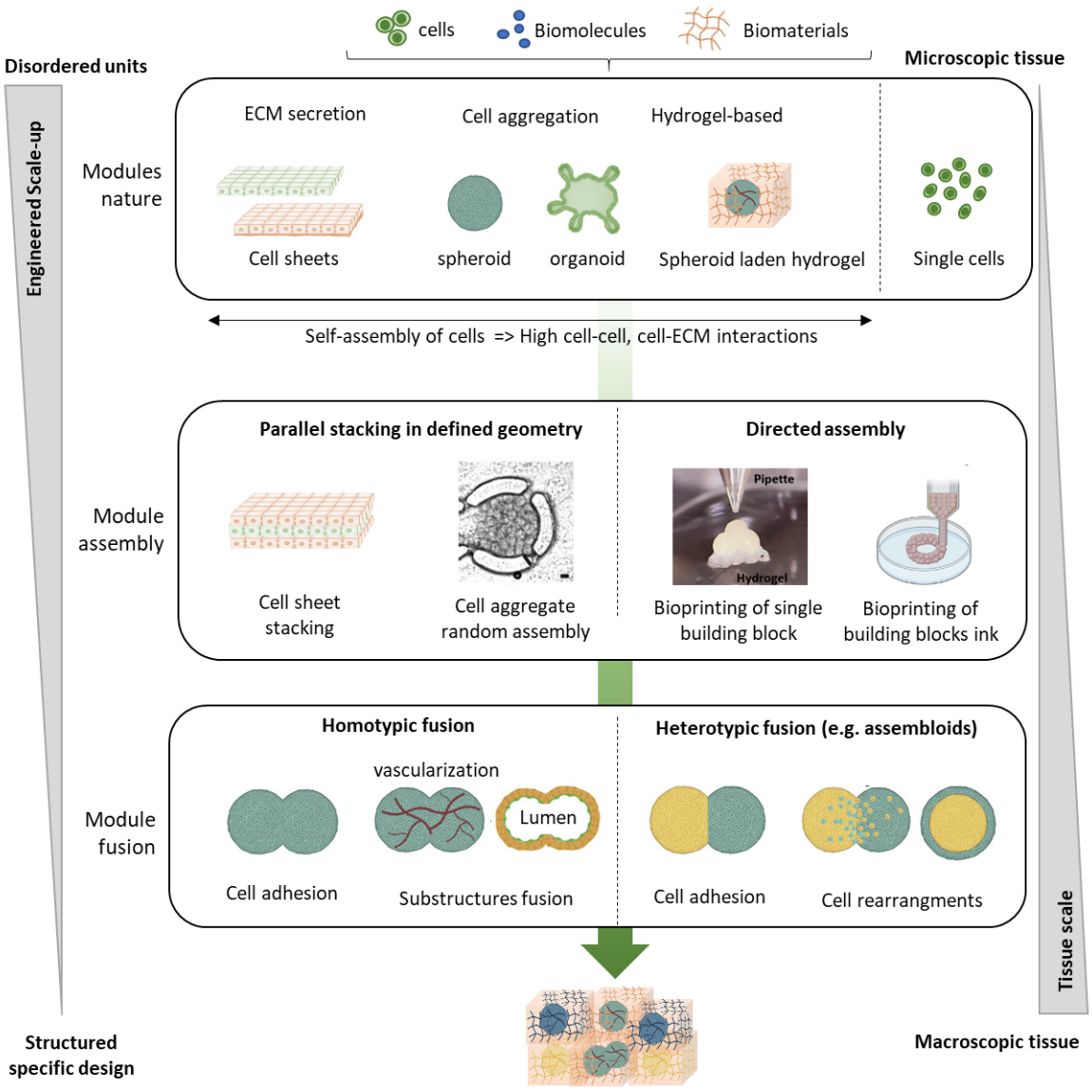

Figure 18. Schematics of tissue-engineered-construct fabrication via modular assembly methodologies. Self-assembled modules units including cell-rich and cell-biomaterial assemblies (e.g cell sheets, spheroids and organoids) can be manipulated and packed together to generate macro-tissue with higher structural ordeals. Advanced methods of directed assembly offer higher control over specific tissue design programming. Resulting engineered tissue are expected to integrate modular architecture and more closely recapitulate native tissue heterogeneity and organ-specific bio-functionality. Adapted from [162].

Once assembled into a 3D structure, building blocks need to fuse together to form a cohesive network. Compact cell aggregates such as spheroids and organoids display striking fusion properties reminiscent of the coalescence of viscous droplets [162]. Efficiency of spheroid fusion can vary depending on the cell adhesion property, spatial separation between spheroids and their environment [180,181]. Interestingly, spheroids embedded in collagen or gelatin-based matrices also exhibit fusion capacity under certain inter-distance [182]. In this context the distance at which spheroid fusion occurs depends on matrix mechanical properties suggesting competition between cell-cell and cell-matrix interactions. To ensure the function of the macro-structure as a whole, building blocks fusion should also enable the fusion of substructures present in each module such as microvasculature or luminal structures [183]. Substructure fusion emerges with time by cell migration within the fused macro-structure.

Engineering of large-scale tissue by tissue building block assembly has already demonstrated impressive results. For instance, assembly of hiPSC-derived cardiac spheroids yield to contractile cardiac tissue with synchronous beating [184]. Besides, modularity of such bottom-up approaches provides the opportunity to assemble building blocks of diverse cell composition and physiology to recreate tissue cell compartments, model their evolution in pathological condition or study tissue interconnectivity [126,162]. Resulting structures are also called assembloids. Thus, Daly et al. used cardiac spheroids containing various ratios of fibroblast and cardiomyocyte to model post-myocardial infarction scarring [178] while Andersen and colleagues succeeded in generating cortico-motor units by fusing spinal, cortical and motor spheroids [185]. Nevertheless, there are several remaining challenges to tackle for efficient and reproducible biomanufacturing of human organs.

First specific limitations to organ generation through building blocks assembly reside in the spatio-temporal resolution of their assembly. To ensure cell viability and minimize process cost, generation of human organs should be done in a practical timescale. However, to date high throughput parallel assembly methods lack necessary spatial resolution where direct printing is a long-lasting process. For this reason, novel approaches of 3D bioprinting using bioinks laden with cell aggregate rather than individual cells are emerging [186]. However, current extrusion or inkjet techniques do not support printing of large cell-aggregates which lead to nozzle clogging. Future bioprinting development is required for rapid patterning of spheroids or organoids into complex and biologically relevant shapes.

On the other hand, a limitation to the reproducibility of macroscopic structures may directly stem from the lack of reproducibility in module generation. As discussed earlier (see II.2.1), organoids exhibit stochasticity in their development, contributing to their significant heterogeneity [95]. Similarly, spheroids generated from multiple cell populations can display variable cellular arrangements, although they are more reproducible due to being primarily governed by cell adhesion and metabolite

gradients [157]. Furthermore, the precise assembly of building blocks alone is insufficient to control the cellular remodeling that occurs within them post-fusion. This necessitates further studies on the parameters governing spheroid fusion behaviors (e.g. adhesion, mixing, or envelopment), including cell composition and maturation state [162]. The maturation state of the modules before and after assembly must also be considered to enable the complete maturation of the resulting macroscopic construct. The introduction of exogenous signals such as growth factors or extracellular matrix components could offer a means to better control tissue fusion and post-fusion maturation.

We have seen that among approaches to generate large scale tissue, 3D printing approaches possess the highest spatial and temporal resolution so far. Combining with FRESH technology, hydrogel based bioprinting hold important promise to generate tissue with accurate macroscopic and microscopic architecture. However, application of single cell 3D bioprinting to generate functional large-scale tissue is still hindered by low printing speed and the use of cell suspension concentration that limit cell interconnectivity as observed in pioneer top down approaches. Alternatively, modular tissue engineering has already yielded impressive results regarding promotion of large-scale tissue self-organization. However, achieving assembly of high number of tissue building blocks with high spatiotemporal resolution remained an important challenge. This observation has led some teams to develop hybrid bioprinting-based systems using organoid-forming cells to promote tissue building block formation directly and precisely within hydrogel (see III.4.)

4. Toward hybrid methods of tissue engineering: Cell injection of organoid-forming cells

By exploiting the important spatial and temporal control over cell deposition enabled by bioprinting, recent studies have shown the potential to generate centimeter-sized epithelial organoids [187,188]. Both of these approaches rely on the localized injection of organoid-forming cells through extrusion into a pre-existing material. Initially, Reid et al. demonstrated the feasibility to dictate localized formation of organoids by injecting a specific number of human breast epithelial cells locally [187]. Thus, by managing the patterning of these cell injections, the authors achieved spatially defined arrays of organoids. Strikingly, when deposited close enough (<200 µm) these clusters of cells promoted the fusion of developing organoids leading to the generation of contiguous luminal structures. These large-scaled luminal structures showed continuous lumen formation. More recently, Brassard et al. took this approach a step further by developing a syringe-based extrusion system allowing for continuous deposition of high concentrated cell suspension into biomaterials with precise geometry down to single cell line resolution [188]. Using this technique, the authors achieved to coerce intestinal stem cells or endothelial cells to evolve spontaneously toward the generation of intestinal tubular-shaped

structures and branched vasculature, respectively. Ensuring high cell confinement through high cell density was reported to be a critical parameter for the spontaneous emergence of contiguous structure, highlighting the importance of cell-cell interaction in the generation of functional tissue construct. Interestingly, intestinal tubes demonstrated several structural and functional features of the *in vivo* intestine. A major improvement of intestinal tubes compared to intestinal organoids, lies in the accessibility of the continuous lumen which allows for its connection to a perfusion system for dead cells removal but also for drug-toxicity assays.

Combining spatial resolution of 3D printing technologies with the self-assembling capacity of stem cells appears to be a promising approach to generate 3D mirco-tissue with *in vivo-like* architecture and functionality.

Altogether, 3D printing technologies, assemblies of pre-formed organ building blocks or their in-situ assembly through hybrids approaches offer important opportunities to generate more and more complex tissue constructs whit physiologically relevant shape and size. Nevertheless, beyond the challenges of their generation, it is important to consider the challenges of maintaining cell viability and functionality in a large sized tissue, inherently exposed to limitations in oxygen and nutrients availability.

5. Engineering vascular-based perfusion systems for long term cell culture and function

A common major challenge to all biomanufacturing procedures for the production of large-scale functional tissue is the necessity to provide cells with proper perfusion system to ensure adequate nutrients delivery and waste disposal [18,19]. In absence of sufficient perfusion, large-scale engineered tissue will develop necrotic areas hindering its functionality and lifespan [124]. A main approach considered for this is engineering of embedded vascular networks within tissue constructs. Beyond, long term cell culture *in* vitro, embedded vascularization is a key factor to consider in the development of transplantable tissue-engineered construct. Indeed, it is expected to promote transplant engraftment and survival in host tissue by favoring transplant integration within host vasculature [18,19].

Although there have been some achievements in engineering single vascular conduits, the creation of complex vascular networks capable of perfusing an entire tissue construct has emerged as a significant challenge within the field of tissue engineering [19]. New culture methods and technological breakthroughs have significantly advanced our capacity to construct intricate vascular networks [189,190]. These methods can be categorized into nature driven and engineering-driven approaches, including the self-assembly of vascular cells, bioprinting, and microfluidic systems.

5.1. Nature-driven: self-assembly of vascular formation

Nature-driven approaches rely on the inherent ability of endothelial cells or endothelial progenitors to self-organize into vascular networks (Figure 19). First demonstration of such ability was reported in 1988, when endothelial cells cultured in 3D laminin and collagen matrix were found to spontaneously form vessel-like structures in vitro [191]. Since then other matrices have demonstrated potential to promote self-organization of endothelial cells including gelatin, fibrin or hyaluronic acid hydrogels [189].

Nevertheless, endothelial cells alone are not sufficient to sustain vessel formation [192]. Natural vascular development involves first the newly formation of vessels and then their stabilization by perivascular cells such as stromal cells or pericytes [193,194]. In absence of stabilization, vessels regress overtime. Hence, efficient generation of vascular networks require co-seeding of endothelial and stromal cells (Figure 19). Such co-culture has proved its efficiency in generating stable vascular networks both *in vitro* and upon *in vivo* implantation. More importantly, such co-culture has been successfully implemented in several protocols for the generation of pre-vascularized 3D tissue constructed from different organs, including skeletal muscle [195] or cardiac tissue [196]. Besides, vessel maturation requires vessels perfusion. While *in vitro* perfusion of self-assembling vascular networks has posed challenges, these vessel-like structures were observed to autonomously establish connections with the host vasculature, resulting in their maturation upon implantation in vivo [197,198].

An important parameter to consider in the co-culture system is the cell sources. Increasing evidence shows that endothelial cells and the perivascular cells associated with them are heterogeneous in populations and present organ-specific features [189]. Recreating the hierarchical structure of complete vascular beds would require the presence of both arterial and venous cells [189]. The physiology of endothelial cells is closely related to its crosstalk with perivascular and parenchymal cells, highlighting the importance of cell sources to generate relevant 3D *ex vivo* models for physiological and pathological conditions [190,193]. Besides, an endogenous source of cells would be preferable when considering personalized medicine or transplantation therapy to respectively maintain patient hallmarks and better avoid immune rejection by the host. Most frequent vascular engineering approaches are based on the use of readily available primary endothelial cell lines (e.g. HUVECs) which do not meet previously discussed criteria [189]. However, organ-specific primary sources of endothelial cells are limited and often do not come with the possibility to combine them with organ-specific stromal cells. A potential source of endothelial cells with distinct identities could be endothelial cells derived from human iPSCs [189]. Another interesting source of both adult primary endothelial

cells or progenitors and stromal cells are the dissociation of connective tissue such as adipose tissue or bone marrow. It was reported that the SVF of adipose tissue possesses high vascularization potential [199]. Hence, adipose SVF constitutes a promising cellular source for the generation of physiologically relevant tissue constructs for clinical applications.

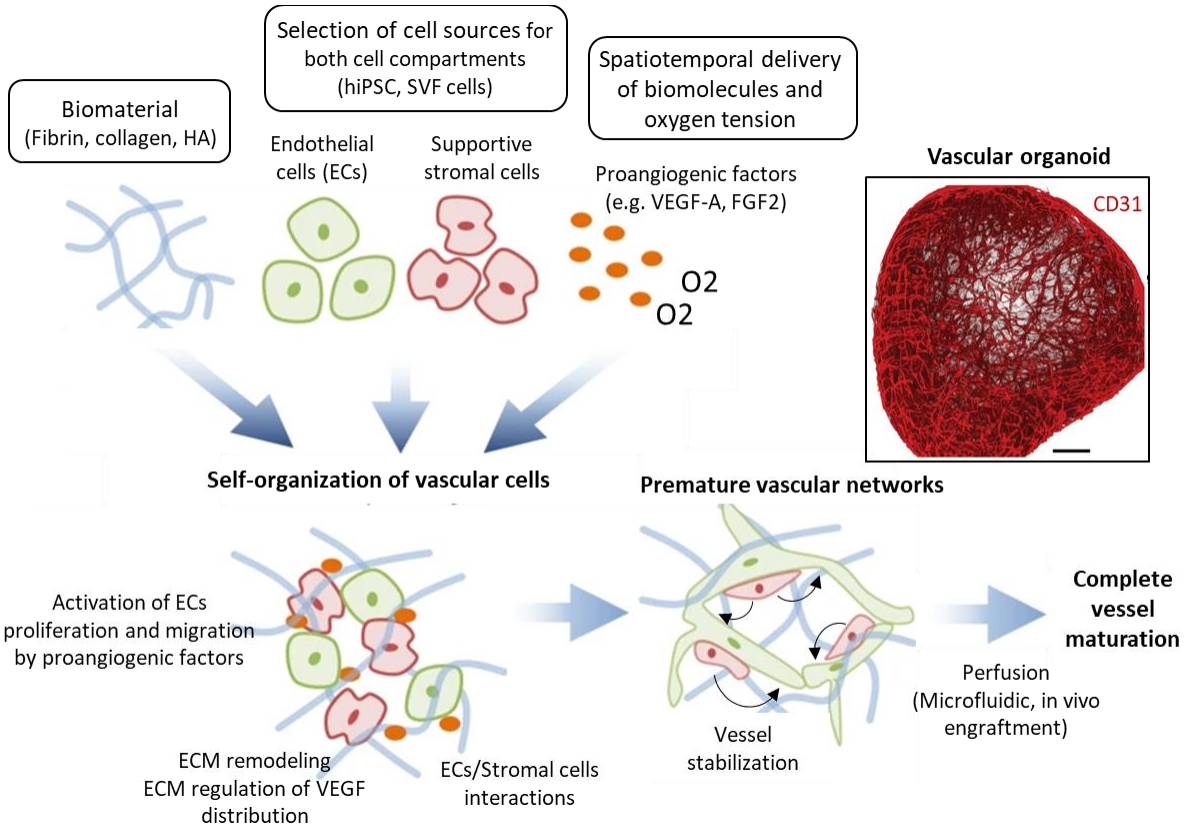

Figure 19. Requirements for in vitro self-assembly and self-organization of vascular networks. Promoting self-assembly of functional vascular network require to provide endothelial cells with supportive stromal cells within a hydrogel. Angiogenesis can be directed using spatiotemporal delivery of proangiogenic factors and by controlling oxygen tension. Cell processes required for self-organization of vascular structure are driven by cell-matrix and cell-cell interactions. Full maturation of vascular networks requires its stabilization by perivascular/stromal cells and vessel perfusion. Adapted from [198,200].

As any other co-culture system, generation of pre-vascularized tissue can be challenging regarding exogenous supply of factors required to both sustain parenchymal cell function and promote vascular formation. These factors include soluble growth factors but also matrix composition [190]. VEGF and FGF-2 are described as the most prominent growth factors to regulate angiogenesis [190] (Figure 19). Several studies aimed to control the spatiotemporal delivery of these angiogenic factors to better drive angiogenesis by engineering hydrogel with growth factors patterning and responsive release [201,202]. In addition, matrix stiffness and porosity were shown to impact endothelial sprouting and

vessel structure. Stiff collagen hydrogel (~20 kPa) promoted the formation of larger multicellular lumens compared to soft hydrogel (~5kPa) which exhibited highly dense networks of thin vessels [203].

Altogether, self-assembly of vascular networks is a reliable solution to engineer embedded vascularization of tissue construct which requires ECM and culture media optimization. Hence it opens the way to the generation of pre-vascularized large-scale tissue construction through the assembly of vascularized block building. Nevertheless, future work is required to improve the spatiotemporal control of vessel distribution for reproducible large-scale tissue constructs.

5.2. Engineering-driven: Generation of "endothelialized" perfusable channels

Engineering-driven methods of vascularization aim to precisely control the number and placement of vessels within a biomaterial. Technological advances in microfabrication and biomaterial-based bioprinting have propelled the field forward. The primary engineering technique for promoting vascular development is the "endothelialization" of pre-generated microfluidic channels [204,205] (Figure 20). Due to the similarities between *in vivo* microvascular networks and microfluidic interconnected channels, microfluidic-based approaches have gained interest to recreate vascularization. These microfluidic channels can either be obtained through microfabrication processes or through sacrificial bioprinting approaches.

Thanks to microfabrication processes microfluidic chips can be designed with high spatial resolution and reproducibility. Besides, the use of open channels allows for *in vitro* system perfusion for vessel maturation without requiring the developmental process of tubulogenesis. First attempts of microfluidic-based approaches relied on microfabrication of microfluidic channels within poly(dimethyl siloxane) (PDMS) molds by creating positive features of microchannel conduits using patterned photoresist [206]. These methods are compatible with generation and study of vascular formation on itself, but do not allow vascular network integration in mesenchymal and parenchymal compartments. Multiple additive and subtractive methods have been developed to generate microfluidic channels in biocompatible material such as hydrogel. Most of these techniques are based on soft-lithography and photolithography [189]. Soft-lithography techniques consist in the use of micropatterned elastomers such as PDMS to replicate topological features into soft material, and thus is a method of choice for patterning interconnected networks into ECM gels. These methods often imply an additive process where two molded gels are fused together [205]. However, molding approaches only allow for planar interconnected networks. Alternatively, development of photosensitive hydrogel has allowed for more volumetric design using photolithography. In photolithography, patterning is directed by light which induces either covalent crosslinking in non-

reticulated photopolymerizable hydrogel or degradation of covalent bond in crosslinked photo-degradable hydrogel [207,208]. Combined with multiphoton microscopy, laser degradation of bulk photo-degradable polymers enables precise micrometric patterning in 3D space.

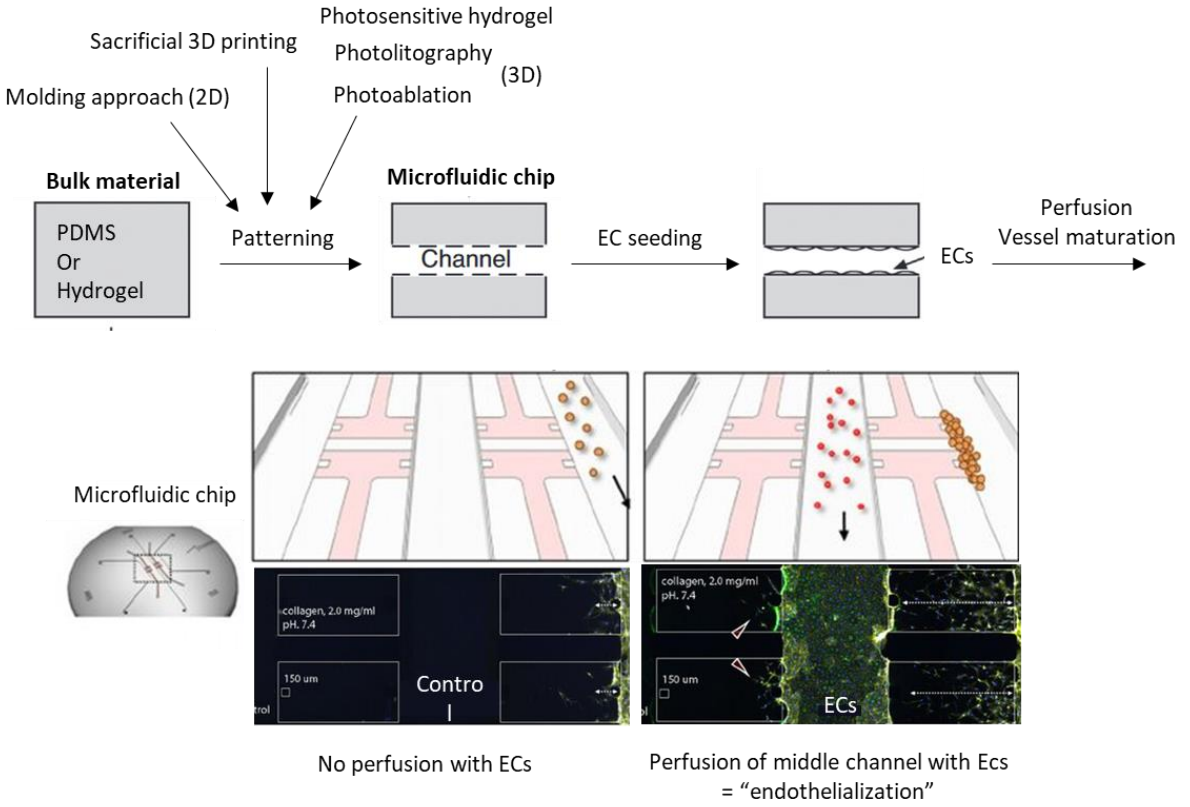

Figure 20. Principle of microfluidic chip "endothelialization" for in vitro vascular development. Microfluidic channels are generated within a bulk material through variable processes before their following "endothelialization" by endothelial cells (ECs) perfusion through intended channel. Molding approaches are cost effective way to generate microfluidic channels in most hydrogels but are limited to planar configuration. Novels approaches were developed based on the use of sacrificial material or photosensitive hydrogels to generate vascular networks in 3D. Bottom images show an example of endothelialization. Middle channel was perfused by GFP expressing ECs. Persistence of ECs in the channel is revealed in green. Adapted from [205,209].

Alternatively, embedded sacrificial 3D printing described in offers a viable option to achieve volumetric vascular networks organization. The printed material can be laden with sacrificial ink which can be dissolved to expose microfluidic networks [210,211]. Several sacrificial materials have been described for sacrificial printing. Some of them, such as carbohydrate-based glass, require first the generation of the sacrificial network, then its encasting into a biomaterial which can be laden with cells [212]. Embedded sacrificial printing relies on polymeric sacrificial ink such as gelatin. An impressive demonstration of this technique is the reported strategy of sacrificial writing into functional tissue

(SWIFT) which permitted printing of sacrificial ink into an assembly of hundred thousands of organ building block (e.g. embryoid bodies, cerebral organoids, cardiac spheroids), generating perfusable embedded channels system in large-scale living tissue [211].

Once generated by microfabrication or by printing strategies, interconnected microfluidic systems can be perfused with vascular cells, resulting in their alignment to the channels referred to as "endothelialization" [204]. However, most of the reported studies focus only on endothelial cells resulting in the generation of single layered endothelial cell networks lacking supporting cells. Besides, self-assembled vascular networks more closely recapitulate native vessel structures than endothelialized microfluidic channels [198]. Therefore, vascular engineering would benefit from hybrid methods combining self-assembling capacity of cells and engineering-driven methods to spatially and temporally drive endothelial vessels morphogenesis. In this direction, injection of high cell density using embedded 3D printing, as described in III.4 was used to promote *in situ* self-organization of endothelial cells and enabled patterning and tubular formation of vascular-like networks in collagen-I hydrogel [188].

We have seen that significant progress has been achieved in the field of vascular engineering, presenting the potential to transform the creation of vascularized tissue on a macroscopic scale into an achievable goal. These advancements pave the way for the generation of physiologically relevant large-scale human tissue with implications in both basic science and clinical applications.

IV. Thermogenic adipose tissues as promising therapeutic targets to restore energy balance in metabolic disorders

Obesity is defined by the World Health Organization as "a situation of abnormal or excessive accumulation of fat in adipose tissue leading to health inconveniences". Despite public health measures to improve modern lifestyle, obesity and diabetes have become a pandemic and represent risk factors for several leading causes of death such as cardiovascular disease, stroke and cancers [213]. The Global Burden of Disease study reported 5 million obesity-related deaths in 2019, with global obesity rates having nearly doubled since 1980 [214,215]. Primary causes for the development of metabolic disorder stem from prolonged disrupted equilibrium between the energy intake from food and the energy expended by the body (Figure 21) [216]. Energy expenditure corresponds to basal and adaptive metabolism including physical exercise, and adaptive thermogenesis. Up to now, current therapeutic options to treat obesity, including pharmacotherapies or surgery, have limited efficacy or important side effects. Therefore, the identification of a new therapeutic approaches able to increase energy expenditure is urgently required.

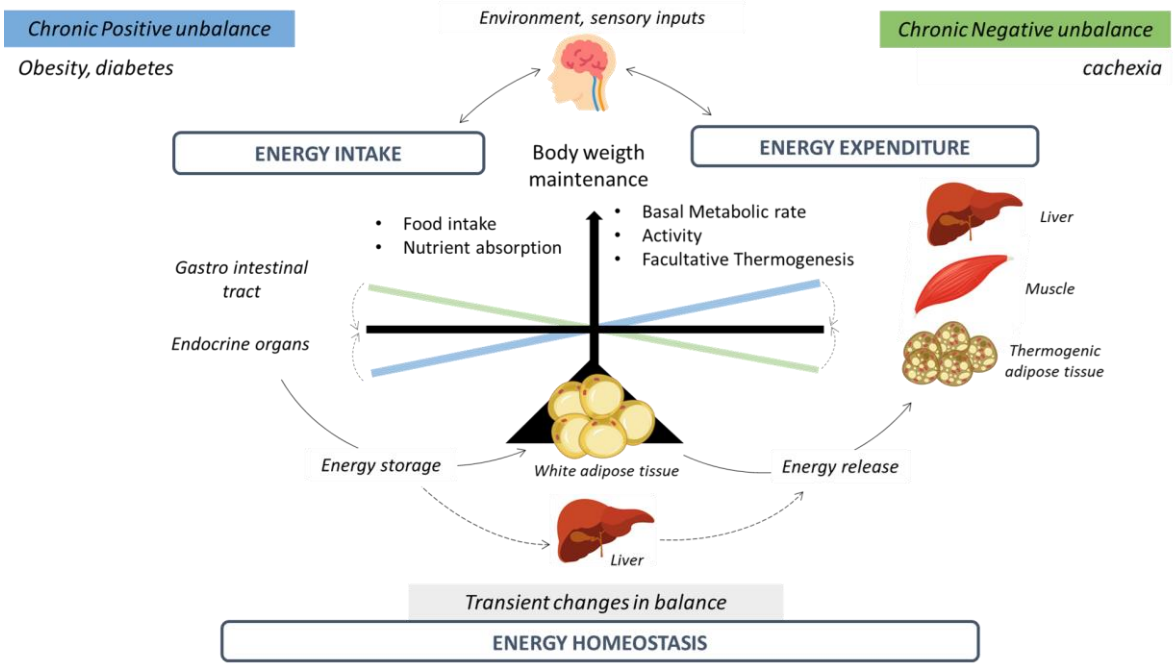

Figure 21. Coordinated regulation of energy homeostasis. Energy homeostasis relies on controls exerted on both energy intake and energy expenditure. Multiple organs intervene in the maintenance of energy balance by regulating energy absorption (e.g. gastrointestinal tract), energy storage, conversion and release (e.g. adipose tissues, liver) and energy dissipation (e.g. muscle, thermogenic adipose tissues). Positive energy unbalance corresponds to energy intake exceeding energy expenditure while negative balance corresponds to the opposite. Disrupted equilibrium in energy balance result in body weight alterations. Prolonged positive or negative energy unbalances induce development of metabolic disorders, obesity and cachexia respectively.

ATs play a central role in regulating whole-body energy and glucose homeostasis. While white adipose tissue (WAT) is the main energy buffer regulating dynamic equilibrium of energy homeostasis, thermogenic ATs are important energy dissipators. Since their discovery in humans, thermogenic ATs have gained renewed interest as therapeutic targets to treat metabolic disorders. However, existing models of human thermogenic ATs are scarce and limited in their ability to model native tissue physiology which impair the study of these tissues and the development of biotherapies [22–25].

In this thesis, we aim to develop relevant 3D models of human thermogenic ATs. To gain a thorough grasp of the importance of developing such models, we will first provide an overview of adipose tissues function as main energy regulators (see IV.1), how maladaptive plasticity of these tissues are associated with pathological conditions (see IV.2) and more specifically how thermogenic ATs can be used to treat metabolic disorders (see IV.3). In line with what has been discussed in II, driving in vitro development of relevant thermogenic AT models requires an understanding of its mature tissue architecture and cell compositions (see IV.4) as well as fundamental basis of its development in vivo (see I). In these sections, WAT characteristics will be described alongside those of thermogenic ATs as most of what we know about ATs physiology is derived from these tissues. However, specific focus will be given to thermogenic ATs specificities. Finally, an overview of the current processes for *in vitro* generation of human thermogenic ATs will be given (see I.6).

1. Adipose tissues: key regulators of energy homeostasis

ATs are largely distributed throughout the body in distinct depots. In addition to its function as a mechanical and insulation barrier to protect inner organs and prevent energy loss, adipose tissues have been recognized as key regulators of energy homeostasis [217]. Historically, adipose tissue has been classified into two main subtypes in mammals based on physiological differences and their respective functions in energy regulation: the white and brown adipose tissue, WAT and BAT respectively.

1.1. Specialized metabolic function and distribution of adipose tissues

WAT is the most abundant form of adipose tissue, representing 3% to 70% of the body mass depending on sex, age and lipid storage associated disorders such as obesity or lipid dystrophy [218,219]. Primary type of WAT is located under the skin and referred to as subcutaneous adipose tissue while visceral WAT surrounds the inner organs [220] (Figure 22). Altogether, WAT depots are the major long-term body's fuel reservoir through its function in energy storage and release [217]. Upon food intake, energy excess is efficiently stored as neutral triglycerides in WAT through fatty acids re-uptake and de novo lipogenesis. WAT is capable of expanding in mass to accommodate excess energy resulting in body

weight alterations [221]. In time of body's energy requirement, adipose tissues release energy through lipids re-mobilization upon the needs of the organism [217]. Triglycerides storage are breakdowns into glycerol and fatty acids through lipolytic pathways and released glycerol and fatty acids are then transported through blood circulation and which will up-take by the tissues according to their needs.

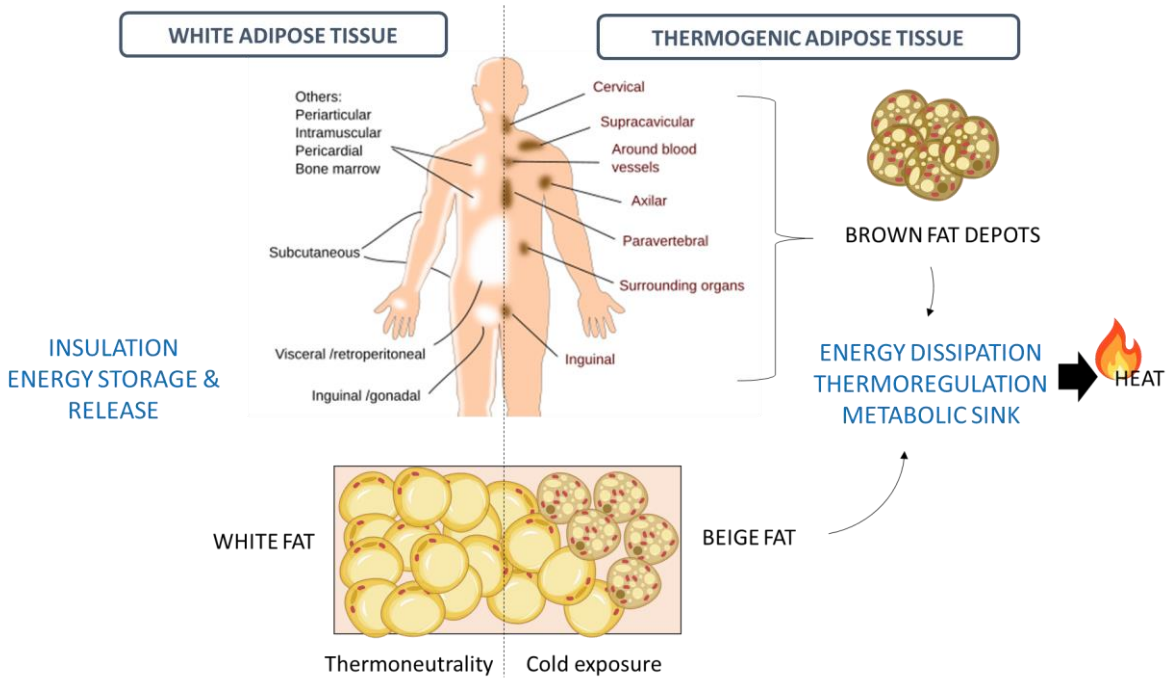

Figure 22. Adipose tissue subtypes distribution and metabolic functions in humans. WAT is largely distributed within the body and play a major role in body insulation as well as in the regulation of energy storage and release. Conversely, thermogenic adipose tissues that comprise BAT and beige AT play are specialized in energy dissipation as heat and consequently contribute to body thermoregulation. Thermogenic AT actively drain metabolite from blood circulation to fuel their thermogenesis and act as a metabolic sink reinforcing their role as energy dissipators. While BAT are localized in specific depots, beige AT emerge in response to environmental stimuli within WAT. Adapted from [222].

Contrary to WAT, BAT is found in small depots with specific locations close to vasculature [223] and specialized in dissipating energy as heat through a process referred to as adaptive non-shivering thermogenesis [224] (Figure 22). The primary function of BAT thermogenesis is its involvement in thermoregulation and the protection of the organism against hypothermia in species sensitive to heat loss, such as newborns, small mammals and hibernating animals. Thermogenic activation of BAT under cold exposure is mediated by β-adrenergic stimulation following the norepinephrine (NE) release from the sympathetic nervous system (SNS) [217]. Thermogenic function of BAT relied on the presence of thermogenic adipocytes within the tissue whose characteristic would be described in IV.4.4.

Thermogenic adipocytes primarily use free fatty acids to activate and fuel their thermogenesis [225] while increasing their glucose consumption [224]. Therefore, thermogenic adipocytes also act as metabolite sink regulating glucose and lipid level in blood circulation.

Until 2009, BAT in humans was thought to be limited to neonate individuals and gradually replaced by WAT with aging [226]. Using ^{18}F-fluorodeoxyglucose (FDG) positron emission tomography/ computed tomography (PET/CT) on adult humans submitted to cold exposure, authors revealed the presence of functional thermogenic depots with increased glucose uptake, although reduced compared to infants [226]. These depots were mainly located within the clavicular/supraclavicular region and surrounding deep organs such as heart, kidney, pancreas or liver [217] (Figure 22). FDG-PET/CT approaches also revealed gender differences with increased mass and activity of thermogenic adipose tissue in women compared to men [227].

In addition to BAT, emerging evidence suggests that mammals possess another type of thermogenic adipocytes referred to as beige or “brite” adipocytes [221,223]. First described in mice, activated beige adipocytes resemble brown adipocytes phenotypically and metabolically (for more details see IV.4.4) However, contrary to BAT depots that develop embryonically [211], beige adipocytes emerge sporadically within WAT depots during postnatal life in response to environmental conditions through a process called “browning” or “beiging” [217,223,224] (Figure 22). (for more details see I.5.2IV.4.4). These environmental stimuli include chronic cold exposure, physical exercise or β-adrenergic stimulation [217]. Subcutaneous WAT has higher beiging potential than visceral WAT [221].

Since the identification of thermogenic fat depots in adult humans, the prevalence of beige adipocytes in adult humans and their developmental origins have been an important debate [228] (for more details see I.5.1). The expression of thermogenic genes selectively expressed in mouse brown versus beige adipocytes have been used to classify human thermogenic fat depots [229,230]. Transcriptional analyses in adult human thermogenic fat revealed that supraclavicular depots most resemble mice beige adipocytes at molecular level, while deep neck and perirenal regions contain classical brown adipocytes [230–232].

1.2. Secretory function of adipose tissues

ATs are not only regulators of energy reserves but also contribute to far-reaching physiological processes such as food intake, insulin sensitivity, immune responses or reproductive function [217]. ATs are involved in a wide range of autocrine, paracrine and endocrine mechanisms which associate energy management with all physiological functions. Here we will more specifically focus on the endocrine function of WAT and thermogenic ATs in energy metabolism. Greater attention will be given to thermogenic AT and related secreted molecules.

Historically, leptin's discovery in 1994 marked the beginning of understanding WAT secretory function [233]. Since then, many other molecules such as adiponectin, resistin, interleukin-6 (IL-6) or tumor necrosis factor-α (TNF-α) were identified [234] (Table 5). Collectively referred to as "adipokines," these secreted factors display diverse roles extensively described elsewhere [234–236]. Leptin regulates body energy homeostasis and the maintenance of body mass by inducing satiety [234]. Adiponectin and resistin play opposites roles in insulin sensitivity, glucose, and lipid metabolism with opposing effects. While adiponectin is the most abundant adipokine in human plasma, mainly secreted by mature adipocytes, resistin is lowly secreted in physiological conditions [235]. Hypoadiponectinemia and hyperresistinemia are associated with to higher risks of insulin resistance and type 2 diabetes [235]. Both TNF-α and IL-6 are pro-inflammatory cytokine with increased secretion contributing to insulin resistance in obese humans WAT [235].

Table 5. Endocrine functions of selected adipokines. Derived from *[235]*.

Adipokine	Physiological roles
Leptin	Satiety, energy balance, reproduction, immunity, vascular
Adiponectin	Insulin sensitivity, glucose and fat metabolism
Resistin	Insulin sensitivity
IL-6	Inflammation, thermogenesis
TNF-α	Inflammation, regulation of adiponectin secretion

Neglected for a long time in favor of WAT, the potential secretory role of beige and brown adipose tissues has recently gained renewed interest [237,238]. Nowadays, the role of thermogenic AT as important endocrine organs is well established and they display distinct secretomes and secretory functions compared to WAT. As opposed to adipokines, these secreted molecules are referred to as “brown adipokines” or “batokines”. Definitions of batokines can vary from study to study as none of them are totally specific to thermogenic AT. Batokines are often qualified as secreted molecules preferentially released by BAT compared to WAT secretome. Numerous studies also defined brown adipokines as secreted factors whose secretion by BAT is increased upon thermogenic activation.

Hereafter, we will focus on the secretory function of thermogenic AT associated with their role in heat-generation and refer to batokines according to this second definition (Table 6). Batokines promote expansion and activation of the thermogenic AT from which they are released but also participate remotely in the thermogenic activation of other AT depots including beiging of WAT depots [238]. These brown adipokines directly target thermogenic adipocytes hyperplasia and activation but also promote the remodeling of supporting structures such as vascularization, innervation and ECM [238]. Moreover, growing evidence supports a role of batokines in the thermogenic activation through immune cells activation and recruitment (For more details see I).

Table 6. Roles of selected human batokines in thermogenesis.

Batokines	Role in thermogenesis	Communication	Target cells/organs
BMP7	Thermogenic adipocyte hyperplasia	Autocrine Endocrine	WAT Thermogenic AT
BMP8	Sensitivity to thermogenic activators	Autocrine Endocrine	WAT Thermogenic AT
VEGF-A	Neo-vascularization, thermogenic activation	Paracrine Autocrine	Vasculature Thermogenic AT
CXCL14	anti-inflammatory environment (macrophage recruitment)	Paracrine	Macrophages
Meteorin-like	anti-inflammatory environment (macrophage recruitment)	Paracrine	Macrophages
GDF15	anti-inflammatory environment (macrophage polarization)	Paracrine	Macrophages
IL-6	Thermogenic activation	Autocrine Endocrine	WAT Thermogenic AT Heart
NGF	Increased sympathetic innervation	Paracrine	SNS
FGF21	Thermogenic adipocyte hyperplasia, differentiation and activation	Paracrine Endocrine	WAT Thermogenic AT Heart

Upon adrenergic stimulation, thermogenic adipocytes elevate bone morphogenetic protein (BMP) release, specifically BMP7 and BMP8. BMP7 supports brown and beige adipocyte development [239] (For more details see I.5.1), while BMP8 sustains their thermogenic activity [240]. BMP8 enhances adipocyte sensitivity to thermogenic activators and contributes to WAT beiging. These cells also increase vascular endothelial growth factor-A (VEGF-A) secretion upon activation, promoting vascularization and boosting thermogenic activity in brown adipocytes [241]. In addition to vasculature, batokines secretion also affects sympathetic innervation through neurite outgrowth induced by secretion of nerve growth factor (NGF) [238]. Brown adipokines also include cytokines such as IL-6, C-X-C motif chemokine ligand-14 (CXCL14), growth-and-differentiation factor-15 (GDF15) and meterorin-like [238]. Upon adrenergic stimulation, CXCL14, GDF15, and meteorin-like foster an anti-inflammatory environment in thermogenic AT, where increased pro-inflammatory status negatively

correlates with thermogenic activity [238]. While both CXCL14 [242] and meteorin-like [243] promote the recruitment of anti-inflammatory macrophages, GDF15 [244] was found to inhibit pro-inflammatory macrophage polarization. IL-6 secretion by BAT rises under cold exposure, sustaining thermogenic function. Transplanting BAT explants from IL-6-KO mice demonstrated compromised energy expenditure and glucose tolerance compared to wild-type BAT explants [245]. IL-6 also drives beiging by beige adipocytes in WAT through autocrine effects, although the underlying mechanisms of thermogenic activation by IL-6 remain unclear [238]. Batokines are also mediators of inter-organ communications as it the case of IL-6 and fibroblast growth factor 21 (FGF21). FGF21 was among the first batokine proposed and is strongly released by BAT under thermogenic activation [238]. FGF21 participates in thermogenic activation of BAT and beiging of WAT while also ensuring cardioprotective functions [238].

While WAT is the most important energy buffer ensuring dynamic energy equilibrium, thermogenic AT contribute to whole-body energy dissipation. *Furthermore, both WAT and thermogenic AT are key regulators of whole-body energy homeostasis as endocrine organs regulating energy metabolism. Plasticity of both WAT expansion and thermogenic activation of beige and brown AT are at the core of energy balance restoration under transient changes in healthy humans. However, chronic energy disequilibrium imposes strain on AT plasticity contributing in the development of pathological disorders as we will see in IV.2.*

2. Pathological dysregulation of adipose tissues metabolic functions

When the organism is submitted to change in energy balance, ATs rapidly adapt their metabolism to protect it respectively against excessive flux of lipids and glucose or against decrease of resting metabolic rate. However, during prolonged energy unbalance or specific pathological conditions, ATs plasticity is challenged. Maladaptation of WAT or BAT/beige AT plasticity contribute to the development of metabolic disorders and/or further aggravate pre-existing pathological situations at the origin of AT function alterations.

2.1. Limits of white adipose tissue expandability and development of obesity and related-metabolic disorders

The initial development of high-fat diet-induced obesity is marked by continuous expansion of WAT in response to caloric excess with adipocytes hypertrophy preceding adipocytes hyperplasia [221]. During first stage of obesity development, expansion of WAT serves as protective mechanism of other tissues from lipotoxicity by capturing circulating lipids [221] (Figure 23). Continuous expansion of WAT is

associated with important tissue remodeling involving impaired vasculature, immune cells infiltration and establishment of tissue fibrosis by ECM remodeling [221,246]. Hypoxia, initiated by adipocyte hypertrophy, plays a role in pathological AT remodeling associated with obesity [247]. Obese individuals exhibit lower AT oxygen consumption and blood flow [247]. As hypertrophic adipocytes outgrow oxygen diffusion limits, hypoxia triggers increased ECM secretion, enhanced ECM reticulation and immune cell recruitment which further aggravate WAT fibrosis and limits its expandability [247] (Figure 23). Several studies correlate adipocyte hypertrophy with impaired capillary architecture and capillary rarefaction suggesting the establishment of a micro-environment non-permissive for angiogenesis [247]. Altered oxygen levels promotes pro-inflammatory state of WAT leading to dysregulated adipocytokines production in obesity (Figure 23). Altogether this pathological AT remodeling contribute to alterations of WAT metabolic functions and expandability leading to the development of unhealthy obesity once lipids buffering capacity of WAT is reached.

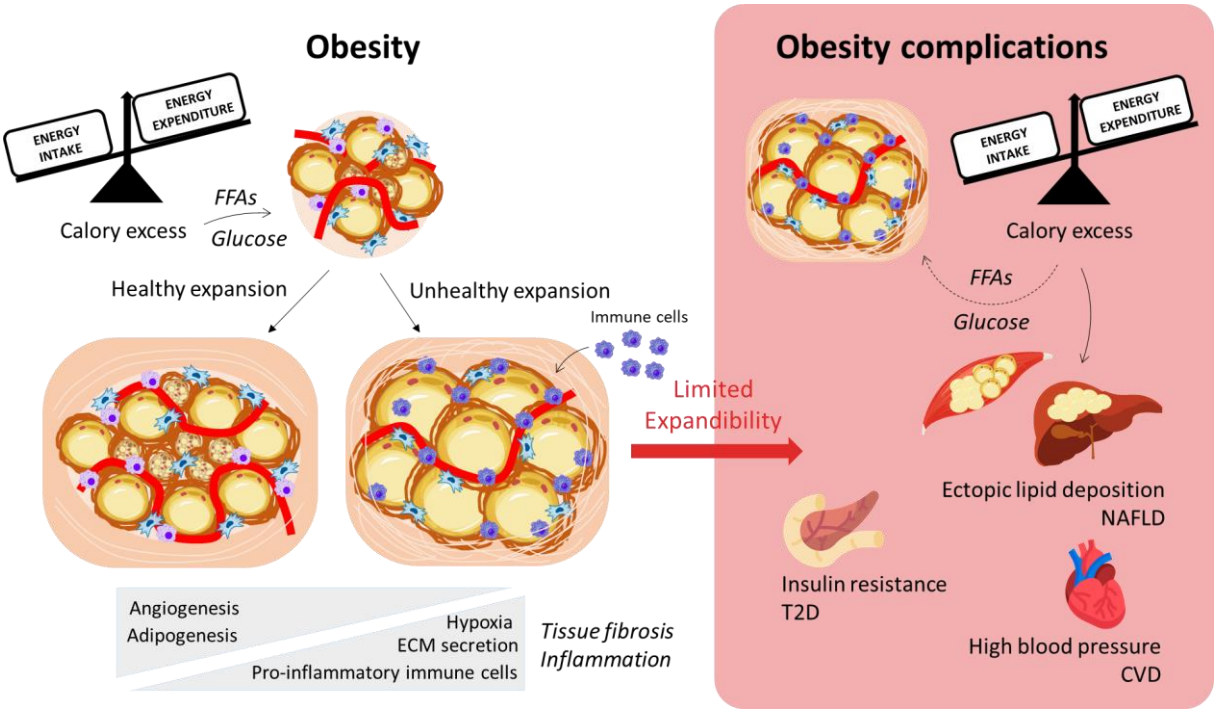

Figure 23. Limit of white adipose tissue expansion in obesity and related dysfunctions. White adipose tissue (WAT) responds to caloric excess through a healthy or unhealthy expansion. Healthy expansion through adipocyte hyperplasia protects against the metabolic complications of obesity. Unhealthy expansion through adipocyte hypertrophy is accompanied by tissue fibrosis and inflammation. Limited expandability of WAT promotes the development of obesity-associated metabolic complications. FFA, free fatty acids; ECM, extracellular matrix; ATM, adipose tissue macrophages; T2D, type 2 diabetes; NAFLD, non-alcoholic fatty liver disease; CVD, cardiovascular disease.

In unhealthy obesity, impaired capacity of adipocytes to uptake circulating glucose and FFA causes hyperglycemia and hypertriglyceridemia [248]. This further leads to ectopic accumulation associated with lipotoxicity in non-adipose tissues such as muscle, liver, heart or kidney [213] (Figure 23). Besides, hypertrophic adipocytes demonstrate important alterations in their metabolism including elevated basal lipolysis and insulin resistance. Overproduction of insulin in response to systemic insulin resistance leads to progressive pancreatic β-cell depletion and the development of type 2 diabetes [213].

Current therapies and management approaches for obesity involve dietary change, pharmacological and surgical strategies [249]. However, their effectiveness in restoring metabolic health and weight is limited. Pharmacotherapies for obesity and diabetes target pancreatic cell function, insulin sensitivity and aim to restore glucose and lipid metabolism [250]. However, many of these drugs show adverse effects. Similarly, while bariatric surgeries address effectively obesity, they can result in long-term complications and relapses [249]. Therefore, developing new strategies to restore energy balance is imperative (For more details see IV.3).

2.2. Dysregulations of thermogenic adipocytes function in pathological conditions

While many studies focus on thermogenic AT activation, relatively few investigate their alterations. Alterations of BAT and beige AT involve are associated with maladaptive plasticity and response to thermogenic activation. This include both pathological contexts leading to loss of thermogenic function of these AT and conversely their hyperactivation.

Decline of thermogenic characteristics of both brown and beige AT which progressively loss their thermogenic function is referred to as “whitening”. Both obesity and aging are associated with reductions in the abundance and activity of thermogenic adipose tissue in both mice and humans [226]. Mechanisms underlying this loss of thermogenic phenotype are still not clear but may involve several factors including vascular rarefactions, pro-inflammatory state of AT, and direct alterations of adipocytes expansion capacity [251].

Hyperactivation of thermogenic adipocytes were also reported in several pathological contexts such as cancer or severe burns [252]. Excessive activation of BAT and beige AT lead to the development of hypermetabolic conditions characterized by important loss of lipidic reserves [252], resulting in cachexia and life-threatening wasting of lean body mass. Such hypermetabolic conditions have been observed in mice models of cancer where some tumors promote adrenergic stimulation [253]. Cancer cachexia is characterized by an important weight loss, chronic inflammation and muscle atrophy and is considered as the cause of death in at least 20% to 30% of all cancers [254]. Thermogenic activation

of human BAT was reported in both adult and pediatric cancer patients. Maladaptive development of beige AT in human subcutaneous WAT was also observed in severe burn injury patients [255]. Sidossis et al. reported that burned patients produce higher levels of epinephrine and norepinephrine as measured in urinary excretion potential in response to inflammation [255]. Elucidating mechanisms to selectively inactivate the improper beiging of human WAT would further help therapeutic management of cancer cachexia and severe burn injury.

Increasing our knowledge of human thermogenic AT physiology and its functional drifts require development of physiologically relevant *in vitro* models. These new *in vitro* models of human thermogenic AT would help to obtain basic science knowledge about a tissue difficult to access in humans with far-reaching therapeutic implication beyond obesity related metabolic disorders.

3. Thermogenic adipocytes-based therapies for metabolic disorders

BAT and beige AT activation is associated with reduced cardiometabolic dysfunctions, dyslipidemia and insulin resistance in obese humans [256,257]. However, as mentioned above in IV.2.2, non-shivering thermogenic capacity of obese humans is impaired by reduction of thermogenic fat mass and functions. Therefore, increase of thermogenic AT activity is a promising strategy to promote a healthier metabolic phenotype in obese and diabetic patients [258]. Two main therapeutic trends are considered to increase thermogenic AT mass in diabetic and obese: 1) *in situ* expansion and activation of thermogenic adipocytes by pharmacological cues, 2) cell transplantation of thermogenic adipocytes.

Strategies to enhance thermogenic AT activity have first focused on *in situ* activation approaches by cold exposure or pharmacological treatments [259]. Cold exposure is the most potent stimulant for expanding and activating brown and beige thermogenic adipocytes in both mice and humans [221]. However, using cold exposure as a treatment for patients is impractical. Hence, efforts have focused on identifying drugs that can mimic effects of cold exposure and activate thermogenesis without adverse effects [259]. These drugs especially include β-adrenergic receptor (β-AR) agonists mimicking adrenergic stimulation by SNS. One example of this drug is mirabegron, a β3-AR agonist approved by the U.S. The Food and Drug Administration [259]. High doses of mirabegron were able to sustain increased BAT activation and energy expenditure in healthy humans, but also induced adverse increased blood pressure [260]. However, lower doses of mirabegron were insufficient to increase BAT activity and weight loss in obese humans, although improvement of insulin sensitivity and β cell function was still observed [261]. In addition to β-AR, other molecules have shown promises in BAT activation either in *in vitro* 2D culture or *in vivo* mice models, some known to activate thermogenic

pathways (e.g. resveratrol, curcumin) and some whose mechanisms of actions remain to be elucidated (e.g. capsaicinoids) [259]. As for any other pharmacotherapy, developing more relevant in vitro models of human BAT as a drug screening platform would significantly promote the translation of pharmaceutical activation of thermogenic adipocytes from bench to bedside.

Cell-based therapies is another approach under study to increase energy expenditure in obese humans [259]. Compared to single molecules, transplantation offers localized inducer delivery and a more lasting effect. The proof of concept for the beneficial effect of thermogenic adipocyte transplantation on energy expenditure and glucose metabolism have already been made in rodents. In most of these studies, thermogenic adipocytes from BAT grafts originated from healthy adult mice and were transplanted in obese or diabetic mice [259]. Such studies were also conducted using transplantation of human brown or beige adipocytes, obtained from *in vitro* differentiation following different protocols [25,262–264] (For more details see I.6.3.). Transplantation of thermogenic adipocytes were reported to increase whole-body energy dissipation in obese mice and restored normoglycemia in diabetic mice [25,263–265]. However, transplantation of human BAT is hindered by the low availability and deep location of these tissues. Thus, transplanting human thermogenic adipocytes requires *in vitro* generation processes able to produce a consequent number of these cells compatible with clinical application. This highlights the importance to develop new engineering processes to generate human thermogenic AT constructs in vitro which are relevant in size and function is required.

To summarize, adipose tissues are under constant remodeling to adapt nutritional status and environment. Prolonged imbalances in energy intake and expenditure lead to pathological changes in white and thermogenic adipose tissue, contributing to obesity and metabolic disorders like diabetes. In obesity, altered white adipose tissue functionality and expansion result in lipid accumulation in non-adipose organs and insulin resistance. This is accompanied by a decline in thermogenic adipose tissue mass and function, limiting energy expenditure. Increase of thermogenic AT mass by pharmacological or cell transplantation approaches have emerged as promising therapeutic strategies to improve metabolic health and counteract obesity. On another hand, pathological hyperactivation of thermogenic fat have been described in cancers and severe burn injuries. Altogether, this underscores the necessity for developing relevant human thermogenic tissue models. Such models are crucial not only for basic science, but also as drug screening platforms or transplantable source of thermogenic adipocytes. In line with the engineering concepts discussed in II and III, developing thermogenic adipose tissue solutions require insights into tissue structure and cell composition (see IV.4) as well as mechanisms contributing to their development and plastic thermogenic activation (see I).

4. Adipose tissue architecture and cell composition

AT are heterogeneous connective tissues highly vascularized and innervated by the SNS. Anatomically human AT are constituted of structural units termed lobules delimited by a connective tissue membrane called septa composed of extracellular matrix [266] (Figure 24). These lobules correspond to clusters of cells surrounded by another matrix compartment called stroma [266]. Lobules are composed of various cells including mature adipocytes and the stromal vascular fraction (SVF) [221]. The adipose SVF is a heterogenous mixture of cells which could be easily isolated by enzymatic dissociation [267]. Freshly isolated SVF contain endothelial cells, endothelial progenitors, adipose progenitors, fibroblasts and immune cells [221]. Collectively these cellular and ECM compartments components constitute the adipose progenitor micro-environment governing their maintenance, proliferation and differentiation. Majority of what is known regarding AT composition and structure is derived from WAT. Hereafter, an overview of the different cellular and acellular components of AT will be given with a specific emphasis on thermogenic AT characteristics when applicable.

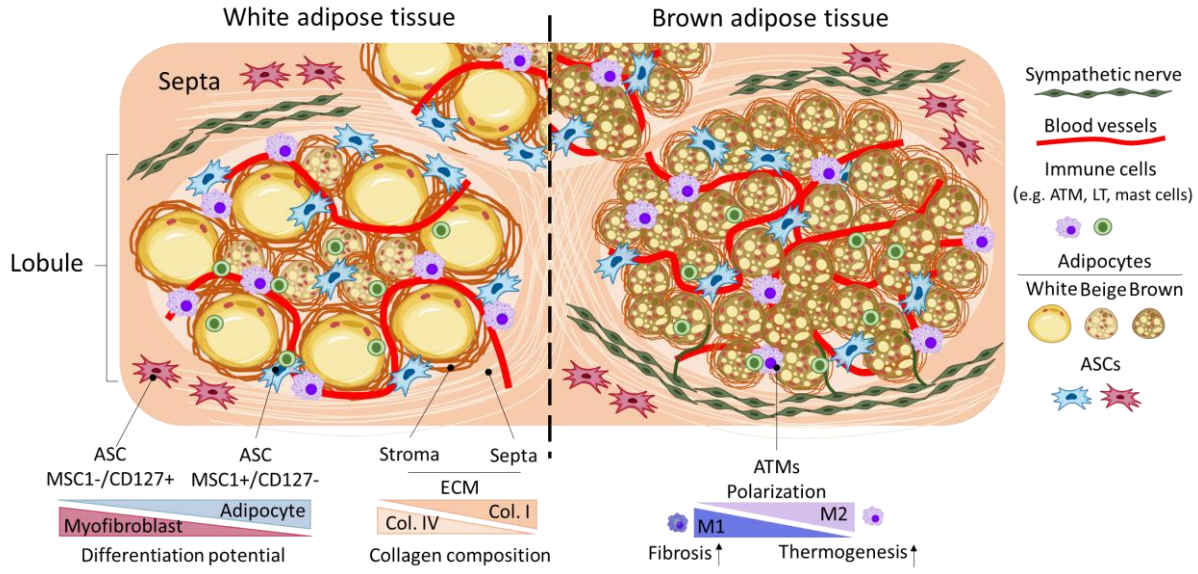

Figure 24. Adipose tissue lobular architecture and cellular microenvironment composition. Adipose tissue consists of clusters of cells arranged in lobules which are separated from each other by an extracellular matrix (ECM) that forms the septa, enriched in collagen I (Col. I). Lobules contain adipocytes, adipose progenitors (ASCs) and immune cells such as adipose tissue macrophage (ATM), lymphocytes (LT) or mast cells as well as dense networks of blood vessels that span into the septa and connect AT to blood circulatory system. In addition to the septa lining the outside of the lobule, the internal stroma also contains a distinct ECM compartment enriched in collagen IV (col. IV) and which contain sympathetic nerves. Distinct population of ASCs are spatially distributed in ATs with highly adipogenic MSCA1+/CD271- ASCs found in the stroma compared to myofibroblastic MSCA1+/CD271- ASCs. Main differences in WAT and BAT compositions involve nature of their adipocytes, vasculature and SNS innervation density. ASC, Adipose-derived mesenchymal stem cells.

4.1. Extra-cellular matrix

In both WAT and BAT, ECM offers structural support to maintain mechanical stability, elasticity, and cell adhesion, while simultaneously serving as a storage site for growth factors and cytokines needed for adipocyte growth and differentiation [268,269].

Within ATs, ECM is divided into stromal and interlobular septa compartments [266] (Figure 24). As any other connective tissue, collagen is a main component of adipose ECM, comprising up to 90% of AT non-cell mass. Scanning electron micrographs show that within the stroma each adipocyte is enveloped by a collagen fiber network that extends into interlobular septa [266]. Main collagen types of adipose ECM include collagen type I, III, and IV, with negligible expression of collagen type II [269]. In addition to collagen, adipose ECM contains fibronectin, elastin and small amounts of laminin [269]. Septa are densely composed of collagen I, III, and elastin, with an enrichment in collagen I compared to the stroma which is more loosely organized [266]. Mature adipocytes are surrounded by an collagen IV-rich ECM constituting the basal lamina [269] (Figure 24).

Adipose tissue ECM undergoes continuous turnover to accommodate dynamic changes required for AT expansion and remodeling [269]. This turnover is the result of a balance between pro-constructive and pro-degradation factors of the ECM. Pro-degradation factors include degrading enzymes from the matrix metalloproteinases (MMPs) family or the fibrinolytic system [269]. Pro-constructive factors include intracellular enzymes involved in the processing of ECM precursors, ECM molecule secretion by adipocytes and stromal cells, and degradation enzyme inhibitors such as tissue inhibitors of MMP (TIMPs) [269]. ECM flexibility also relies on crosslinking agents like lysyl oxidase enzymes [269].

Much of our understanding of adipose tissue ECM composition and remodeling relate to WAT, with limited insight into its relevance in BAT and WAT beiging. In vitro studies revealed that activation of thermogenesis through cAMP treatment induces changes in ECM component secretion and gene expression in mice brown adipocytes with an increase of collagen and laminin secretion [237]. Recent in vivo studies also revealed ECM-related gene remodeling in response to thermogenesis activation upon cold exposure [270]. However, observed secretions did not always align with respective gene expression changes, necessitating further proteomic investigations to comprehensively grasp ECM remodeling within BAT in response to thermogenic activation [237].

4.2. Innervation

Both WAT and BAT are highly innervated tissues, with BAT being more densely innervated than WAT. ATs receive bidirectional innervation with sympathetic efferent fibers that relay information from the central nervous system, while sensory afferent fibers transmit signals from the fat to the brain [271]. Innervation is key for AT to sense body nutritional status and external environment and thus is crucial for AT plasticity to maintain whole-body energy balance. Sympathetic innervation is well recognized for its importance in the regulation of adipogenesis, lipolysis and thermogenesis. Upon activation, sympathetic fibers release catecholamines, including epinephrine and norepinephrine, which primarily influence adipocyte metabolism via β-AR activation. Although less explored, recent findings suggest that sensory innervation of AT acts as a brake for sympathetic activation [271].

SNS innervation is especially important in BAT at both adipocyte and endothelial vessel levels [221] (Figure 24). Short-term cold exposure triggers β-adrenergic activation which induces lipolysis, FFA mediated UCP1 activation and prompts the transcription of thermogenic genes for non-shivering thermogenesis [221] while prolonged β-adrenergic stimulation induces BAT expansion by activating proliferation and differentiation of precursor cells [272,273] (For more details see I.5.2). In WAT, available data suggest that cold/β-adrenergic signaling induces fat depots “beiging” through both thermogenic activation of masked beige adipocytes and *de novo* beige fat differentiation [221]. More in depth description of thermogenic activation pathways at the molecular level will be given in I.5.2. As WAT is less innervated than BAT, it has been suggested that WAT "beiging" in response to cold might involve both sympathetic innervation and local production of norepinephrine and cytokines by immune cells [274] (See I.4.6).

4.3. Vascularization

Both white and BAT are extensively vascularized, with BAT exhibiting a denser network, contributing to its characteristic color [223] (Figure 24). When normalized to cytoplasmic volume, ATs are among the tissues with the highest metabolic turnover in the body, underlining the significance of vascularization for optimal oxygen and metabolite transport. Vessels facilitate the exchange of hormones, cytokines, and growth factors, supporting the endocrine role of ATs in inter-organ communications and providing vital factors for adipocyte function and survival.

Each AT lobule is supplied with a vascular unit composed of arterioles and venules which are subdivided into terminal capillaries surrounding individual adipocytes [275]. Almost each adipocyte is in direct contact with one or more capillaries. The dynamic of AT growth is thus importantly associated

with that of its vasculature. Indeed, WAT and BAT expansion is accompanied by the sprouting or branching of capillaries from existing blood vessels through angiogenesis while their mass reduction is associated with vessel regression [275]. Besides, the vascular bed highly controls alteration of the AT microenvironment including acidosis or hypoxia which influences adipocyte function and differentiation (see I.5.1).

Vascularization has a specific role in thermogenic ATs. It ensures O_2, FFA and glucose supply to fuel thermogenesis and to delivers heat to the whole organism. Increased vascularity is associated both with thermogenic activation of BAT and beige AT and increased of their mass [264,275]. Under thermogenic induction conditions such as cold exposure, endothelial cells produce paracrine factors that directly participates in increasing angiogenesis associated with increased energy expenditure [241] (for more details see I.5.3).

4.4. Adipocytes

Adipocytes are the primary components of AT located within the stroma of the AT lobules in close association with capillaries (Figure 24). These functional units, responsible for triglyceride storage of the tissues, exhibit diverse subtypes with unique physiology and morphology that regulate energy homeostasis, respective to WAT, BAT and beige AT [248]. Especially, adipocytes subtypes vary in size, mitochondria density, lipid storage capacity and associated metabolic functions.

Mature white adipocytes are specialized in fat storage and release to accommodate metabolic needs of organisms. They are characterized by a low mitochondria density and storage of lipids in large unique droplets, occupying over 90% of the cell volume [248] (Figure 25). Their size can varies from 20 to 200 µm based on metabolic needs, controlled by lipid droplet expansion or consumption [276]. Lipid removal within lipid droplet occurs either enzymatic hydrolysis from lipases (lipolysis) regulated by the presence of perilipin proteins at the lipid droplet's periphery or a selective form of autophagy (lipophagy) [248,277].

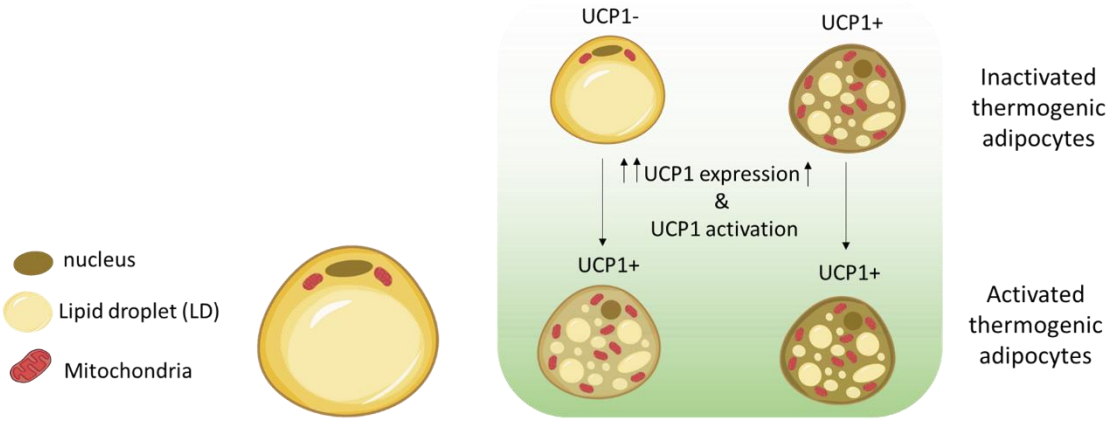

	White adipocyte	Beige adipocyte	Brown adipocyte
UCP1 expression	Negative	Inducible	High
Mitochondria density	Low/Undetectable	Medium/Inducible	High
LD morphology	One large lipid droplet	Heterogeneous droplet size, changing	Small multiple droplet
Function	Fat metabolism (storage & release)	Heat generation, others ?	Heat generation, others?

Figure 25. Characteristics of white, beige and brown adipocytes. The figure represents the distinct properties of white, beige, and brown adipocytes which support their specific metabolic functions. Characteristics of brown and beige adipocytes are given in their activated thermogenic state. Inactivated beige adipocytes possess white-like characteristics. While white adipocytes are specialized in fat storage and release, thermogenic adipocytes are specialized in fat burning leading to heat generation. Thermogenic adipocytes have a main role in thermoregulation but their activation in other context than cold exposure imply the existence of others functions of this fat burning capacity.

Unlike white adipocytes, thermogenic adipocytes meaning brown and beige types specialize in energy expenditure through fat burning by uncoupled mitochondrial respiration [248] (Figure 25). First identified in mice, brown and activated beige adipocytes share similar morphology and biochemical traits. Ranging from 15 to 60 µm in diameter, they are smaller than white adipocytes. Both are characterized by storage of lipids as multilocular droplets and high density in mitochondria which form a dense network around these lipid droplets. The inducible thermogenic ability of these adipocytes is conferred by their abundance in mitochondria and their specific expression of uncoupling protein 1 (UCP1), a proton transport protein of the inner mitochondrial membrane [224,225] (Figure 26). Upon activation, UCP1 uncouples cellular respiration from ATP synthesis by dissipating the mitochondrial H+ gradient, thus converting the energy of substrate oxidation into heat [225]. Activation of UCP1 protein is mediated by FFAs which are also the main oxidation substrate of uncoupled mitochondrial respiration. These FFAs are either generated by lipolysis of adipocytes triglyceride storage or actively drained from blood circulation following β-adrenergic triggering [225] (Figure 26) (For more details see I.5.2).

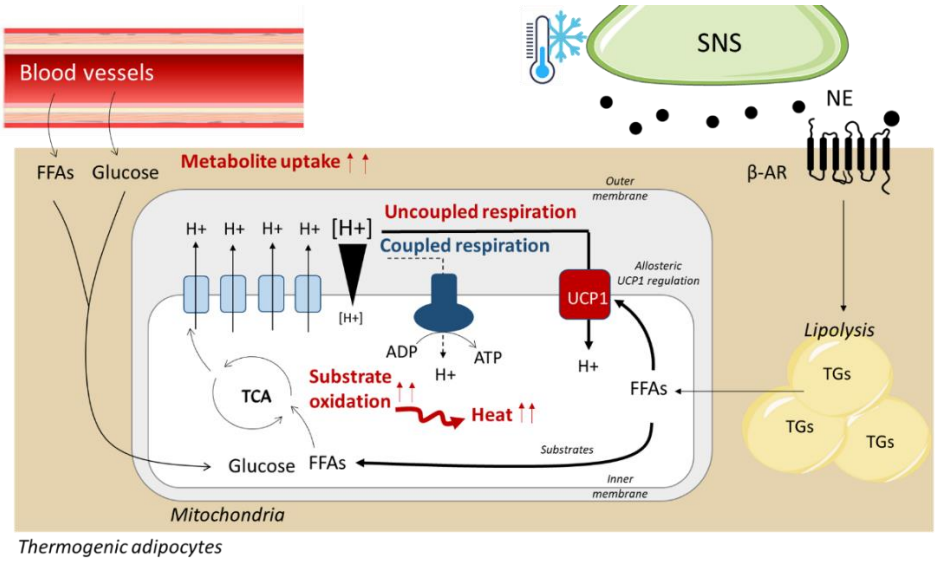

Figure 26. Principles of UCP1-dependent non-shivering thermogenesis in thermogenic adipocytes. Thermogenic adipocytes are characterized by expression of UCP1, a proton transport protein localized in the inner membrane of their mitochondria. UCP1 protein is the main effector of energy expenditure. In the absence of thermogenic activation, mitochondria generate ATP via coupled respiration. Upon thermogenic activation, UCP1 uncouples substrate oxidation from ATP production, by dissipating H+ gradient, leading to heat generation (uncoupled respiration). Under cold exposure, norepinephrine (NE) is released by the sympathetic nervous system (SNS) and induces β-adrenergic stimulation which triggers generation of free fatty acids (FFAs) from triglycerides (TGs) storage. These FFAs induced allosteric activation of UCP1 allowing its proton transport. Glucose and FFAs are main substrates used to sustain the increased mitochondrial respiration activity.

Brown and beige adipocytes differ in their inducibility of UCP1 expression [221,225] (Figure 26). While brown adipocytes strongly expressed UCP1 in “basal conditions”, continuous adrenergic stimulation is required in beige adipocytes for sustained high UCP1 levels and mitochondrial density [225]. In absence of stimulation, increasing evidence suggests that beige adipocytes become “masked” and exhibit white adipocyte-like morphology [231,278]. Upon stimulation, masked beige adipocytes can swiftly activate their thermogenic program by increasing UCP1 expression and mitochondria biogenesis (Figure 26). In mice, brown fat depots consistently contain brown adipocytes, while in adult humans, they tend to be more diverse, housing both UCP1+ and UCP1- adipocytes [229–232].

4.5. Adipocytes progenitors: adipose derived mesenchymal stem cells

Mature adipocytes are unable to divide and are renewed by proliferation and differentiation of adipose progenitors also referred to as adipose-derived mesenchymal stem cells (ASCs). This process is at the core of hyperplastic expansion of both WAT and BAT. Several studies shown that ASCs populations within AT are heterogeneous within a given fat depot and differ by their differentiation potential and

spatial distributions. Specific characteristics and developmental origins of ASCs within WAT and BAT will be covered in I.5.1. Hereafter, we will focus on common characteristics of ASCs within fat depots.

Such as bone marrow mesenchymal stem cells, ASCs are multipotent cells that can differentiate *in vitro* into multiple lineages including adipogenesis, osteogenesis, chondrogenesis [279] and myofibroblasts [280] (for more details see I.5.1). Due to their plasticity, ASC maintenance and differentiation rely on their microenvironment. ASCs are mainly located close to endothelial vessels and for this reason endothelial cells are considered a niche for these cells (Figure 24). Beyond differentiation, ASCs are recognized for their paracrine activities releasing factors like cytokines, angiogenic, trophic, and growth factors [279].

Common ASC surface markers were identified via SVF adipose tissue sorting, followed by in vitro assays for proliferation and adipocyte differentiation. In freshly isolated SVF, CD45 negative, CD34 positive, CD31 positive cells exhibit *in vitro* clonal expansion and mesenchymal properties. Further populations subsets were identified based on the expression of additional cell surface markers in human subcutaneous WAT while less is known in human BAT or beige AT. Estève et al. categorized three CD45+/CD34+/CD31+ subtypes using MSCA1 and CD271, known to be expressed in bone marrow progenitors with adipogenic potential [281]. MSCA1+/CD271- subset was reported to have the highest adipogenic potential and seen as committed adipogenic progenitors [281]. MSCA1-/CD271+ and MSCA-/CD271- demonstrated delayed adipocyte differentiation onset, suggesting more immature state toward the adipogenic program [281]. Moreover, MSCA1-/CD271+ exhibited higher myofibroblastic potential [281]. Interestingly, progenitor subsets are organized spatially in distinct environments within WAT [266]. Committed MSCA1+ cells were mainly found are in lobule stroma, while MSCA1-/CD271+ were enriched in septa, contributing to its fibrous production [266] (Figure 24).

4.6. Immune cells

ATs house almost all types of immune cell, spanning resident and recruited populations, contributing to various aspects of AT homeostasis and remodeling including cell debris clearance, angiogenesis, ECM remodeling and triggering inflammatory responses [221,282]. Main immune cell populations include adipose tissue macrophages (ATMs), lymphocytes, mast and dendritic cells [282] (Figure 24). It is now well established that metabolic processes activate modulation of both the innate and the adaptive immune system, also referred to as immunometabolic regulation of energy homeostasis [282]. Roles of immune cells in the regulation of AT function have been extensively reviewed elsewhere, especially in WAT [282,283]. Hereafter, we will focus on thermogenic AT and more

specifically ATM populations that have been recently proposed to participates in thermogenesis activation.

In AT, ATMs are the most prominent immune cell population, expanding as AT mass grows from increased adiposity [282,283]. In healthy humans WAT, ATM represents about 5% of adipose cells, but this number can rise to 50% in obese patients constituting the primary source of inflammation. However, ATM recruitment was also described in response to activation of non-shivering thermogenesis in BAT and beiging of WAT [221].

Cold exposure triggers recruitment of alternatively activated ATM, known for their anti-inflammatory properties (Figure 24) [274]. Studies reveal that these macrophages become activated and polarized through molecules like CXCL14, meterorin-like, or GDF15, released by activated thermogenic adipocytes [242–244]. This interaction underscores the dynamic relationship between thermogenic adipocytes and macrophages. Nguyen et al. initially identified a subset of these alternatively activated macrophages expressing tyrosine hydroxylase, an enzyme linked to catecholamine synthesis, which could release NE to support thermogenesis [284]. However, this result is called into question by other studies presenting contradictory data [274,285], leaving the mechanisms behind the role of anti-inflammatory macrophages in thermogenesis uncertain. A recent study showed that macrophages enhance local SNS activation in subcutaneous WAT during cold exposure, offering a new understanding of the interplay between macrophage and thermogenic activation [286]. Inversely, infiltration of pro-inflammatory macrophages and related cytokines were shown to correlate with decreased response to thermogenic stimuli in mice [274].

To summarize, adipose tissues are complex organs, where nervous, immune, and endothelial cells, along with adipose lineage cells, create a dynamic ecosystem that sustains tissue function and flexibility. Main differences between WAT, BAT and beige AT lie in the characteristic of their adipocytes. Non-adipocyte cellular and acellular components of AT are fairly common to BAT and WAT, expect their proportions that support their specific functions. Generating relevant models of human thermogenic aims to recapitulate this complex cell microenvironment and its dynamic in vitro. As discussed in II, engineering methods for in vitro development of a given tissue requires an understanding of its development and maintenance in vivo. Moving forward, we will overview the mechanisms that contribute to thermogenic AT development and activation in humans (see I). A specific focus would be given to adipocyte lineage and vascularization.

5. Understanding thermogenic adipose tissue development and activation

Engineering brown or beige AT require insight about intrinsic and extrinsic cues driving adipocyte differentiation and adipocyte thermogenic activation. Besides, being able to engineer embedded vasculature require to understand the mechanisms of neo-vascularization within AT and its interplay with adipogenesis.

5.1. Adipocytes development: common process and specificity to thermogenic fat

The development of white and brown adipocytes within their respective tissue is mediated by the differentiation of resident progenitors through a multi-step process called adipogenesis. For beige adipocytes, their development stem from both *de novo* differentiation of adipose progenitors and the conversion of white-like adipocytes into activated beige adipocytes through thermogenic program activation [221]. Processes leading to beige adipocyte activation will be cover in I.5.2). Here, we will focus on adipogenesis regulation which involves two main phases: adipogenic commitment of multipotent ASC into pre-adipocytes and terminal differentiation of pre-adipocytes into mature adipocytes [287].

Pre-adipocytes are morphologically indistinguishable from ASCs and are characterized by their restricted differentiation potential [287]. During terminal differentiation, pre-adipocytes progressively acquire morphological and functional characteristics of mature adipocytes through cascade of transcriptional activation [287]. While adipogenesis process has been extensively studied *in vitro* using chemical treatments and genetic manipulations, our understanding largely comes from pre-adipocyte cell line differentiations. For this reason, the transcriptional program underlying the preadipocytes commitment from ASCs is still poorly understood compared to the mechanisms of preadipocyte differentiation into mature adipocytes.

Several studies indicated an important role of the TGF-β superfamily in adipocyte lineage restriction of ASCs with an antagonist role of the BMPs and TGFβs subfamilies [280,288,289] (Figure 27). BMP4 and BMP7 promote adipogenic commitment of ASCs and differentiation while TGF-β inhibits it and rather promotes their myofibroblastic differentiation [280]. Myofibroblasts are contractile, α-smooth muscle actin-positive cells characterized by their important ECM production [290]. Myofibroblasts mediate wound contractions but their abnormal presence or persistence in tissue is a driving force of fibrosis development [290,291]. BMP7 specifically supports brown and beige pre-adipocyte commitment, while BMP4 promotes both white and beige/brown commitment in mice and human models [289]. However, expression of BMP4 at later stage was found to inhibit differentiation of pre-adipocyte into

mature thermogenic adipocytes in mice and positively correlate with obesity in human subjects [288]. Apart from TGF-β superfamily members, Wnt and Hedgehog signaling also modulate pre-adipocyte commitment by inhibiting adipogenesis [287].

In addition to growth factors, adipogenesis initiation is modulated by other microenvironmental cues including cell-cell and cell-ECM interactions, pH and local oxygen tension (Figure 27). Adipose progenitors and pre-adipocytes respond to ECM stiffening by dampening adipogenesis through mechanotransduction pathways such as YAP-TAZ pathway [268]. *In vitro* assays of ASCs differentiation have shown that restriction of ASC multipotency depends on substrate rigidity [292]. ASCs cultured *in vitro* on soft or rigid substrates preferentially commit to adipocyte or osteogenic lineage, respectively [292]. Hypoxia was reported to increase TGF-β secretion of mesenchymal stem cells [293] and inhibit adipogenesis [247]. This suggests that depending on environmental cues, ASC can switch between adipogenic and myofibroblastic engagement which may contribute to AT fibrosis in obesity [247].

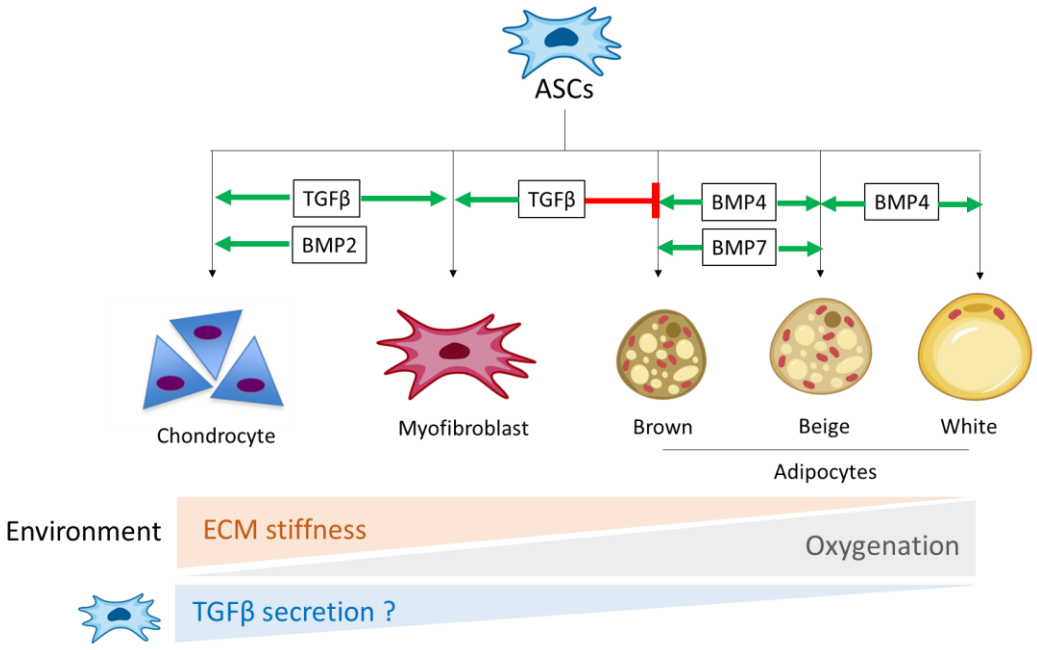

Figure 27: Effect of TGFβ/BMP subfamilies and related microenvironment factors on differentiation potential of multipotent adipose-derived mesenchymal stromal cells (ASCs). TGFβ and BMP subfamilies differentially promotes ASC commitment toward chondrocyte, myofibroblast and adipocyte lineages. TGFβ pathway activation inhibits ASC commitment to adipocyte lineages and favors their myofibroblastic or chondrocyte commitment. Specific BMP members intervenes to favor beige/brown adipogenesis over white adipogenesis. Extrinsic cues of the microenvironment also affect ASC commitment. ASC commitment to adipocyte correlates with low extracellular matrix (ECM) stiffness and high relative oxygen levels. Increased of TGFβ secretion by ASCs in response to low oxygen level may explain how hypoxia inhibits adipogenesis.

Terminal differentiation phase of pre-adipocytes starts with cell cycle arrest and activation of a transcriptional program common to white and beige/brown adipogenesis [287] (Figure 28). This common adipogenic program activates adipocyte-specific genes related to lipid accumulation, hormone sensitivity, ECM production, and secretory function. Under stimulation by pro-adipogenic factors, pre-adipocytes sequentially start to express members of CCAAT/enhancer-binding proteins (C/EBP) family starting with C/EBPβ and C/EBPδ which induces C/EBPα and PPARγ expression [287] (Figure 28). PPARγ is the master regulator of adipogenesis being both necessary and sufficient to induce adipogenesis. PPARγ also promote the maintenance of adipocyte differentiated states [287]. PPARγ and C/EBP transcriptional factors drive the upregulation of genes responsible for fatty acids transport such as fatty acid binding protein 4 (FABP4) or secreted hormones such as adiponectin in the late stage of adipogenesis [287].

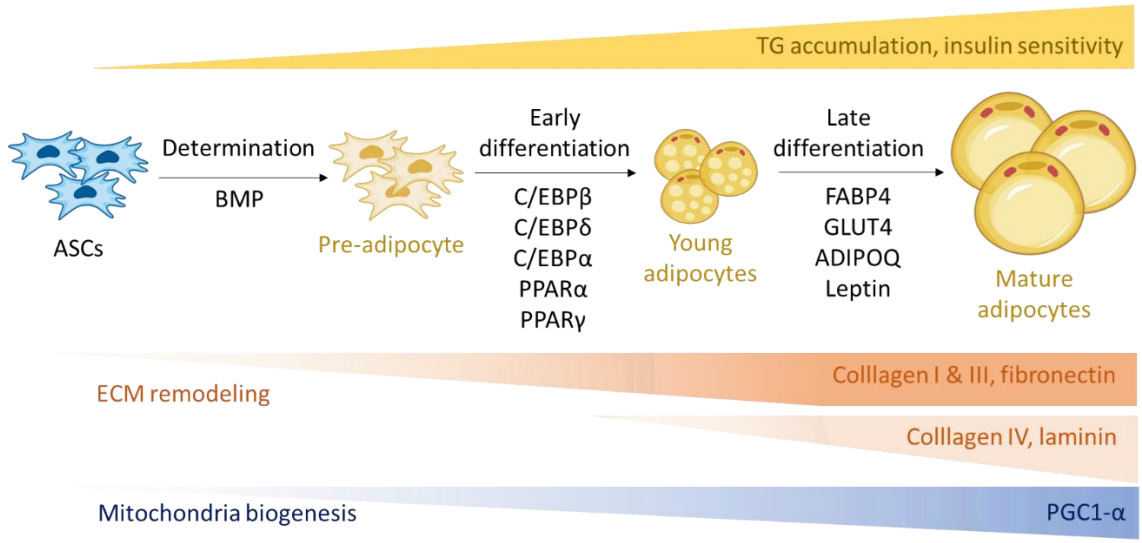

Figure 28. Common adipocyte differentiation program. The figure describes the transcriptional programs common to white and beige/brown adipogenesis. ASC commitment to preadipocyte under BMP induction is followed by cascade of transcriptional induction that target adipocyte-specific genes related to lipid accumulation, hormone sensitivity, ECM production, and mitochondrial function. As adipogenesis progress, cells progressively accumulate triglyceride (TGs) in lipid droplets and secrete ECM components. Adipocyte differentiation is also accompanied by increased in mitochondria content through mitochondria biogenesis under the control of PGC1-α expression.

Adipocyte differentiation is marked by an increase in ECM production, especially collagen synthesis, which is crucial for preadipocyte-to-adipocyte transition [269] (Figure 28). Studies reported that inhibition of collagen synthesis impaired adipogenesis [294] while culture of human mesenchymal stem cells with collagen type I or denature collagen type IV promoted adipocyte differentiation [295,296]. Inversely, activation of ECM degradation factors ensures space availability for white

adipocyte growth during AT expansion and initiates early stages of angiogenesis, essential for healthy AT growth [269].

Specific activation of thermogenic transcriptional programs underlying mature beige and brown generation involves *de novo* mitochondrial biogenesis and the expression of essential thermogenic components such as UCP1 [297]. Major regulators of the thermogenic adipogenic lineage include transcriptional factors such as the PR domain containing 16 (PDRM16) or coactivators of PPARγ binding (PGC1-α) to thermogenic gene promoters. Conversely, studies in mice reported that the multi-C2H2 zinc finger transcriptional coregulator (zfp423) negatively regulates PPARγ occupancy, and consequently maintain white adipocyte identity by inhibiting thermogenic program activation [298].

Are all adipose progenitors equally capable of supporting white, brown, and beige adipogenesis under the same cues? Some studies indicate that brown and beige adipogenesis might be partially driven by cell-autonomous factors in adipose progenitors. For instance, pre-adipocytes isolated from BAT differentiate into UCP1-expressing adipocytes, while those from WAT require additional β-adrenergic stimulation for UCP1 expression [297]. Lineage tracing in mice showed that adipose progenitors in BAT and WAT have distinct embryonic origins. It has been classically reported that brown adipocytes stem from Myf5+/Pax7+ precursors, suggesting common embryonic origin with skeletal smooth muscle cells, while beige and white adipocytes stem from Myf5-/Pax7- [299,300] (Figure 29). However, this binary model has since been challenged. Some white and beige adipocytes stem from Myf5+ progenitors in some white fat depots [301] while a subpopulation of Myf5- progenitors give rise to brown adipocytes in perirenal and peri-aortic BAT [302].

The origin of beige pre-adipocyte development in WAT, whether from dedicated beige precursors or shared white/beige precursors, remains debated [228,303]. Distinct populations of adipose progenitors have been identified in WAT based on the expression of mesenchymal makers such as PDGFRs (α and β). Tang et al study describes a PDGFRβ+ ASC population with high adipogenic potential, and refers to them as white adipose progenitors [304], although their beige potential was untested. Others studies identified PDGFR β-/PDGFRα+ ASCs as adipose progenitors with white and beige adipogenic potential [305] (Figure 29). Overall, these findings indicate that beige adipogenesis likely arises from bi-potential precursor cells capable of differentiating into both white and beige adipocytes. However, data are insufficient to confirm the existence of distinct "true" white precursors that cannot support beige adipogenesis

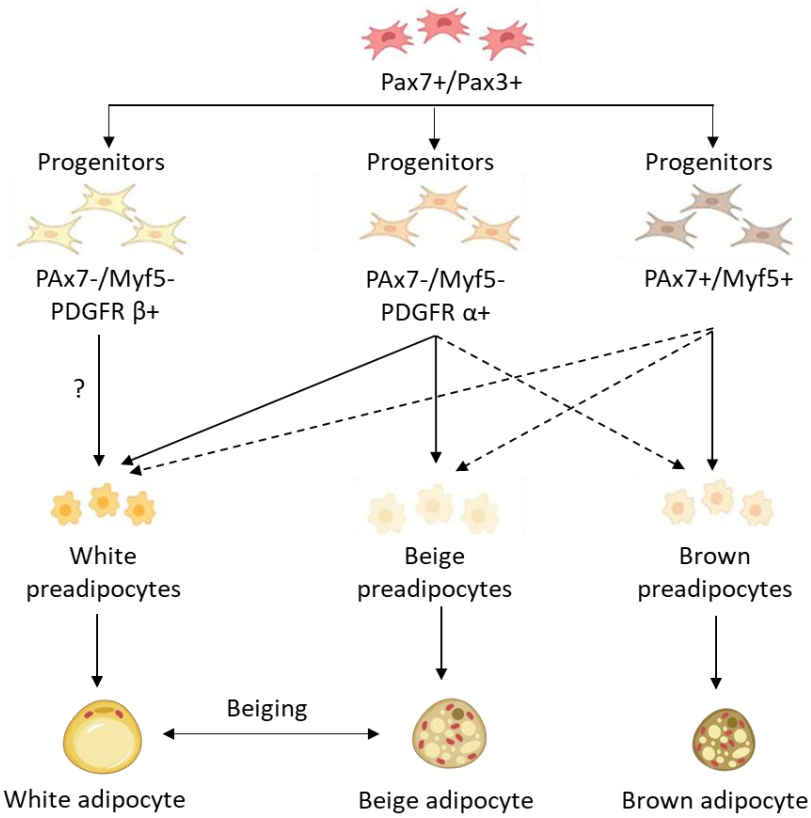

Figure 29. Developmental origins of white, brown and beige adipocytes. Adapted from *[251,306]*. Classical developmental view postulate that white and beige adipocytes derived mostly from Pax7-/Myf5- cells wile brown adipocytes derived from $Pax7^{+}/Myf5^{+}$ lineage. White and beige adipocyte likely arise from bi-potential precursors characterized by PGFRα+ expression. Until now markers specific beige or white precursors cells have not been clearly identified although PGFRβ+ has been proposed as white precursor marker.

5.2. Thermogenesis activation and transcriptional regulation of UCP1

Non-shivering thermogenesis is mainly mediated by UCP1 protein located in the inner membrane of mitochondria and its activation by long FFAs [225]. Hence, thermogenic activity depends on several factors which are UCP1 expression, activation of lipolysis for the production of free fatty acids from triglycerides and mitochondrial biogenesis. In absence of stimulation brown adipocytes already possess a high number of mitochondria equipped with UCP1 protein. Thus, brown adipocytes exhibit fast activating thermogenesis which initially rely on lipolytic pathway activation. Conversely, effective thermogenic activation of "masked" beige adipocytes requires primary upregulation of the thermogenic gene program in addition to lipolysis activation.

Numerous studies have aimed to identify positive and negative regulators involved in thermogenic adipocyte development and activation. Among them, cAMP-PKA signaling pathway was found critical to coordinate induction of UCP1 expression, lipolysis activation and mitochondria biogenesis [307]

(Figure 30). Classically cAMP-PKA pathway is activated by binding of β-AR to norepinephrine which is released by the SNS upon cold exposure. β-AR activation leads to increased cAMP level which acts as a second cell messenger to activate PKA [307]. On one hand, PKA activation induces lipolysis through activation of triglyceride lipases, promoting FFA release for mitochondrial utilization. On the other hand, PKA activation induces UCP1 upregulation in a p38 MAPK-dependent manner through activation and upregulation of transcription factors and co-activators such as PPARγ coactivator 1α (PGC1α) [307]. PGC1α upregulates UCP1 expression by promoting recruitment of essential transcription factors such as PPARγ to UCP1 promoter. PPARγ recruitment also depends on other co-activators including thyroid hormone receptors and retinoic acid receptors. As the master regulator of mitochondrial biogenesis, PGC1α expression links thermogenesis activation to mitochondria development [308].

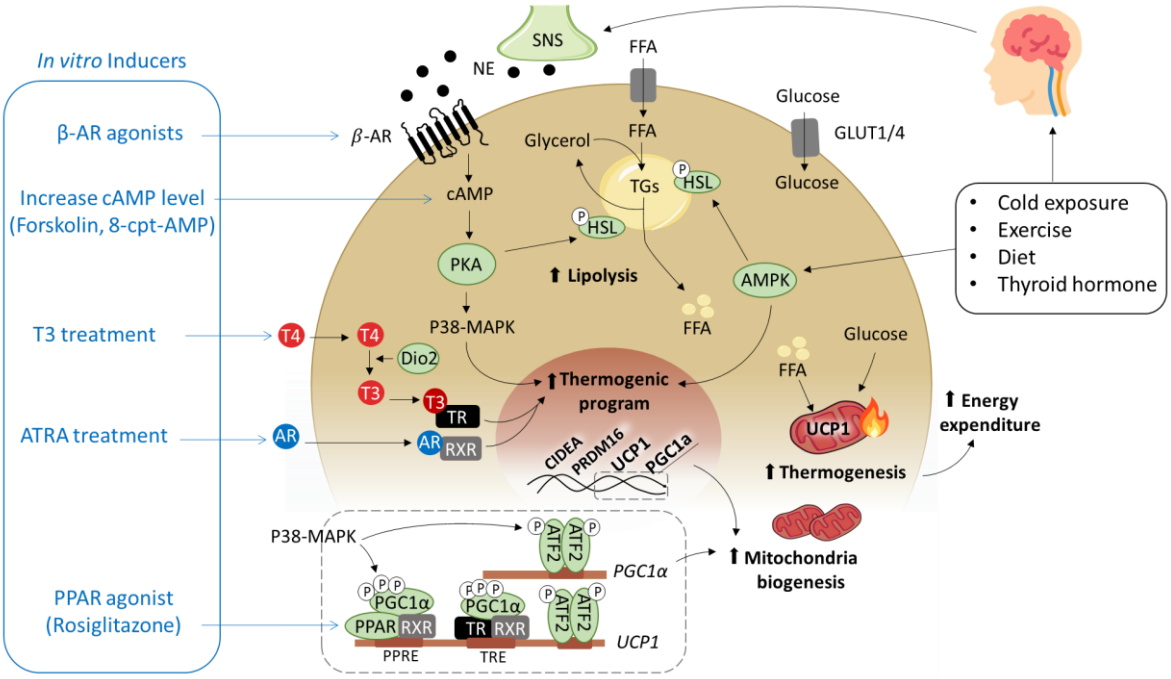

Figure 30. Thermogenesis activation mechanisms in brown and beige adipocytes. Detailed overview of thermogenic activation through norepinephrine, excreted by the SNS, or through direct activation of AMPK under control of central nervous system. Norepinephrine can bind the β3-adrenergic receptor, which will subsequently activate cAMP and PKA. PKA increases lipolysis by the activation of hormone-sensitive lipase (HSL) which hydrolyses the triglycerides (TGs) to release free fatty acids (FFA) that will enter the mitochondria and will eventually be used for heat production by uncoupling protein 1 (UCP1) in the electron transport chain. Chronic effect of PKA activation increasing thermogenic program through P38-MAPK pathway that contributes to recruitment of co-activators on UCP1 and PGC1α promoters. Thyroid hormones (T4 and T3) and retinoic acid increase thermogenic activation by increasing UCP1 expression. In vitro most common inducers that have been described in the literature to activate thermogenesis are shown. TR, thyroid receptor; RXR, retinoid X receptor.

Others positive regulators of non-shivering thermogenesis activation are thyroid hormones and retinoic acid [309,310]. Thyroid hormones (TH) are essential to this activation in response to cold exposure as hypothyroid patients are more prone to hypothermia during prolonged cold exposure [310]. ATs expressed 5-deiodinase type 2 (Dio2) which catalyzes the intracellular conversion of thyroixine (T4) to its active metabolite 3,5,3'-triiodothyronine (T3). Increase of Dio2 expression by noradrenergic induction increases intracellular level of T3. T3 contributes to thermogenic activation by promoting FFA mobilization from TGs storage to fuel thermogenesis but also through its interaction with thyroid hormone receptors (TR). Activated TRs act as co-activators binding to TH response elements (TREs) located in the promoter region of UCP1 promoter (Figure 30) [310]. Similarly, UCP1 promoter contain peroxisome-proliferator-responsive element (PPRE) which recruit activated retinoic acid receptor (RARs) as co-activators (Figure 30), explaining UCP1 responsiveness to retinoids treatments (9 cis retinoic acid, all-trans retinoic acid) in brown adipocyte *in vitro* [311,312].

Because of their pivotal function in triggering thermogenesis cascades, the primary methods employed for inducing in vitro thermogenesis involve β-AR agonists and artificial elevation of cAMP levels (e.g. forskolin, 8-cpt-AMP) (Figure 30). In mice, thermogenesis activation is primarily driven by β3-AR activation [313], whereas it is more controversial in humans [314–316]. Research findings have indicated contradictory significance of β3-AR activation, highlighting the possibility of a more prominent involvement of β2-AR and β1-AR activation in human thermogenesis [314–316]. Additionally, robust in vitro induction of thermogenic programs very often relies on the use of rosiglitazone, an agonist of PPARγ.

Another important factor of sustained active thermogenesis are glucose and lipids uptake to fuel mitochondrial respiration. However, the majority of glucose consumption does not fuel oxidative metabolism. Instead, glycolysis products are exported by the cells as pyruvate or lactate. Hence, thermogenesis activation is marked by increased glucose intake and increased lactate release [317].

5.3. Interplay between adipocyte and vascularization development in adipose tissue

Both during embryonic development and post-natal expansion of AT, vascular development appears to be closely coordinated in time and space with the formation of adipocytes clusters [275,303]. This suggests a strong interplay between vascular and adipocyte development. As mentioned previously, AT expansion is mediated by two mechanisms, hyperplastic growth and hypertrophic growth. Adipocyte hyperplasia is the main process of AT growth during embryonic development whereas post-natal growth is mostly driven by adipocyte hypertrophy. In both cases, AT growth is accompanied by neovascularization (Figure 31). However, the development sequence of vascularization and fat cluster expansion is fundamentally different depending on hyperplastic or hypertrophic adipose expansion. Neovascularization precedes adipocyte hyperplasia while it follows adipocyte hypertrophy [318].

Neovascularization is mediated by two main processes, vasculogenesis and angiogenesis. Vasculogenesis requires the recruitment of endothelial cell progenitors and their de novo differentiation into functional blood vessels. On the other hand, angiogenesis involves the proliferation, migration and remodeling of quiescent endothelial cells from preexisting vessels.

Until recently, vasculogenesis was considered to be restricted to embryogenesis. However, circulating progenitor cells, able to induce angiogenesis in limb or myocardial ischemia models, have been identified in some adult tissues [319]. Circulating progenitor cells are characterized by the expression of CD34 and CD133 markers. Based on CD34 and CD31 expression, distinct populations of endothelial cells were identified among the CD45 negative fraction of human SVF cells. While CD34 positive and CD31 positive cells constitute the mature endothelial cells, CD34 negative and CD31 positive cells demonstrate clonal expansion of endothelial cells *in vitro* [319]. These cells were proposed to be endothelial progenitor cells of adipose SVF and can be used as an endogenous source to engineer vascularized *in vitro* models of AT. Interestingly, it has been reported that culture conditions promoting endothelial cell proliferation also promoted the proliferation of ASCs with beige adipogenic potential supporting a functional relationship between microvasculature development and beige AT development [264].

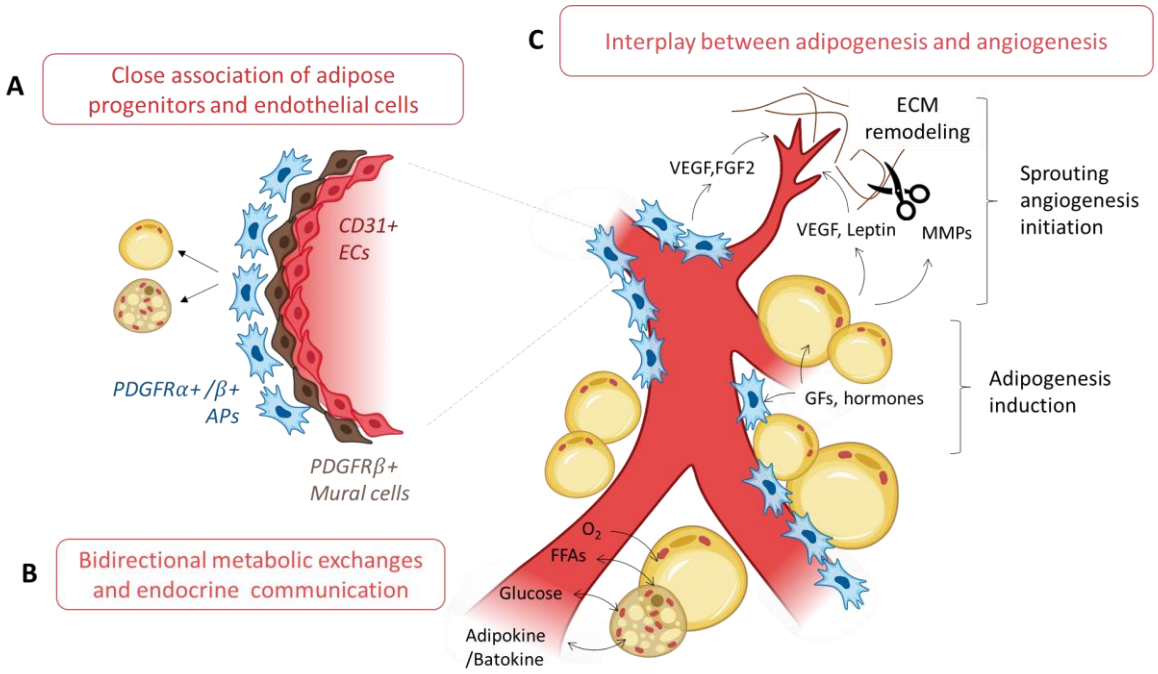

Figure 31. Functional and developmental cross-talks between adipose tissue vasculature and adipocytes. A) Adipose tissue (AT) vasculature supports metabolic and endocrine functions of adipocytes by ensuring exchanges of O_2, metabolite substrates and hormones. B) Vasculature constitutes a niche for adipose progenitors (APs). PGDFR-α+/ β+ adipose progenitors (APs) are found in a perivascular position adjacent to endothelial cells (ECs). C) Inter-organ communication participating in AT expansion through growth factors and hormones is supported by AT vasculature. Healthy AT expansion induces mild hypoxia leading to vasculature expansion. APs and adipocyte participate in initiation of sprouting angiogenesis by secreting pro-angiogenic growth factors (e.g. VEGF, FGF2) and hormones (Leptin). Adipocytes secrete matrix metalloproteinases (MMPs) participating in extracellular matrix (ECM) remodeling required for elongation of vascular sprout.

Despite the presence of endothelial progenitors within the tissue, angiogenesis remains the main process of postnatal vascular development in AT. Angiogenesis initiation depends on the balance between soluble pro-angiogenic and anti-angiogenic factors. The major pro-angiogenic factors are the members of the VEGF family which regulate proliferation, sprouting and tube formation of endothelial cells [190]. Besides, angiogenesis relies on endothelial cell invasion and migration across basement membranes. Thus, angiogenesis is strongly dependent on ECM degradation and deposition [190].

The functional link between fat cell and endothelial cell expansion is directly regulated by the secretory function of adipocytes and adipose progenitors (Figure 31). ASCs secrete high levels of VEGF and FGF-2 among other angiogenic-related molecules [279]. Adipocytes also secrete pro-angiogenic factors such as VEGF, IL-6 or leptin and ECM remodeling mediators such as MMPs [275]. In healthy AT, adipocyte hypertrophy induces mild hypoxia which enhances the secretion of pro-angiogenic factors [318]. However, excessive adipocyte hypertrophy in obesity induce increased secretion of collagen and

anti-angiogenic factors by hypertrophic adipocytes. In addition, high free fatty acid levels affect proliferation of endothelial cells and progenitors [320]. Therefore, an increasing number of studies highlight the important functional relationship between adipocyte and endothelial cells in physiological and pathological conditions both at the metabolic and developmental level.

We have described in the previous paragraphs what parameters intervene in the developmental processes involved in the generation of thermogenic adipocytes from adipogenesis to thermogenic activation mechanisms. These processes highlight the importance of selecting appropriate adipose progenitor source and providing them with specific biochemical and biomechanical cues to direct their differentiation. In I.6, we will provide an overview of the current state of translating this understanding into bio-fabrication processes for in vitro generation of thermogenic AT constructs.

6. *In vitro* generation of human brown and beige adipose tissue

Brown and beige ATs hold promise as therapeutic targets for metabolic disorders, but effective strategies require a deeper understanding of human thermogenic fat physiology. Although rodent studies have been informative, it is now clear that human thermogenic fat possesses unique characteristics in activation and potential, necessitating human-specific *in vitro* models. Besides, transplantation of human BAT is hindered by the low availability and deep location of these tissues. Thus, advancing these approaches require development of engineering process to produce transplantable and functional thermogenic adipocytes *in vitro* associated with effective implantation methods. Altogether, there is a clear need for engineered human thermogenic AT constructs that faithfully replicate tissue microenvironment and native functions.

Tissues engineering approaches for the generation of AT *in* vitro have predominantly focused on WAT for metabolic studies or soft tissue reconstruction. WAT constructs have been obtained from various protocols, as reviewed elsewhere [321,322]. On the other hand, only a handful of approaches have been described for *in vitro* generation of human thermogenic AT. The following section will provide insight on cell sources available for *in vitro* generation of thermogenic adipocytes, current approaches to generate ex vivo 3D models and transplant thermogenic adipocytes.

6.1. Human cell sources for *in vitro* generation of thermogenic adipocytes

Three main options can be considered to culture adipocytes *in vitro*: culture of freshly isolated mature adipocytes, the use of AT explant, or *in vitro* differentiation of cells into adipocytes. While mature adipocytes are notoriously difficult to isolate and maintain *in vitro*, AT explant display limited long-term viability and may undergo transcriptional alterations [323]. Furthermore, due to the low

availability of human BAT, *in vitro* generation of new thermogenic adipocytes appears to be the most suitable option to study and engineer thermogenic AT models.

While white adipocytes are mostly derived *in vitro* from primary ASCs or pre-adipocytes cell lines, more various protocols have been described for *in vitro* generation of human thermogenic adipocytes. Mostly driven by the scarceness of BAT in humans and their deep location, these protocols encompass a variety of starting material including primary adipose progenitors derived from BAT or WAT, immortalized or not, pluripotent stem cells but also fibroblast or muscle cells (Table 7). Here we will mainly focus on adult and pluripotent stem cells sources [324].

Table 7. Cell sources to generate human thermogenic adipocytes in vitro

Cell source	Origin	Genetic Modification	Sub-cloning	Availability	Clinical compatibility	Ref.
Primary brown adipose progenitors	Non viable infant BAT, adult supraclavicular and neck BAT	No	No	Low	Yes	[325]
Immortalized brown adipose progenitors	Non viable infant BAT, (Paz6), adult supraclavicular and neck BAT	Yes (mTERT)	Yes	Medium	No	[326,327]
Primary muscle cells	Fetal and adult human CD34+ muscle progenitors	No	Yes	Medium	Yes	[328]
Primary dermal fibroblast	Adult human	Yes (CEBPB, C-MYC) No	Yes No	Medium	Yes Yes	[329] [330]
MSCs	Adult human bone marrow	Yes (PPPARGC1A)	No	High	Yes	[331]
hMADS	Infant human WAT	No	Yes	High	No	[332]
Primay ASCs	Adult human WAT	No	No	High	Yes	[333]
hPSCs	Human embryonic stem cells (EBs)	Yes (Pax3, PRDM16)	Yes	Medium	Yes	[329,334]
hiPSCs	hiPSC spheroids	No	Yes	High	Yes	[335]

Giving cell-autonomous effect on adipogenesis, it is noteworthy that the source of adipose progenitors will influence the potential thermogenic fate of these cells when considering in vitro engineering of thermogenic tissue.

Adipose progenitors can be harvested from primary human BAT SVF and differentiated in vitro. Most of these cell models are derived from non-viable human fetal interscapular BAT or from adult human supraclavicular regions [324]. Once differentiated into brown adipocytes, these cellular models exhibit UCP1 expression, lipolytic response to cAMP and increased oxygen consumption in response to β-adrenergic stimulation [327,336,337]. However, due to the low availability of human primary BAT, the majority of these cells have been subcloned and immortalized to obtain readily available material for long term study of human BAT. A more heterogeneous immortalized model has been generated from human adult deep neck regions without subcloning.

A more readily accessible source of primary adipose progenitors is human WAT SVF. Although initially used as a primary source for the generation of white adipocytes, several studies have reported the possibility to generate thermogenic adipocytes from WAT-derived ASC, freshly isolated or cryopreserved [324]. These protocols often involve the use of an adipogenic cocktail containing BMP7 to promote beige/brown adipogenesis and chronic stimulation of the thermogenic transcriptional program with PPARγ agonist [333,338]. From our knowledge, stopping the stimulation of the thermogenic transcriptional program results in reduced UCP1 expression, implying a beige phenotype for these thermogenic adipocytes. Hence, the self-renewal capacity of ASCs and their readily accessibility in WAT, make WAT-derived ASCs an unlimited starting material to generate beige adipocytes.

A potential unlimited source to generate brown adipocytes resides in the use of pluripotent stem cells. Mature brown adipocytes were generated from human embryonic stem cells or hiPSCs using various protocols [324]. Most of these protocols involve gene transfer to promote the expression of brown adipose progenitor markers or beige/brown adipogenesis effectors. However, a study successfully generated brown adipose progenitors from hiPSC without gene transfer especially through the use of TGFβ inhibition, making them more suitable for clinical applications [338]. Interestingly, generation of brown adipose progenitors from these pluripotent stem cell requires in all cases first stage of cell culture as 3D aggregates, embryonic bodies or hiPSC spheroids, highlighting the importance of 3D environment in the generation of relevant thermogenic AT models.

6.2. Current 3D models of thermogenic AT

The development of 3D AT models has already yielded results, especially in generating white adipocytes in vitro. Indeed, several studies highlight the effectiveness of these 3D techniques in producing adipocytes that closely resemble mature white adipocytes in terms of morphology, transcriptional profiles and metabolic functions [339]. Additionally, some studies have aimed to recreate the cellular complexity of native AT by introducing vascular [322] and immune components [340]. Regarding thermogenic ATs, few models have been described, primarily focusing only on the generation of functional thermogenic adipocytes (Table 8) [22–25]. When tested, generated 3D thermogenic AT constructs yield higher beige/brown adipogenesis than their 2D counterpart, demonstrating better promotion of thermogenic phenotype from 3D cell structuration [23,341].

Table 8. Current 3D models of human thermogenic adipose tissue.

Engineered construct			ECs	Metabolic assessment of generated thermogenic adipocytes				Ref.
Cells	Material	Cell assembly		Control	UCP1	Glucose intake	Cell respiration	
Human adult ASCs from WAT	PEGDA 5% photo-polymerized hydrogel	Isolated cells in hydrogel	No	WAs	Chronic induction, mRNA, protein	/	Increased uncoupled respiration, Replated cells, Normalized	[23]
Human immortalized BAPs	HAMA/GelMA /HA/Gelatin photo-polymerized hydrogel	Bioprinting of isolated cells/hydrogel	No	Internal control (Stiff porous)	Chronic stimulation, mRNA, protein	Increase (^{3}H 2-DOG)	Increased basal levels, Replated cells, Not normalized	[22]
Human MVFs	Fibrin hydrogel Chemically cross-linked hydrogel	Explant in hydrogel	Yes	WAs NDs cells	Chronic induction, mRNA	Tendency vs ND cells (ISGU)	Increased basal levels vs ND cells, Not normalized	[24]
Human immortalized BAPs	Thermosensitive PEGDA	Spheroid in non - adhesive hydrogel	No	WAs	Chronic induction, mRNA, protein	Increase (^{3}H 2-DOG)	Increased basal levels, Replated cells Not normalized	[25]

ASC: adipose derived mesenchymal stromal cells; BAPs: brown adipose progenitors; MVFs: microvascular fragments. Functional assesment control: WAs: White adipocytes generated from the same precursors than thermogenic adipocytes but using a white adipogenic cocktail; NDs: precursors cells maintained in growth medium. Chronic stimulation: Brown/beige inducers present for more than one week in the differentiation medium before assessment of beige/brown markers expression

Some studies use scaffold-free models based on the self-aggregation of adipose progenitors into cell-aggregates. Brown adipose spheroids were obtained from both primary brown adipose progenitors from mice BAT and recently immortalized human brown adipose progenitors [25,341]. In both studies, assessment of thermogenic phenotype from AT construct was limited to the successful demonstration of UCP1 expression at the end of the differentiation.

On the other hand, some studies employed hydrogel to encapsulate primary human ASCs or immortalized human brown adipose progenitors from adult neck BAT [22,23]. Yang et al. used utilized a cell suspension of ASCs from subcutaneous WAT, seeded in a 5% PEGDA hydrogel, to create a beige adipose construct exhibiting increased UCP1 expression associated with increased uncoupling respiration compared to WAT construct [23]. Kuss et al. engineered 3D BAT models through bioprinting of immortalized brown adipose progenitors within photocrosslinkable methacrylated hyaluronic acid (HAMA) and GelMA hydrogels [22]. Authors used UV light exposure as well as printing spacing parameters to adjust for stiffness and porosity. They demonstrated that stiff and porous scaffolds achieved higher thermogenic gene expression compared to other conditions, suggesting that beige/brown adipogenesis is better promoted in a stiffer environment compared to white adipogenesis [22]. Stiff porous scaffold condition also led to the highest glucose consumption and maximal respiration.

Notably, Kuss et al. revealed that pre-exposure to angiogenic factors using EGM medium promoted greater brown adipogenesis of human brown adipose progenitors, aligning with previous findings highlighting the role of vascularization in favoring thermogenic activity [22]. Despite its significance, only one approach to engineer vascularized BAT has been proposed by Brey team and relies on the culture of microvascular fragments (MVF) from subcutaneous rodent WAT [342]. MVF cultivated in brown adipogenic medium exhibited higher thermogenic gene expression but no differences in uncoupling respiration compared to white adipogenic condition. Similarly, the team demonstrated this method using human MVF to create AT constructs expressing beige adipocyte markers [24]. However, uncoupling respiration differences were solely observed between undifferentiated and differentiated conditions (WAT and BAT), potentially influenced by the uncoupling effect of lipids themselves.

All of these studies demonstrate the feasibility of generating 3D constructs of human thermogenic AT containing UCP1-expressing cells. However, none of these studies demonstrate full functional maturation of these adipocytes and especially their responsiveness to environmental changes. Key functional characteristics of thermogenic adipocytes rely on their ability to respond to environmental signals by acquiring an active thermogenic state, marked by increased UCP1 content and enhanced respiration and glucose consumption. In existing 3D models, only the overall metabolic activity of

thermogenic AT constructs is evaluated in comparison to cells obtained from different culture protocols, such as undifferentiated cells or white adipocytes, rather than assessing the metabolic plasticity of these adipocytes in response to environmental cues. Paradoxically, this assessment of AT plasticity is more commonly observed in studies focusing on generating 3D WAT constructs, where the "beiging" potential of AT constructs in response to elevated cAMP levels or β-adrenergic stimulation is demonstrated [343]. However, in that case, studies generally focus only on the inducibility of UCP1 without conducting detailed metabolic analyses. Hence, the field still lacks vascularized 3D models of human thermogenic AT that can display both mature thermogenic activity and its responsiveness to induction. Additionally, the secretory function of thermogenic AT, another important functional aspect, is often overlooked in the assessment of the functionality of these 3D models.

6.3. Current strategies of human thermogenic adipocytes transplantation

Until now, the majority of transplantation investigations have relied on mouse BAT due to the deep-seated locations of human BAT. Isolating sufficient human BAT for transplantation and research is challenging. Thus, it is necessary to produce human thermogenic fat *in vitro*. Effective transplantation approaches necessitate the successful generation of thermogenic adipocytes and implantation techniques that establish an appropriate microenvironment to ensure their post-transplantation retention, viability, and functionality. Some protocols have been proposed in the literature which vary in the source of the transplanted cell used and their transplantation methods (Table 9).

Table 9. Existing strategies for human thermogenic adipocytes transplantations.

Cells	Culture type	Supportive material	Mice	Engraftment site	Metabolic effect	refs
Human adult ASCs from WAT	2D culture	Matrigel	NOD-scidIL2rgnul HFD	Subcutaneous, dorsal region	Increased glucose fasting	[264]
hPSC-derived BAPs	2D culture	/	ICR mice	Subcutaneous, thoracic-sternum region	Increased glucose fasting	[262]
CRIPSR engineered human WAPs	2D culture	Matrigel	Nude mice HDF	Subcutaneous, thoracic-sternum region	Decreased body weight Increased glucose fasting	[263]
Human immortalized BAPs	3D spheroids	/	Immune deficient Rag1$^{-/-}$ HFD	Kidney	Increased glucose fasting	[25]

ASC: adipose derived mesenchymal stromal cells; BAPs: brown adipose progenitors; WAPs: white adipose progenitors.

Until now, reported transplantation studies of human thermogenic adipocytes involve transplantation of fully differentiated UCP1 expressing adipocytes in immunodeficient mice. These adipocytes have been derived from various cell sources including immortalized brown adipose progenitors [25], hPSC [262], genetically modified white adipose progenitors [263] or ASC from human WAT [264]. After transplantations, these cells were proved to maintain thermogenic activity which correlated with improved metabolic parameters such as glucose tolerance in healthy [344] and high fat diet (HFD) induced-obese mice [25,263,264].

Until very recently, only approaches that have been described employed generation of cells in 2D cell culture followed by their harvesting before transplantation. Some of these studies directly transplanted the cells within engraftment site [262]. However, these approaches led to low survival rate of the cells as cell suspensions alone often shown limitations in cell retention at engraftment site [107]. To promote cell survival, some of these studies used Matrigel [25,264] as a supportive hydrogel. Matrigel efficiently promoted survival of the engrafted cells and the maintenance of their functionality. Nevertheless, it is worth to note that even though Matrigel enhances cell retention, important number of cells are still loss post transplantation requiring important number of transplanted cells [25]. For instance, Tsang et al. study use 1.5-2x10^7 cells per animal. Considering that human body volume is about 1000 times of mouse body volume, it can be expected that 1.5-2x10^{10} cells would be required to translate this approach in humans. Besides, use of 2D cell culture imposes enzymatic treatment of the cells to retrieved differentiated adipocytes which lead to an important loss of this cell due to their fragility. Consequently, we can comprehend that clinical translation of these approaches would have important costs. Recently, Wang et al. demonstrated the first transplantation of Matrigel-free engineered 3D human thermogenic construct using brown adipose spheroids derived from immortalized brown adipose progenitors [25]. Using this approach, author demonstrated that significant effect on metabolic health of transplanted mice could be obtained with reduced cell dosage [25]. This highlights the promise of using engineered tissue therapy instead of cells to enhance cell survival and functionality.

Regarding engraftment sites, various of them have been described in the literature for mice and human thermogenic fat transplantation. Main consideration in this choice reside in a site that can promote vascular engraftment and maintain cell functionality post transplantation. It is known that neovascularization of the graft is crucial for its survival. Besides, vascular engraftment is even more key when considering therapeutic effect of thermogenic fat transplantation given that sustaining of non-shivering thermogenesis requires active draining of metabolites from blood circulation. Furthermore, it has been proposed that beneficial effects of transplanted thermogenic adipocytes on host metabolism relies on their endocrine function [259]. The subcutaneous transplantation method

is widely used due to its surgical accessibility and vascularization potential [259]. Alternative graft sites, like muscle [344] and kidney [25,345], have been suggested for their potential to create a pro-thermogenic environment and sustain adipocyte functionality. This is primarily because the muscle site benefits from its rich sympathetic innervation, while the kidney site offers intrinsic norepinephrine production, crucial for acute thermogenic activation.

Altogether these results demonstrate the potential of human thermogenic fat transplantation to enhance metabolic health and counteract metabolic disorders. Wang et al. demonstrated promising results for the use of 3D transplantable human thermogenic AT as ATMP, as opposed to conventional 2D cell culture. However, there is still a lack for approaches that can be translated for clinical applications. Indeed, for now existing approaches relies either on the use of Matrigel or on the use of Matrigel-free immortalized cells. Hence, innovative engineering approaches for creating human thermogenic adipose tissue constructs that are designed with clinical translation in mind are still needed.

Thesis objectives and hypotheses

General Framework:

As previously discussed in introduction, there are significant challenges within the field of biomedical sciences and engineering, particularly in the development of relevant 3D models of functional adult tissues. These innovative models offer a pathway toward gaining a deeper fundamental understanding of human native tissue biology. This applies to both the physiology/physiopathology of the targeted tissue and the mechanisms governing its integrity maintenance and drift. Biomedical implications lie in the potential of these models for therapeutic advancement, serving as models to decipher pathological development, identify targets and drug screening platforms or as ATMPs to favor tissue regeneration or to support organ with defective metabolism.

This thesis aligns with **the aim of developing functional multi-purposes adult tissue models while exploring the impact of biochemical and biophysical parameters on their formation.**

Hence, the key objective of this work has been to **develop adaptable tissue engineering approaches** that enable:

- The production of vascularized and functional human adult tissue constructs.
- Customization of their size to meet specific application requirements
- The study of the influence of microenvironment parameters on cellular organization.

Specific Context: Human Beige Adipose Tissue Engineering

As a target tissue, our team is particularly interested in the study of beige and brown adipose tissue in humans. As presented in Introduction part IV, there is a significant lack of physiologically relevant models for this less accessible and less understood tissue in humans. These models hold promises in finding therapeutic solutions, whether based on small molecules or cell therapy, to address the global rise in obesity and diabetes.

Methodology and hypotheses:

Our tissue engineering methodology relies on the selection of a relevant cell source and the definition of an initial permissive 3D microenvironment using tunable hydrogel to guide the self-organization of these cells toward the desired phenotype (See bibliographic introduction part II et III).

Based on previous work, we selected the SVF of human subcutaneous WAT as an endogenous source of ASCs and endothelial progenitors. ASCs possess the advantages to act as progenitors for generating adipocyte parenchymal cells, but also as pro-angiogenic support cells for vascularization, and form key components of the mesenchyme. Additionally, as multipotent mesenchymal cells, ASCs are an ideal

source for studying the influence of the microenvironment on cellular behavior. To promote cell interactions and favor the emergence of organized cellular compartments in 3D, we chose to pre-aggregate these cells into spheroids.

Specific objectives:

Starting with SVF-derived spheroids, **Objective 1 was to define the biochemical and biomechanical conditions that enable the development of beige adipose tissue organoids from cell aggregates at different tissue scales.** We aimed to generate organoids presenting sustained cell viability, functional adipocyte compartment with inducible beige adipocyte related function including metabolic and secretory adaptation, as well as vascular compartment with maturation potential.

Engineering methods involved:

1. Optimizing the differentiation medium to promote both adipogenesis and angiogenesis in a 3D model of spheroids maintained without hydrogel
2. Optimizing spheroid embedding in hydrogel to support cell colonization and viability
3. Scaling up of the engineering approach toward the generation of beige adipose microtissues through spheroid patterning and GelMA molding approaches to replicate environment specified at the individual spheroid level within a multi-spheroid setting

These results have been the subject two patents (n° N° 23 305 136.6, N° 22 306 953.5) and a recent publication in *Advanced Science* journal presented in part I of the results section.

Objective 2 aimed to develop culture systems for a more precise examination of how mass transport and matrix composition impact the rearrangement and organization of spheroid cells within hydrogel. Preliminary results are presented in part II of result section.

Objective 3 consisted in exploring the application of these beige adipose microtissues for in vivo transplantation to treat metabolic diseases. Preliminary transplantation assays were initially conducted in healthy mice to assess for transplantation feasibility. Part III of the results section presents these preliminary findings, mainly led by Laurence Vaysse, Christophe Guissard and Audrey Carrière.

Results and discussion

I. Engineering 3D microenvironment for the generation of physiological human beige adipose tissue constructs

1. Article: Scalable generation of generation of pre-vascularized and functional human beige adipose tissue organoids

The following section is presented as a published article:

Advanced Sciences, September, 20th 2023, https://doi.org/10.1002/advs.202301499

ADVANCED SCIENCE Open Access
www.advancedscience.com

Scalable Generation of Pre-Vascularized and Functional Human Beige Adipose Organoids

*Mélanie Escudero, Laurence Vaysse, Gozde Eke, Marion Peyrou, Francesc Villarroya, Sophie Bonnel, Yannick Jeanson, Louisa Boyer, Christophe Vieu, Benoit Chaput, Xi Yao, Frédéric Deschaseaux, Mélissa Parny, Isabelle Raymond-Letron, Christian Dani, Audrey Carrière, Laurent Malaquin, and Louis Casteilla**

Obesity and type 2 diabetes are becoming a global sociobiomedical burden. Beige adipocytes are emerging as key inducible actors and putative relevant therapeutic targets for improving metabolic health. However, in vitro models of human beige adipose tissue are currently lacking and hinder research into this cell type and biotherapy development. Unlike traditional bottom-up engineering approaches that aim to generate building blocks, here a scalable system is proposed to generate pre-vascularized and functional human beige adipose tissue organoids using the human stromal vascular fraction of white adipose tissue as a source of adipose and endothelial progenitors. This engineered method uses a defined biomechanical and chemical environment using tumor growth factor β (TGFβ) pathway inhibition and specific gelatin methacryloyl (GelMA) embedding parameters to promote the self-organization of spheroids in GelMA hydrogel, facilitating beige adipogenesis and vascularization. The resulting vascularized organoids display key features of native beige adipose tissue including inducible Uncoupling Protein-1 (UCP1) expression, increased uncoupled mitochondrial respiration, and batokines secretion. The controlled assembly of spheroids allows to translate organoid morphogenesis to a macroscopic scale, generating vascularized centimeter-scale beige adipose micro-tissues. This approach represents a significant advancement in developing in vitro human beige adipose tissue models and facilitates broad applications ranging from basic research to biotherapies.

1. Introduction

Despite public health initiatives, type 2 diabetes and obesity have reached worldwide pandemic proportions and are associated with the leading cause of death. Both metabolic disorders are characterized by an imbalance between energy intake and energy expenditure. Adipose tissues are key regulators of this energy balance.[1] While white adipose tissues (WAT) are the main energy storage of the organism, brown and beige adipose tissues are characterized by their inducible ability to dissipate energy upon activation, thanks to their specific uncoupling oxidative phosphorylation from ATP synthesis by the expression of the mitochondrial protein, uncoupling protein-1 (UCP1).[1,2] Brown and beige adipose tissues also secrete the so-called adipokines and batokines, supporting communication with surrounding cells as well as with distant organs.[3]

Contrary to brown adipose tissues, which are found in restricted depots, beige adipocytes may exhibit a white-like phenotype and reside within specific WAT depots. These cells can be induced to display inducible thermogenic features through a reversible mechanism called "beiging".[4–6]

M. Escudero, L. Vaysse, S. Bonnel, Y. Jeanson, F. Deschaseaux, M. Parny, I. Raymond-Letron, A. Carrière, L. Casteilla
RESTORE Research Center
Université de Toulouse, INSERM 1301, CNRS 5070, EFS, ENVT
Toulouse 31100, France
E-mail: louis.casteilla@inserm.fr

The ORCID identification number(s) for the author(s) of this article can be found under https://doi.org/10.1002/advs.202301499

DOI: 10.1002/advs.202301499

M. Escudero, G. Eke, L. Boyer, C. Vieu, L. Malaquin
LAAS-CNRS
Université de Toulouse, CNRS, INSA
Toulouse 31400, France

M. Peyrou, F. Villarroya
CIBER "Fisiopatologia de la Obesidad y Nutrición", Department of Biochemistry and Molecular Biomedicine
University of Barcelona
Madrid 28029, Spain

B. Chaput
Service de Chirurgie plastique, reconstructrice et esthétique
Centre Hospitalier Universitaire Rangueil
Toulouse 31400, France

In addition to cold exposure, several pathophysiological conditions activate beiging, including physical exercise[7] and intermittent fasting.[8] In adult humans, brown and beige adipocytes mass has been negatively correlated with obesity and aging.[9,10] Therefore, activation or mass increase of human beige adipose tissue have been investigated as therapeutic approaches to counteract metabolic disorders. As a consequence, developing models for investigating the emergence and maintenance of beige adipose tissue in humans has broad therapeutic interest for metabolic diseases including obesity and diabetes but also for aging. Such models would help to screen for drugs that can modulate intrinsic plasticity but also open the way for new biotherapy strategies. Indeed, the therapeutically beneficial effects of murine or human brown/beige adipocyte transplantation have been demonstrated in rodents where normoglycemia was recovered in diabetic mice and energy expenditure increased in obese mice.[11–14] However, translating this approach to patients requires developments in tissue engineering to allow the generation of human beige adipose tissue transplants that are clinically relevant in size and function. Recently, multiple approaches have been developed, including ours, to generate WAT models reproducing the 3D architecture and metabolic function of native tissues.[15–20] However, studies reporting relevant 3D beige adipose tissue models are scarcer, even more so with human cells. Approaches to engineering human beige adipose tissue largely rely on the differentiation of adipose progenitors in the absence of the vascular compartment[21,22] or the use of explant-based culture[23] that is prone to limited cell viability over time.[24]

When cultivated under suitable conditions, stem cells can undergo in vivo-like morphogenesis and turn into structures containing a self-organized cluster of cells called organoids. Such cultures possess the highest functional complexity and maturity obtained to date in vitro.[25] However, growing organoids beyond the millimeter scale often leads to cell necrosis and/or incomplete maturation.[26] These size limitations hinder recapitulation of the large-scale features of tissue architecture and the development of organoid-based therapeutic approaches. Recent tissue engineering approaches have been directed toward initiating and controlling cell autonomous modes of organogenesis at the microscopic and macroscopic scales while integrating a vascular system to sustain cell viability and function.[27] Most of these approaches, use bottom-up engineering strategies involving the generation of building blocks and subsequently their assembly.

In this process, critical parameters have been identified for driving multicellular responses toward in vitro tissue complexity.[28] They include 1) controlling the cell types present to recapitulate tissue cell composition, 2) engineering chemically and mechanically permissive environments to promote intrinsic development programs, and 3) controlling the 3D patterning of cell clusters to define the shape and size of the final tissue construct. In pursuit of these aims, engineered biomaterials, such as hydrogels, are promising tools to promote the spatiotemporal growth of organoids and shape-guided morphogenesis.[28] Their porous structure provides both physical support for cell adhesion, proliferation, and migration as well as molecular diffusion properties close to the native extracellular matrix.[29] Hydrogels open the way toward robust, scalable processes for 3D structuration using bioprinting technology.[30] Photopolymerizable gelatin methacryloyl hydrogels (GelMA) have been increasingly used for tissue engineering applications to define microenvironments that are hard to achieve with other naturally derived hydrogels such as Matrigel.[29,31,32]

Here we develop a straightforward, multiscale approach promoting the 3D self-organization of spheroids into prevascularized human beige adipose organoids. Contrary to classic bottom-up engineering approaches which aim to generate building blocks followed by their ultimate assembly,[33,34] we developed a scalable guided-assembly strategy of spheroids. The system is based on GelMA hydrogel and stromal vascular fraction (SVF) cells from human WAT as a source of endothelial progenitors and multipotent adipose-derived mesenchymal stem cells (ASC). We defined a controlled biochemical and mechanical environment allowing ASC commitment toward the beige adipocyte lineage while ensuring vascular development at the microscopic scale through tumor growth factor β (TGFβ) pathway inhibition and tuning of GelMA porosity and mechanical properties by varying gelatin percentages to embed individual spheroids. The functionality of the resulting micro-scaled construct and its translation to a multi-spheroid macro-scaled tissue construct was then demonstrated (**Figure 1**).

2. Experimental Section

2.1. Hydrogel Preparation

2.1.1. GelMA Synthesis

A solution of porcine skin gelatin type A (110 bloom, Sigma, USA) was prepared in carbonate-bicarbonate (CB, 0.25 M) buffer (0.075 mol Na2CO3 and 0.175 mol NaHCO3 in 1 L of dH2O, adjusted to pH 9 using 5 M NaOH or 6 M HCl). Gelatin (20%, w/v) was dissolved in CB buffer (60 C for 1–2 h), the solution cooled to 50 °C and methacrylic anhydride (Sigma, USA) was added with magnetic stirring (3 h at 50 °C; methacrylic anhydride/gelatin feeding ratio: 0.1 mL g^{-1}). The pH was readjusted to 7.4 to terminate the reaction and the solution was filtered and dialyzed (MW CO 10 000) against distilled water (3 days at 40 °C) to remove excess methacrylic acid and salts. Dialysate was changed every 12 h. This solution was lyophilized for 3 days and stored at 4 °C until further use.[35] 1H-proton magnetic resonance spectroscopy (Bruker) quantified methacyloyl substitution to be 63%.[36]

To prepare GelMA solution, lyophilized GelMA was dissolved in D-PBS (5, 8, 10, or 15% w/v) with photoinitiator lithium phenyl-2,4,6-trimethyl-benzoylphosphinate (LAP, 0.1% w/v, Sigma, USA). GelMA solution was kept at 4 °C until use.

X. Yao, C. Dani
Faculté de Médecine
Université Côte d'Azur
INSERM, CNRS, iBV, Nice 06103, France
M. Parny, I. Raymond-Letron
LabHPEC, Histology and Pathology Department
Université de Toulouse, ENVT
Toulouse 31076, France

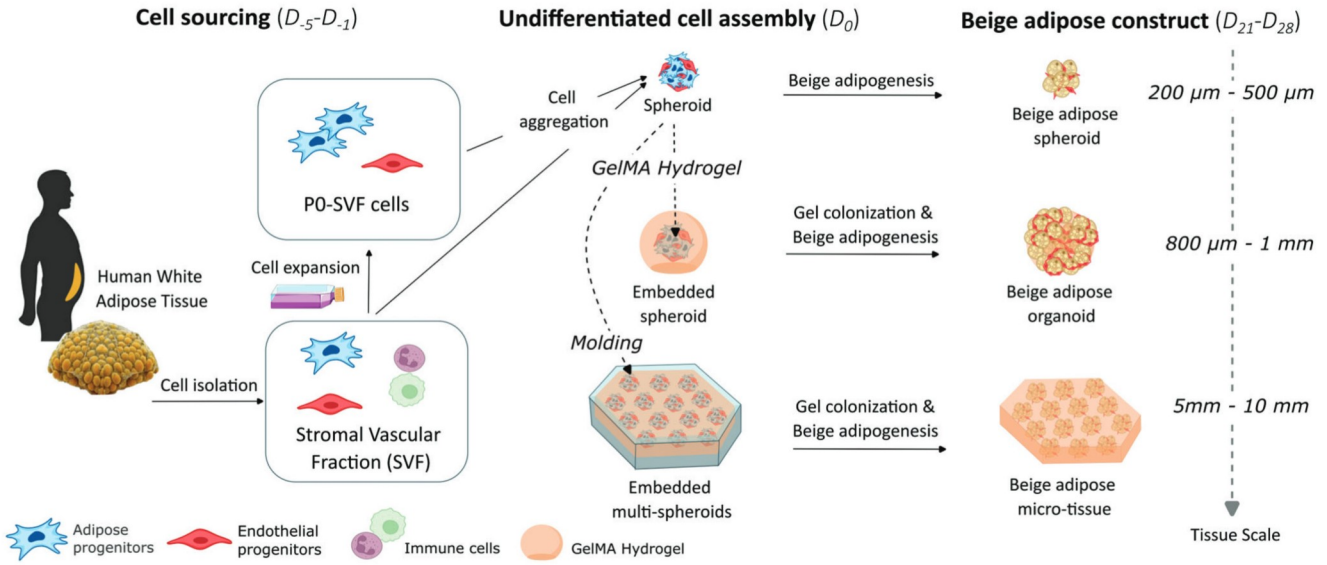

Figure 1. Multiscale approaches to generate vascularized human beige adipose tissue constructs. SVF cells purified from human white adipose tissue were used directly or after amplification in 2D culture to generate spheroids. Spheroids can be individually embedded or multiply assembled using a GelMA mold. A specific combination of volume per spheroid, percentage, and reticulation of GelMA embedding condition in an optimized cocktail medium leads to the generation of functional human beige organoids as well as beige micro-tissue.

2.1.2. GelMA Rheological Characterization

A mechanical tester (Mark-10 ESM, USA) was used to test the storage modulus of GelMA hydrogels. The system was operated with a 5 N load cell at a displacement speed of 5 mm min^{-1} speed with a 20% deformation threshold. GelMA solutions prepared as described above were introduced in cylindrical molds (6 mm in diameter × 4 mm in thickness) and crosslinked by exposing them to 405 nm light (Formlabs, USA) at room temperature (RT) for various durations (10 s–3 min). The samples were kept in PBS for 8 h before testing. Conservation moduli of hydrogels were calculated from the slope of the very first linear region of the stress–strain curve. The evolution of the mechanical properties was also investigated by performing mechanical tests for 7 days (immersion in PBS at 37 °C) after preparation ($n = 5$).

2.1.3. Electron Microscopy

Hydrogel samples were frozen in liquid nitrogen, lyophilized for 6 h and sputter coated with Au (10 nm). Morphology was analyzed with a scanning electron microscope (Hitachi S-4800S-4800, Japan). Dimensional analysis of porosity and pore sizes was performed with Image J software (NIH).

2.2. Preparation of Anti-Adhesive PDMS Surface and Molds for GelMA Molding

Polydimethylsiloxane (PDMS) molds were prepared by casting on 3D-printed templates. 3D templates were obtained by stereolithography using a DWS 29J+ system (DWS, Italy) and DL260 photoresist (DWS, Italy). Once fabricated, the 3D templates were treated using perfluorodecyltrochlorosilane (FDTS) after SiO2 coating using the SPD system. PDMS (Sylgard 184, Dow Corning) was prepared in a 10:1 (Base:Curing agent) ratio, degassed under vacuum, and poured into the 3D-printed mold. Crosslinking of PDMS was performed for 2 h at 60 °C. PDMS molds were then removed manually from the templates. PDMS molds were then incubated overnight at RT with an anti-adhesive treatment using pluronic F127 (20 mg mL^{-1}, Sigma, USA) followed by three washes in D-PBS and air-drying before use. For GelMA droplet formation, a flat pluronic-coated PDMS surface was prepared similarly by pouring PDMS into a petri dish. After curing, pluronic treatment was performed without further removal of PDMS.

2.3. Generation of Beige Adipose Tissue Spheroids and Culture

2.3.1. Isolation and Amplification of SVF Cells from Human Adipose Tissue

Human SVF was isolated from abdominal dermolipectomy (plastic surgery department, CHU Toulouse, France) of female donors (body mass index ranging from 22.3 to 27.9 kg m^{-2}). The experimental protocols were approved by the French research ministry's institutional ethics committee (No: DC-2015-23-49) and informed consent was obtained from all subjects in accordance with institutional guidelines on human tissue handling and use. Adipose tissue was mechanically dissociated and enzymatically digested for 45 min at 37 °C using collagenase NB4 (13.6 U mL^{-1}, Coger, Germany) in α-Minimum Essential Medium (Life-Technologies, UK), supplemented with amphotericin B (0.1% v/v, Life-Technologies, UK), and streptomycin/penicillin (1% v/v, Life-Technologies, UK) hereafter named αMEM-ASP. After filtration on a 100 µm nylon net filter (Steriflip, Millipore, USA) and centrifugation (600 g, 10 min),

cells were washed in αMEM-ASP and centrifuged again (600 g, 5 min). The cell pellet was resuspended in erythrocyte lysis buffer (eBioscience RBC Lysis Buffer Multi-species, Life-Technologies, UK) and incubated for 5 min at room temperature (RT). Isolated SVF cells were then centrifuged (600 g, 5 min) and resuspended in Endothelial Growth Medium-2 (EGM2, PromoCell, Germany) supplemented with ASP. Cells were seeded directly in suspension for SVF spheroid formation or at 4000 cells cm^{-2} in 2D culture for further amplification. 2D cultures were maintained in EGM2 until they reached 80% confluency and the medium was changed every 3 days. The resulting amplified cells (P0-SVF) were used for spheroid formation or adipocyte differentiation in 2D cultures.

2.3.2. Spheroid Formation

Spheroids were formed from either SVF or P0-SVF cells. To promote cell aggregation, 50 000 cells were seeded in a reduced volume of EGM2 medium (50 µL) in ultra-low attachment (ULA) 96-well round-bottom plates (Corning Incorporated Life Sciences, USA) and maintained overnight under stirring (150 rpm). For SVF cells, to further improve cell aggregation, cell seeding was followed by plate centrifugation (600 g for 5 min). The following day, EGM2 (150 µL) was added to each well. Cells were maintained in the proliferation medium until spheroid formation, i.e., 5 days for SVF-spheroids and 1 day for P0-SVF-spheroids.

2.3.3. Individual Spheroid Embedding

To generate GelMA embedded spheroids, once formed, spheroids were mixed with pre-warmed GelMA/0.1% LAP solution (37 °C, 10 min). Spheroids were then individually pipetted in a defined volume of GelMA/0.1% LAP solution (1.5 µL, 3 µL) and dispensed onto an anti-adhesive PDMS surface, prepared as described above. GelMA droplets containing one spheroid were then photo-crosslinked via exposure to 405 nm light for 40 s (Form cure, Formlabs, Germany). It has to be noted that for GelMA 5%, crosslinking duration was increased to 60 s as lower durations did not permit the generation of droplets solid enough for manipulation. Embedded spheroids were individually transferred into 24-well flat-bottom ULA plates (Corning Incorporated, Lifes Sciences, USA) and maintained in an EGM2 proliferation medium for 7 days before differentiation. Half of the medium was changed every 2–3 days.

2.3.4. Multi-Spheroid Construct Generation

Multi-spheroid constructs were prepared by casting GelMA and positioning spheroids on a PDMS mold template with spherical cavities (Diameter: 1400 µm, height: 700 µm). Spheroids were handled using a manual aspiration method and positioned, thanks to a digital camera, in the middle of the mold microwell filled with GelMA. When all the spheroids (14 spheroids per mold) were precisely positioned, GelMA was cured for 40 s with 405 nm light (Form cure, Formlabs, Germany). The GelMA multi-spheroid construct was unmolded before the culture process.

2.3.5. Adipocyte Cell Differentiation in 2D and 3D Cultures

Differentiation onset varied according to the type of culture. For 2D culture, P0-SVF cells were first seeded at 80 000 cells cm^{-2} on gelatin (0.1%, Sigma, USA) coated plates in EGM2 medium. Differentiation was then initiated when cells reached confluency. For spheroids in the absence of GelMA hydrogel, differentiation was initiated once spheroids were formed. For GelMA embedded spheroids, either individually or in multiple constructs, differentiation was initiated after a proliferation phase of 7 days in EGM2 medium. For all types of cultures, cells were differentiated for 21 days with appropriate adipogenic cocktails. Half of the medium was changed every 3–4 days. Cells were differentiated using variations of an adipogenic cocktail previously described by the team.[18] These adipogenic cocktails consist of αMEM-ASP supplemented with fetal bovine serum (FBS) (2%), insulin (5 5 µg mL^{-1}), apotransferin (10 µg mL^{-1}, Sigma, USA), bone morphogenetic protein 7 (BMP7, 50 ng mL^{-1}, MiltenyiBiotec, France) with or without intralipids (0.2% diluted from 20% emulsion, Sigma, USA). When specified, the TGFβ pathway inhibitor SB431542 (MiltenyiBiotec, Germany), also referred to as SB4, was added to the adipogenic cocktail (5 µM). For treatment with UCP1 inducers, cells were treated 3 days prior to the end of the differentiation process with rosiglitazone (100 nM, Sigma, USA), 3,3′′,5-triiodo-L-thyronine (T3, 0.2 nM, Sigma, USA), all-trans retinoic acid protected from light (0.1 µM, Sigma, USA), 8-(4-chlorophenylthio) -adenosine 3′′,5′′-cyclic monophosphate (8-CPT-cAMP, 200 µM, Abcam, UK). All-trans retinoic acid treatment was renewed every day until the end of the culture to overcome its molecular instability.

2.4. Cell Viability Assay

2.4.1. Spheroid Size Measurements

Imaging of spheroid size was performed during the culture process at indicated times using a Nikon eclipse TE2000-5 microscope with a 10X objective. Spheroid area was measured using Fiji software (National Institutes of Health, USA). Six to eight spheroids were measured for each time point per human sample. Nine human samples were analyzed.

2.4.2. Propidium Iodide Staining

3D image-based cell viability quantification was conducted by staining free spheroids and embedded spheroids with propidium iodide (10 µg mL^{-1}, Invitrogen, USA) in a culture medium for 1 h at 37 °C. After three D-PBS washes, samples were fixed with 4% paraformaldehyde. The fixed cultures were permeabilized and stained with DAPI as described above. Samples were washed three times with D-PBS (30 min, RT) and cleared for at least 48 h with Scale S4 solution[37] before imaging. All samples were imaged using a confocal microscope (LSM 880, Carl Zeiss, France). The total number of nuclei and IP+ nuclei were quantified using ImageJ. Prior to nuclei counting, the DAPI signal was segmented using two-dimensional (2D) Stardist plugging,[38] a deep-learning-based method for 2D nucleus detection. The mean

of three spheroids or GelMA-embedded spheroids was calculated for each condition per human sample. For quantification on embedded multi-spheroid constructs, the mean of two peripheral and two central spheroids was calculated to take into account a putative heterogeneity. The average viability percentage was calculated as the number of propidium iodide + nuclei/DAPI+ nuclei per slice.

2.5. DNA Quantification

DNA quantification was performed to assess cell proliferation and maintenance. DNA was extracted from an average of 24 spheroids or five GelMA-embedded spheroids according to the blood and tissue DNA extraction kit (Qiagen) manual. Spheroids were washed with D-PBS and lysed ALT/proteinase K buffer (200 µL) overnight under mixing (800 rpm). To ensure DNA purity, RNase A (Qiagen) was added to the samples and incubated for 2 min at RT before the addition of a 1:1 AL/100% ethanol mix. DNA was detected with the 1x QubitTM High sensitivity ds-DNA kit according to the manufacturer's instructions. Fluorescence intensities were measured with Qubit 4.0 fluorometer (Invitrogen, CRCT, Toulouse). Data were expressed as DNA quantity/spheroids (ng).

2.6. RNA Extraction and Quantitative Relative Real-Time PCR

Cell samples were homogenized in QIAzol lysis reagent (Qiagen, USA). 3D culture samples were further disrupted for 2 min at 30 Hz using Tissue Lyser (Qiagen). To avoid extraction bias, a pool of 14 embedded single spheroids was used to compare with the expression of one embedded multi-spheroid made of 14 spheroids. Total RNA was isolated using phenol-chloroform extractions followed by Quick-RNA microprep kit procedure (Zymo Research, USA) and reverse transcribed into cDNA using high capacity cDNA reverse transcription kit (Applied Biosystems, USA). qPCR was performed using a StepOne system (Applied Biosystems, USA) with Fast SYBR Green Master Mix supplemented with 1/10e diluted cDNA and primers (300 nM) listed in Table S1 (Supporting Information). Relative gene expression was calculated by the $2-\Delta\Delta CT$ method. The ΔCt was obtained by normalizing mean expression values of each gene to the geometric mean of the reference genes, ribosomal protein lateral stalk subunit P0 (RPLP0), glucuronidase beta (GUSB), peptidylprolyl isomerase A (PPIA), and tyrosine 3-monooxygenase/tryptophan 5-monooxygenase activation protein zeta (YWAZ). The $\Delta\Delta Ct$ was calculated by normalizing conditions to 2D undifferentiated cells for 2D experiments or to non-embedded undifferentiated spheroids for 3D culture experiments.

2.7. Immunofluorescence Analysis

2D and 3D cultures were fixed with 4% paraformaldehyde at RT. In the case of 3D culture, after D-PBS washing, samples were permeabilized and blocked in D-PBS solution supplemented with Triton X-100 (1%, Sigma, USA) and horse serum (3%, Jackson Immunoresearch, UK) for 3 h at RT. Samples were then incubated with the primary antibody in D-PBS solution supplemented with horse serum (1%) and Triton X-100 (1%), at the appropriate dilution (Table S2, Supporting Information), overnight at RT. After three washes in D-PBS, secondary antibodies coupled to Alexa-488, Alexa- 594 or Alexa-647, (1:500, Life Technologies, UK) in D-PBS supplemented with horse serum (1%) and Triton X-100 (1%) were added as specified, 3 h at RT. For lipid droplet staining, 493-Bodipy (2 µg mL^{-1}, Life Technologies, UK) was added to the solution. After D-PBS washes, nuclei were stained with DAPI (2 µg mL^{-1}), 1 h at RT (Sigma, USA). For 2D culture, the same protocol was used but incubation durations were shortened for the different steps. For 3D culture imaging, samples were cleared for at least 48 h in Scale S4 solution[39] composed of (w/v) D-(-)-sorbitol (40%, Sigma, USA), glycerol (10% w/v, Euromedex, France), urea (4 M, Sigma, USA), Triton X-100 (0.2%), dimethylsulfoxide (20% v/v, Sigma, USA). Samples were analyzed by confocal imaging (LSM 880, Carl Zeiss, France) and images were processed using Fiji software (National Institutes of Health, USA).

2.8. ProteinSimple Capillary Immunoassay

For western analysis, 24 spheroids or 12 embedded spheroids were washed with PBS 1x and resuspended in ice-cold RIPA buffer (100 µL, Sigma, R0278, USA) adjusted with SDS (2%) and completed with anti-protease and phosphatase inhibitors. For protein extraction from mouse tissues, the volume of the complete RIPA buffer was adjusted (1 mL per 100 mg). Samples were mechanically dissociated with Precellys tissue homogenizer at 4 °C. Protein lysates were then transferred into other tubes and sonicated with an ultrasonic homogenizer twice for 30 s in ice at 20 kHz. Samples were centrifuged for 10 min at 10 000 rpm and whole protein cell extracts were quantified by the Lowry method. Samples were run with proteinSimple capillary electrophoresis immunoassay according to the ProteinSimple user manual. Briefly, protein extracts (1.5 ng $well^{-1}$) were mixed with dithiothreitol (40 mM, DTT) and master mix (ProteinSimple). Samples were heated at 95 °C for 5 min and dispensed into a designated plate along with blocking reagent, primary antibodies Horseradish peroxidase (HRP)-conjugated secondary antibodies, chemiluminescent substrate, and total protein detection reagents. All electrophoresis and immunodetection steps were automatized within the capillary system (ProteinSimple Jess). Chemiluminescence intensities were quantified with Compass software (ProteinSimple) and normalized to the total protein signal.

2.9. Lipolysis Assay

A lipolysis assay measuring glycerol release was conducted on embedded spheroids after differentiation using Free Glycerol Reagent kit (Sigma, USA) according to the manufacturer's recommendations. At the end of the differentiation, protocol-embedded spheroids were transferred into 96 wells of ULA plate in phenol red-free DMEM medium (90 µL) supplemented with glucose (5 mM). After 24 h of lipolysis stimulation with 8 cpt-AMPc (200 µM), media (20 µL) was collected and added to the

reaction mix. After 15 min of incubation, absorbance was read at OD 540 nm, and glycerol released was calculated using a standard curve. Four days prior to the experiment, the adipogenic medium was depleted of insulin to prevent lipolysis inhibition. Data are normalized by DNA quantity.

2.10. Metabolic Functionality

2.10.1. Lactate and Glucose Measurements

Extracellular levels of lactate and glucose were measured after treatment with UCP1 inducers to assess the change in metabolic activity of embedded spheroids. Lactate and glucose levels were measured with the Lactate Pro II test meter (Arkray) and Contour XT TS (Bayer), respectively. To account for increases in molecular concentration that could arise from medium evaporation, differences in glucose and lactate levels were calculated in comparison to evaporation in control wells without cells. Data are normalized to DNA quantity.

2.10.2. Seahorse Metabolic Assay

Metabolic profiling of embedded spheroids was performed by evaluating the oxygen consumption rate (OCR) of cells using the Seahorse XF24 Extracellular Flux Analyzer (Seahorse Biosciences) in the XF24 islet capture plate. Two embedded spheroids were placed in a well of an islet capture microplate (Agilent). Once in position, the culture medium was replaced with assay XF Seahorse DMEM medium (500 µL) supplemented with glutamine (2 mM), glucose (10 mM), and pyruvate (1 mM). Embedded spheroids were incubated for 45 min in a CO_2-free incubator at 37 °C prior to metabolic analysis. During Seahorse XF cell Mito stress run, cells were first exposed to 8cpt-AMP (200 µM) to assess for adrenergic stimulation. Sequential injections of inhibitors of key components of cellular respiration were used to determine metabolic parameters such as basal, maximal, or uncoupled respiration. First, oligomycin (3 µM) was added to inhibit ATP synthase and reveal uncoupled respiration. Then, uncoupler FCCP (3 µM) was added to induce maximal respiration. Finally, a mix of rotenone (3 µM) and antimycin A (3 µM) that inhibit complexes I and III in the electron transport chain was added to determine non-mitochondrial respiration. Basal and maximal respirations were calculated by subtracting non-mitochondrial respiration from OCR obtained before oligomycin injection and after FCCP injection, respectively. All values were expressed as a percentage of maximal respiration. Five human samples were analyzed. For each condition, five wells were used to measure mean OCR values from each human donor.

2.11. Measurement of Organoid Protein-Secreted Factors

Levels of secreted interleukin-6 (IL6), meterorin-like, growth/differentiation facto-r-15 (GDF15), and chemokine C-X-C ligand-14 (CXCL14) were measured using ELISA. Medium was collected at the end of the culture process and stored at −80 °C. IL6, meterorin-like, GDF15 and CXCL14 levels were determined using commercial ELISA kits (R & D Systems, Minneapolis, USA, # D6050, # DY7867-05, # DY957; Ray Biotech, Peachtree Corners, USA, # ELH-CXCL14, respectively). Medium that had not been in contact with cells was used as a detection control for ELISA assays. Data are normalized to DNA quantity.

2.12. Statistical Analysis

All results are presented as mean values of independent experiments, each from a different donor, ± standard deviation. The normal distribution of data was tested using the Kolmogorow–Smirnow test and homoscedasticity with Levene test. Significant differences among groups were evaluated using parametric two-sample *t*-test students or one-way analysis of variance (ANOVA-1) followed by post hoc analysis with Tukey's multiple comparison test unless stated otherwise. Significant fold differences compared to a reference control were analyzed by one-sample *t*-test. For qPCR analysis, statistical tests were performed on log2 fold change ($-\Delta\Delta Ct$ values).[40] p-values ≤ 0.05 were considered significant.

3. Results

3.1. TGFβ Inhibition Promotes Beige Adipogenesis and Vascular Network in 3D Spheroid Model using P0-SVF

Within adipose tissue, adipocytes reside in close proximity to blood vessels which are known to have a key role in beige adipose tissue physiology. Thus, it is very important to preserve the two cell compartments for the generation of a physiologically relevant adipose tissue model. To promote commitment to beige adipose tissue while preserving endothelial cell development in a 3D context, we first optimized a differentiation medium based on an adipogenic cocktail previously developed by our team.[18] In particular, the removal of intralipids known to promote hypertrophy of white adipocytes[41] was investigated. Although the lower adiponectin (*ADIPOQ*) mRNA levels and lipid content showed an overall reduction of adipocyte differentiation, *UCP1* expression increased significantly when intralipid levels were removed in 2D culture conditions. This was associated with increased cluster of differentiation 31 (CD31) expression and the development of branched CD31+ cell networks (Figure S1A,B, Supporting Information). This beige adipogenic medium was then tested on 3D spheroids generated from amplified SVF cells (P0-SVF cells). Spheroid formation was associated with the loss of a certain number of cells mostly located in the inner part of the spheroid (2.84% +/− 0.66% positive cells by propidium iodide staining, data not shown). Once in culture, spheroid size significantly decreased along differentiation (**Figure 2**A, in gray), associated with reduced DNA content (Figure 2B, in gray). 3% of dead cells were also observed by day 21, as revealed by propidium iodide staining (Figure 2C, in gray). In contrast to 2D culture, the adipogenic medium was not sufficient to induce adipocyte differentiation of P0-SVF cells when cultivated as spheroids. Indeed, levels of adipocyte-specific mRNAs were comparable to undifferentiated cells (D0) (Figure 2D, in gray), and perilipin staining revealed a lack of this lipid droplet-associated protein (Figure 2E, middle panel).

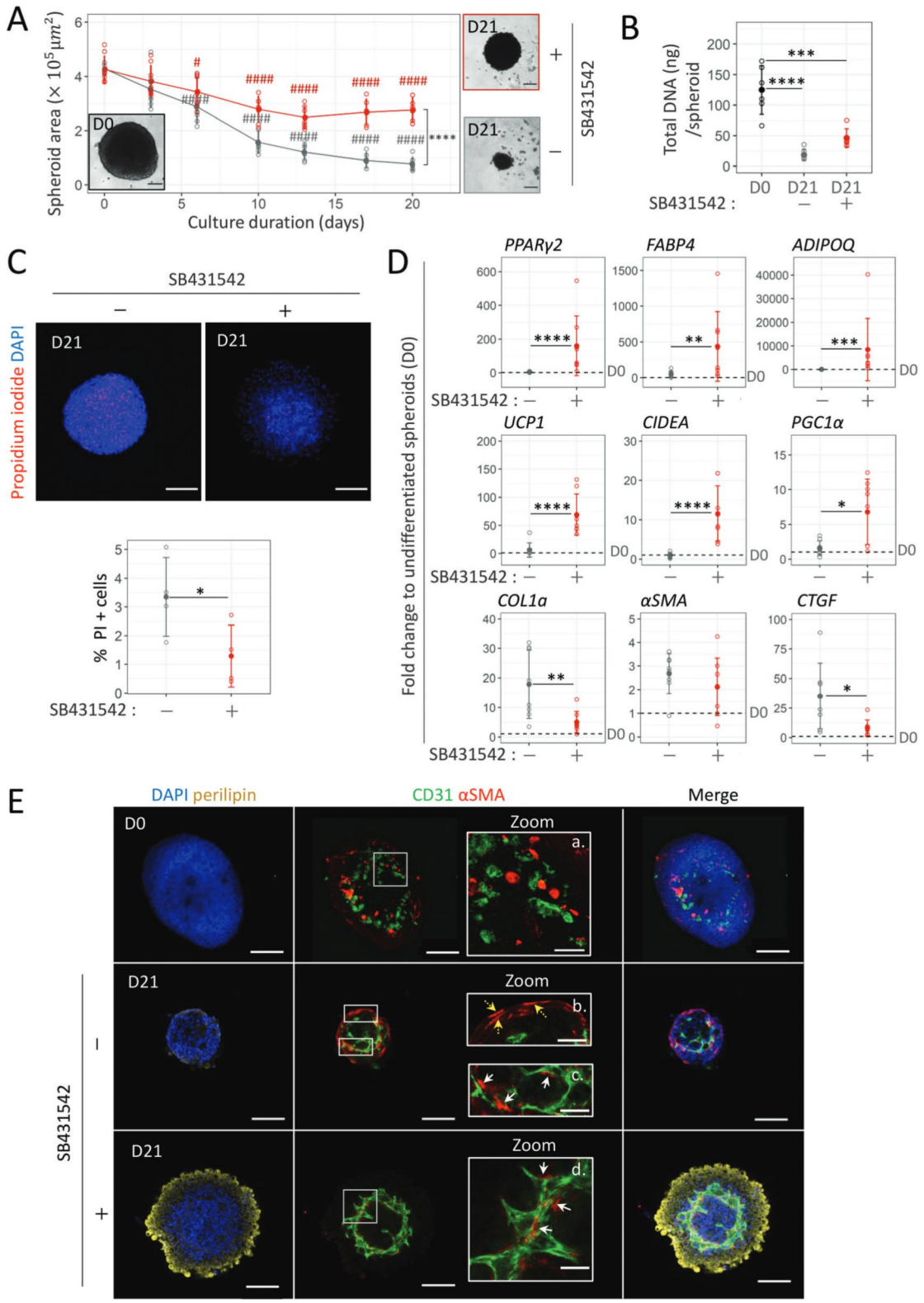

Figure 2. TGFβ inhibition promotes adipocyte differentiation and vascular formation while preventing the shrinking of 3D spheroids. A). Changes in spheroid size with differentiation duration in adipogenic medium in the absence (bottom curve, in gray) or presence (top curve, in red) of SB431542 (5 μM), an inhibitor of TGFβ pathway (n = 9). Brightfield images of spheroids before and after differentiation in each media. Statistical analysis was performed by two-way ANOVA followed by post-hoc Tukey's multiple comparisons (#: D0 versus Dx time point for each culture media, *: – vs + SB431542). B) Average DNA content per spheroid before (D0) and after differentiation (D21) in adipogenic medium with (in red) or without SB431542

Regarding endothelial cell development, while CD31 positive and α smooth muscle actin (αSMA) positive cells were disorganized at day 0 (D0, zoom a. and D21, zoom c., Figure 2E) this medium enabled the self-organization of CD31+ endothelial cells into pseudo-vascular networks in spheroids. These CD31+ cells aligned with αSMA-expressing cells akin to mural cells. However, we also observed αSMA+ cells independent of CD31+ endothelial cells at the periphery of the spheroid (D21, zoom b, Figure 2E). Taken together with the upregulation of collagen 1 (*COL1a*) and connective tissue growth factor (*CTGF*) mRNA levels compared to undifferentiated spheroids (Figure 2D, in gray), these data suggest induction of myofibroblast differentiation.

Since the TGFβ pathway favors ASC differentiation into myofibroblasts at the expense of adipogenesis,[42] spheroids were treated with an inhibitor of the TGFβ pathway, SB431542, throughout the differentiation process. TGFβ pathway inhibition significantly reduced spheroid shrinking during differentiation (Figure 2A, in red), loss of DNA content (Figure 2B, in red), and cell death (Figure 2C, in red). Interestingly, in P0-SVF spheroids, TGFβ pathway inhibition led to a significant increase in gene expression of adipogenesis markers, including increased beige-specific transcripts (*UCP1*, *CIDEA*, and *PGC1α*). This increase was also associated with a decrease in the expression of myofibroblast markers *CTGF* and *COL1a* (Figure 2D, in red). Immunofluorescence experiments also revealed that TGFβ inhibition did promote the appearance of perilipin-expressing cells, which were mainly located at the periphery of the spheroid (Figure 2E, lower panel). Notably, TGFβ inhibition decreased the presence of αSMA+ cells at the periphery of the spheroids but did not interfere with the development of αSMA+ cells found in the vicinity of CD31+ endothelial cells inside the spheroid (Figure 2E, zoom d). Although TGFβ pathway inhibition limited spheroid shrinking, it was not sufficient to completely avoid spheroid size reduction and loss of DNA content during differentiation. We hypothesized that providing spheroids with an appropriate biomechanical environment through hydrogel embedding might further help to generate tissue constructs containing an increased number of viable cells while further increasing beige adipocyte differentiation and vascular formation.

3.2. Adequate GelMA Embedding of Spheroid Supports Cell Mass Expansion using P0-SVF

To find a suitable biomechanical environment ensuring cell mass expansion after embedding D0 spheroid inside GelMA (Figure **3**A), different parameters of hydrogel embedding were studied (Figures 3 and 4). GelMA stiffness was tuned by varying gel percentage and photopolymerization time (Figure 3). The stiffness of the hydrogel alone remained below 8 kPa, within the range of beige adipose tissue stiffness,[43] when a GelMA percentage of up to 10% (w/v) and a 1 min cross-linking time was used. The resulting substrate appeared stable after 7 days in culture (Figure 3B).

To generate stable reticulated GelMA droplets for spheroid embedding while limiting exposition to free radical and subsequent phototoxicity,[44,45] a short crosslinking duration (40 s) was privileged. This duration generated hydrogels with Young's modulus ranging from 2 to 30 kPa (5%: 1.97 ± 0.4, 8%: 4.02 ± 1.07, 10%: 6.11 ± 0.15, and 15%: 30.36 ± 3.49) (Figure 3B). Scanning electron microscope images of GelMA hydrogel cross-sections highlighted the presence of interconnected and macro-porous structures in 10% GelMA hydrogel photopolymerized for 40 s (Figure 3C).

In combination with GelMA stiffness, the hydrogel volume used for spheroid embedding was investigated to promote cell survival and expansion (**Figure 4**A). Brightfield images revealed important hydrogel remodeling after 7 days of culture with GelMA 5%, especially with 1.5 µL (Figure 4A). Total DNA content was measured to account for total cell expansion (Figure 4C). Except for GelMA 5%, the DNA content was significantly higher in the presence of the hydrogel compared to spheroid alone, regardless of hydrogel volume. However, DNA content tended to be higher or equivalent to 1.5 µL compared to 3 µL (Figure 4C). Hence, 1.5 µL was identified as the optimal droplet volume to promote high DNA content independently of hydrogel composition (Figure 4C). In addition, the evolution of the initial spheroid was studied by evaluating the internal cell mass expansion area with DAPI staining (Figure 4D). Under 1.5 µL condition, the highest internal mass expansion was observed for 10% GelMA.the highest internal mass expansion was observed for 10% GelMA. Overall, these results identified 1.5 µL droplet volume and 10% GelMA as optimal GelMA embedding conditions. These conditions were used for subsequent experiments.

3.3. Differentiation After Cell Mass Expansion Generates Vascularized Human Beige Adipose Organoid using P0-SVF

The effect of GelMA embedding on long-term maintenance and differentiation of P0-SVF cells was investigated (**Figure 5**A).

(in gray) ($n = 6$). C) Confocal imaging and quantification of propidium iodide (dead cells in red) staining with respect to DAPI (blue) staining within P0-SVF spheroids after differentiation with (in red) or without SB431542 (in gray) ($n = 4$). D) Gene expression analysis of beige adipocyte markers (*UCP1*, *CIDEA*, and *PGC1α*), generic adipocyte markers (*PPARγ2*, *FABP4*, and *ADIPOQ*), and myofibroblast markers (*αSMA*, *COL1a*, and *CTGF*) in spheroids after 21 days of differentiation in the presence or absence of SB431542 ($n = 8$). Data are expressed relative to undifferentiated spheroids. E) Immunofluorescence analysis within P0-SVF spheroids at days 0 and 21 of differentiation under each media condition. Specific antibodies against human lipids containing cells marker perilipin (yellow), endothelial cell marker CD31 (green), and α-smooth muscle actin (SMA) (red) were used. DAPI staining highlights cell nuclei. Immunofluorescence images of lipids-containing cells, endothelial cells, and pericytes revealed by perilipin (yellow), CD31 (green), and αSMA (red) staining, respectively, within P0-SVF spheroids at day 0 and 21 of differentiation under each media condition. DAPI staining highlights cell nuclei. Scale bar: 200 µm. White squares (a–d) show areas enlarged to highlight the organization of endothelial cells and αSMA+ cells inside spheroids. Scale bar: 50 µm. Under both conditions, αSMA+ cells that aligned with CD31+ cells could be observed (white arrows). In the absence of SB431542 in adipogenic medium, peripheral αSMA+ cells can also be observed (yellow arrows) independently of CD31+ cells. All quantitative values are shown as mean ± standard deviation. Statistical analyses were performed by two-sample *t*-test or two ways ANOVA. Statistical significances: $^{*}p \leq 0.05$, $^{**}p < 0.01$, $^{***}p < 0.001$, and $^{****}p < 0.0001$.

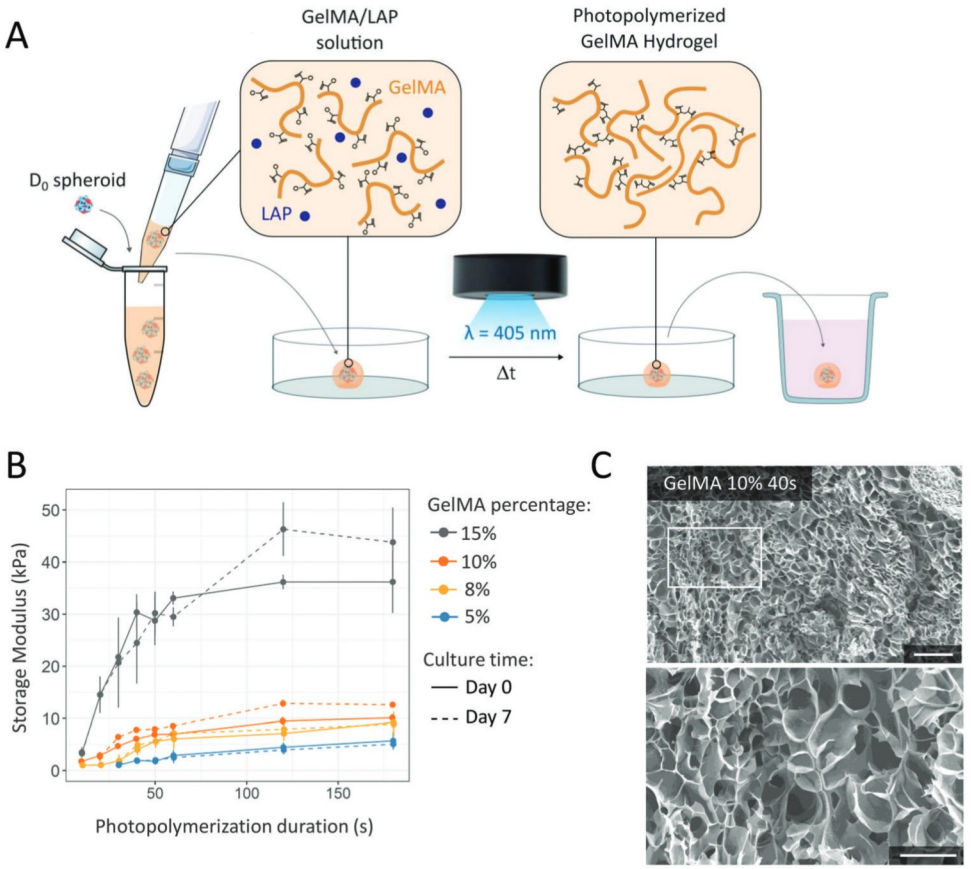

Figure 3. GelMA hydrogel processing and characterization of mechanical properties. A) Spheroid embedding in GelMA. Briefly, spheroids were collected and mixed with GelMA/0.1% LAP solution, then pipetted individually in a fixed volume of GelMA. Droplets containing spheroids were dispensed on an anti-adhesive PDMS surface before crosslinking with 405 nm light. Photo-crosslinked GelMA-spheroid droplets were further collected for culture. B) Mechanical characterization of GelMA hydrogel depending on GelMA percentage (5%, 8%, 10%, and 15%) and photo-polymerization duration by rheological testing. Storage moduli of the hydrogels were calculated according to their stress–strain curves ($n = 5$). Data were obtained once samples were formed (Day 0) and after samples were kept in PBS at 37 °C in a CO_2 incubator for a week (Day 7). Data are shown as mean ± standard deviation. C) Scanning electron microscopy of GelMA 10% cross sections. Scales: 200 µm. Bottom image shows a higher magnification of the outlined area from the top image. Scales: 100 µm.

GelMA embedding promoted the generation of tissue constructs with increased cell number compared to non-embedded spheroids, as demonstrated by DNA quantification (Figure 5B). Under these conditions, almost no dead cells were detected by PI staining (Figure 5C). Interestingly, this result was also true in the absence of TGFβ inhibition (Figure S2A, Supporting Information).

Regarding beige adipocyte differentiation, P0-SVF cells embedded in GelMA exhibited an increased expression of adipocyte markers such as *PPARγ2*, *FABP4*, and *ADIPOQ* during differentiation (D21 versus D0), comparable to spheroids without hydrogel embedding after differentiation (Figure 5D). Therefore, P0-SVF spheroids embedded in GelMA maintained their adipocyte differentiation potential. It is noteworthy that the total amount of RNA per construct was higher in embedded versus non-embedded spheroid (-GelMA: 259.6 ± 105.0 ng per spheroid vs + GelMA: 101.4 ± 49.5 ng per spheroid, two-sample *t*-test: $p = 0.002$, data not shown) meaning that the total yield of adipocyte differentiation is the highest in the embedded spheroids. Interestingly, the expression of beige adipocyte markers, including *UCP1* and *CIDEA* was significantly higher in embedded conditions compared to spheroids cultured alone (Figure 5D). Immunofluorescence experiments after differentiation confirmed the presence of adipocytes stained by BODIPY (Figure 5E). In the absence of TGFβ inhibition, such adipogenesis induction was not observed with no BODIPY signal detected (Figure S2B, Supporting Information). Hence, GelMA embedding in combination with TGFβ inhibition promoted ASC differentiation toward the beige adipocyte phenotype while also increasing cell mass expansion. Within embedded spheroids, adipocytes were found in close proximity to the endothelial network revealed by endothelial CD31+ cells aligned with αSMA+ cells (Figure 5E). This arrangement contrasted with spheroids cultured alone where adipocytes and endothelial cell compartments were present at different locations within the spheroid, i.e., at the periphery and in the center, respectively (Figure 2E). Moreover, immunohistochemistry analyses highlighted ongoing vascular lumen formation within embedded spheroids delimited by CD31+ and CD146 + cells (Figure S6A, Supporting Information). These tubular structures were closely

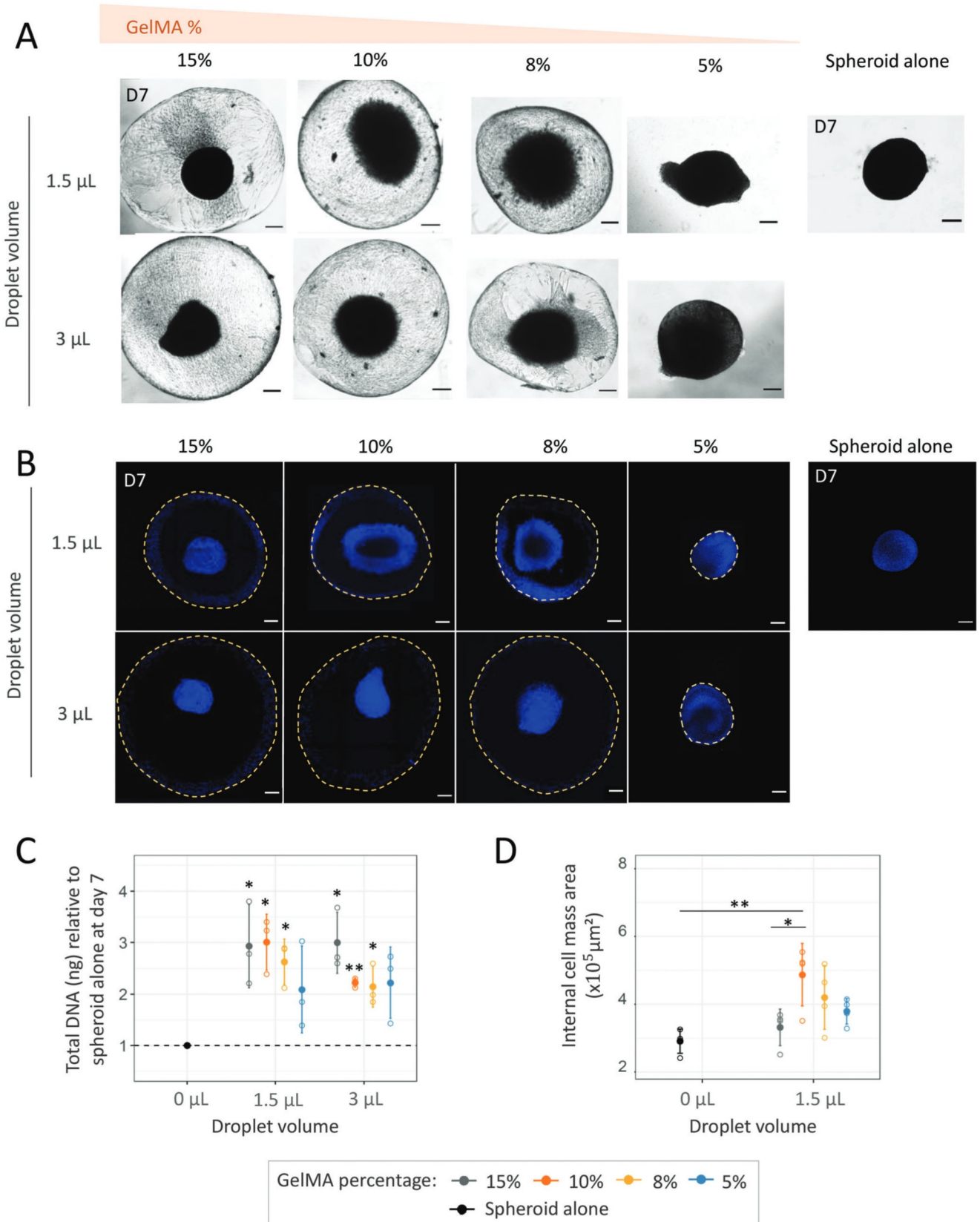

Figure 4. Optimal GelMA embedding parameters to promote cell mass expansion. P0-SVF spheroids embedded in 3 or 1.5 µL of GelMA (15%, 10%, 8%, and 5%) were maintained for 7 days in EGM2 proliferation medium. Spheroids maintained without GelMA (spheroid alone) were used as controls.

associated with αSMA+ cells (Figure S6B, Supporting Information) suggesting initiation of structural stabilization. Therefore, GelMA embedding promoted the generation of vascularized beige adipose organoids that more closely recapitulated in vivo-like adipose tissue cell organization.

3.4. Human Beige Adipose Organoids Exhibit Metabolic and Secretory Functionality Following Activation by Canonical Beige Inducers

Next, the functionality of the vascularized beige adipose organoids resulting from these culture conditions was assessed. Treating differentiated embedded spheroids with cAMP significantly increased glycerol release within the supernatant, demonstrating that embedded spheroids show cAMP-induced lipolysis (**Figure 6**A). Treatment of differentiated embedded spheroids with a cocktail of canonical thermogenic inducers containing a cell-permeable cAMP analog, i.e., 8-CPT-cAMP,[46] rosiglitazone (PPARγ agonist),[47] retinoid acid[48] and thyroid hormone (T3),[49] strongly increased *UCP1, CIDEA*, and *PGC1α* mRNA levels (Figure 6B) demonstrating the responsiveness of adipocytes in embedded spheroids to thermogenic pathway modulation. Embedded organoids were responsive to each inducer individually, but the combination of these inducers was the most efficient to promote significant upregulation of beige adipocyte markers (Figure S3, Supporting Information). This increase was concomitant with an increase in UCP1 protein content compared to untreated embedded spheroids where almost no UCP1 protein could be detected (Figure 6C; Figure S4, Supporting Information). The presence of UCP1 protein in perilipin-expressing adipocytes was confirmed by immunofluorescence analysis (Figure 6D).

To further characterize metabolic function under activation conditions, the oxygen consumption rate (OCR) of differentiated organoids was quantified using seahorse technology. The contribution of basal respiration to maximal respiration tended to increase after UCP1 induction, suggesting that cells were metabolically closer to their maximal oxidative capacities (Figure 6E). Although additional cAMP did not further increase basal OCR, the contribution of uncoupled respiration to maximal respiration was significantly increased in response to the UCP1 cocktail of inducers (Figure 6E), as expected for mature beige adipocytes. Additionally, differentiated embedded spheroids exhibited a significant increase in lactate release after activation with the UCP1 cocktail inducers. In this condition, glucose uptake also tended to be increased but did not reach statistical significance (Figure 6F). These results are consistent with increased metabolic activity as expected from UCP1 induction.

Finally, the secretion of batokines, known to be released by activated brown/beige adipocytes[3] such as meteorin-like,[50] IL6,[51,52] GDF15[53] or CXCL14,[54] were quantified within organoid supernatants. Levels of meteorin-like, IL6, and CXCL14 were significantly increased in the supernatant of beige organoids activated with the cocktail of inducers compared to controls (Figure 6G), while GDF15 levels remained within the same range for both conditions. Altogether, these data clearly demonstrated that differentiated embedded spheroids displayed many metabolic and paracrine features of functional beige adipose tissue.

3.5. TGFβ Inhibition and GelMA Embedding Unlock Beige Adipogenesis in Vascularized Organoid from Native Human Stromal-Vascular Fraction Cells

The SVF obtained directly after adipose tissue digestion contains heterogeneous cell populations comprising ASC, endothelial progenitors but also hematopoietic cells.[55] SVF models, therefore, more closely recapitulate patient tissue heterogeneity than amplified P0-SVF cells. The method for generating beige adipose tissue organoids was evaluated using SVF cells directly isolated from native adipose tissue. As observed with P0-SVF cells, GelMA embedding significantly decreased SVF cell mortality after 21 days of differentiation compared to spheroids cultivated without hydrogel (**Figure 7**A). Indeed, in the absence of GelMA, the percentage of dead SVF cells was even higher than in P0-SVF spheroids at day 21 (SVF: 3.76% ± 1.82%, Figure 7A vs P0-SVF: 1.29% ± 1.07%, Figure 5A, two-sample *t*-test: $p = 0.058$). GelMA embedding also promoted more homogeneous and slightly increased DNA levels in embedded SVF spheroids compared to SVF spheroids cultured alone (Figure 7B).

In contrast to P0-SVF cells, adipogenic medium containing the TGFβ pathway inhibitor was not sufficient to induce robust adipocyte differentiation from SVF cells in the three-dimensional (3D) spheroid model without hydrogel, as revealed by low mRNA levels of adipocytes markers *FABP4*, *PPARγ2*, and *ADIPOQ* (Figure 7C) and by lack of BODIPY staining (Figure 7D).

Interestingly, combining GelMA embedding with TGFβ inhibition led to a significant increase in expression of adipogenesis and beige adipocytes markers (Figure 7C). Immunofluorescence analysis performed on differentiated embedded SVF spheroids revealed the presence of adipocytes in between CD31+ and αSMA+ cell networks (Figure 7D).

Next, the beiging potential of SVF beige adipose organoid was then assessed. Treatment of SVF organoids with the UCP1 induction cocktail led to a significant increase in the expression of beige adipocyte markers *UCP1*, *CIDEA*, and *PGC1α* (Figure 7E). An increase of UCP1 at the protein level was also detected in SVF organoids with induction compared to controls (Figure 7F), although its overall expression remained lower than with P0-SVF cells (Figure S5, Supporting Information). These results validated the feasibility of generating adipose organoids containing UCP1-expressing cells directly from patient tissue cells (SVF

A) Representative brightfield images of whole GelMA-spheroid droplets and spheroids alone at day 7. B) Immunofluorescence confocal images of DAPI staining (cell nuclei) to assess spheroid morphology depending on GelMA percentage and droplet volume. Images are z projections of confocal slices, from top to bottom, of spheroids inside the hydrogel. Yellow dashed lines highlight the delimitation of the GelMA droplet. C) Average DNA content per embedded spheroid. Data are expressed relative to spheroid alone. D) Quantification of spheroid area inside hydrogel from confocal z-projections. All quantitative values are shown as mean ± standard deviations. Statistical analysis was performed by one or two-sample *t*-tests. Statistical significances: $^{*}p \leq 0.05$ and $^{**}p < 0.01$.

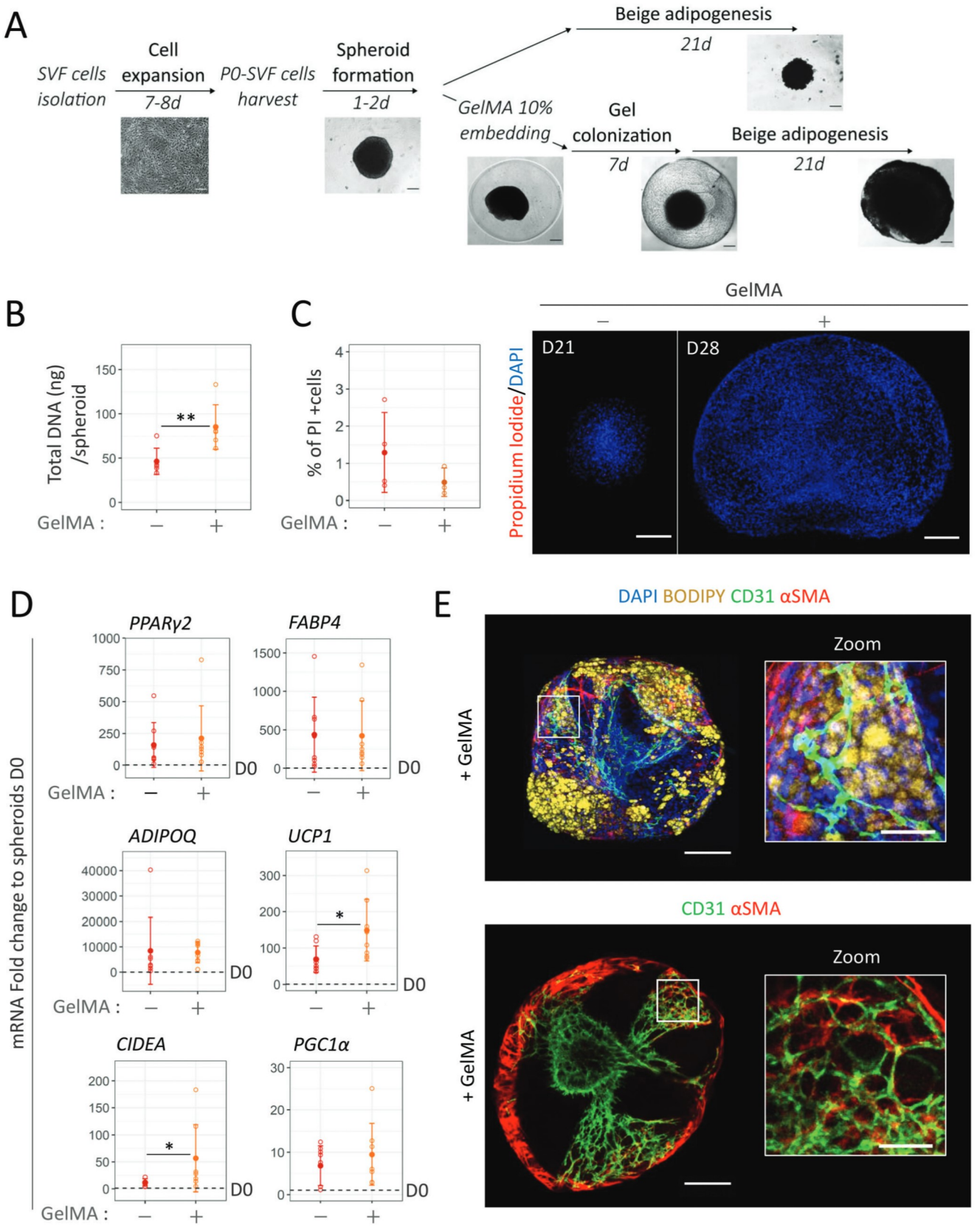

Figure 5. GelMA embedding promotes beige adipogenesis, vascular formation, and long-term cell maintenance. A) Culture of adipose tissue organoids and spheroids derived from P0-SVF cells. Spheroids embedded or not in GelMA 10% were analyzed after differentiation in an adipogenic medium

cells) using this newly developed GelMA embedding engineering approach (Figure 1).

3.6. From Beige Adipose Organoid Generation to Micro-Tissue Generation

The beige organoid method was next translated to the macroscale level using P0-SVF cells to engineer beige adipose microtissue at the centimetric scale. For this purpose, we introduced a guided-assembly approach of multiple D0 spheroids in GelMA using micro-fabricated PDMS molds composed of 14 cavities (**Figure 8**A). This mold was specifically designed to preserve the GelMA volume per spheroid established for beige adipose organoid generation in Section 2.2. Thanks to a syringe-based aspiration system, D0 spheroids were successfully deposited in the center of the cavities before photo-polymerization and complete removal of the construct from the mold (Figure 8B). In the same way as embedded single spheroids (Ssp), the resulting embedded multi-spheroid constructs (Msp) were allowed to proliferate for 7 days followed by 21 days of differentiation in adipogenic medium containing SB431542. An increase in tissue construct size did not impact cell mortality compared to single embedded spheroids as revealed by propidium iodide staining (Ssp: 0.49% ± 0.38% Figure 5C vs Msp: 0.37% ± 0.14%, $n = 3$, Figure S7A, Supporting Information, two-sample t-test: $p = 0.61$).

The expression of both adipogenic and beige adipocyte markers in embedded multi-spheroid constructs (Msp) derived from P0-SVF cells was consistent with an equivalent number of embedded single spheroids (Ssp) (Figure 8C). In addition, BODIPY staining revealed the abundant presence of adipocytes on most of the tissue construct, surrounded by a continuous network of CD31+ cells connecting different cavities (Figure 8D). As observed in embedded single spheroids, these CD31+ cells were frequently aligned with αSMA+ cells (Figure S7B, Supporting Information). This organization recapitulates in vivo-like adipose tissue structure. To further confirm the beige adipocyte identity of the cells, differentiated embedded multi-spheroids were treated with UCP1 inducers. Again, consistent with embedded spheroids, the UCP1 induction cocktail reproducibly led to the increased gene expression of beige adipocyte markers in treated multi-spheroids compared to control embedded multi-spheroids (Figure 8E). Increased UCP1 expression was further confirmed at the protein level (Figure 8F) in a comparable manner to individually embedded spheroids. Taken together, these results demonstrate that GelMA embedding can be scaled from single to multiple spheroids allowing the generation of centimetric size tissue constructs without hindering beige adipocyte differentiation. Moreover, this approach resulted in the generation of a pre-vascularized beige adipose micro-tissue. Importantly, the initial shape and size (20 mm^2) of the beige adipose micro-tissue were mostly maintained, even after 28 days of culture, allowing easy handling for potential biomedical and research applications.

4. Discussion

Relevant models of human beige adipose tissue are critical to better understand beige adipocyte physiology, a question of increasing importance in light of metabolic disorders[2] but also as described in aging.[9,10] Human 3D adipocyte cultures have been shown to recapitulate the phenotype of mature white adipocytes.[15–18,20] However, the field still lacks a system that truly recapitulates human beige adipose tissue biology, particularly the plasticity of this cell type. The few existing 3D-engineered human beige adipose tissue models focus on beige adipogenesis and either lack the vascular compartment,[21,22] known for its importance in beige adipose tissue physiology,[56] or are based on vascular explant culture.[23] Here, we developed a modular and scalable engineering process that generates functional mature vascularized human beige adipose tissues through guided differentiation and self-organization of human adult primary cells. Researchers could tailor the system for applications ranging from basic research to clinical uses.

Across tissue scales, exposure to beige adipogenic medium promoted the development of GelMA-embedded spheroids into pre-vascularized human beige adipose organoids that display functional features specific to beige adipose tissue. These organoids responded to canonical beige inducers with the significant upregulation of specific markers such as UCP1 mRNA and protein. In addition, the embedded organoids showed higher uncoupled respiration rates associated with the improvement of glucose uptake and lipolytic activity, key parameters for thermogenic activity.[57,58] Moreover, upon activation, the organoids recapitulated increased secretion of paracrine factors such as meteorin-like, CXCL14, or IL6, which are essential for the beneficial effects of brown/beige adipose tissues on systemic metabolism.[12] In addition, organoids contained a self-organized vascular system in close proximity to adipocytes, as found in vivo. This organization was associated with an improved commitment toward the beige adipocyte lineage compared to differentiated spheroids where such vascular proximity was not observed. These data are consistent with previous studies demonstrating a correlation between angiogenesis and increased plasticity of adipose tissue toward the beige phenotype, highlighting the importance of sustaining both the vascular and adipocyte compartments for a fully relevant beige adipose tissue in vitro model.[59,60] Mural cells, including perivascular smooth muscle cells and pericytes, are both important components of vascular tube formation through vessel stabilization[61,62] and potential mesenchymal stem cell niches.[63] Importantly, pseudo-vascular networks within organoids possess the ability to undergo vascular tubule formation that is aligned with αSMA expressing cells occupying

containing SB431542. Scale bar: 200 µm. B) Average DNA content per spheroid ($n = 6$). C) Confocal imaging and quantification of propidium iodide (Dead cells in red) staining in regard to DAPI (blue) staining within spheroids. Scale bar: 200 µm. (-GelMA: $n = 4$, +GelMA $n = 3$). E) Gene expression analysis of beige adipocytes markers (*UCP1*, *CIDEA*, and *PGC1α)* and generic adipocyte markers (*PPARγ2*, *FABP4*, and *ADIPOQ*) ($n = 8$). Quantification is expressed relative to non-embedded undifferentiated spheroids (D0). F) Immunofluorescence analysis. Specific antibodies against human endothelial cell marker CD31 (green) and α-smooth muscle actin (SMA) (red) were used. Lipids containing cells were revealed by bodipy staining. DAPI staining highlights cell nuclei. Scale bar: 200 µm. White squared images are zoomed areas. Scale bar: 50 µm. All statistical analyses were performed by a two-sample t-test. Statistical significance: $^{*}p \leq 0.05$ and $^{**}p < 0.01$.

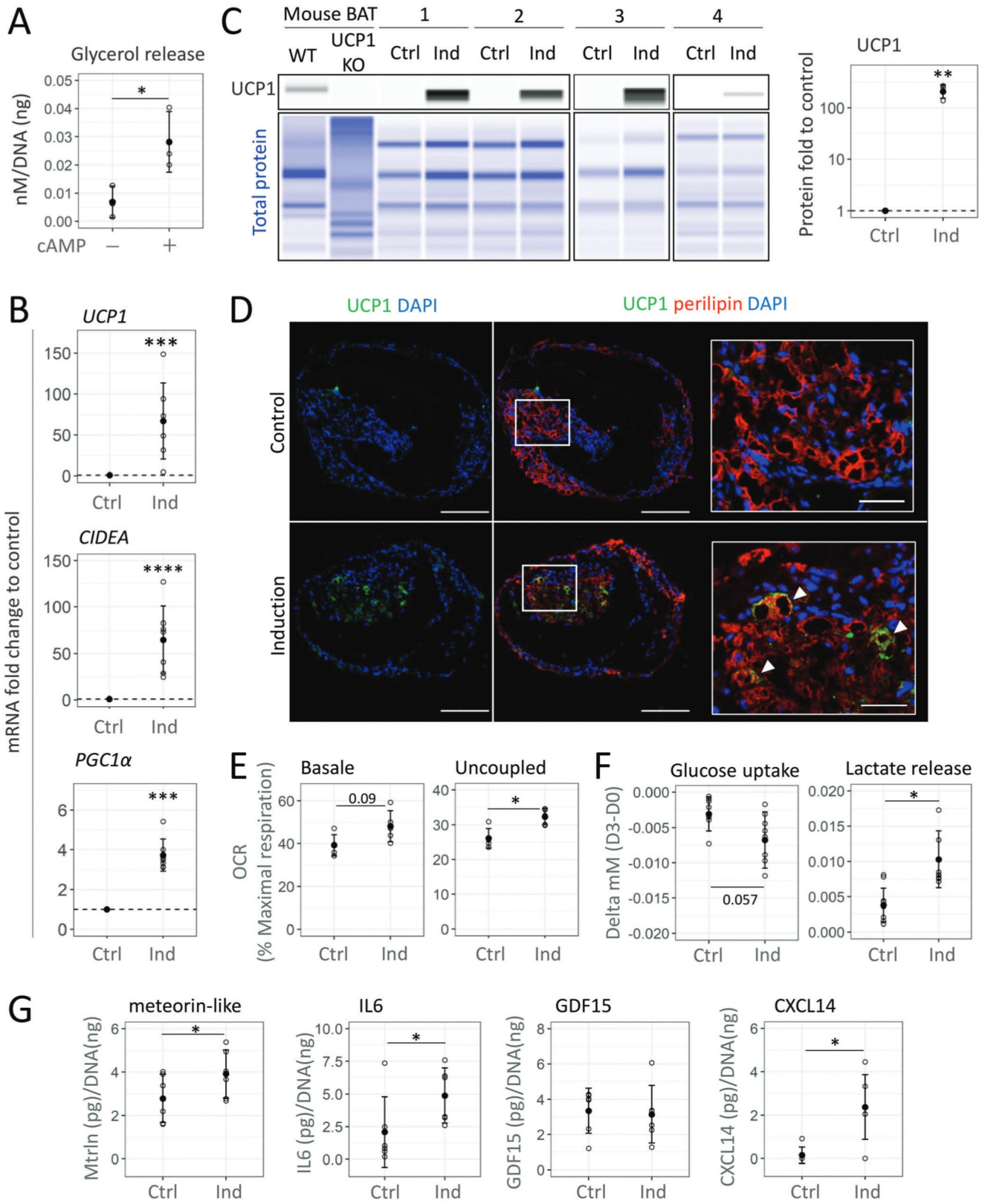

Figure 6. Activation of beige adipose organoids by canonical UCP1 inducers. Beige adipose organoids derived from P0-SVF cells were treated (Ind) or not (Ctrl) with UCP1 inducers for the last three days of culture. A) Evaluation of lipolysis measured as glycerol release with or without stimulation (n = 3). B) Gene expression analysis of beige adipocytes markers (*UCP1*, *CIDEA*, and *PGC1α*). Fold changes are expressed relative to the Ctrl condition (n = 7). C) Expression of UCP1 protein under control (Ctrl) or induction (Ind) conditions derived from four different donors. Murine brown adipose

a pericellular position akin to perivascular smooth muscle cells. These data suggest vessel structural maturation. However, these structures seem to be still under development as only a few cells expressing other canonical pericytes markers (CD146,[64] Platelet derived growth factor receptor PDGFRβ,[65] Figure S6B, Supporting Information) were found close to endothelial cell networks.

This complex phenotype in culture, which resembles native tissue organization, results from a combination of the optimized biomaterial we have used, the conditions of its use, and the culture media we have developed.

Generation of organoids from various organs often relies on the use of Matrigel®,[25,26,28] a mouse tumor extracellular matrix extract that is ill-defined and whose biomechanical features are not tunable and incompatible with good manufacturing practice (GMP)-compliant procedure. GelMA with its tunable mechanical properties close to those of adipose tissue and its excellent biocompatibility[31] appears to be a promising alternative for engineering soft collagen-rich tissue such as adipose tissue.[66] Furthermore, the very recent development of GMP-grade GelMA definitively opened up its use for putative clinical applications (Rousselot® Biomedical).

The optimal combination of volume per spheroid, percentage, and reticulation of GelMA embedding conditions is important to support cell mass expansion contributing to the development of beige adipose organoids. Defining this combination was critical to translating our engineering process from single to multiple spheroid assemblies. We tuned GelMA concentrations (5–10%) to generate substrates of known biochemical composition and a Storage's modulus between 1.97 and 6.11 kPa that matches the stiffness range of white (≈1–3 kPa)[67] and beige (≈4–6 kPa)[43] adipose tissue. Maximum cell expansion and viability inside hydrogel were found for 10% GelMA and a droplet volume of 1.5 µL. A GelMA percentage below 10% showed a higher variability and collapse of the hydrogel on itself, especially for 5% GelMA substrates supporting tissues with a lower DNA content. This GelMA collapse would result from increased degradation kinetics and lower stiffness favoring contraction during cell proliferation.[68]

This study highlights the importance of defining a physicochemical environment with proper mechanical stability and porosity that allows cells to expand over time and self-organize at various tissue scales.

Self-organized vascular formation in close proximity to adipocytes was achieved via the refinement of our previously published medium.[18] Inhibition of the TGFβ pathway has been shown to favor the differentiation of adipose progenitors toward adipogenesis,[69] including toward the beige lineage.[70] Furthermore, such inhibition decreases ASC differentiation into myofibroblasts. This observation is consistent with a study from Di Stefano et al. demonstrating that ASC spheroids display increased TGFβ expression compared to 2D culture which suggests higher activation of the pro-myofibrolastic TGFβ pathway.[71] As TGFβ also inhibits vascular formation,[72] the use of SB431542, a TGFβ inhibitor, is a viable alternative in 3D culture to promote beige adipogenesis while maintaining endothelial cell network. Remarkably, we found a combined positive effect of TGFβ inhibition and GelMA embedding on beige adipocyte commitment of amplified SVF cells. This effect was even more potent with crude SVF cells where a defined combination of chemical and mechanical cues was a necessary and sufficient condition to unlock beige adipogenesis. The physiological distribution of endothelial cells in between adipocytes suggests an increased ability of cells into GelMA hydrogel to self-organize compared to unembedded spheroids. The emergence of these pseudo-vascular networks from the internal cell mass within organoids implied increased angiogenic potential of ASCs in close contact with cell aggregates as previously described.[73] In addition, unstained cells from immunofluorescence analyses revealed non-adipocytes and non-vascular cell compartments which could suggest the presence of undifferentiated progenitor cells. Further extensive investigations will be required to better characterize organoids' cell composition. The presence of progenitor cells in the organoid such as found in the native tissue could be relevant for its long-term cell maintenance.

Simultaneous embedding of pre-assembled spheroids using a molding approach represents a simple, practical, and rapid way to generate microtissue with variable sizes. Tuning of a single factor, i.e., matrix volume to spheroid ratio, is sufficient to achieve comparable phenotypes in tissues grown at a micro and macro scale. Besides, the beneficial effect of GelMA embedding on cell spheroid viability is maintained with increasing tissue size. This is especially important as the main challenge of large-scale biofabrication is to maintain an adequate supply of nutrients/oxygen and avoid cell viability issues. These data suggest that it may be possible to construct custom tissues that meet specific cell requirements by using the matrix-to-cell ratio as a scaling factor. Generating centimeter-sized tissue efficiently is particularly crucial when aiming to translate studies on beige adipose tissue transplantation from mice[11–14] to biomedical applications in obese or diabetic patients. In this context, the successful implantation of a substantial number of cells is necessary to potentially achieve therapeutic effectiveness. Additionally, these beige adipose micro-tissues remained easy to handle at the end of the culture process facilitating surgical implantation and displayed embedded vasculature that may help to sustain micro-tissue integration and viability after implantation. Moreover, it is reasonable to assume that a micro-tissue of significant size would be less sensitive to the effect of the environment, and would retain the desired function for a longer period after transplantation.

tissue (BAT) from wild-type (WT) and UCP1 KO mouse were used as positive and negative controls, respectively. Quantification of UCP1 expression was normalized by total protein signal and expressed as fold change to control condition ($n = 4$). D) Immunofluorescence images of UCP1 staining (green). Lipid-containing cells were revealed by perilipin staining (red) and cell nuclei by DAPI staining. Scale bar: 200 µm. White squares show areas at higher magnifications where UCP1+ cells (white arrowheads) could be observed. Scale: 50 µm. E) Evaluation of basal (left) and uncoupled cell respiration (right) under control or induction conditions with Seahorse XF24 ($n = 5$). F) Measure of glucose uptake and lactate release during the three days of treatment ($n = 6$). G) Evaluation of meteorin-like, IL-6, GDF15, and CXCL14 secretions ($n = 6$). Measurements of glycerol and lactate release, glucose uptake, meteorin-like, IL6, GDF15, and CXCL14 levels were normalized relative to DNA quantity/spheroid. All quantitative data are expressed as mean ± standard deviation. Statistical analysis of fold change to control was performed by one-sample t-test while statistical analysis for means comparisons was performed by paired two-sample t-test. Statistical significances: $^{*}p \leq 0.05$, $^{**}p < 0.01$, $^{***}p < 0.01$, and $^{****}p < 0.0001$.

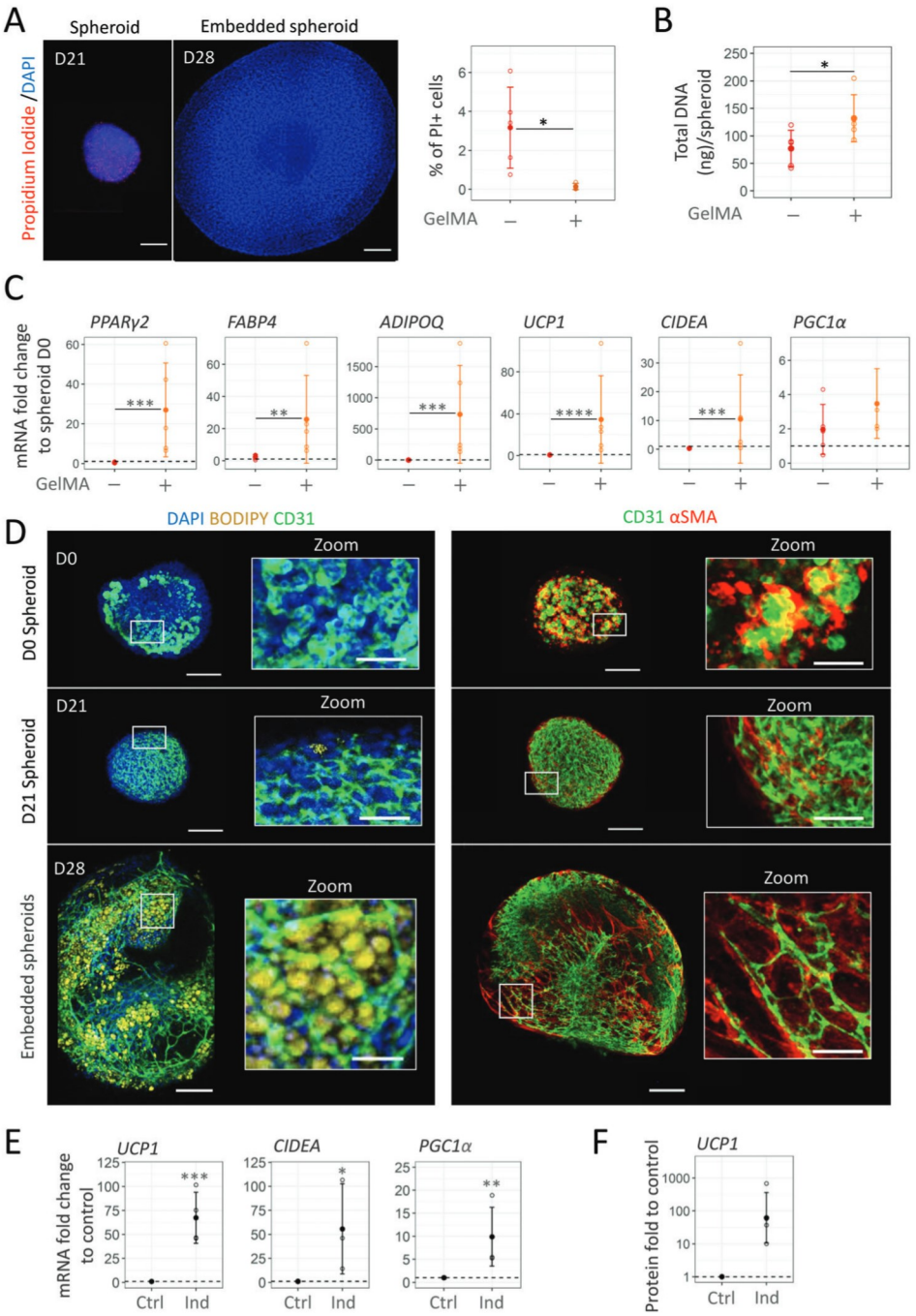

Figure 7. Combination of TGFβ inhibition and GelMA embedding unlocks beige adipogenesis and promotes vascular formation from SVF cells. A–E) Spheroids obtained directly from freshly isolated human stromal vascular fraction were embedded or not in GelMA 10% and analyzed at day 21 of differentiation in adipogenic medium with SB431542. A) Confocal images and quantification of propidium iodide (dead cells, red) staining relative to DAPI (blue) staining ($n = 5$). Scale bar: 200 µm. Statistical analysis was performed by two-sample *t*-tests. B) Average DNA content per spheroid with or without GelMA ($n = 5$). C) Immunofluorescence analysis. Specific antibodies against human endothelial cell marker CD31 (green) and α-smooth muscle actin (SMA) (red) were used. Lipids containing cells were revealed by bodipy staining. DAPI staining highlights cell nuclei. White squares are zoomed areas showing endothelial cell organization. Scales: 200 µm. D) Gene expression analysis of beige adipocytes markers (*UCP1*, *CIDEA*, and *PGC1α*) and generic adipocyte markers (*PPARγ2*, *FABP4*, and *ADIPOQ*) in spheroids embedded or not in GelMA ($n = 8$) after 21 days of differentiation. Data are expressed relative to non-embedded undifferentiated spheroids (D0). E-G) To assess beiging potential, GelMA 10% embedded SVF spheroid were treated (Ind) or not (Ctrl) with UCP1 inducers for the last three days of differentiation. E) Gene expression analysis of brown adipocytes markers (*UCP1*, *CIDEA*, and *PGC1α*). Fold changes are expressed relative to controls ($n = 3$). F) Quantification of normalized UCP1 protein expression expressed as fold change relative to control condition ($n = 3$). All quantitative data are expressed as mean ± standard deviation. Statistical analysis of fold change to control was performed by one-sample *t*-test while statistical analysis for means comparisons was performed by paired two-sample *t*-test. Statistical significance: $^{*}p \leq 0.05$, $^{**}p < 0.01$, $^{***}p < 0.01$, and $^{****}p < 0.0001$.

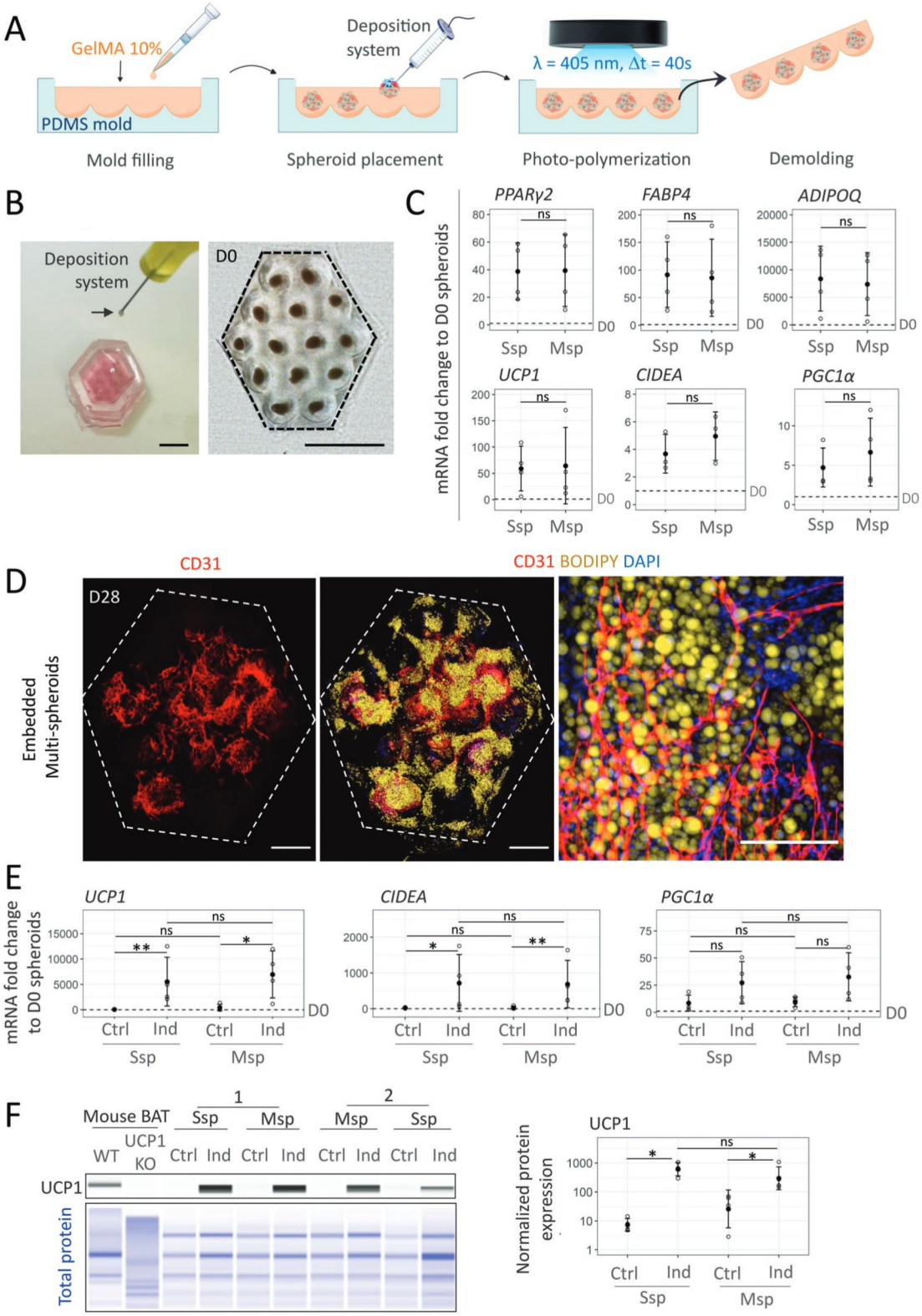

Figure 8. Generation of vascularized beige adipose micro-tissue by multi-spheroid assembly in GelMA. A) Engineering of multi-spheroid tissue constructs. B) Macroscopic view of spheroid deposition in the PDMS mold and GelMA multi-spheroid construct after demolding. Dotted lines highlight the contours of the GelMA construct. Scale: 2.5 mm. C) Gene expression analysis of beige adipocytes markers (*UCP1*, *CIDEA*, and *PGC1α)* and generic adipocyte markers (*PPARγ2*, *FABP4*, and *ADIPOQ*) in individually embedded spheroids (1sp) compared to multi-spheroid construct (14 sp) generated from P0-SVF cells, at the end of the culture process. Fold change relative to non-embedded undifferentiated spheroids (D0) is shown ($n = 4$). Statistical

Regardless of tissue size, cell sources should also be a modulable parameter to consider in organoid applications. As discussed above, the promise of cell-based therapies comes with several challenges including obtaining sufficient cells to display significant therapeutic efficacy with consistent cell quality. Ex vivo expansion of SVF cells, such as P0-SVF cells, allows the production of a large number of relatively homogeneous ASCs compared to native SVF. P0-SVF cells produced organoids with the highest thermogenic potential regarding total UCP1 protein quantity and metabolic functionality, making them a preferred cell source for therapeutic implantation or high throughput drug screening. However, changes in expression profile and functional drift can be observed from ASCs amplification.[74,75] Therefore, despite their lower thermogenic potential, organoids generated from crude SVF represent a promising tool for precision medicine with personalized drug screening as they are more susceptible to conserve native cell heterogeneity and hallmarks of patient metabolism as found in vivo. In conclusion, we propose a convenient process for the generation of functional vascularized 3D human beige adipose organoids and micro-tissue through the definition of a permissive microenvironment and its translation to a macroscale level. We demonstrated that fully functional vascularized beige adipose organoids containing inducible adipocytes could be generated from both amplified and native SVF cells. Such models will help to elucidate the development and function of a tissue that is difficult to access in adult humans while reducing animal use. Indeed, organoids could be used to better understand the underlying mechanisms of beige tissue activation in physiological or pathophysiological conditions. Generating patient-derived organoids can be easily considered for disease modeling and drug screening. Therefore, we believe that these models will help to efficiently select relevant targets and compounds for therapeutic use in humans, thus bridging the gap between the bench and the bedside. Through their scalability, these new human beige adipose tissue models open the door to more relevant in vitro studies for basic research and a wide range of therapeutic applications from bioassays to biotherapies.

Supporting Information

Supporting Information is available from the Wiley Online Library or from the author.

Acknowledgements

The work was supported by the French National Agency for Research (hiPSC-Adipospheres ANR-18-CE18-0006, Printiss Project, grant ANR21 CE1941) and the LAAS-CNRS micro and nanotechnologies platform, a member of the French Renatech network. It was partly supported as part of the MultiFAB project funded by FEDER European Regional Funds and French Région Occitanie (grant agreement number 16007407/MP0011594) and by the HoliFAB project funded by the European Union's Horizon 2020 research and innovation program (grant agreement No. 760927). This work bearing the reference CARe – Graduate School N°ANR-18-EURE-0003 benefited from a State grant managed by the Agence Nationale de la Recherche under the Programme "Investissements d'Avenir". This work was partly supported by Grant PID2020-114112RB-I00 from MCIN/AEI/10.13039/501100011033, Spain, co-financed by the European Regional Development Fund. SimpleWestern and Seahorse analysis was performed at the We-Met platform facility at I2MC institute (Toulouse). The authors would especially like to thank Alexandre Lucas, head of the We-Met platform, along with Steven Fried and Corinne Bernis for their advice and great assistance. The authors greatly thank Adeline Girel, Isabelle Castan (Restore, Toulouse), Jean Baptiste Doucet, Daniel Ferri Angulo, Julie Foncy, Sandrine Assié (LAAS, Toulouse), and Corinne Lorenzo (Restore, Toulouse) for their assistance with cell culture, RT-qPCR, lipolysis and spheroid encapsulation experiments and cell imaging, respectively. The authors acknowledge the zootechnical core facility (Anexplo-Genotoul platform) for their technical assistance. The authors thank Théo Herail for his help in some RT-qPCR analysis and Philippe Kemoun for the discussion on mural cells.

Conflict of Interest

L.C. Is co-founder, shareholder and discloses consultancy work for CellEasy company. L.C., L.V., L.M., G.E., C.D., A.C., M.E. have filed 2 patents (EP22306953, EP 233051366) related to this work. All other co-authors display no conflict of interest.

Author Contributions

M.E. and L.V. contributed equally to this work and are co-first authors. G.E., L.V., L.B., C.V., and L.M. designed the GelMA construct. M.E. and L.V. conducted cell experiments and performed functional assays. M.P. and F.V. performed ELISA experiments to determine paracrine activity. Y.J. contributed to metabolic studies. F.D. designed the initial media culture. I.R.L. and M.P. performed immunochemistry experiments to identify perivascular cells. S.B. and X.Y. participated to cell culture. B.C. provided human cells. M.E., L.V., I.R.L., A.C., L.M., and L.C. analyzed the data and wrote the manuscript. L.V., C.D., A.C., L.M., and L.C. designed and supervised the research. L.V., C.D., A.C., L.M., and L.C. designed the research. AC, LM and LC contributed equally to the supervision of this work and are co-last authors. All authors revised and approved the final version of the manuscript.

Data Availability Statement

The data that support the findings of this study are available from the corresponding author upon reasonable request.

analysis was performed by a two-sample *t*-test. D) Immunofluorescence images of lipids-containing cells and endothelial cells revealed by BODIPY (yellow) and CD31 (red) stainings, respectively, within embedded multi-spheroid P0-SVF construct at the end of the culture process. DAPI staining highlights cell nuclei. Scale bar: 1000 µm. The right image depicts a magnified area. Scale bar: 200 µm. E–G) Assessment of embedded multi-spheroid construct (14sp) response to UCP1 inducers in comparison to individually embedded spheroids (1sp). For each type of construct, cells were treated or not (Ind versus Ctrl) with UCP1 inducers for the last three days of culture. E) Gene expression analysis of beige adipocytes markers (*UCP1*, *CIDEA*, and *PGC1α*). Fold changes are expressed relative to non-embedded undifferentiated spheroids (D0) ($n = 4$). Statistical analysis was performed by one-way ANOVA followed by Tukey's comparison. F) UCP1 protein expression of multi-spheroid (14 sp) and individual embedded spheroid (1sp) under control and induction conditions derived from two different donors. Wild type (WT) and UCP1 KO mouse brown adipose tissue (BAT) were used as positive and negative controls, respectively. Quantification of UCP1 expression normalized to total protein signal ($n = 4$). Statistical analysis was performed by Kruskal Wallis analysis followed by paired wise Wilcoxson test with Bonferoni correction. All quantitative data are expressed as mean ± standard deviation. Statistical significances: ns. non-significant, $^{*}p \leq 0.05$ and $^{**}p \leq 0.01$.

Keywords

adipose-derived stroma/stem cells (ASC), beige and brown adipocytes, guided-assembly, hydrogels, microtissues, organoid morphogenesis, stromal vascular fraction

Received: March 7, 2023
Revised: August 7, 2023
Published online:

[1] A. Sakers, M. K. De Siqueira, P. Seale, C. J. Villanueva, *Cell* **2022**, *185*, 419.
[2] B. Cannon, J. Nedergaard, *Physiol. Rev.* **2004**, *84*, 277.
[3] F. Villarroya, A. Gavaldà-Navarro, M. Peyrou, J. Villarroya, M. Giralt, *Trends Endocrinol Metab* **2017**, *28*, 855.
[4] D. Loncar, *Cell Tissue Res.* **1991**, *266*, 149.
[5] B. Cousin, S. Cinti, M. Morroni, S. Raimbault, D. Ricquier, L. Pénicaud, L. Casteilla, *J. Cell Sci.* **1992**, *103*, 931.
[6] P. Young, J. R. Arch, M. Ashwell, *FEBS Lett.* **1984**, *167*, 10.
[7] P. Boström, J. Wu, M. P. Jedrychowski, A. Korde, L. Ye, J. C. Lo, K. A. Rasbach, E. A. Boström, J. H. Choi, J. Z. Long, S. Kajimura, M. C. Zingaretti, B. F. Vind, H. Tu, S. Cinti, K. Højlund, S. P. Gygi, B. M. Spiegelman, *Nature* **2012**, *481*, 463.
[8] G. Li, C. Xie, S. Lu, R. G. Nichols, Y. Tian, L. Li, D. Patel, Y. Ma, C. N. Brocker, T. Yan, K. W. Krausz, R. Xiang, O. Gavrilova, A. D. Patterson, F. J. Gonzalez, *Cell Metab.* **2017**, *26*, 672.
[9] G. da N Silva, A. A. Amato, *Front Cell Dev Biol* **2022**, *10*, 955612.
[10] D. C. Berry, Y. Jiang, R. W. Arpke, E. L. Close, A. Uchida, D. Reading, E. D. Berglund, M. Kyba, J. M. Graff, *Cell Metab.* **2017**, *25*, 481.
[11] V. Dani, X. Yao, C. Dani, *Rev Endocr Metab Disord* **2022**, *23*, 103.
[12] J. D. White, R. S. Dewal, K. I. Stanford, *Mol Aspects Med* **2019**, *68*, 74.
[13] E. Tsagkaraki, S. M. Nicoloro, T. DeSouza, J. Solivan-Rivera, A. Desai, L. M. Lifshitz, Y. Shen, M. Kelly, A. Guilherme, F. Henriques, N. Amrani, R. Ibraheim, T. C. Rodriguez, K. Luk, S. Maitland, R. H. Friedline, L. Tauer, X. Hu, J. K. Kim, S. A. Wolfe, E. J. Sontheimer, S. Corvera, M. P. Czech, *Nat. Commun.* **2021**, *12*, 6931.
[14] A. M. Singh, L. Zhang, J. Avery, A. Yin, Y. Du, H. Wang, Z. Li, H. Fu, H. Yin, S. Dalton, *Nat. Commun.* **2020**, *11*, 2758.
[15] W. Hu, M. A. Lazar, *Nat Rev Endocrinol* **2022**, *18*, 744.
[16] J. Rogal, J. Roosz, C. Teufel, M. Cipriano, R. Xu, W. Eisler, M. Weiss, K. Schenke-Layland, P. Loskill, *Adv. Sci.* **2022**, *9*, 2104451.
[17] A. J. Klingelhutz, F. A. Gourronc, A. Chaly, D. A. Wadkins, A. J. Burand, K. R. Markan, S. O. Idiga, M. Wu, M. J. Potthoff, J. A. Ankrum, *Sci. Rep.* **2018**, *8*, 523.
[18] S. Muller, I. Ader, J. Creff, H. Leménager, P. Achard, L. Casteilla, L. Sensebé, A. Carrière, F. Deschaseaux, *Sci. Rep.* **2019**, *9*, 7250.
[19] V. Dani, S. Bruni-Favier, B. Chignon-Sicard, A. Loubat, A. Doglio, C. Dani, *Cells* **2022**, *11*, 2798.
[20] J. X. Shen, M. Couchet, J. Dufau, T. de Castro Barbosa, M. H. Ulbrich, M. Helmstädter, A. M. Kemas, R. Zandi Shafagh, M.-A. Marques, J. B. Hansen, N. Mejhert, D. Langin, M. Rydén, V. M. Lauschke, *Adv. Sci.* **2021**, *8*, 2100106.
[21] M. Kuss, J. Kim, D. Qi, S. Wu, Y. Lei, S. Chung, B. Duan, *Acta Biomater.* **2018**, *71*, 486.
[22] J. P. Yang, A. E. Anderson, A. McCartney, X. Ory, G. Ma, E. Pappalardo, J. Bader, J. H. Elisseeff, *Tissue Eng., Part A* **2017**, *23*, 253.
[23] M. A. Gonzalez Porras, K. Stojkova, F. M. Acosta, C. R. Rathbone, E. M. Brey, *Front Bioeng Biotechnol* **2022**, *10*, 906395.
[24] N. Schopow, S. Kallendrusch, S. Gong, F. Rapp, J. Körfer, M. Gericke, N. Spindler, C. Josten, S. Langer, I. Bechmann, *PLoS One* **2020**, *15*, e0233152.
[25] M. Hofer, M. P. Lutolf, *Nat. Rev. Mater.* **2021**, *6*, 402.
[26] F. Kaluthantrige Don, M. Huch, *Trends Mol Med* **2021**, *27*, 416.
[27] Y. Shao, J. Fu, *Cell Stem Cell* **2022**, *29*, 722.
[28] J. A. Brassard, M. P. Lutolf, *Cell Stem Cell* **2019**, *24*, 860.
[29] B. Cecen, A. Bal-Ozturk, G. Yasayan, E. Alarcin, P. Kocak, R. Tutar, L. D. Kozaci, S. R. Shin, A. K. Miri, *J. Biomed. Mater. Res., Part A* **2022**, *110*, 1147.
[30] S. Vanaei, M. S. Parizi, S. Vanaei, F. Salemizadehparizi, H. R. Vanaei, *Eng. Regen.* **2021**, *2*, 1.
[31] K. Yue, G. Trujillo-de Santiago, M. M. Alvarez, A. Tamayol, N. Annabi, A. Khademhosseini, *Biomaterials* **2015**, *73*, 254.
[32] M. Cuvellier, F. Ezan, H. Oliveira, S. Rose, J.-C. Fricain, S. Langouët, V. Legagneux, G. Baffet, *Biomaterials* **2021**, *269*, 120611.
[33] K. J. Wolf, J. D. Weiss, S. G. M. Uzel, M. A. Skylar-Scott, J. A. Lewis, *Cell Stem Cell* **2022**, *29*, 667.
[34] G. Eke, L. Vaysse, X. Yao, M. Escudero, A. Carrière, E. Trevisiol, C. Vieu, C. Dani, L. Casteilla, L. Malaquin, *Cells* **2022**, *11*, 1394.
[35] H. Shirahama, B. H. Lee, L. P. Tan, N.-J. Cho, *Sci. Rep.* **2016**, *6*, 31036.
[36] G. Eke, N. Mangir, N. Hasirci, S. MacNeil, V. Hasirci, *Biomaterials* **2017**, *129*, 188.
[37] H. Hama, H. Kurokawa, H. Kawano, R. Ando, T. Shimogori, H. Noda, K. Fukami, A. Sakaue-Sawano, A. Miyawaki, *Nat. Neurosci.* **2011**, *14*, 1481.
[38] U. Schmidt, M. Weigert, C. Broaddus, G. Myers, **2018**, pp. 265–273.
[39] H. Hama, H. Hioki, K. Namiki, T. Hoshida, H. Kurokawa, F. Ishidate, T. Kaneko, T. Akagi, T. Saito, T. Saido, A. Miyawaki, *Nat. Neurosci.* **2015**, *18*, 1518.
[40] A. Ståhlberg, V. Rusnakova, A. Forootan, M. Anderova, M. Kubista, *Methods* **2013**, *59*, 80.
[41] A. Ioannidou, S. Alatar, R. Schipper, F. Baganha, M. Åhlander, A. Hornell, R. M. Fisher, C. E. Hagberg, *J Physiol* **2022**, *600*, 869.
[42] B. Chignon-Sicard, M. Kouidhi, X. Yao, A. Delerue-Audegond, P. Villageois, P. Peraldi, P. Ferrari, Y. Rival, D. Piwnica, J. Aubert, C. Dani, *Sci. Rep.* **2017**, *7*, 2954.
[43] K. M. Tharp, M. S. Kang, G. A. Timblin, J. Dempersmier, G. E. Dempsey, P.-J. H. Zushin, J. Benavides, C. Choi, C. X. Li, A. K. Jha, S. Kajimura, K. E. Healy, H. S. Sul, K. Saijo, S. Kumar, A. Stahl, *Cell Metab.* **2018**, *27*, 602.
[44] K. S. Lim, B. J. Klotz, G. C. J. Lindberg, F. P. W. Melchels, G. J. Hooper, J. Malda, D. Gawlitta, T. B. F. Woodfield, *Macromol. Biosci.* **2019**, *19*, 1900098.
[45] B. D. Fairbanks, M. P. Schwartz, C. N. Bowman, K. S. Anseth, *Biomaterials* **2009**, *30*, 6702.
[46] Y. W. Chung, F. Ahmad, Y. Tang, S. C. Hockman, H. J. Kee, K. Berger, E. Guirguis, Y. H. Choi, D. M. Schimel, A. M. Aponte, S. Park, E. Degerman, V. C. Manganiello, *Sci. Rep.* **2017**, *7*, 40445.
[47] T. Teruel, R. Hernandez, M. Benito, M. Lorenzo, *J. Biol. Chem.* **2003**, *278*, 263.
[48] R. Alvarez, J. de Andrés, P. Yubero, O. Viñas, T. Mampel, R. Iglesias, M. Giralt, F. Villarroya, *J. Biol. Chem.* **1995**, *270*, 5666.
[49] J.-Y. Lee, N. Takahashi, M. Yasubuchi, Y.-I. Kim, H. Hashizaki, M.-J. Kim, T. Sakamoto, T. Goto, T. Kawada, *Am. J. Physiol. Cell Physiol.* **2012**, *302*, C463.
[50] R. R. Rao, J. Z. Long, J. P. White, K. J. Svensson, J. Lou, I. Lokurkar, M. P. Jedrychowski, J. L. Ruas, C. D. Wrann, J. C. Lo, D. M. Camera, J. Lachey, S. Gygi, J. Seehra, J. A. Hawley, B. M. Spiegelman, *Cell* **2014**, *157*, 1279.
[51] H. Qing, R. Desrouleaux, K. Israni-Winger, Y. S. Mineur, N. Fogelman, C. Zhang, S. Rashed, N. W. Palm, R. Sinha, M. R. Picciotto, R. J. Perry, A. Wang, *Cell* **2020**, *182*, 372.
[52] L. Burýšek, J. Houštěk, *FEBS Lett.* **1997**, *411*, 83.
[53] L. Campderrós, R. Moure, M. Cairó, A. Gavaldà-Navarro, T. Quesada-López, R. Cereijo, M. Giralt, J. Villarroya, F. Villarroya, *Obes. Silver Spring Md.* **2019**, *27*, 1606.
[54] R. Cereijo, A. Gavaldà-Navarro, M. Cairó, T. Quesada-López, J. Villarroya, S. Morón-Ros, D. Sánchez-Infantes, M. Peyrou, R. Iglesias,

T. Mampel, J.-V. Turatsinze, D. L. Eizirik, M. Giralt, F. Villarroya, *Cell Metab.* **2018**, *28*, 750.
[55] V. M. Ramakrishnan, N. L. Boyd, *Tissue Eng Part B Rev* **2018**, *24*, 289.
[56] K.-V. Tran, O. Gealekman, A. Frontini, M. C. Zingaretti, M. Morroni, A. Giordano, A. Smorlesi, J. Perugini, R. De Matteis, A. Sbarbati, S. Corvera, S. Cinti, *Cell Metab.* **2012**, *15*, 222.
[57] A. C. Carpentier, D. P. Blondin, K. A. Virtanen, D. Richard, F. Haman, É. E. Turcotte, *Front. Endocrinol.* **2018**, *9*, 447.
[58] Z. Wang, Q. A. Wang, Y. Liu, L. Jiang, *FEBS J.* **2021**, *288*, 3647.
[59] B. Wang, X. Fu, X. Liang, J. M. Deavila, Z. Wang, L. Zhao, Q. Tian, J. Zhao, N. A. Gomez, S. C. Trombetta, M.-J. Zhu, M. Du, *Cell Discov.* **2017**, *3*, 1.
[60] J. Park, M. Kim, K. Sun, Y. A. An, X. Gu, P. E. Scherer, *Diabetes* **2017**, *66*, 1479.
[61] J. Xu, T. Gong, C. F. Zhang, *FASEB J.* **2017**, *31*, 1775.
[62] M. Crisan, M. Corselli, W. C. W. Chen, B. Péault, *J. Cell. Mol. Med.* **2012**, *16*, 2851.
[63] M. Crisan, S. Yap, L. Casteilla, C.-W. Chen, M. Corselli, T. S. Park, G. Andriolo, B. Sun, B. Zheng, L. Zhang, C. Norotte, P.-N. Teng, J. Traas, R. Schugar, B. M. Deasy, S. Badylak, H.-J. Buhring, J.-P. Giacobino, L. Lazzari, J. Huard, B. Péault, *Cell Stem Cell* **2008**, *3*, 301.
[64] Q. Li, Y. Yu, J. Bischoff, J. B. Mulliken, B. R. Olsen, *J Pathol* **2003**, *201*, 296.
[65] L. E. Olson, P. Soriano, *Dev. Cell* **2011**, *20*, 815.
[66] S. Bupphathong, C. Quiroz, W. Huang, P.-F. Chung, H.-Y. Tao, C.-H. Lin, *Pharmaceuticals* **2022**, *15*, 171.
[67] N. Alkhouli, J. Mansfield, E. Green, J. Bell, B. Knight, N. Liversedge, J. C. Tham, R. Welbourn, A. C. Shore, K. Kos, C. P. Winlove, *Am. J. Physiol.-Endocrinol. Metab.* **2013**, *305*, E1427.
[68] P. Chansoria, S. Asif, K. Polkoff, J. Chung, J. A. Piedrahita, R. A. Shirwaiker, *ACS Biomater. Sci. Eng.* **2021**, *7*, 5175.
[69] H. Leménager, L. M. A. Fiévet, F. Guilloton, A. Naji, J.-G. Descamps, B. Chaput, N. Suganuma, J.-C. Pagès, L. Sensebé, A. Carrière, L. Casteilla, F. Deschaseaux, *Stem Cells* **2020**, *38*, 782.
[70] A.-L. Hafner, J. Contet, C. Ravaud, X. Yao, P. Villageois, K. Suknuntha, K. Annab, P. Peraldi, B. Binetruy, I. I. Slukvin, A. Ladoux, C. Dani, *Sci. Rep.* **2016**, *6*, 32490.
[71] A. B. Di Stefano, F. Grisafi, M. Perez-Alea, M. Castiglia, M. Di Simone, S. Meraviglia, A. Cordova, F. Moschella, F. Toia, *Gene* **2021**, *768*, 145269.
[72] M. Jarad, E. A. Kuczynski, J. Morrison, A. M. Viloria-Petit, B. L. Coomber, *BMC Cell Biol* **2017**, *18*, 10.
[73] J. Yu, Y.-C. Hsu, J.-K. Lee, N.-C. Cheng, *Stem Cell Res Ther* **2022**, *13*, 276.
[74] E. Jones, R. Schäfer, *Methods Mol. Biol. Clifton NJ* **2015**, *1235*, 105.
[75] D. S. Kim, M. W. Lee, K. H. Yoo, T.-H. Lee, H. J. Kim, I. K. Jang, Y. H. Chun, H. J. Kim, S. J. Park, S. H. Lee, M. H. Son, H. L. Jung, K. W. Sung, H. H. Koo, *PLoS One* **2014**, *9*, e83363.

ADVANCED SCIENCE
Open Access

Supporting Information

for *Adv. Sci.*, DOI 10.1002/advs.202301499

Scalable Generation of Pre-Vascularized and Functional Human Beige Adipose Organoids

*Mélanie Escudero, Laurence Vaysse, Gozde Eke, Marion Peyrou, Francesc Villarroya, Sophie Bonnel, Yannick Jeanson, Louisa Boyer, Christophe Vieu, Benoit Chaput, Xi Yao, Frédéric Deschaseaux, Mélissa Parny, Isabelle Raymond-Letron, Christian Dani, Audrey Carrière, Laurent Malaquin and Louis Casteilla**

Supporting Information

Scalable Generation of Pre-Vascularized and Functional Human Beige Adipose Organoids

Mélanie Escudero§[1, 2] Laurence Vaysse§[1], Gozde Eke[2], Marion Peyrou[3], Francesc Villarroya[3] Sophie Bonnel[1], Yannick Jeanson[1], Louisa Boyer[2], Christophe Vieu[2], Benoit Chaput[4], Xi Yao[5], Frédéric Deschazeaux[1], Mélissa Parny[1,6], Isabelle Raymond-Letron[1,6], Christian Dani[5], Audrey Carrière[1], Laurent Malaquin*[2], Louis Casteilla[1]**

Immunohistochemistry protocol:

Embedded spheroids were fixed overnight in 4% buffered formalin for 24h before storage in PBS at 4°C. After paraffin embedding, 3µm thickness paraffin sections were dewaxed (successive toluene and descending alcohols bathes) and stained with haematoxilin and eosin. CD31 and CD146 labelling of 3-µm serial sections of paraffin-embedded blocks were performed out after antigen retrieval (Ptlink high pH, reference K800021-2, Dako for CD31 labelling and Ptlink low pH, reference K8005, Dako for CD146 labelling) for 30 min at 96°C. Anti-human CD31 murine monoclonal antibody (M0823, clone JC70A, dilution 1:120) or CD146 rabbit monoclonal antibody (ab75769, Abcam, dilution 1:250) were incubated for 50 min at room temperature. Staining was carried out with EnVision Flex (reference K8000, Dako) for 30 min at room temperature, followed by DAB as a chromogen (reference K8000, 10 min room temperature). Slides were then counterstained with hematoxylin (reference C0283, DIAPATH). The stained slides were scanned (Panoramic Desk, 3D Histec) or imaged by light microscopy on a Nikon Eclipse Ci-L microscope with a DS138 Fi3 Camera and NIS Elements D software.

Table S1: List of primer used for qPCR and qRT-PCR analyses.

Gene		Sequence (5'-3')
RPLP0	Forward	CGTCCTCGTGGAAGTGACAT
	Reverse	TAGTTGGACTTCCAGGTCGC
GUSB	Forward	AGCCAGTTCCTCATCAATGG
	Reverse	GGTAGTGGCTGGTACGGAAA
PPIA	Forward	GCCGAGGAAAACCGTGTACTAT
	Reverse	TCTTTGGGACCTTGTCTGCAA
YWAZ	Forward	AGCAGGCTGAGCGATATGAT
	Reverse	TCTCAGCACCTTCCGTCTTT
FABP4	Forward	AAACTGGTGGTGGAATGCGT
	Reverse	GCGAACTTCAGTCCAGGTCA
PPARGγ2	Forward	GATACACTGTCTGCAAACATATCA
	Reverse	CACGGAGCTGATCCCAA
ADIPOQ	Forward	CAGAGATGGCACCCCTGGTG
	Reverse	TTCACCGATGTCTCCCTTAG
UCP1	Forward	GTGTGCCCAACTGTGCAATG
	Reverse	CCAGGATCCAAGTCGCAAGA
CIDEA	Forward	AGTCCTGTTGACCCCGCTC
	Reverse	GCTATTCCCGACCTCTTCGG
PGC1-α	Forward	CCGCACGCACCGAAA
	Reverse	TCGTGCTGATATTCCTCGTAGCT
CD31	Forward	GGAAAGCTGTCCCTGATGC
	Reverse	CATCTGGCCTTGCTGTCTAA
vWF	Forward	GATGGAGTCCAGCACCAGTT
	Reverse	GCTACTTCACACAGGCCACA
αSMA	Forward	CTATGCCTCTGGACGCACAACT
	Reverse	CAGATCCAGACGCATGATGGCA
COL1	Forward	GCTAACCCCCTCCCCAGCCA
	Reverse	GAGCAGGAGCCGGAGGTCCA
CTGF	Forward	TGCCCGGGAAATGCTGCGAG
	Reverse	CAGTCGGTAAGCCGCGAGGG

Table S2. List of antibodies and dyes used for immunofluorescence cell characterization.

Type	Name	Dilution	Company	Cat. No.
Primary antibodies	Anti-Human CD31 Rabbit monoclonal (Clone: EP78)	1:200	Epitomics (Burlingame, USA)	AC-0083A
	Anti-Human CD31 Mouse monoclonal (Clone: JC70A)	1:200	Dako-Agilent (Paris, France)	M0823
	Anti-perilipin Guinea pig polyclonal	1:100	Progen (Heidelberg,Germany)	GP29
	Anti-αSMA mouse monoclonal (Clone: 1A4)	1:100	Dako-Agilent (Paris, France)	M0851
	Anti-human/mouse UCP1 monoclonal mouse IgG_{2B}	1:500	R&D Systems Biotechne (Mineapolis, USA)	MAB6158
	Anti-CD146 Rabbit monoclonal	1:200	Abcam (Cambridge, UK)	ab75769
	Anti-PDGFRβ Rabbit polyclonal	1:50	DiagOmics (Blagnac, France)	A2180-20
Secondary antibodies	Alexa Fluor 488 Goat anti-rabbit IgG	1:500	Life technologies (Paisley, UK)	A11008
	Alexa Fluor 594 Goat anti-rabbit IgG	1:500	Life technologies (Paisley, UK)	A21207
	Alexa Fluor 647 Goat anti-Guinea Pig IgG Highly Cross-Adsorbed	1:500	Life technologies (Paisley, UK)	A21450
	Alexa Fluor 594 Goat anti-mouse IgG	1:500	Life technologies (Paisley, UK)	A11005
Dyes	BODIPY™ 493/503 (4,4-Difluoro-1,3,5,7,8-Pentamethyl-4-Bora-3a,4a-Diaza-*s*-Indacene)	1:500	Life technologies (Paisley, UK)	D3922
	DAPI (4',6-Diamidino-2-Phenylindole, Dihydrochloride)	1:5000	Life technologies (Paisley, UK)	D1306
	Propidium Iodide solution in water 1.0 mg/mL	1:100	Life technologies (Paisley, UK)	P3566

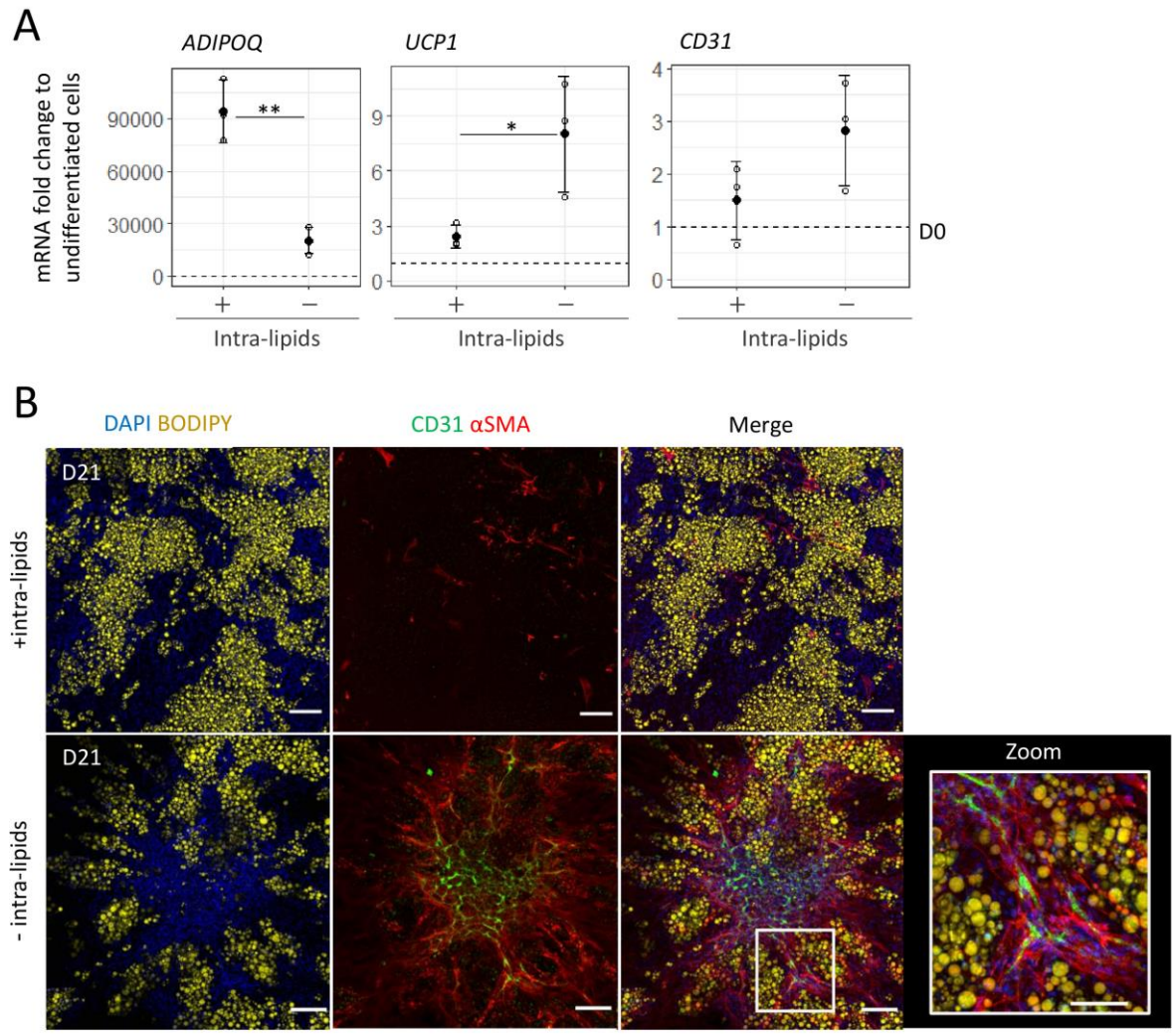

Figure S1. Development of a beige adipogenic cocktail that preserves endothelial cells from P0-SVF cells. P0-SVF cells were maintained in 2D culture for 21 days of differentiation either in an adipogenic cocktail containing intralipids or deprived of intralipids. A) Gene expression analysis of *UCP1* beige adipocytes marker, *ADIPOQ* generic adipocyte marker, and *CD31* endothelial cell marker. Fold changes are expressed relative to undifferentiated cells (D0). Data are expressed as mean ± standard deviation of three independent experiments from different human donors. Statistical analysis was performed by two sample t-test. *p<0.05, ** p<0.01. B) Immunofluorescence analysis. Specific antibodies against human endothelial cell marker CD31 (green) and α-smooth muscle actin (SMA) (red) were used. Lipids containing cells were revealed by bodipy staining. DAPI staining highlights cell nuclei. White square is a zoomed area showing endothelial cells organization aligned with αSMA+ cells in between adipocytes clusters derived from P0-SVF cells under deprived intralipid conditions (Scale bar: 100 µm).

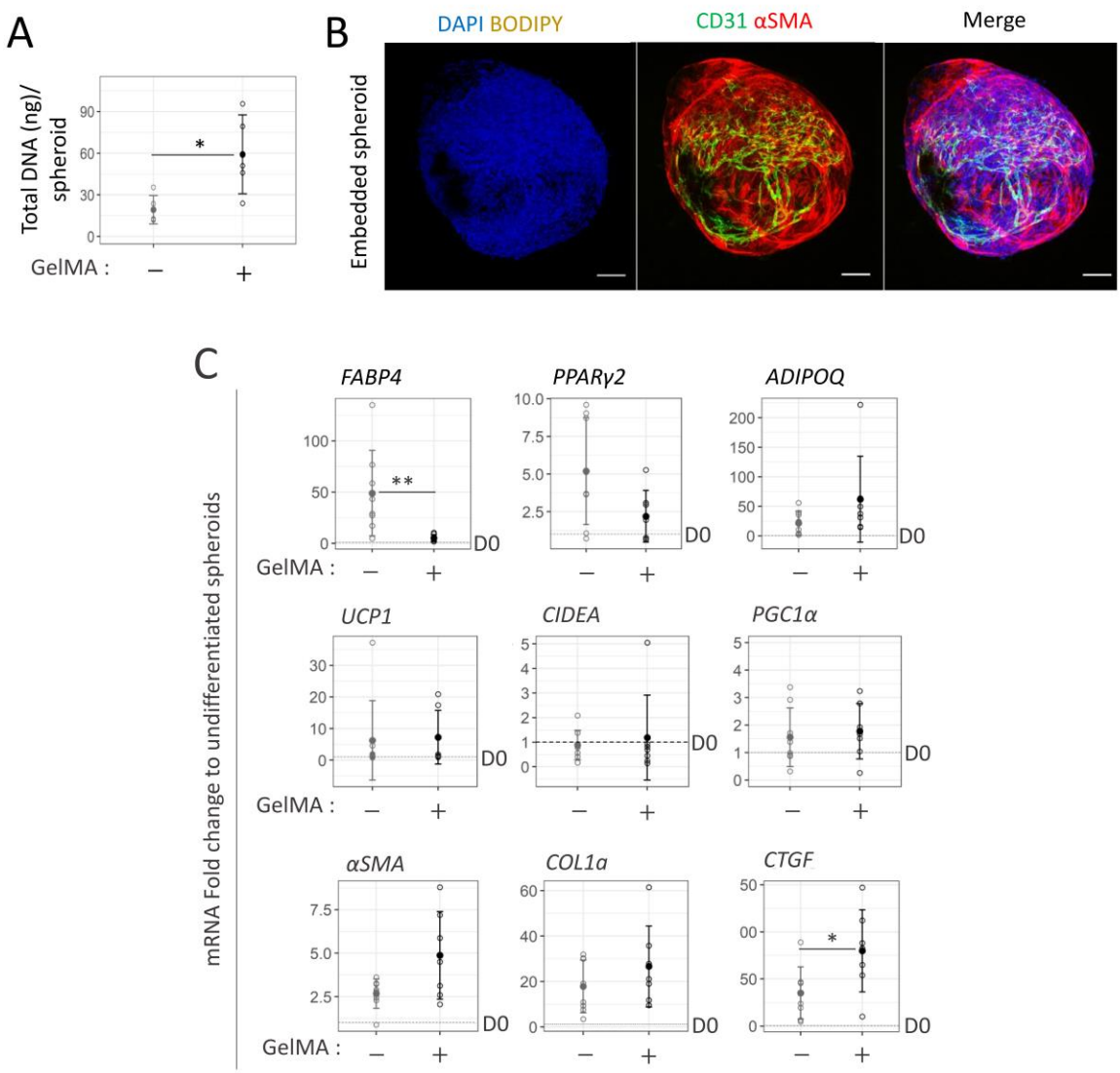

Figure S2. GelMA 10% embedding promotes cell expansion and vascular formation from P0-SVF cells but is not sufficient to induce adipogenesis in absence of TGFβ inhibition. P0-SVF spheroids embedded or not in 10% GelMA were analyzed after differentiation in adipogenic medium. A) Average DNA content per spheroid (n = 6). B) Immunofluorescence images of lipid-containing cells, endothelial cells and pericytes revealed by BODIPY (yellow), CD31 (green) and αSMA (red) stainings respectively. DAPI staining highlights cell nuclei. Scale bar: 200 µm.C) Gene expression analysis of beige adipocyte markers (*UCP1*, *CIDEA*, *PGC1a)*, generic adipocyte markers (*PPARγ2*, *FABP4*, *ADIPOQ*) and myofibroblast markers (*αSMA*, *COL1a*, *CTGF*).

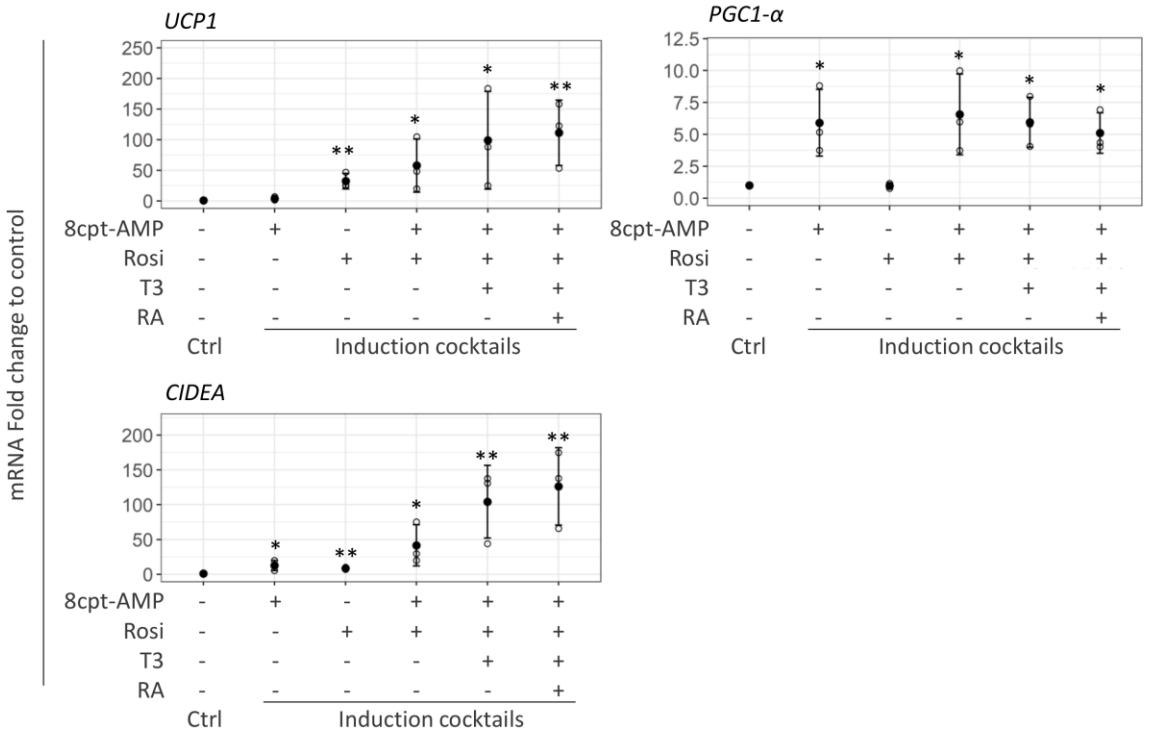

Figure S3. **Gene expression response of P0-SVF beige adipose organoids to combination of UCP1 inducers.** Beige adipose organoids derived from P0-SVF cells were treated (induction cocktails) or not (Ctrl) with combinations of UCP1 inducers for the last three days of culture. 8cpt-AMP: 200 µM, rosiglitazone (Rosi): 1 µM, triiodothyronine (T3): 0.2 nM, all-trans retinoid acid (RA): 0.1 µM. Analysis of brown adipocytes markers (*UCP1*, *CIDEA*, *PGC1α*). Fold changes are expressed relative to controls (n=3). All quantitative data are expressed as mean +/- standard deviation. Statistical analysis of fold change to control was performed by one sample t-test. Statistical significance: * $p \leq 0.05$, ** $p < 0.01$

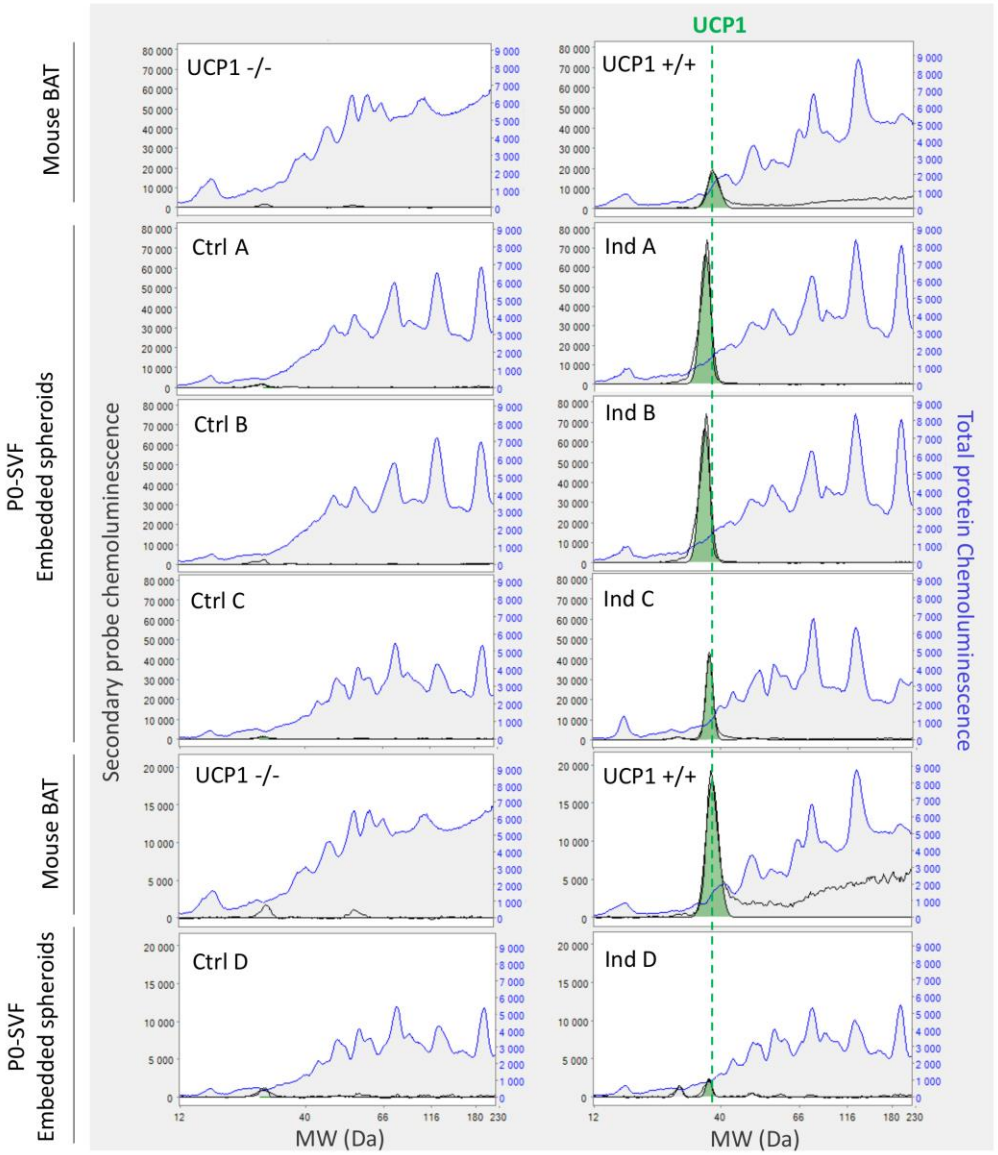

Figure S4. Characterization of UCP1 expression in P0-SVF organoids by proteinSimple capillary electrophoresis immunoassay under control (Ctrl) or induction (Ind) conditions. Brown adipose tissues from wild type mouse (BAT UCP1 +/+) and UCP1 KO mouse (BAT UCP1 -/-) were used as positive and negative controls respectively. Data are shown as chemiluminescence chromatograms of anti-UCP1 antibody signals (secondary probe chemiluminescence) and total protein chemiluminescence from four different human donors. Fitted specific UCP1 peak is highlighted in green.

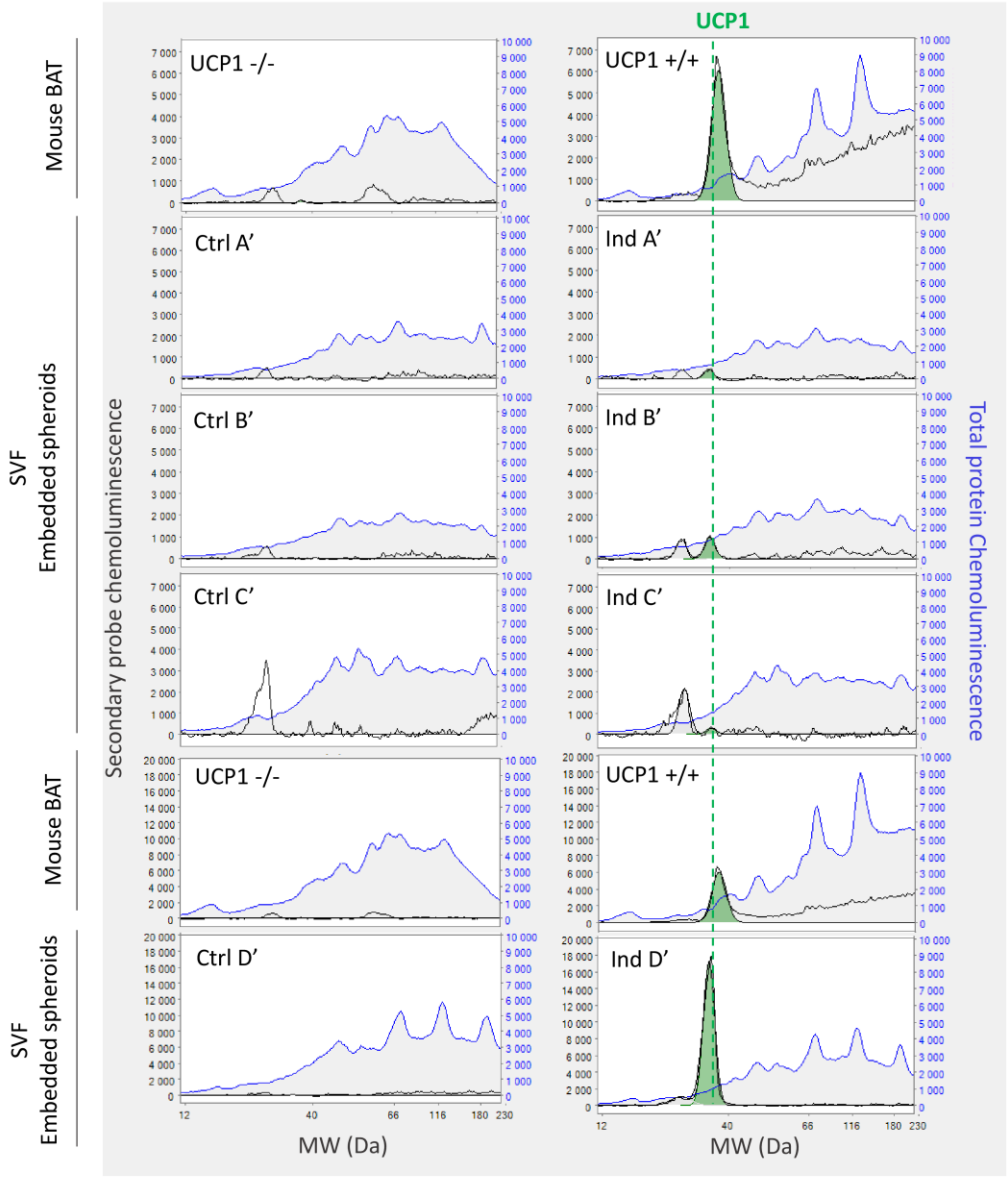

Figure S5. Characterization of UCP1 expression in SVF organoids by proteinSimple capillary electrophoresis immunoassay under control (Ctrl) or induction condition (Ind). Brown adipose tissues from wild type mouse (BAT UCP1 +/+) and UCP1 KO mouse (BAT UCP1 -/-) were used as positive and negative controls respectively. Data are shown as chemiluminescence chromatograms of anti-UCP1 antibody signals (secondary probe chemiluminescence) and total protein chemiluminescence from four different human donors. Fitted specific UCP1 peak is highlighted in green.

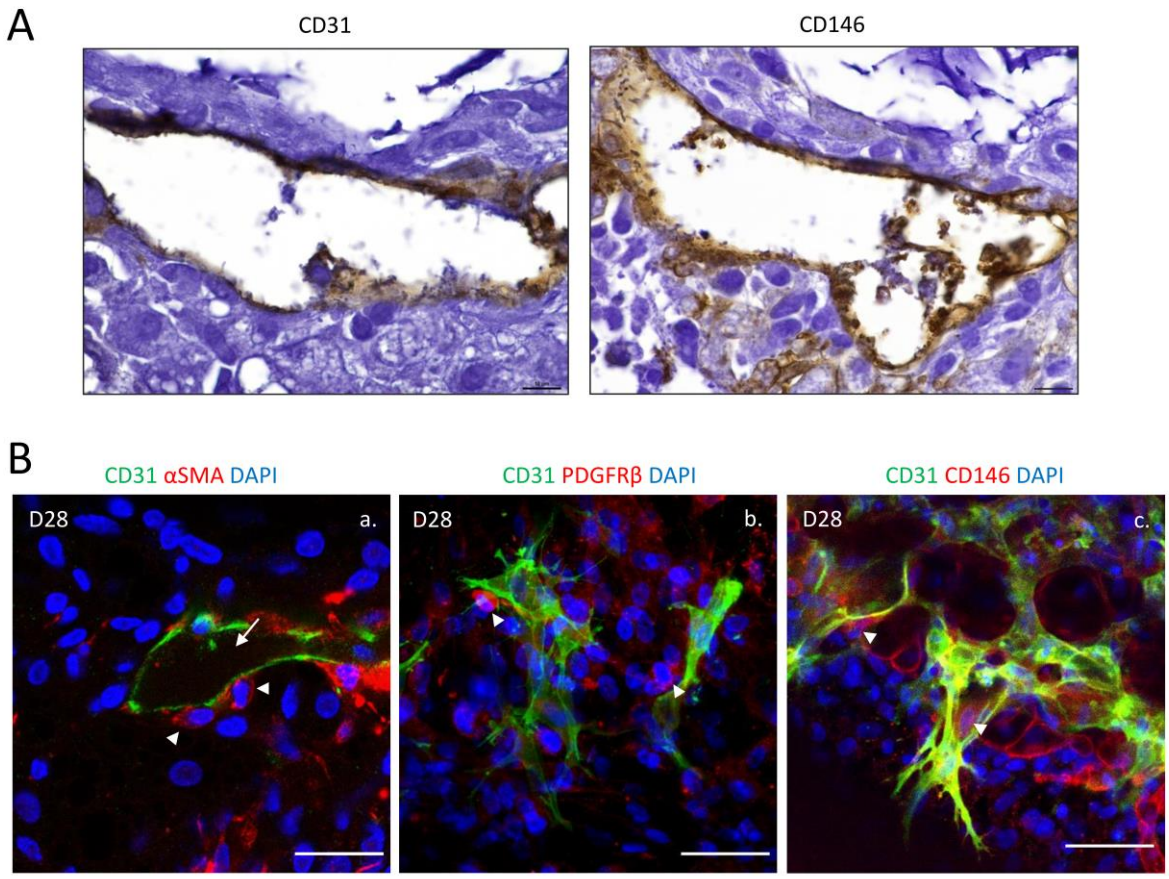

Figure S6: Characterization of vascular lumen formation and perivascular cells within P0-SVF beige adipose tissue organoids. A) Specific anti human CD31 (left) and CD146 (right) were used to characterize the blind developing vascular channels on serial 3 µm sections. The brown positive labelling highlights the positivity of cells delimiting the vascular lumen. Scale bar: 10µm B) Expression of perivascular cells markers was analyzed by immunofluorescence within P0-SVF organoids at the end of the differentiation using confocal imaging. Specific antibodies against human endothelial cell marker CD31 (green) was used in combination of α-smooth muscle actin (SMA) (panel a, red), PDGFRβ (panel b, red) or perivascular and endothelial cell marker CD146 (panel c, red) antibodies. DAPI staining highlights cell nuclei. αSMA expressing cell (panel a, white arrowheads) in close association of endothelial cells showing lumen formation (white arrow) was observed. Some PDGFRβ+ cells (panel b, white arrowheads) associated with CD31+ endothelial cells were also found. Some CD146+/CD31- cells (white arrows) were also observed closely associated to CD31+/CD146+ endothelial cell network. Scale bar: 50 µm.

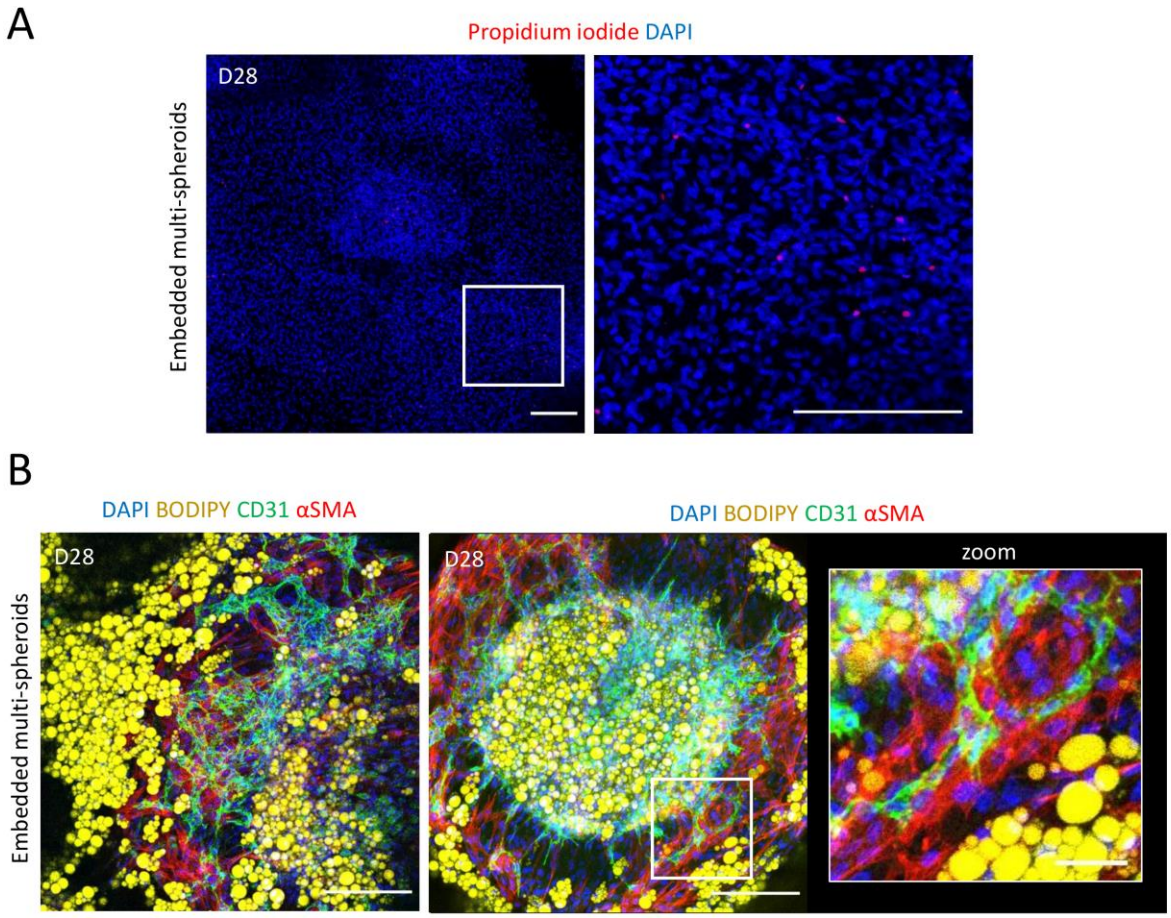

Figure S7. Immunofluorescence characterization of embedded multi-spheroids derived from P0-SVF cells A) Representative confocal images of propidium iodide (Dead cells in red) staining in regards to DAPI (blue) staining within embedded multi-spheroid at day 28. Scale bar: 200 µm. B) Immunofluorescence analysis of P0-SVF embedded multi-spheroids at the end of the differentiation. Specific antibodies against human endothelial cell marker CD31 (green) and α-smooth muscle actin (SMA) (red) were used. Lipids containing cells were revealed by bodipy staining. DAPI staining highlights cell nuclei. Scale bar: 200 µm. Images are two representative areas of embedded multi-spheroids. White squared image shows zoomed area. Scale bar: 50 µm.

2. Discussion and perspectives

2.1 Engineered organoids as physiological mimicking of human beige adipose tissue

We have described innovative methods for the generation of vascularized human beige adipose organoids and micro-tissues using freshly isolated or amplified SVF cells. Through this study, primary focus was given to the characterization and functionality assessment of adipocyte and vascular compartment. In regards to these cellular compartments, organoids were shown to recapitulate cellular architecture and key functions of native thermogenic AT. Here we propose further directions to complete validation of physiological relevance of these novel human beige adipose tissue models.

Further characterization of organoids cell heterogeneity and dynamic

AT are complex organs, in which immune, nervous and endothelial cells together with adipose lineage cells form a dynamic ecosystem that supports tissue integrity and plasticity. Preserving this diversity of cells and their dynamic interactions is essential when developing in vitro models that aim to replicate native tissue physiology. Such endeavors have been described in the literature for the generation of complex 3D WAT models recapitulating non-adipose cell compartments such as endothelial cells [322] or immune cells [340]. However, models of thermogenic fat mainly rely on differentiation of adipose progenitors in the absence of other cellular compartments, even more so with human cells. Recent approaches have been described to obtain vascularized thermogenic AT constructs [24,342] but rely on the use of explant-based methods difficult to adapt for flexible generation of AT constructs. Also, most models lack the immune cell compartment, in which macrophages were recently demonstrated to participate in the regulation of thermogenic activity in brown and beige AT.

For the generation of tissue construct recapitulating native dynamic cellular ecosystem, choice of cell sources is utterly important and would require heterogeneous cell sources. The stromal vascular fraction (SVF) of adult AT constitutes a unique and convenient source not only of adult adipose stem cells but also of different cell types including endothelial and immune cells. Here, we have demonstrated that beige adipose organoids derived from both freshly isolated or amplified SVF cells displayed premature vascular and perivascular compartments in close association with adipocyte clusters mirroring cellular architecture of native adipose tissue. However, immunofluorescence analyses have unveiled the existence of unmarked cells within organoids. These cells may correspond to more immature state of vascular and adipocyte lineages or they can also indicate the presence of other cell type lineages. This indicates that organoids hold potential for recapitulating AT cellular ecosystem beyond mature adipocytes and endothelial cells. More in-depth characterization of organoids at the population and single cell levels using cytometry or transcriptomic analysis are

required to better characterize cell heterogeneity within organoids. This would help to identify whether organoids contain non-adipose and non-vascular compartments but also diversity of cell types and maturation states within each compartment.

Preliminary assays of cell populations characterization using cytometry within organoids have met technical challenges. Nevertheless, preliminary cytometry data indicate the presence of CD45+ immune cells within human SVF-derived spheroids maintained in beige adipogenic medium (data not shown), consistent with generation of SVF-derived adipose spheroid containing immune cells in mice [340]. This suggests that 3D culture allows to maintain immune cell compartments present in freshly isolated SVF cells. Additional experiments and protocol improvements are required to validate the presence and significance of immune cells in spheroid models and to investigate their presence in organoids.

In addition to the immune cell compartment, further attention should be given in the adipocyte lineage. Adipocyte compartment of beige adipose tissue displays inherent heterogeneity regarding all stages of adipocyte differentiation. Such heterogeneity was observed in the UCP1 expression of adipocytes within activated beige adipose organoids suggesting the presence of “true” white adipocytes and beiges adipocytes able of thermogenic activation. The source of beige pre-adipocyte development in WAT, whether it arises from dedicated beige precursors or shared white/beige precursors, remains a subject of debate [228]. Characterization of adipocyte and adipose progenitor populations and their heterogeneity at the single cell levels at different times during organoid development may provide insight on human beige adipocyte development which is still poorly understood. Due to the fragility of adipocytes upon cell isolations processes, such characterization would require single nuclei RNA sequencing approaches as it has been described for the characterization of adipocyte population within human BAT deep neck biopsies [346]. This approach would also allow for extensive characterization of non-adipose-related cell populations as an alternative to cytometry. Furthermore, maintaining progenitor pools is a crucial aspect of organoid systems to ensure their long-term culture and function. Mandl et al. demonstrated the persistence of quiescent ASC populations within adipose organoids derived from ASC spheroids of white adipose tissue origin using cell colony formation assays [347]. A similar approach can be applied to beige adipose organoids to investigate the presence of stem cell populations and evaluate their proliferation capacity. Additionally, if ASCs can be derived from beige adipose organoid digestion, it would be valuable to assess their potential for beige adipogenesis and compare it to white adipose tissue-derived ASCs to determine whether beige adipose organoids favor the generation of a beige adipose progenitor niche.

Further characterization of organoids functions

Such as mentioned in Introduction IV, thermogenic fat are important regulators of systemic metabolism through their metabolic and secretory functions. Beige adipose organoids recapitulate key metabolic features supporting thermogenic activity including inducible UCP1 expression associated with uncoupled respiration, glucose uptake and lipolysis activation. A distinctive aspect of our research is the evaluation of endocrine activity, which is often neglected when assessing thermogenic adipose tissue models, particularly in 3D models. Upon activation, organoids recapitulate increased paracrine secretion of some batokines. Further metabolomic and proteomic analysis of these secretions using high-resolution mass spectrometry-based approaches would be of valuable information to compare with established secretomes of differentiated human brown and white adipose progenitors [348]. Proteomic-mapping of matched conditioned media from activated and unactivated beige adipose organoids could allow to identify novel factors implicated in thermogenic activation of beige adipocytes. One role of batokines is to promote BAT expansion and browning of WAT. Using conditioned media from activated organoids, their efficiency to induce thermogenic activation through paracrine communication can be evaluated on unactivated organoids or models of WAT. These conditioned media can be further used to dissect the role of batokines in inter-organ communications through cell treatment approaches using non-adipose cell models.

Another important functional aspect of brown and beige adipose tissue is their responsiveness to environmental changes allowing metabolic adaptation of the organism. An originality of this work is the evaluation of beige adipocyte activation with rather acute stimulation compared to other existing 3D models of human thermogenic AT. In previous studies, thermogenic adipocytes were generated using differentiation media containing beige/brown inducers like rosiglitazone for extended periods (over a week) and were then compared to undifferentiated cells or white adipocytes obtained through different protocols [23,24,349]. Consequently, these studies did not fully explore the plasticity of beige adipocytes. *In vivo*, environmental conditions such as cold exposure are relayed to adipocytes through adrenergic stimulation by the sympathetic nervous system. In our research, we targeted signaling pathways downstream of beta-adrenergic receptors, mimicking the increased levels of cAMP typically induced by their activation. Similar approaches have been used to assess browning plasticity in other 2D models of human adipocytes, especially those derived from ASCs of WAT [21,350]. Although thermogenic activation by beta-adrenergic agonists is well-established in mice [313], its applicability in humans is more debated [314–316]. Besides, low expression of β-adrenergic receptors has been observed in adipocytes derived from SVF of WAT [351]. This may explain the use of non-adrenergic thermogenic inducers in previous literature. Very preliminary testing of treatments with specific and

nonspecific β-adrenergic agonists as replacements for our induction cocktail did not result in UCP1 induction within organoids. Further drug screening and characterization of beta receptor expression within beige adipose organoids would be required to evaluate whether they can also recapitulate adrenergic dependence of thermogenic activation from native adipose tissue.

Although work remains to be done to further validate their physiological relevance, these organoids represent one of the most advanced human beige adipose tissue models available. Systematic comparison of engineered tissue construct with native material is limited for human beige AT as data on thermogenic human fat are derived from BAT biopsies or indirect techniques such as MRI or PET-scan which do not inform on cell tissue identities and organization. Nevertheless, comparison with transcriptomic and proteomic signatures of human BAT, WAT [21,352–354] as well as murine beige AT [355] would help to position human beige adipose organoids to these references. Besides, this work paves the way for physiopathological studies. Generating organoids from lean and obese patients from various ages may help to understand whether obesity and aging-related deficiencies in thermogenic fat stem from impaired resident progenitor development and function. Additionally, these beige adipose organoids can be integrated with other 3D models like neural, muscle, or cancer spheroids through microphysiological systems or assembloid approaches to investigate inter-organ communication in both physiological and pathological thermogenic activation.

2.2 Generalization of the 3D microenvironment engineering approach to other tissues and systems

The success in producing functional adipose tissue organoids relied on the pre-aggregation of cells within an appropriate microenvironment. Even though the features of this environment were originally tailored for adipose tissue generation, we think that some general principles and hypotheses from the results we have obtained for *in vitro* tissue development can be extracted.

Deciphering the role of TGFβ inhibition in ASC differentiation: Implications of 3D structuring on modulation of chemical environment for specific cell type development

In the absence of a perfused vasculature, 3D cell microenvironments inherently include relative hypoxia and increased cell tension, both of which are known to impact the paracrine secretion of MSCs. While hypoxia is known to promote TGFβ secretion from MSCs [356], activation of mechanotransduction pathway by forces exerted on cells by cell-matrix interactions can promote differentiation of MSC into myofibroblast [357], also known to secrete TGFβ. Besides, it is known that treatment of ASC with TGFβ promotes their differentiation into myofibroblast [358]. As differentiation

of ASC into myofibroblast is done at the expense of adipocyte differentiation, this could explain the requirement of TGFβ inhibition to promote adipogenesis in 3D compared to 2D cultures.

This study highlights that when employing models that involve MSCs or fibroblast-like cells, it is critical to consider the 3D microenvironment and the development of tension that may directly promote a myofibroblastic phenotype [356]. This highlights the key importance of inhibitions in regulating developmental processes. The creation of a permissive microenvironment, essential for the development of complex 3D tissues in vitro, also implies the creation of a non-permissive microenvironment for certain cell types. Addressing this concern may entail TGFβ inhibition independently to adipose tissue context. Indeed, as for P0-SVF derived spheroids, inhibiting TGFβ significantly limited spheroid shrinking and cell loss from SVF-derived spheroids even though it did not correlate with adipogenesis initiation. This suggests that inhibition of myofibroblastic phenotype through TGFβ inhibition may play a role in enhancing cell survival and organization independently of adipocyte differentiation. This approach might be relevant for various 3D models of mesenchymal tissues, provided that its impact on the specific cell compartments necessary for a particular tissue target is carefully evaluated.

Understanding the role of hydrogel in cellular organization

Engineering approaches for recapitulating native tissue microenvironment entail to introduce ECM mimicry through the use of biomaterial, especially hydrogels. Matrigel, an undefined mixture of ECM and growth factors, is often a critical component of organoid culture. It is well acknowledged that its presence is essential for the development of complex structures like the budding of intestinal organoids. However, due to Matrigel undefined composition, few studies consider the significance of this result in understanding the role of the biomaterial and its properties in organoids emergence.

A comparison between spheroid and our organoid models obtained from hydrogel-embedded spheroids reveals how providing a matrix environment can affect cell distribution. In spheroids, vascular and adipocyte compartment were found in distinct locations with vascular compartment in the inner part of the spheroids while adipocytes were located at the periphery of the spheroids. It is known that in spheroids, cells can rearrange themselves by cell sorting processes which result in cell types distributed into concentric layers of cells based on adhesiveness but also gradient oxygen diffusion [139,157]. While hypoxia promotes angiogenesis, it inhibits adipogenesis [359]. It could explain why endothelial cells could be found closer to the center of the spheroid which might be more deprived of oxygen while adipocytes developed from ASC closer to the oxygen rich peripheric environment of the spheroid. Hence, in spheroid configuration, distribution of specialized cell

compartments seems to be primarily influenced by the initial cell distribution and the diffusion gradients inherent to 3D organization. Conversely, in presence of hydrogel, equivalent undifferentiated spheroids reproducibly developed into organoids configuration where vascular and adipocyte cell populations could be found in close association with a structure closer to native tissue. This highlights the importance of the matrix compartment to promote dynamic cell rearrangements for the emergence of complex tissue architecture.

What is the role of the matrix in facilitating these cellular rearrangements, and how its chemical and physical parameters impact these processes?

Large-scale rearrangements of cell distribution are typically described as morphogenetic movements during development. These cell rearrangements are essential in tissue shaping by allowing interactions between cell compartments that were initially separated. These morphogenetic mechanisms involve collective cell migration and its regulation through dynamic change of cell-cell and cell-matrix interactions. In embryos, tissue patterning and morphogenesis are thus dependent from the progressive secretion of ECM by cells which introduce cell-matrix coupling as development progresses. Although secretion of matrix by spheroid cell has been described, it might be insufficient to counterbalance cohesive cell-cell interactions induced by cell aggregation and promote long-range rearrangement of cells. Hence, as previously proposed in existing literature, providing cells with ECM mimicry may be regarded as a method for creating a matrix compartment that can serve as physical support for cell migration, compensating for inadequate matrix secretion by the cells during early tissue development.

Moreover, morphogenetic cell processes that give rise to tissue shaping require cell response dynamics with constant remodeling of the environment. Providing aggregated cells with a hydrogel environment can be interpreted as a mechanism for disrupting cell cohesion and promoting dynamic cell movement through heterogeneity in cell-cell and cell-ECM interactions. It is important to note that spheroid cells within a hydrogel are not equally exposed to the same balance of cell-cell vs cell-ECM interactions as only cells at the periphery of the spheroids can initially interact with the matrix. This local and heterogeneous mechanical coupling of cells within spheroids differs from cell suspension dispersed in a hydrogel surrounded by a similar mechanical environment and more closely correlates with recent approaches of local high-density cell injections within hydrogel [30,31]. These approaches have demonstrated impressive potential to drive tissue morphogenesis, we can thus hypothesize that introducing imbalance between cell-cell and cell-matrix interactions may be a critical factor to initiate symmetry breaking and induce collective morphogenetic cell movements.

This study also gives some insight on which parameters might affect cell distribution within 3D matrices to promote cell rearrangement over time. Within GelMA hydrogel, GelMA concentration is negatively correlated with its porosity and degradation speed [360,361]. In most GelMA conditions we tested, we observed a heterogeneous colonization pattern within the GelMA droplet after the proliferation phase. This included both multi-layers of cells located at the periphery of the droplet and a cell mass within the droplet. This cell mass corresponded to the initial spheroid whose expansion increased with reducing GelMA concentration. This colonization heterogeneity suggests two modes of cell migration within the hydrogel: individualized migration of cells from the spheroids to the surface and collective migration of spheroid cells remaining connected to each other. Colonization of the GelMA surface may result from cells migrating along diffusion gradients toward nutrient and oxygen rich areas. On the other hand, the expansion of the inner cell mass in response to lowering GelMA concentration may indicate a positive effect of increased porosity on promoting collective cell development within the hydrogel. However, lowest GelMA concentration tested led to rapid loss of the matrix compartment which promoted rearrangement of cells into a configuration close to spheroid. This highlights the requirement of adequate hydrogel mechanical integrity to sustain the matrix compartment over a period of time compatible with tissue construct generation. Therefore, we can propose that creating an optimal hydrogel environment for facilitating cell rearrangement involves finding a balance between the biophysical properties of the hydrogel. This balance should support cell migration without imposing mechanical constraints while maintaining enough mechanical integrity for cells to reshape their surroundings without causing the hydrogel to collapse.

Cell microenvironment is typically subdivided into two main components: biochemical and biophysical environments, respectively targeted in tissue engineering approach by providing cells with growth factors and ECM-like biomaterial. In respect to this avenue, this study demonstrates that transitioning from 2D to 3D culture requires careful culture media optimization. This study also underscores the critical role of the matrix environment in cellular organization, emphasizing the need to optimize matrix properties for the development of tissue models that closely mimic native tissue architecture and function. However, through this study we can propose that culture media may also be used to modulate biophysical aspect of the microenvironment such as cell tension through promotion or not of certain cell type development while the effect of the biomaterial can also be understood in its effect on chemical factors distribution. In particular, the observations of spheroid cell colonization within GelMA droplet raised multiple fundamental questions regarding the impact of cell-cell vs cell-matrix interactions as well as the impact of mass transport on initiation of collective cell behaviors that can lead to tissue structuration. How to address these questions will be the focus of the following section. While initially optimized for adipose tissue generation, multipotency of ASC and easy tunability of

GelMA hydrogels make this engineering approach transposable for other tissue generation. This underscores the potential of this system to address essential aspects of tissue generation beyond adipose tissue.

II. Preliminary development of cell culture system to study spheroid cell rearrangement in response to mass transport and matrix compositions

1. Objectives and hypotheses:

Our observations have revealed that providing cellular aggregates with surrounding hydrogel plays a pivotal role in driving the necessary cellular rearrangements for the formation of tissue architecture. To gain a deeper understanding of this process, it is essential to explore how this biomaterial influences these cellular rearrangements and to pinpoint the specific parameters that can be adjusted to either facilitate or constrain these cellular movements.

What are the biophysical and biochemical parameters controlling the distribution and evolution of cell organization from a cellular aggregate within a matrix environment?

Spatial rearrangements of cells involved several cell processes including cell survival, cell proliferation and cell migration which alter the number and spatial distribution of cells. Therefore, addressing the question of factors that govern cell distribution within a hydrogel primary encompass investigating the factors that oversee these cellular processes in 3D matrices. Within a 3D matrix environment, proliferation and migration entail morphological changes in cells, cell-cell and cell-matrix interactions, matrix remodeling, as well as accessibility to soluble factors (e.g. oxygen, nutrients, and growth factors). Thus, understanding how to promote these cellular movements essentially involves exploring how the 3D environment, especially the matrix, can influence and regulate these factors and their dynamics. It is worth noticing that these factors will also strongly influence the long-term behavior of cells comprising their differentiation and further spatial arrangement but as a first instance our motivation is to understand the mechanisms involved in the early stages of the tissue development.

In a situation where a spheroid is surrounded by a layer of hydrogel exposed to a culture medium, we can theorize that spheroid cells are subjected to the interaction of multiple gradients of factors (Figure 32) including cell-cell, cell-matrix interactions and mass transport. Furthermore, the 3D matrix serves as both a supportive structure, based on cell adhesiveness to the matrix, and an obstacle on all cell surfaces during their movement within the environment. The question then arises of how a cell migrating from a spheroid will respond to these gradients in a matrix environment that simultaneously supports and constrains migration.

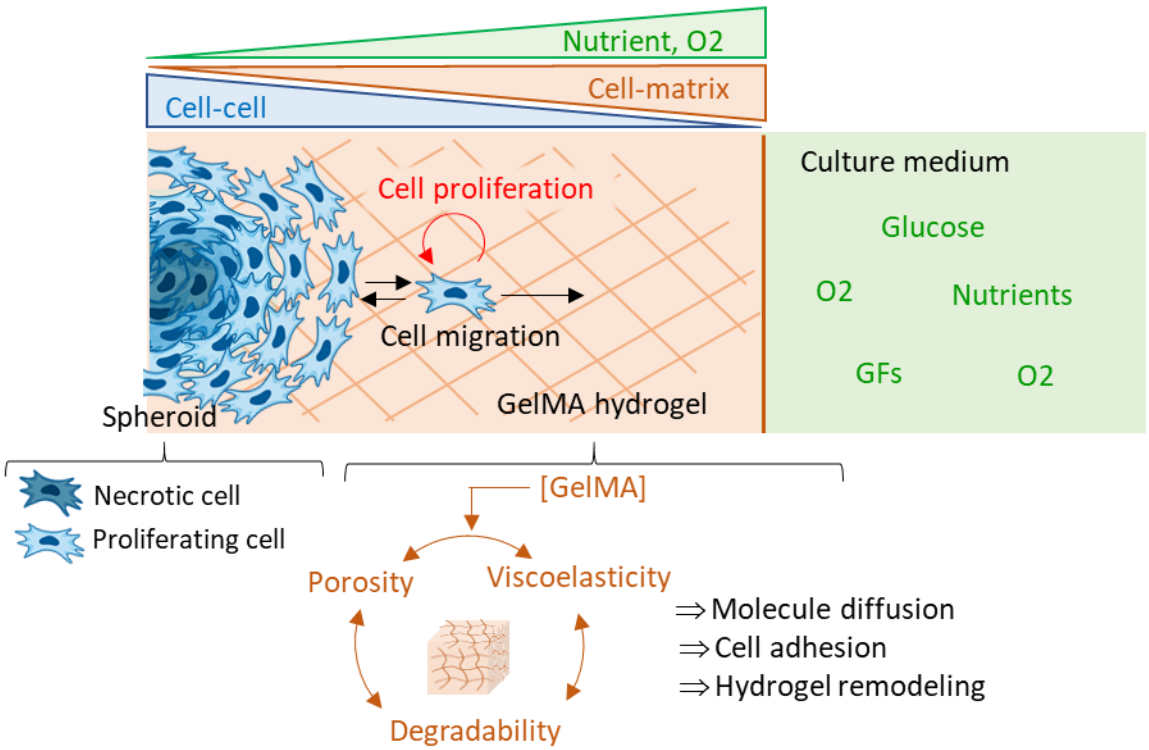

Figure 32. Within 3D matrix migration of spheroid cells are influenced by asymmetric distribution of driving forces including cell-cell, cell-matrix interactions and soluble biochemical factors availability. Distribution of these gradients and their dynamic remodeling by the cells would be dependent on hydrogel composition and its subsequent biophysical parameters which are coupled to each other (e.g. porosity, viscoelasticity and degradability).

In our experiments, heterogeneous patterns of colonization were observed including areas of colonization within the hydrogel and peripheral colonization on the GelMA surface. Accumulation of cells at the surface was observed regardless of the GelMA concentration. The surface can be perceived as an area rich in oxygen and nutrients, as well as a region where cells can migrate without physical constraints imposed by the hydrogel. Conversely, the colonization of cells within the gel was favored by a decrease in GelMA concentration, which is known from the literature to correlate with increased porosity, gel degradability, and reduced gel stiffness [360,361]. These conditions could thus facilitate lower mechanical resistance to migration while promoting mass transport. Consistently, the softening of the hydrogel was shown to promote the proliferation of cancer cells compared to stiff hydrogel in 3D while at a given stiffness increased viscoelasticity promoted faster cell spreading and migration [362].

Therefore, we can hypothesize that the colonization of cells from a cellular aggregate within a matrix environment will depend on **interactions between mass transport, the biophysical parameters of the hydrogel, hydrogel remodeling by cells and cell-cell interactions**. These interactions can be understood as the following:

- the interaction between mass transport, matrix volume and the initial porosity of the hydrogel that will govern nutrient and oxygen gradients
- the interaction between cell-matrix adhesiveness, local rigidity of the matrix, hydrogel porosity, hydrogel viscoelasticity and degradability that will govern the compromise between physically supporting cell spreading and mechanically constraining cell movements in a dynamic manner

- balance between cell-cell interactions and cell-matrix interactions that will govern collective cell rearrangement over single cell migration

In order to address these hypotheses, we aim to develop a cell culture device that would enable a certain control of these parameters for a more precise examination of their impact on the colonization of spheroid cells within hydrogel. Main requirements that drive the device development are:

- Providing control over the position of spheroids relative to the interface between the medium and the hydrogel to regulate the impact of matrix volume on mass transfer for a given hydrogel composition
- Providing control over the position of spheroids relative to each other when considering multi-spheroid setting
- Ensuring that spheroids are surrounded by a defined matrix environment
- Enabling monitoring of cell morphological changes and spreading from the spheroids over time

It has to be noted that biophysical parameters including porosity, cell adhesiveness, degradability and viscoelasticity are often coupled within hydrogels and their decoupling requires careful modification of polymeric architecture. By modifying monomer concentrations or reticulation protocols, these physical parameters can be varied all at once (Figure 32). For GelMA hydrogel, modulation of GelMA percentage and photo-polymerization duration allow to generate hydrogel from soft highly degradable and porous hydrogel to stiff hydrogel with low porosity and degradability. Therefore, using such a system with various GelMA compositions can be used as a first basis to understand the overall effect of hydrogel porosity and degradability on spheroid cell colonization. More in depth characterization of

the influence of each biophysical parameter of hydrogel on cell distribution would require chemist expertise for the potential modification of GelMA polymeric architecture or use of polymers combinations.

2. Device design and first development steps

To achieve this objective, we chose to adapt a cell culture chip device previously developed within the laboratory in the collaboration with IRSD by Audrey Ferrand and Duvan Rojas Garcia for the study of intestinal development (Patent N° 21305235)[363]. This culture chip, composed of two glass coverslips held together by a frame (Figure 33A), allow hydrogel molding and culture monitoring through imaging.

In our case, this chip offers several advantages. It can be used to unilaterally expose the system to a culture medium to create a hydrogel/medium interface (Figure 33A), enable photopolymerization of GelMA directly within the chip to control the matrix environment, and allow for culture monitoring through imaging.

A hydrogel molding approach was developed to control the positioning of spheroids within GelMA. The principle involves generating a two-layered patterned GelMA in which cavities of specific thickness and depth within GelMA hydrogel (Figure 33A). Generation of these patterns requires pattern molding in a first layer of GelMA using photopolymerization and designed molds (Figure 33B). After demolding, spheroids are deposited, and the cavities are filled with new GelMA solution (Figure 33B).

A first design that we have considered consist in simple cavity (Design 1) in which variation of cavities depth allow to adjust the distance of the spheroid to the GelMA-medium interface (H1), while the GelMA environment can be modified using different GelMA compositions (Figure 2A). On one hand, this approach allows for the study of spheroid cell colonization within a matrix compartment with variable porosity but defined geometry. On the other hand, by creating two matrix compartments, it enables the investigation of the impact of the presence of interfaces between two hydrogels on spheroid migration. This distance of the spheroid to the GelMA/GelMA interface (H2) can be modulated by adjusting cavity thickness (Figure 33A). In a recent study, authors observed that within a hydrogel, spheroid cells adopt different migration paths depending on the proximity of a spheroid to an interface, either medium/hydrogel or hydrogel/hydrogel interfaces [364]. Here, using such a system, a more systematic analysis of the effect of these distances on spheroid cell behavior can be planned. To reduce the influence of the hydrogel/hydrogel surface on the investigation of cell migration in response to H1 variations, we suggested a design featuring interconnected double cavities (Figure 33A, design 2). This design comprises a larger top cavity that defines H1 and H2 dimensions and

a narrower bottom cavity intended to secure the spheroid position while exposing both its top and bottom portions to the inner matrix compartment.

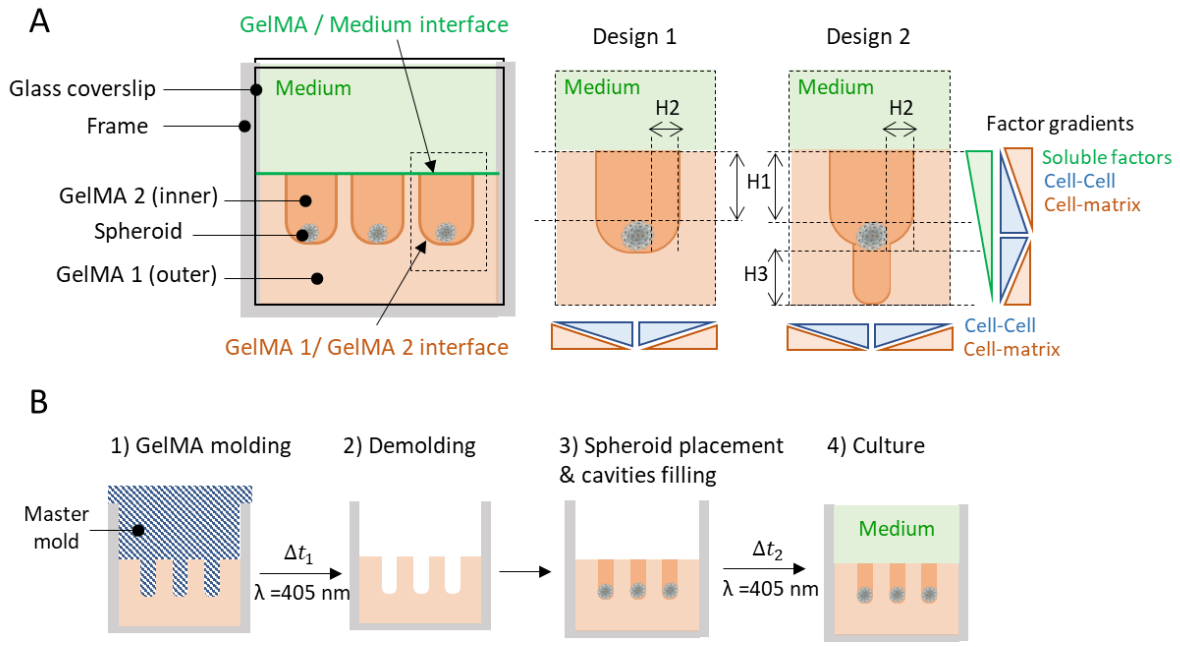

Figure 33. Design of cell culture chip and principle of GelMA patterning to study impact of mass transport, matrix composition and hydrogel interfaces on spheroid cell colonization. A) Design of cell culture chip and GelMA patterns. Chip are composed of two glass coverslips (20x20 mm) held together by a 3D printed frame (DS3000). Chips are filled with 3 compartments: a medium compartment and two matrix compartments composed of a layer of GelMA (GelMA 1) patterned with cavities and cavities filled with spheroid and GelMA (GelMA 2). Design 1: Simple cavity pattern. Design 2: Double interconnected cavities pattern. H1: variable spheroid distance to GelMA/medium interface, H2: variable spheroid distance to GelMA 1/GelMA 2 interface. H3 determined the depth of the lower section of the inner matrix compartment. B) Image of cell culture chip C) Principle of GelMA patterning using molding approach.

To generate cavities with designed dimensions, preliminary development steps have consisted in the generation of molds comprising pillars, using stereolithography (DWS 29J+ printer), whose shape can be replicated in GelMA hydrogel. To ensure correct demolding, mold material should not be chemically reactive to GelMA which preclude the use of acrylate-based UV-curable resins commonly used in stereolithography. On the other hand, based on our prior experience with multi-spheroid constructs (refer to Result I.1), we are aware that PDMS is a suitable material for molding GelMA. Consequently, PDMS was chosen as the mold material. PDMS molds with designed pillars were generated by 3D printing counter-molds, casting PDMS followed by its reticulation and demolding (Figure 33B).

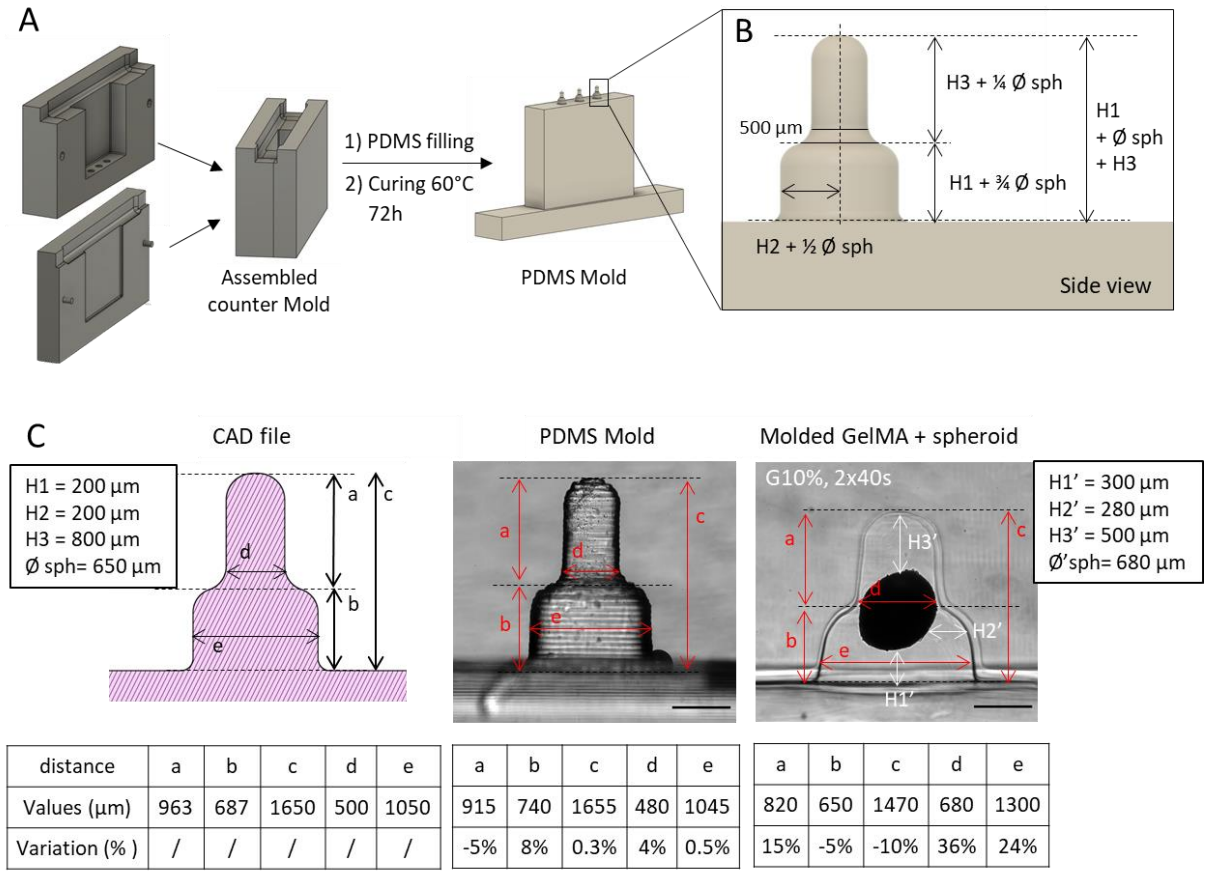

distance	a	b	c	d	e
Values (µm)	963	687	1650	500	1050
Variation (%)	/	/	/	/	/

a	b	c	d	e
915	740	1655	480	1045
-5%	8%	0.3%	4%	0.5%

a	b	c	d	e
820	650	1470	680	1300
15%	-5%	-10%	36%	24%

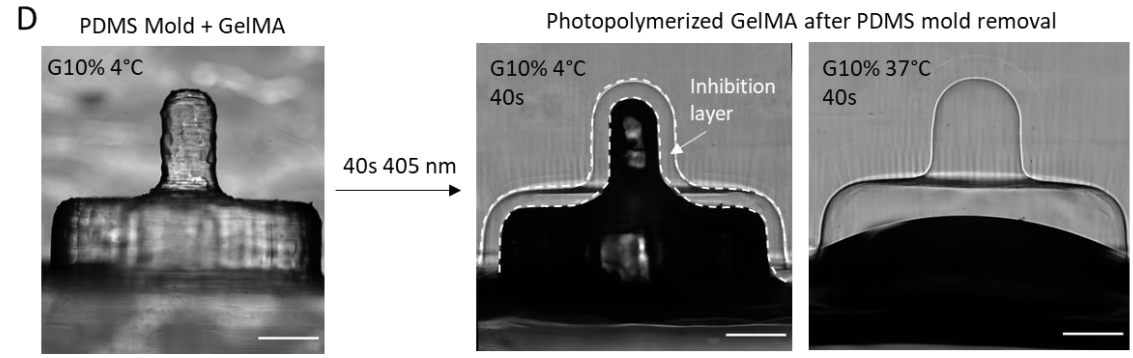

Figure 34. Mold generation and preliminary molding assays. A) Principle of PDMS mold generation. To facilitate PDMS mold removal, counter molds are 3D printed as two parts and assembled together before PDMS pouring. After curing, counter-mold is disassembled to obtain PDMS mold with intended design (CAD file). B) Side view of CAD file of mold for the generation of double interconnected cavities (Design 2). File is zoomed at the level of one pillar and shows how pillar dimensions are linked to intended spheroid distances to interfaces (H1, H2, H3) and average diameter (Øsph) of spheroid. C) Example of dimensions replication from CAD file (left image) to PDMS mold (middle image), to molded GelMA after GelMA filling and spheroid deposition (GelMA 10%, 2x40s of photopolymerization). Tables show expected and measured dimensions highlighted on images. D) Evidence of inhibition layer to photopolymerization in GelMA hydrogel. Scale bar: 500 µm.

Using this approach, we could generate PDMS molds with pillars of different shapes whose height and thickness can be modulated (Figure 34A). Dimensions of pillars are designed by considering average spheroid diameter in addition to intended distances H1 and H2. The design of interconnected cavities considered that a segment of the spheroid enters the lower part to better control spheroid location (Figure 34B). Preliminary tests showed that PDMS mold can replicate CAD file dimensions with less than 10% variations (Figure 34C, left and middle image). Using these molds, GelMA patterns can be generated followed by spheroid deposition (Figure 34C, right image). However, important variations in cavities dimensions from CAD file can be observed in patterned GelMA, especially for widths (Figure 34C, right image). For this reason, spheroids could not be deposited as expected leading to increased dimensions of H1 and H2 compared to intended ones. As PDMS is porous to oxygen, oxygen inhibition may explain the problem of molding fidelity we met within patterned GelMA using PDMS molds. Such photopolymerization inhibition have been described in acrylates hydrogels due to oxygen inhibition [365,366]. This phenomenon was confirmed by additional experiments where demolding of GelMA maintained gelled at 4°C showed that following photopolymerization a layer of GelMA surrounding the PDMS mold was not fully cross-linked (Figure 34D). Further experiments using approaches to lower oxygen concentrations in GelMA are required to confirm this effect and assess whether molding fidelity can be improved. Otherwise, it will be necessary to systematically characterize the width of this inhibition layer depending on patterns in order to recalibrate the mold dimensions accordingly.

Nevertheless, preliminary culture experiments have shown that such systems hold potential to study evolution of spheroid cell colonization within GelMA hydrogel over several days of culture. Spheroids deposited in simple or interconnected cavities and maintained in proliferation medium showed change in spheroid morphology followed by progressive cell spreading from the spheroid (Figure 35). Strikingly, cell colonization was limited to inner matrix compartment suggesting a confinement effect of the GelMA/GelMA interface, as well as the local establishment of a physical barrier to migration. Further characterization of GelMA porosity and stiffness in patterned GelMA are required to assess whether this can be due to a local densification of GelMA networks impairing cell movement. On another hand, first experiments using simple cavity design have revealed that cells adopt different morphology depending on their location within patterned GelMA 10% and 5% as revealed by phalloidin staining (Figure 35A). Cells seemed to adopt more branched structure at the proximity of GelMA/medium interface compared to the cells close to bottom GelMA/GelMA interface. While in GelMA 10% cells seemed to be completely confined by the GelMA/GelMA interface, within GelMA 5% some cells branching could be observed at its proximity suggesting lower cell confinement. Additionally, proliferating cells, revealed by Ki67 staining, seemed to be asymmetrically distributed along cavity depth in GelMA 10% with increased number close to GelMA/medium interface.

Proliferating cell distribution seemed more important and more homogeneous in GelMA 5%. Furthermore, preliminary assay using double cavities design in GelMA 10% showed that spheroid cell seemed to preferentially migrate toward GelMA/medium interface as revealed by absence of cells in the bottom section (Figure 35B).

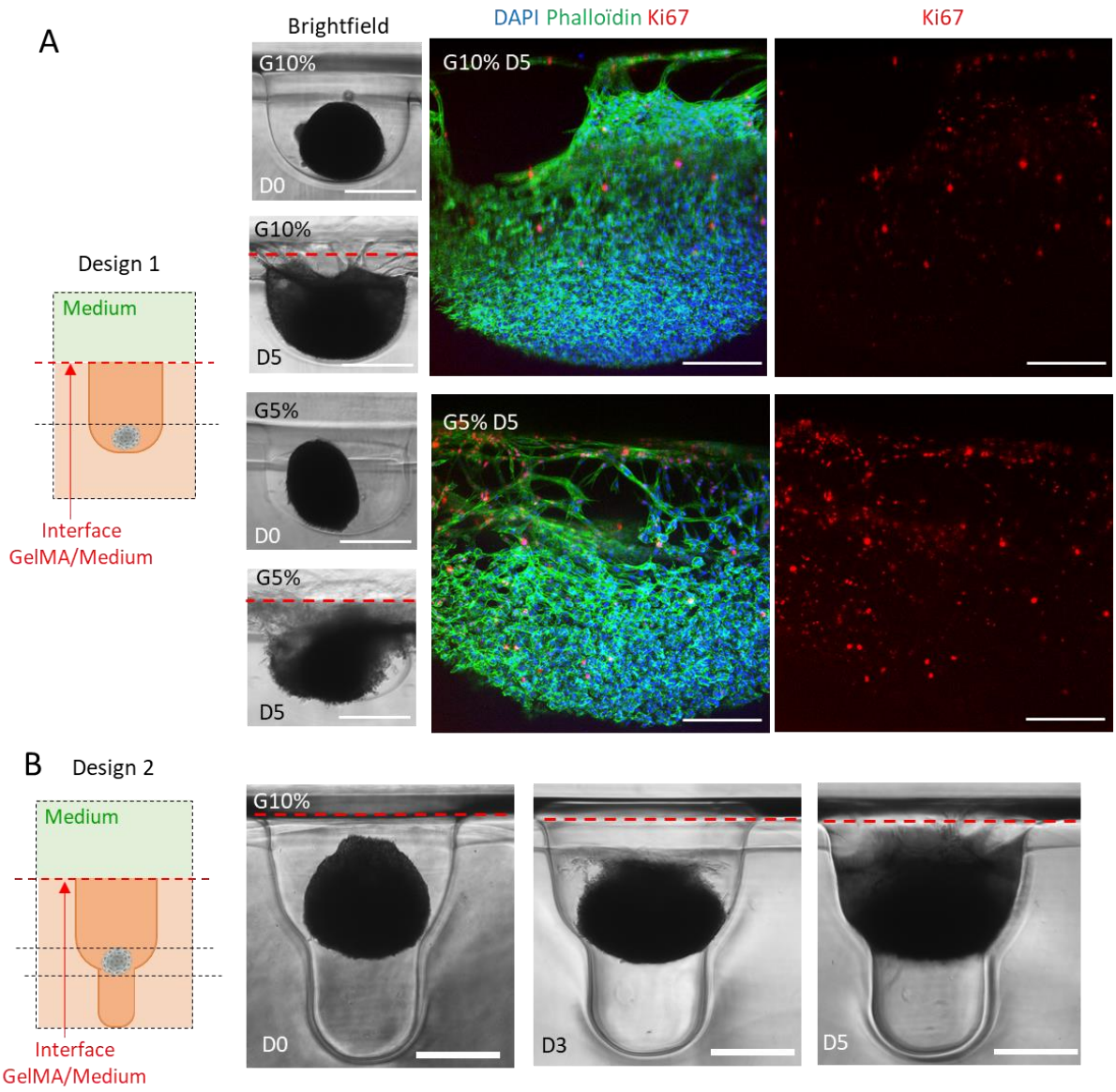

Figure 35. Preliminary assessment of cell culture feasibility in patterned GelMA. Spheroids obtained from amplified SVF cells were seeded in GelMA patterns made of simple cavity (A, Design 1) or double cavities (B, Design 2) and maintained in proliferation medium. A) Confocal imaging of phalloidin and anti-Ki67 staining to respectively assess cell morphology and proliferation within patterned GelMA 10% (top images) or GelMA 5% (bottom images) after 5 days of culture. Scale bar: 200 µm. Left images show brightfield observations at day 0 (D0) or day 5 of culture (D5) for both GelMA compositions. Scale bar: 500 µm B) Evolution of spheroid cell migration in patterned GelMA 10% made of double cavities. Scale bar: 500 µm. Red dotted line indicates theoretical GelMA/medium interface

This study marks the initial efforts in creating a cell culture system for investigating spheroid colonization in 3D hydrogels in response to mass transport and matrix compositions through GelMA molding approaches. Protocols for the generation of patterned GelMA have been partly established. While molds of specified dimensions can be successfully fabricated, their replication within GelMA requires either improved protocols for better control of photopolymerization or molds calibration to compensate photopolymerization inhibition. Despite the need for improved molding protocols, first observations of cell migration and proliferation in preliminary cell culture assays seem to show that cells tend to migrate and more actively proliferate toward GelMA/medium interface which would be consistent with our hypotheses regarding the colonization of cells along accessibility of soluble factors gradient. Lowering GelMA percentage known to increase GelMA porosity [360,361] seemed to favor a more homogeneous repartition and an increased number of the proliferating cells as it has been observed with previously with cancer cells [362]. This would be consistent with the hypothesis that increased porosity may improve accessibility of cells with nutrients and oxygen favoring their organization. Further characterization of molecule diffusion using Dextran of given molecular weight will be conducted to evaluate the effective presence of gradient diffusion within GelMA pattern and how it is affected by GelMA concentration. On another hand, an interesting observation that we can derive from this result is the establishment of a migration barrier at the interface between two GelMA compartments. This might be due to a decreased of porosity due to the interpenetration of the second GelMA solution within first reticulated hydrogel before the second photopolymerization. Characterization of GelMA porosity is further required to assess for this potential densification of GelMA network at this interface. As previously mentioned decreased porosity could mechanically constrain cell movement which may explain this result. Besides, it may also induce a barrier for mass transport that will further impair development of cells outside the interface. Consistent with this hypothesis, decreasing GelMA percentage seemed to favor cell rearrangement at the GelMA/GelMA interface which may indicate lower mechanical constraint impose by increasing porosity. Besides, low GelMA percentage are associated with increased GelMA degradability and thus this result is consistent with the hypothesis that cell rearrangement within 3D matrices require proper matrix porosity associated with capacity of cells to remodel this environment. Compared to experiments on embedded spheroids in GelMA droplets, described in part I of result section, these results show a similar driving effect of GelMA/medium interface. However, colonization of the inner cavity within patterned GelMA 10% seemed more homogeneous than what we could have observed previously. Thus, this system holds promise to further characterize driving force of spheroid colonization and identify parameters that could be implemented to promote distribution of cells within early stage of organoid formation. Besides this study has revealed inhibition effect of GelMA photopolymerization that is expected to also affect generation of any GelMA-based contruction.

III. Tissue therapy for the treatment of metabolic disorders: Preliminary transplantation assays

1. Introduction

As mentioned before, a main objective of this thesis is to engineer multi-purposes tissue constructs. This includes their application as a cell source for therapeutic purposes. In the case of metabolic diseases tissues, cell transplantation has emerged as an alternative strategy to traditional pharmacological approaches for increasing thermogenic adipose tissue mass. This approach aims to enhance thermogenic adipose tissue function, ultimately improving metabolic outcomes in individuals with obesity and diabetes. The development of *in vitro* methods for producing transplantable human thermogenic cells has demonstrated promise in enhancing insulin sensitivity and promoting weight loss following transplantation in mouse models [25,262,263,344]. Nevertheless, most of these proof-of-concept studies relied on human thermogenic adipocytes derived from immortalized cell lines or genetically modified cells, often co-transplanted with Matrigel to enhance cell survival. Consequently, these approaches are not readily applicable for therapeutic use in humans.

In Results part I, we described an engineering approach to generate functional and vascularized human beige adipose micro-tissue using well-defined and biocompatible GelMA hydrogel. These beige adipose micro-tissues are derived from amplified SVF-cells (P0-SVF) of human subcutaneous WAT, an easily accessible cell source in adult humans promising for autologous transplantation of thermogenic AT. Our objective is to explore the application of these beige adipose microtissues for in vivo transplantation to treat metabolic diseases. In this section, we will outline the initial stages of our research, consisting in preliminary engraftment studies in healthy immunodeficient mice to evaluate:

- Persistence and survival of human cells after transplantation
- Functional maturation of human endothelial networks and integration with host vasculature
- Maintenance of beige adipocytes phenotype after transplantation

Immunodeficient NSG mice model was selected for transplantation due to their suitability for xenogeneic grafting and for developing metabolic disorders. Indeed, models of high fat diet-induced glucose intolerant NSG have previously been developed by Min's research team to investigate the effects of transplanting human beige adipocytes in obese mice [264]. Beige adipocytes are characterized by their inducibility in UCP1 expression. Since sustaining UCP1 expression in beige adipocytes relies on continuous thermogenic stimulation, initial transplantation experiments were

conducted using unstimulated beige adipose micro-tissues. Subsequently, two preliminary protocols were tested to induce UCP1 expression within the transplants in vivo: one involving cold exposure, a potent thermogenic activator (Figure 36A), and the other adapting in vitro pharmacological UCP1 induction defined in Result part I to in vivo injection (Figure 36B). Human microtissues were transplanted beneath interscapular mice BAT depot (Figure 36C). This engraftment site was selected based on the hypothesis that thermogenic function of mouse BAT would make it a suitable host environment to maintain for thermogenic plasticity of human beige adipocytes, as they can integrate into the existing thermogenic processes.

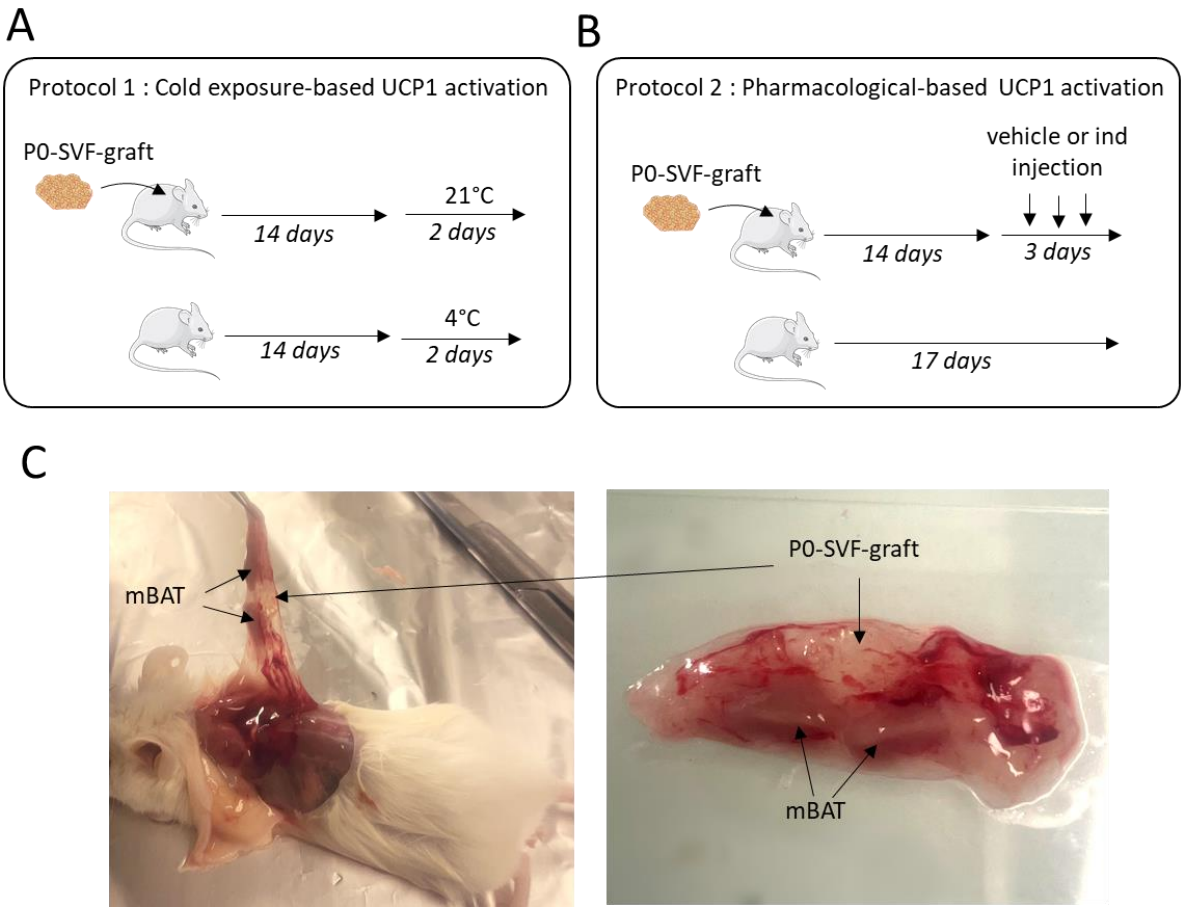

Figure 36. Preliminary transplantation assays protocols. A) Phase image of human beige adipose micro-tissue surrounded by interscapular BAT (mBAT) of NSG mice at sacrifice. Human transplants were found intricated with mice tissue in close proximity to mice vasculature (right) B-C) Schematic of transplantation protocols. Transplanted mice were subjected to UCP1 induction after 14 days post-transplantation surgery using either B) cold exposure (left, n=3-4 per group) or C) pharmacological approach (right, n=3-4 per group) to induce UCP1 in vivo. Injections of thermogenic inducers (Ind) or vehicle were performed next to BAT and right inguinal WAT. The two protocols correspond to distinct experiments.

2. Material and methods

The materials and methods employed in this section overlap with protocols previously described (refer to Chapter 3: Results I.2). Thus, only the methods unique to this section will be outlined below.

Transplantation studies:

This work was submitted to and approved by the Regional Ethic Committee and registered to the French Ministère de la Recherche. Except stated otherwise, animals were kept under controlled light (12-hr light/dark cycles; 07h00–19h00), temperature (20 °C–22 °C), hygrometry (40% ± 20%) and fed ad libitum a normal chow diet (8.4% fat, Safe®A04, Safe lab). For all experiments reported male NSG were used at 8-12 weeks of age. Mice were purchased from Charles River Laboratories (Saint-Germain-Nuelles, France). Mice were transplanted with differentiated human beige adipose micro-tissue generated using previously described protocol (See Result part I). During the procedure, the animals were subjected to general anesthesia with 3% isoflurane and maintained at a regulated temperature using a heating pad. An incision was carefully created in the interscapular region of each mouse, allowing for the insertion of human micro-tissues or GelMA alone between mice BAT and underneath muscle layer. Subsequently, the incision was meticulously closed using 2 to 3 sutures, employing 5.0 suture thread along with a C3 needle.

After 14 days of transplantation surgery, mice were submitted to UCP1 induction protocols before retrieval of transplanted human graft, mice BAT and mice inguinal WATs. For one experiment (Figure 1B, cold exposure-based UCP1 activation), a group of mice was kept two days at 4°C (n=3) while another group was kept at 21°C (n=4). For another experiment (Figure 1C, pharmacological-based UCP1 activation) mice received three daily paired subcutaneous injections of inducers (n=4) or vehicle (n=4) next to mice BAT and right inguinal WAT. Injections were performed using 29G needle on mice kept under anesthesia (2% isoflurane). Inducers injection consisted in 500 µL of PBS solution containing rosiglitazone (1 µM, Sigma, USA), 3,3',5-triiodo-L-thyronine (T3, 0.2 nM, Sigma, USA), all-trans retinoic acid protected from light (0.1 µM, Sigma, USA) and 8-(4-chlorophenylthio) -adenosine 3',5'-cyclic monophosphate (8-CPT-cAMP, 200 µM, Abcam, UK). Non-transplanted mice were used as a control (n=3). At the end of the protocol, euthanasia of the animals was performed under anesthesia (3% isoflurane) using cervical dislocation.

To label blood vessels, some animals received a retro-orbital injection of human and mice specific lectins conducted under general anesthesia (3% Isoflurane). 100 µl of human lectins coupled with rhodamine (Eurobio Scientific, RL-1102) were administered 30 minutes before euthanasia, followed by the injection of 100 µl of murine lectins coupled with fluorescein (Eurobio Scientific, FL-1201), 20

minutes before euthanasia. In that scenario, the animals received a ketamine injection prior to thoracic opening, aortic section, and intracardiac perfusion with heparinized NaCl to wash unspecific signal.

Immunofluorescence and immunohistochemistry:

Tissues were fixed with 4% PFA at room temperature overnight, washed with D-PBS and kept at 4°C before staining. For immunofluorescence analysis, 200 µm thick sections were obtained via 2% agarose embedding and section using vibroslice. Sections were then stained following the same protocols than embedded multi-spheroids described in Results I. For immunohistochemistry analysis, 3 µm thick sections were obtained via paraffin embedding and section. Sections were dewaxed (successive toluene and descending alcohols bathes) and stained with haematoxilin and eosin. Primary antibody labelling of 3-µm serial sections were performed out after antigen retrieval for 30 min at 96°C. Primary antibody were incubated for 50 min at room temperature. Staining was carried out with EnVision Flex (reference K8000, Dako) for 30 min at room temperature, followed by DAB as a chromogen (reference K8000, 10 min room temperature). Slides were then counterstained with hematoxylin (reference C0283, DIAPATH). The stained slides were scanned (Panoramic Desk, 3D Histec) or imaged by light microscopy on a Nikon Eclipse Ci-L microscope with a DS138 Fi3 Camera and NIS Elements D software. Antibodies and dyes are listed in Table 5.

Table 10. List of antibodies and dyes used for immunofluorescence and immunochemistry cell characterization

Type	Name	Dilution	Company	Cat. No.
Primary antibodies	Anti - Human KU80 Rabbit IgG (Clone: C48E7)	1:400	Cell Signaling Technology (Massachusetts, USA)	2180S
	Anti-Human CD31 Rabbit monoclonal (Clone: EP78)	1:200	Epitomics (Burlingame, USA)	AC-0083A
Mouse lectin staining	Griffonia Simplicifolia Lectin I Fluorescein	100 µL	Eurobio Scientific (France)	FL-1101
Human lectin staining	Ulex Europeaeus Agglutinin I Rhodamine	100 µL	Eurobio Scientific (France)	RL1062

RNA extraction and quantitative real time PCR (RT-qPCR):

After retrieval tissue were maintained in RNA later buffer overnight at -20°C before transferring them at -80°C before RNA extraction. It has to be noted that transplanted human graft were separated as best as possible from surrounding mice tissue to avoid contamination from mice mRNA and promote human mRNA detection. For RNA extraction, tissues were homogenized in QIAzol lysis reagent (Qiagen, US) and disrupted for 3 x 2 min at 30 Hz using Tissue Lyser (Qiagen). mRNA isolation, reverse transcription and qPCR steps were performed as previously described. Reverse transcription was performed on 1 µg RNA. Primers are listed in table 6. Relative gene expression was calculated by the $2^{-\Delta CT}$ method. The ΔCt was obtained by normalizing mean expression values of each gene to reference genes: m36B4 for mice target genes and geometric mean of GUSB and PPIA for human target genes. Mouse and human primers specificity were confirmed using cDNA from *in vitro* human organoids and mice tissues respectively.

Table 11. List of primer used for qRT-PCR analyses

Specificity	**Gene**		**Sequence (5'-3')**
Human	*GUSB*	Forward	AGCCAGTTCCTCATCAATGG
		Reverse	GGTAGTGGCTGGTACGGAAA
Human	*PPIA*	Forward	GCCGAGGAAAACCGTGTACTAT
		Reverse	TCTTTGGGACCTTGTCTGCAA
Human	*UCP1*	Forward	GTGTGCCCAACTGTGCAATG
		Reverse	CCAGGATCCAAGTCGCAAGA
Human	*PGC1-α*	Forward	CCGCACGCACCGAAA
		Reverse	TCGTGCTGATATTCCTCGTAGCT
Human	*ADIPOQ*	Forward	CAGAGATGGCACCCCTGGTG
		Reverse	TTCACCGATGTCTCCCTTAG
Mice	*m36B4*	Forward	AGTCGGAGGAATCAGATGAGGAT
		Reverse	GGCTGACTTGGTTGCTTTGG
Mice	*mUCP1*	Forward	GACCGACGGCCTTTTTCAA
		Reverse	AAAGCACACAAACATGATGACGTT
Mice	*mCD45*	Forward	CTTCAGTGGTCCCATTGTGGTG
		Reverse	TCAGACACCTCTGTCGCCTTAG

3. Results

For preliminary tests, human beige micro-tissues were generated from P0-SVF cells as we previously demonstrated their highest beiging potential compared to freshly isolated SVF cells. Human cells were differentiated for 28 days to obtain unactivated beige micro-tissue before transplantation under BAT of NSG mice. Transplanted mice did not display signs of inflammation over post-transplantation duration.

In a first experiment (protocol 1), engraftment potential of vascularized beige micro-tissue was assessed after 16 days by evaluating the maintenance of human grafts *in vivo* and their capacity to establish vascular connections with host vasculature. It has to be noted that due to facilities issues, mice could not be kept at thermoneutrality (30°C). For this reason, transplanted mice were either kept at 21°C (n=3) or transferred at 4°C (n=4) for two days in an attempt to induce thermogenic activation within human transplants.

At day of sacrifice, human grafts were still distinguishable (Figure 36A) and found closely intricated with surrounding tissue requiring dissection to get separated human transplant from mice BAT (Figure 36A). For most mice, some mice vessels could be macroscopically observed around the human graft (Figure 1A). Hematoxylin and eosin staining showed human transplant adjacent to mice BAT without apparent signs of immune rejection as expected from immunodeficient mice (Figure 37A, a.). To assess human cell presence, tissue sections were stained with specific human antibodies against human vimentin, an intermediate filament protein expressed in most mesenchymal cells, and human ku80, component of DNA binding Ku complex. Both of these proteins were strongly detected in transplants demonstrating an important survival of human cells (Figure 37A, b-c.). Besides, clusters of human adipocytes could be found inside the transplant (Figure 37B, c.). Regarding vascularization, human vimentin staining revealed the presence of small unstained vessel lumens within the transplant, suggesting that host mice blood vessels grew into the transplanted human micro-tissue (Figure 37B, a. red arrow). Furthermore, human CD31 staining revealed the presence of human tubular vascular structure demonstrating maturation of pre-formed endothelial cells networks in human micro-tissues (Figure 37B, c). Strikingly, these human vessel lumens were filled with unstained small cells reminiscent of mice erythrocytes. This result suggested functional perfusion between human and mice vasculature. To confirm the connection of human vascular networks to the recipient circulatory system, mice were injected with human and mouse specific lectins before euthanasia. Both human and mouse lectin signals could be found within the transplant in some location close to the adjacent mice tissue (Figure 37B) indicating perfusion of some human vessels by host vasculature.

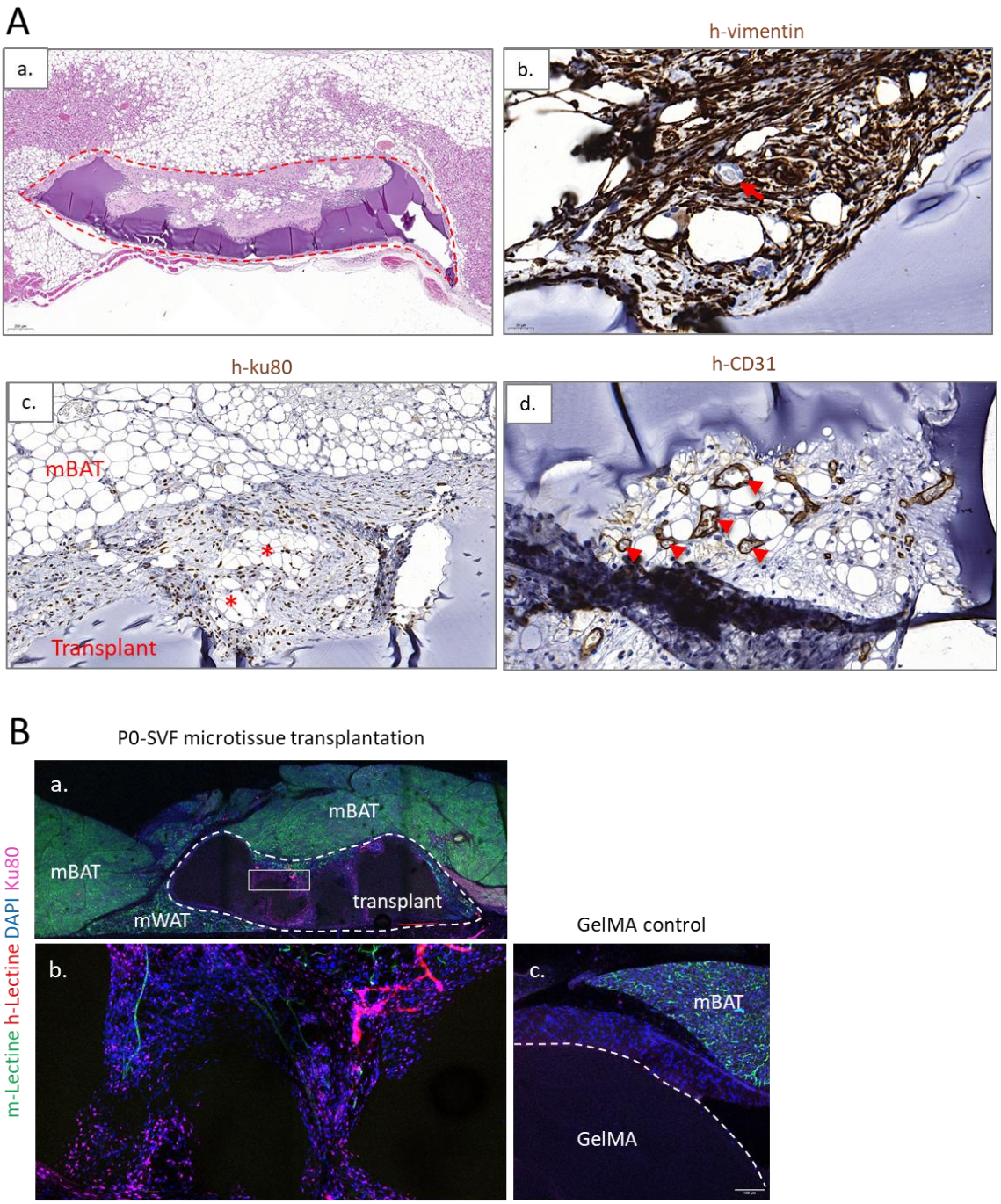

Figure 37. Evaluation of transplanted micro-tissue survival and vascular engraftment. A) Histological characterization of human cells within transplant. (a.) Hematoxylin and eosin staining, transplant is outlined. (b,c) Human vimentin (b.) and human Ku80 (c.) immunostainings were used to evaluate the presence of human cells. Red arrows depict unstained mice vascular lumens. (d.) Human endothelial cells were revealed by human CD31 immunostaining. Red arrowheads depict human vessel lumens in which cells reminiscent of mice erythrocytes could be detected. B) Detection of human (red) and mice (green) specific lectin within transplant and surrounding mice tissue (mBAT, mWAT). Human Ku80 (pink) immunostaining revealed human cells. Transplant and adjacent mice tissues are labelled. (b.) shows magnified white squared area. (c.) Transplantation of GelMA without cells was used as a negative control of human lectin staining.

Regarding UCP1 induction, transplanted mice maintained at 4°C showed increased UCP1 (*mUCP1*) expression within BAT compared to ones maintained at 21°C, suggesting the effectiveness of this method to increase host thermogenic activity (Figure 38B). However, human *UCP1* (*hUCP1*) remained barely detectable in the transplant in both conditions similarly to unactivated state of beige adipose micro-tissue before transplantation (Figure 38C). This was associated with an overall decrease of human adiponectin (*hADIPOQ*) expression in human transplants (Figure 38C). Thermogenic activation by cold exposure strongly relies on sympathetic innervation that relays information to adipose tissue through adrenergic stimulation. Hence, lack of UCP1 induction in human transplant under cold exposure may come from improper innervation of the graft, given that establishment of innervation can be a long-lasting process.

In a second experiment, as an alternative to cold exposure to avoid requirement of sympathetic innervation, we tested a pharmacological approach to induce UCP1 expression *in* vivo. This approach was based on previously established protocol that demonstrated robust *in vitro* UCP1 induction in human beige adipose micro-tissue. This protocol consists in treatment of cells with a cocktail of canonical thermogenic inducers containing a cell permeable cAMP analog i.e. 8-CPT-cAMP[367], rosiglitazone (PPARγ agonist) [312] retinoid acid [311] and thyroid hormone [310] for three days. As a first approach, this protocol was adapted for *in vivo* condition through the use of three daily injections of induction cocktail in mice before sacrifice. Inducers or vehicles were injected close to transplantation site and in proximity to one inguinal WAT depot, aiming to trigger thermogenic activation within the human graft and evaluate the potential browning of the mice WAT, respectively. However, injection of inducers neither increased *mUCP1* in mice BAT and inguinal WAT nor *hUCP1* in human grafts compared to vehicle injection (Figure 38C-D). As for cold exposure experiment, our preliminary results suggest an overall decreased expression of hADIPOQ within human graft (Figure 38F). Additionally, to assess a potential inflammatory effect of the injections, mRNA expression of mouse CD45 (mCD45), a marker of nucleated hematopoietic cells was assessed. mCD45 tended to increase in human graft compared to surrounding BAT in both injection conditions while it was increased in mouse inguinal WAT in induction condition, suggesting a specific inflammatory effect of injected inducers on mice AT.

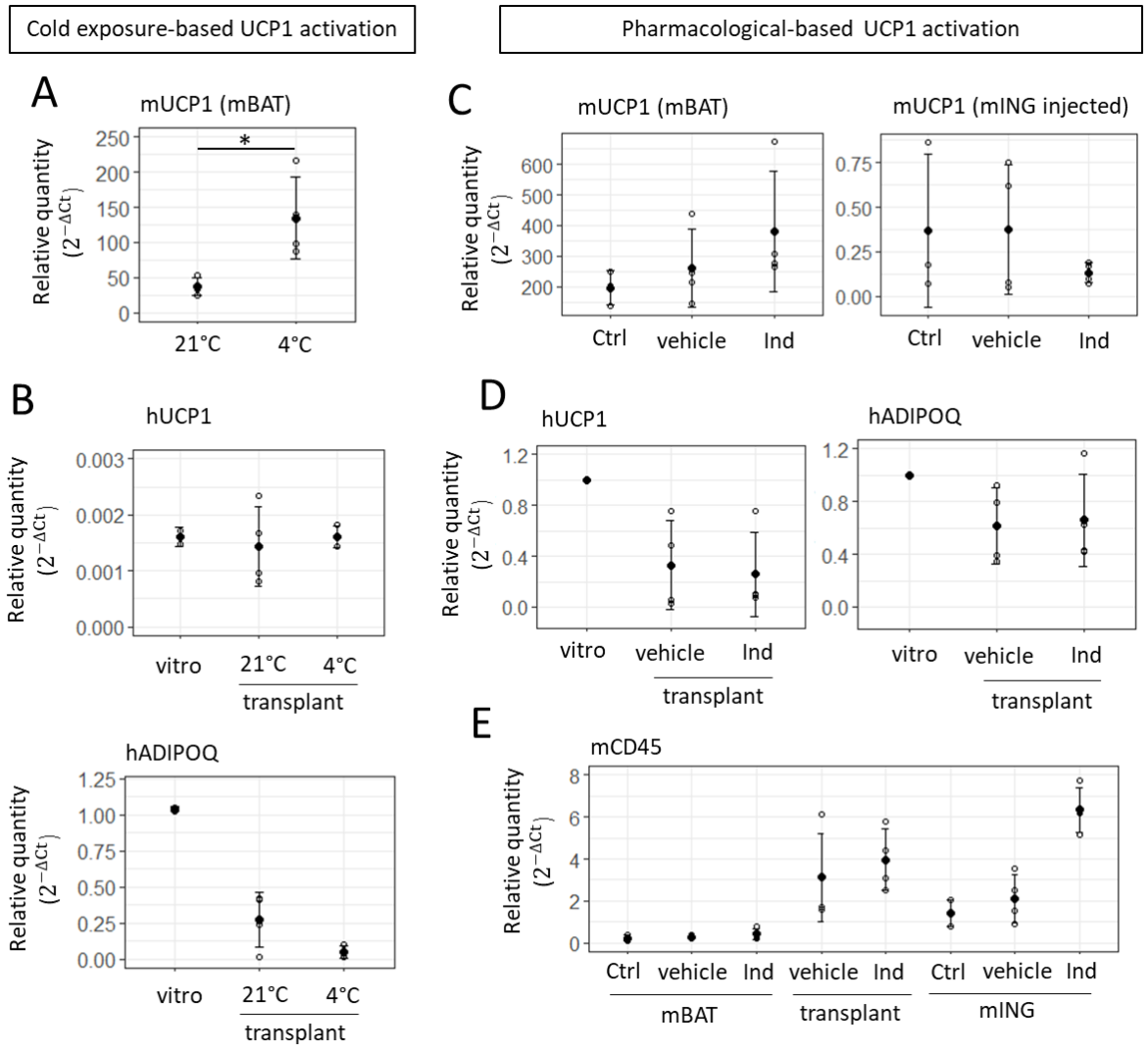

Figure 38. Evaluation of UCP1 induction within human beige micro-tissue after transplantation. After 14 days post-transplantation surgery, transplanted mice were subjected to UCP1 induction A-B) Transplantation study using cold exposure as UCP1 inducers A) Gene expression analysis of mice UCP1 (mUCP1) in mouse BAT (mBAT) in absence (21°C, n=3) or in presence of cold exposure (4°C, n=4). B) Gene expression analysis of human UCP1 and human adiponectin, marker of mature adipocyte within human graft before (vitro) and after transplantation (under 21°C or 4°C condition). C-E) Transplantation study using pharmacological approach to induce UCP1 in vivo. Injections of thermogenic inducers were performed next to BAT and right inguinal WAT. C) Gene expression of mUCP1 in mBAT and right inguinal under non-transplanted (Ctrl), vehicle injection (vehicle) and inducer injection (ind) conditions. D) Gene expression analysis of human UCP1 and human adiponectin within human graft before (vitro, n=1) and after transplantation under vehicle or inducers injection conditions (n=4). E) Gene expression of mouse CD45 in paired human transplant, surrounding mice BAT and injected inguinal WAT under vehicle and inducers injection condition (n=4). Non-transplanted (Ctrl) mBAT and right inguinal WAT are used as control to assess basal CD45 level in host tissue (n=3). All quantitative values are shown as mean ± standard deviation. Statistical analyses were performed by two sample t-test. Statistical significance: * < 0.05.

4. Discussion

The objective of thermogenic AT transplantation in the context of metabolic disorders is to increase whole body energy expenditure and enhance glucose tolerance. Prerequisites for such an approach are successful generation of thermogenic adipocytes and creating a suitable microenvironment that supports their retention, long-term survival and function after transplantation.

For successful thermogenic adipose tissue transplantation, the type of thermogenic adipocytes generated is a crucial consideration. Brown adipocytes express UCP1 constitutively, whereas beige adipocytes require sustained thermogenic activation to maintain high UCP1 levels. Thus, the retention of thermogenic capacity in brown adipose grafts is directly linked to adipocyte survival, while for transplanted beige adipocytes, this retention also necessitates the maintenance of adipocyte plasticity. Brown adipocytes may initially seem more favorable for therapeutic strategies. However, due to the scarcity and limited accessibility of human BAT, primary brown adipose progenitors are not a reliable source for cell transplantation. Most methods for in vitro generation of brown adipocytes rely on immortalized cell lines or genetically modified cells, which are not suitable for clinical applications [25,262,263,344]. Therefore, it is currently challenging to envision engineered brown adipose tissue as a viable option for therapeutic transplantation. As an alternative, several studies including ours have demonstrated the possibility to generate human beige adipocytes using SVF of human subcutaneous WAT. Contrary to human BAT, subcutaneous WAT is an easily accessible source which opens the way to autologous transplantation, avoiding immune rejection issues. Consequently, in the long term, engineering beige adipose tissue appears to be more viable than brown adipose tissue for therapeutic applications. Min et al. demonstrated the beneficial effect of beige adipocyte transplantation derived from human WAT to improve glucose tolerance in NSG obese mice [264].

In some studies, creation of a microenvironment favorable to survival and retention of transplanted thermogenic adipocytes involves embedding of adipocyte cell suspension into Matrigel before transplantation [263,264]. While Matrigel was proved to increase transplanted cell survival, its use remains incompatible with clinical transplantation. From our previous work, we demonstrated that pre-vascularized human beige adipose micro-tissues could be generated using a biocompatible GelMA hydrogel with defined composition. Here, preliminary xeno-transplantation assays in NSG mice demonstrated the feasibility of these micro-tissue engraftment with maintenance of human cells survival over several weeks post-transplantation. Histological analysis revealed that an important number of human cells can be found in retrieved transplants which include human adipocytes and endothelial cells. These assays demonstrated the functionality of human micro-tissue vasculature which was able to mature *in vivo* and establish interconnections with the recipient vascularization.

Engineered beige adipose micro-tissues exhibit the ability to get perfused by host vasculature which may contribute to the survival of human cells but also represent a critical factor when considering a therapeutic effect of these transplanted cells. Indeed, transplanted thermogenic adipose grafts have to be able to uptake host metabolites to operate their role of metabolic sink once activated to expect reduced hyperglycemia in diabetic and obese hosts. Besides, it has been shown that BAT transplantation induces systemic effect on host metabolism through its endocrine activity which relies on its integration into host vasculature [368]. Hence, these preliminary experiments highlighted the promising potential of human beige adipose micro-tissues transplantation regarding overall human cells maintenance and establishment of functional vascular compartment supportive of adipocyte function.

However, despite survival of human cells, in these first trials, the thermogenic adipogenic program was not successfully induced within the transplanted human beige adipocytes *in vivo* using cold exposure or pharmacological inducers. Absence of UCP1 induction in the graft may be explained either by inappropriate thermogenic stimulation protocols or a loss of the beige adipocyte phenotype *in vivo*.

Histological comparison between in vitro micro-tissue before transplantation and harvested transplant should be conducted to evaluate the change of cell populations within the graft over post-transplantation duration. Besides, evaluation of transplant state after different duration post-transplantation surgery would give insights on the evolution of the graft within the mice. These cell populations include vasculature, innervation, immune cells, adipocyte and progenitor compartments. Despite that maintenance of human adipocytes was observed by histological analysis, mRNA expression of mature adipocyte markers seemed to be overall decreased in the graft after transplantation. This may indicate either a loss of adipocytes or an impairment of adipocyte function. Several hypotheses can be proposed. Loss of adipocytes may arise from mechanical loss during initial surgical procedure or from exposure to hostile host environment impairing cell viability prior to human vasculature integration. In case of loss of mature adipocytes, sustaining the beige adipogenic phenotype within the graft would necessitate the continued generation of human beige adipocytes within the graft *in vivo*. Therefore, it would be important to assess the presence of adipose progenitors within human transplant pre and post-transplantation. Additionally, several factors can impact beige adipocyte function and their renewal *in vivo*. Firstly, local inflammation could contribute to negatively impacting beiging potential of WAT and impaired adipogenesis [213]. As expected of immunodeficient mice models, no signs of immune-rejection of the grafts were histologically observed. Nevertheless, increased expression of mice CD45 within human grafts may indicate a recruitment of some immune cells that can participate in local inflammation. Further histological characterization is required to

confirm the presence of mouse immune cells within human transplant. Besides, the pro and anti-inflammatory nature of these cells should be considered.

On another hand, mice BAT might not constitute a suitable host environment to maintain for thermogenic plasticity of human beige adipocytes contrary to our first hypothesis. Due to facilities challenges, NSG mice could not be maintained at thermoneutrality during these experiments. Consequently, mice were under constant thermogenic activation. This activation may subject human adipocytes to metabolic stresses prior to establishment of vasculature or innervation that could contribute to their integration into thermogenic processes. Hence, over the weeks before initiating UCP1 stimulation protocol, inactivated human beige adipocytes may serve as a source of fatty acids to fuel adjacent tissue thermogenesis. This could potentially contribute to inadequate thermogenic activation at the time of UCP1 stimulation. In these trials un-activated beige adipocytes have been transplanted, *in* vitro pre-activation of the grafts as described in Min et al. study may help to better preserve cell plasticity [269]. Additionally, further experiments would need to explore approaches which may expose the graft to a less competitive environment. This can be considered either by selecting another graft site or by reducing the thermogenic capacity of the mic. Maintaining NSG mice under thermoneutrality conditions could be a potential solution to reduce thermogenic activation, but it will require specialized animal facilities. Another option will be to use UCP1-KO mice however these kinds of models will have to be developed in immunodeficient mice to allow xenogeneic transplantation of human beige adipose tissue in mices. Opting for a change in the transplantation site may offer a more viable approach in the continuation of our ongoing research. Potential engraftment sites encompass subcutaneous transplantation s in the dorsal regions or close to the kidney capsule known to favor neovascularization and for its catecholamine secretion that can promote thermogenic activation.

In addition to the transplantation protocol, the nature and timing of the thermogenic program activation protocol should be considered. Absence of UCP1 stimulation by cold exposure may be due to the absence of innervation of the human graft by the host sympathetic nervous system which are often described several months post-transplantation. Pharmacological activation represents a more flexible stimulation protocol to evaluate retention of graft thermogenic activity over several days to several weeks post-surgery durations. In our first trials, the use of UCP1 stimulation cocktail established for *in vitro* thermogenic induction of human micro-tissue showed variable results on mice thermogenic activation. A first step to improve the pharmacological approach of *in vivo* thermogenic activation would be to determine a minimal stimulation cocktail able to induce thermogenic activation of both host mice AT and human graft without adverse effects. This will enable checking of cocktail

induction effectiveness independently of human graft retention phenotype. Delivery techniques of pharmaceutics should also be considered. Providing local and continuous delivery of inducers to the graft using osmotic pumps may help to promote maintenance of transplanted human beige adipocytes identity and confer them with better selective advantage than short-time systemic induction.

Overall, these preliminary transplantations assays demonstrated the feasibility of the transplantation of our engineered human micro-tissues and the functionality of their embedded vasculature. Currently, we have been unable to establish the persistence of the beige phenotype in these transplanted structures. Nonetheless, the favorable survival of human cells and their integration into the host tissue holds promise for the ongoing experiments. Our forthcoming endeavors require a more comprehensive examination of the graft progression over time to precisely identify the reasons behind the lack of a response to thermogenic activation. Furthermore, changes in the design of the transplantation studies including engraftment and UCP1 stimulation protocols as well as differentiation state of the graft need to be considered for further experiments.

General conclusion and perspectives

The emergence of approaches for *in vitro* generation of 3D complex tissue construct have marked a turning point in our ability to model and understand living tissues. Thanks to their potential to replicate part of cell spatial organization within specific environment these 3D models are invaluable tools to gain deeper understanding of tissue physiology and physiopathology. Besides, engineered 3D tissues have far reaching implications in the development of innovative therapies either serving to identify putative targets, as models for drug screening approaches or as ATMPs to instruct or support specific organ functions.

During this thesis, our work more specifically focused in the study of human beige adipose tissues for which very few 3D models have been already described [22–25]. We develop innovative engineering approach based on 3D microenvironment engineering to guide self-organization of cell aggregates derived from human adult SVF of WAT towards generation of functional and vascularized human beige adipose organoids. These organoids recapitulate tissue architecture associated with key secretory and metabolic features of native adult beige AT. By the use of controlled biochemical and biomechanical environment, translation of 3D microenvironment was achieved also at macroscopic scale to obtain functional micro-tissues opening the way to transplantation application. Altogether, these models represent promising physiological *ex vivo* models to study human beige AT physiopathology and to identify putative thermogenic drugs. Hence, thorough this work we have achieved our primary aim to develop adaptable tissue engineering approaches for the generation of multi-purposes adult tissue models.

In the following stages, these human beige adipose organoids could be integrated into microfluidic chip to be used as drug screening platform. Organoid-on-chip represent promising approach to control for drug delivery while monitoring change in organoid environment as readout of cell responses [369]. Thermogenic activation of beige AT is characterized by metabolic adaptation that result in heat generation. It has also been proposed that thermogenic activation correlates with change in redox environment [370]. Therefore, we can imagine to implement microfluidic chip in an oxygen-controlled microenvironment with temperature, potential redox sensors or O2 and CO2 sensors to monitor metabolic rate [371–373]. Combining such approach with micro-pipetting platform would also allow to monitor medium composition in nutrients as well as adapting it accordingly to avoid oxidative stress and aberrant metabolic activity of cells commonly observed in non-physiological culture conditions [374].

To enable the incorporation of organoids into clinical and industrial settings, it is essential to meet specific criteria, including the need for a high-throughput production process and the minimization of batch-to-batch variations [375]. These include the need for large-scale production of high cell quality.

Large-scale manufacturing processes of ASC for clinical application have already been described and involve the use of bioreactors [376]. Until now, these approaches focused only on ASC production but they may be adapted for amplification of both ASC and endothelial progenitors. We have demonstrated that beige adipose organoids can be obtained from SVF cells derived from single amplification process. Generation of organoids derived from SVF cells after different passages as well as from cryopreserved cells should be tested to determine which framework of large-scale cell production can be adopted. The main challenge to overcome is the maintenance of endothelial progenitors which are expected to decrease in proportion during SVF amplification due to clonal selection [377]. Besides, SVF cells show donor-dependent heterogeneity, proliferation and differentiation potential. Thus, standardize process would require routine characterization of the cells prior to seeding for example through cell cytometry. An alternative would be to use biobank of defined patient/donor cells which rise several ethical concern including ownership of the cells and potential applications [378]. While high production of ASC spheroids through parallel processing can be envisioned, the development of organoid also includes the need for large-scale production of standardized and parallel processing for spheroids positioning in hydrogel. This will require to explore automated spheroid deposition process such as described by Ayan et al. [379] combine with high throughput automation systems.

A second objective of this work was to explore the parameters that govern the *in vitro* development of organ substitute. We suppose that the main reason for which organoids better recapitulate tissue function compared to 2D culture or spheroids models relies on their capacity to recapitulate part of the different organ-specific cell compartments in an architecture mirroring native one. Therefore, success of functional tissue *in vitro* generation would reside in guiding altogether spatial rearrangement and differentiation of a cell source into spatially organized various cell types.

In this endeavor a crucial parameter to consider is the cell source. Creating tissue constructs containing multiple tissue-specific cell types can be achieved using a mix of progenitor cells that will subsequently differentiate into specific cell types or using stem cell-based approach which allow for development of several cell types from an initially homogenous cell population. These stem cells can be either obtained from fetal (ESCs) and adult tissues (adult stem cells) or generated *in* vitro by reprogramming of somatic cells (iPSCs). hiPSC have the advantages that they can be produced in high quantity and be derived into wide range of cells compared to adult stem cells whose access is often limited in humans and show restricted differentiation lineages. However, up to now hiPSC-derived organoids display immature functionality. Conversely, organoids derived from adult stem cells present higher functionality but only allow for the development of parenchymal cells lacking vascular and mesenchymal compartments. Here we have described the potential of the SVF as a mixture of progenitor cells and multipotent ASC

as a promising and readily available cell source for the generation of vascularized organoids containing parenchymal and mesenchymal cells. Thus, we believe that the use of SVF is often underestimated as a potential cellular source for organoid generation. Furthermore, it may be conceivable to combine SVF cells with other adult stem cell sources to enable the generation of a vascularized mesenchymal compartment that supports specific parenchyma. Inversely, differentiating hiPSC-derived cells in presence of adult stem cells may favor their functional maturation.

Once the cell source selected, cells should be provided with a 3D microenvironment driving the development of required cells in time and space. Multipotent cells are especially sensitive to their environment as extrinsic chemical and biophysical cues will promote their differentiation toward a cell type or another. Generation of differentiated cells from multipotent stem cells involve interacting balances of differentiation processes. Therefore, the promotion of specific cell types will come at the cost of the development of others. For this reason, careful attention should be given to the engineering of microenvironment permissive to the differentiation of intended cell types while also preventing the development and selection of competing cells. This can be adjusted through the use of inhibitions as we have observed with inhibition of TGFβ pathway. In addition to driving multiple cell types development, engineered microenvironment should favor their spatial rearrangement to ensure the emergence of tissue architecture supporting tissue function. In this study we identified that providing cell with ECM-like material was a prerequisite to promote this process. Besides, we could observe that cell distributions within GelMA hydrogel varied with its concentration upon which its mechanical and physical properties depend. These results strongly indicate that self-organization is importantly affected by biomechanical environment. Further mechanical characterization of the different GelMA hydrogels should be conducted to correlate this behavior with specific biophysical parameters such as hydrogel porosity, viscoelasticity or degradability and their evolution along the culture. Thanks to its tunability and controlled definition, GelMA hydrogels offer opportunities to derive principles to drive self-organization of cells where approaches relying on undefined Matrigel might be strongly limited by the variability and poor tunability of this material. To better advance our understanding of the biophysical factors influencing cellular organization within a 3D matrix, it would require to develop and use custom-designed hydrogels that allow for the independent manipulation of its mechanical properties. Besides, it would be interesting to compare experiments performed using cell aggregates and high-density cell suspension either locality injected [187,188] or dispersed in hydrogel of given composition. This would allow to study influence of cell-cell vs cell-matrix interactions on cell organization as strong cell-cell interaction induced by cell preaggregation may slow down initial cell rearrangements.

In conclusion, given ASC multipotency and tunability of GelMA hydrogel, methods described in this work could be easily adapted for the development of other mesenchymal tissues but also to derive principles of controlled organoid engineering beyond stochastic differentiation and self-organization of cells, as traditionally seen with Matrigel-based methods. Understanding and achieving precise control over environmental parameters is not only vital for process reproducibility but also for their scalability to different tissue scales as shown in this study for the generation of micro-tissue. We believe that such approaches can contribute to the conceptualization of a theoretical framework for the processes underlying self-organization of cells. Understanding self-organization processes require to understand how cell states dynamically evolve along collective cell rearrangements shaping their microenvironment but also influenced by it. Importance of spatial organization as a motor and not only a consequence of self-organizing process is often overlooked. The revolution of single cell omics has unveiled important cell heterogeneity and cell fates variability resulting from inherent stochasticity and dynamic of events in interacting systems. This has provided a different perspective on cellular development and self-organization processes, which had historically been seen as a sequence of predetermined events within the embryo. Stochasticity of self-organization processes in organoids is much more apparent as it leads to important variability in morphology and functions. Thus, combining organoids generation with controlled environment is a powerful tool to decipher what parameters influence cell selection and fate processes to guide robust tissue organization. To this aim, single cell spatial organization and temporal evolution within organoids along its development should be addressed using spatially resolved omics [380] and live cell imaging at single cell resolution [381]. Such approaches have been performed to study cellular heterogeneity during collective cell behavior of intestinal organoid development within Matrigel [382]. By revisiting our understanding of tissue development processes, application of these strategies using organoids and hydrogels with tunable mechanical and chemical properties brings the opportunities for unprecedented cross-investigations in basic science and engineering strategies.

Annexes

I. Scientific contributions:

Scientific productions:

Articles:

- M. Escudero, L. Vaysse, G. Eke, M. Peyrou, F. Villarroya, S. Bonnel, Y. Jeanson, L. Boyer, C. Vieu, B. Chaput, X. Yao, F. Deschaseaux, M. Parny, I. Raymond-Letron, C. Dani, A. Carrière, L. Malaquin, L. Casteilla, Scalable Generation of Pre-Vascularized and Functional Human Beige Adipose Organoids, Advanced Science. n/a (n.d.) 2301499. https://doi.org/10.1002/advs.202301499.

- G. Eke, L. Vaysse, X. Yao, M. Escudero, A. Carrière, E. Trevisiol, C. Vieu, C. Dani, L. Casteilla, L. Malaquin, Cell Aggregate Assembly through Microengineering for Functional Tissue Emergence, Cells. 11 (2022) 1394. https://doi.org/10.3390/cells11091394.

- Fournié, B. Venzac, E. Trevisiol, J. Foncy, J. Roul, S. Assie-Souleille, M. Escudero, P. Joseph, A. Reitz, L. Malaquin, A microfluidics-assisted photopolymerization method for high-resolution multimaterial 3D printing, Additive Manufacturing. 72 (2023) 103629. https://doi.org/10.1016/j.addma.2023.103629.

Patents:

- N° 22 306 953.5, "Method for generating pre-vascularized 3D cell aggregates", 20th December 2022
- N° 23 305 136.6, "Methods for preparing a 3D pre-vascularized adipose tissue construct, said 3D pre-vascularized adipose tissue construct and uses therof", 2nd February 2023

Scientific communications:

- Oral presentation CARe interdisciplinary and international phD seminar, Toulouse 7th December 2021
- Poster presentation during FSSCR annual meeting 2021, "*Guided assembly of cell aggregates by hydrogel-embedding to generate vascularized and metabolically active human brown/beige adipose tissues*", Montpellier 9-10th November 2021
- Poster presentation during ISSCR annual meeting 2023, "*A scalable approach to generate pre-vascularized and functional human beige adipose organoids*", Boston 14-17th June 2023

Scientific popularization:

- Participation to "Fête de la Sciences" LAAS CNRS, 14th October 2022
- Oral presentation Pint of Sciences "Plutôt muscle ou plutôt gras ? Question simple, réponses complexes", Toulouse 24th May 2023

cells

MDPI

Review

Cell Aggregate Assembly through Microengineering for Functional Tissue Emergence

Gozde Eke [1], Laurence Vaysse [2], Xi Yao [3], Mélanie Escudero [2], Audrey Carrière [2], Emmanuelle Trevisiol [1,†], Christophe Vieu [1], Christian Dani [3], Louis Casteilla [2] and Laurent Malaquin [1,*]

[1] Laboratoire d'Analyse et d'Architecture des Systèmes, Centre National de la Recherche Scientifique (LAAS-CNRS), Université de Toulouse, INSA, UPS, 31400 Toulouse, France; gekecevik@laas.fr (G.E.); emmanuelle.trevisiol@laas.fr (E.T.); cvieu@laas.fr (C.V.)

[2] RESTORE Research Center, Université de Toulouse, INSERM 1301, CNRS 5070, EFS, ENVT, 31100 Toulouse, France; laurence.vaysse@inserm.fr (L.V.); melanie.escudero@inserm.fr (M.E.); audrey.carriere-pazat@inserm.fr (A.C.); louis.casteilla@inserm.fr (L.C.)

[3] Institut de Biologie Valrose, Université Côte d'Azur, 06108 Nice, France; yao.xi@univ-cotedazur.fr (X.Y.); christian.dani@univ-cotedazur.fr (C.D.)

* Correspondence: laurent.malaquin@laas.fr; Tel.: +33-(0)5-6133-6384

† Current affiliation: Toulouse Biotechnology Institute (TBI), Université de Toulouse, CNRS, INRAE, INSA, 31031 Toulouse, France.

Abstract: Compared to cell suspensions or monolayers, 3D cell aggregates provide cellular interactions organized in space and heterogeneity that better resume the real organization of native tissues. They represent powerful tools to narrow down the gap between in vitro and in vivo models, thanks to their self-evolving capabilities. Recent strategies have demonstrated their potential as building blocks to generate microtissues. Developing specific methodologies capable of organizing these cell aggregates into 3D architectures and environments has become essential to convert them into functional microtissues adapted for regenerative medicine or pharmaceutical screening purposes. Although the techniques for producing individual cell aggregates have been on the market for over a decade, the methodology for engineering functional tissues starting from them is still a young and quickly evolving field of research. In this review, we first present a panorama of emerging cell aggregates microfabrication and assembly technologies. We further discuss the perspectives opened in the establishment of functional tissues with a specific focus on controlled architecture and heterogeneity to favor cell differentiation and proliferation.

Keywords: cell spheroids; organoids; cell aggregates; functional microtissues; microfabrication; assembly technologies; micropatterning; microengineering technology

Citation: Eke, G.; Vaysse, L.; Yao, X.; Escudero, M.; Carrière, A.; Trevisiol, E.; Vieu, C.; Dani, C.; Casteilla, L.; Malaquin, L. Cell Aggregate Assembly through Microengineering for Functional Tissue Emergence. *Cells* **2022**, *11*, 1394. https://doi.org/10.3390/cells11091394

Academic Editor: Alexander V. Ljubimov

Received: 11 February 2022
Accepted: 15 April 2022
Published: 20 April 2022

1. Introduction

In comparison with individual cell suspensions, three-dimensional (3D) cell aggregates provide key advantages for the creation of functional microtissues [1–4]. The cell aggregation process gives rise to multicellular assemblies with arbitrary shapes and numbers of cells that include different types of structures based on their complexity level: clusters, spheroids, multicellular spheroids, and organoids. Compared to suspensions of isolated cells, such 3D cell aggregates provide cellular interactions that better resume the real organization of native tissues [5–9]. Furthermore, the co-culture of different cell types in these aggregates (such as endothelial or immune cells) can facilitate ECM secretion, promote pre-vascularized networks and allow more accurate recapitulations of physiological tissular microenvironments [10,11]. This perspective has strongly motivated the development of methods to generate large-scale constructs by organizing multiple cell aggregates in controlled architectures to achieve large-scale functional constructs [12,13]. Intriguing approaches such as 3D bioprinting and micro-robotic placements through magnetic, acoustic,

and pressure actuation methods have been proposed in this direction. To our mind, a broad analysis of the technical concerns and scientific opportunities behind these first attempts could be fruitful for the bioengineers targeting the generation of functional tissues.

In this paper, we review the emerging spheroid/organoid handling technologies and their perspectives on building functional microtissues (Figure 1). We describe the recent and promising routes suggested in the literature and propose a synthesis of the challenges identified for regenerative medicine or drug assessment applications. We also address the improvements in the building of functional biological artifacts from cell aggregates compared to construction schemes based on individual cells. Finally, we discuss combinatorial methods for making pre-mature microtissue models of increased efficiency to shorten the healing time when implanted into humans.

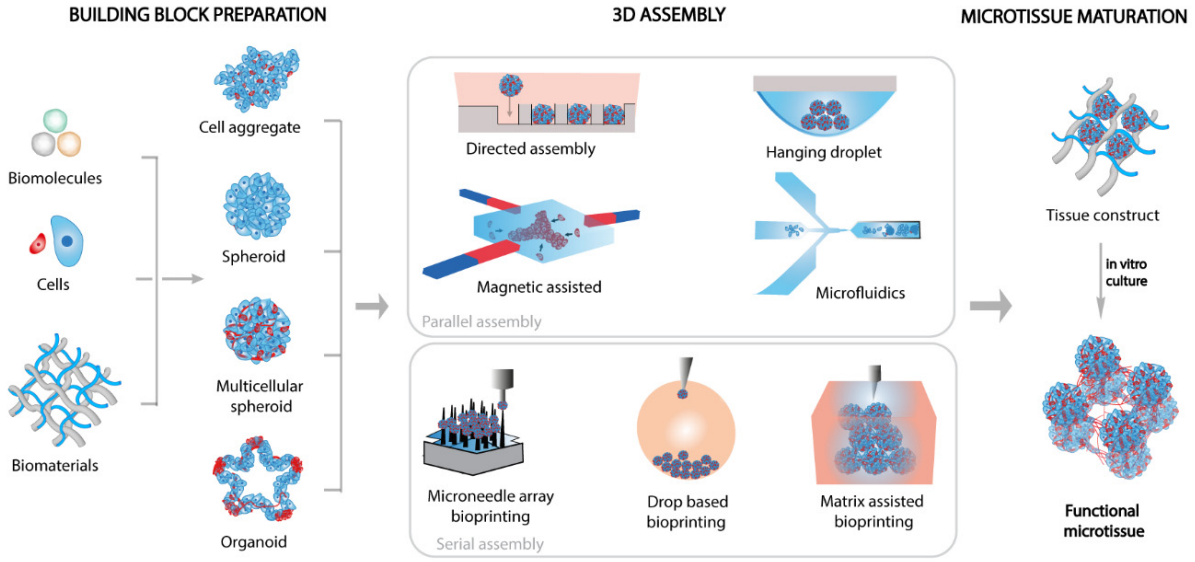

Figure 1. Illustration of microtissue fabrication by assembling in space different types of engineered cell aggregates. Emblematic assembly techniques are displayed with popular multicellular structures such as aggregates, spheroids, and organoids.

2. Engineering Novel Building Blocks for Microtissue Formation

Despite considerable progress in tissue engineering, the development of relevant tissue models reproducing the cell population diversity, the cellular organization, and the environment found in organs is a major challenge. The behavior of mammalian cells in a tissue is indeed governed by specific three-dimensional (3D) microenvironments that involve a dynamic interplay between biochemical signals provided by the extracellular matrix (ECM), cell-cell interactions, and soluble factors. Moreover, the physical properties of the microenvironment, including stiffness, geometry, and topography act in concert with biochemical signals to impact cell fate, tissue homeostasis, and functionality [14,15]. Current 2D culture models have demonstrated the ability to form de novo extracellular matrices (ECMs) from seeded cells, but this planar configuration cannot reproduce certain key physiological features of the in vivo native environment, including the dynamic cell-ECM, cell-cell interactions, and the heterogeneity and complexity of cell architectures in 3D (e.g., tubular structures as intestine; hollow, nontubular, viscous organs as vagina; solid organs as liver and bone) [16,17]. To date, one of the major bottlenecks in tissue engineering is the organization in 3D of multiple cell types associated with specific matrix compositions to initiate the structural organization of tissues. In this respect, embedded mammalian cells within hydrogel materials have been largely investigated to generate 3D tissue structures [18]. This approach has attracted significant interest due to the tunability of the properties of the embedding material. This versatility has been used to mimic natural ECM to control the porosity of the microenvironment, which is crucial for cell proliferation

and transplantation and to shape the biological artifact in 3D [19–21]. Many studies have attempted to engineer cell-laden structures with ideal geometric shapes that can induce tissue fusion to produce 3D constructs. There is now a deeper appreciation of the development of these small pieces of tissues, often called microtissues, to recreate the complexity of native architectures and favor their integration and maturation in vivo (Box 1). Even if they cannot fully mimic in vivo situations, microtissues built up from well-controlled and tunable matrices, and cell types have generated interesting results for organotypic studies and transplantation [11,22]. However, some limitations of this approach have been reported and discussed such as relatively low cell density, the lack of cell-cell interaction, and the poor diffusion of metabolites within the structure. Altogether these effects affect cell viability and impede the emergence of advanced tissular functions [23,24].

Box 1. Definition of different types of cell aggregates.

Cell aggregate: Cell aggregation is a generic term describing the clustering and adhesion of initially separate cells to form an aggregate. The aggregate morphology permits re-establishment of the cell-cell contacts normally present in tissues; therefore, cell function and survival are often enhanced in aggregate culture.

Spheroid: Spheroids are generated from primary cells or immortalized cell lines. The common composition is one cell type. However, multicellular spheroids loaded with different cell types can be formed when a culture medium is optimized for co-culturing.

Organoid: Organoids originate from tissue-derived adult stem cells, embryonic stem cells, or induced pluripotent stem cells, capable of self-renewal and multi/pluripotency. In suitable conditions, these immature cells are able to give rise to the different phenotypes present in tissues. Therefore, a key difference separating organoids from spheroids is that organoids better represent the in vivo cellular heterogeneity and physiological functionality of the organ.

Assembloid: Assembloids are the next generation of organoids. They combine organoids generated from different organs or different regions of an organ. Culture media optimization, mentioned for the generation of multicellular spheroids, is even more critical to assembling organoids.

The use of cell aggregates (Box 1) as a building block for the formation of microtissues requires the development of specific methods capable of creating 3D architectures while providing a suitable microenvironment to promote tissue maturation and reach a functional state. Methods such as directed assembly, magnetic assembly, microfluidic assembly, or hanging droplets benefit from spontaneous interaction mechanisms in confined geometries and provide parallel processes to assemble a large number of entities in a single step. These methods usually provide simple construction approaches, but they often lack the degree of accuracy and control required to create complex architectures with arbitrary arrangements. In this respect, bioprinting has recently emerged as a sequential but versatile technique for the creation of custom 3D configurations of cellular aggregates. Bioprinting gathers several methods that allow the direct placement of cells or cell aggregates with or without, together with a biomaterial mimicking extracellular matrix (ECM). It includes droplet-based or robotic handling methods that have shown considerable potential for creating complex architectures from cell aggregates.

Here, we outline several methodologies and summarize their merits and limitations for the creation of microtissue constructs (Table 1). These technologies will be further discussed in the following paragraphs.

Table 1. Comparison of assembly methodologies of cell aggregates for tissue constructs.

Method	Directed Assembly	Magnetic Assisted	Microfluidic Handling	Hanging Droplets	Bioprinting		
					Drop Based	Microneedle Arrays	Pressure Driven
Assembly Process	**Parallel**	**Parallel**	**Parallel**	**Parallel**	**Serial**	**Serial**	**Serial**
Working principle	Spheroids confinement in patterned templates or scaffolds	Inclusion of magnetic nano/ microparticles within spheroids	Use of convective flow in confined geometry to trap spheroids	Merging of neighboring droplets containing spheroids	Use of single spheroid loaded droplets as carriers	Use of a robotic arm to trap spheroids in an array of needles	Deposition of spheroids by aspiration system into, temporary or not, hydrogels
Cell types	Rat cardiomyocytes, rat cardiac fibroblasts, human pluripotent stem cells, equine cartilage cells	Microvascular endothelial cells, rat embryonic spinal cord cells	Patient-derived parental and metastatic OSCC tumor cells, Human HepG2 hepatocytes	Human HepG2 hepatocytes, HEK293T cells	Human microvascular endothelial cells (HMVEC), HUVECs	Human dermal fibroblasts, human aortic smooth muscle cells, micro-mini pig mesenchymal stem cells.	Human iPSC-derived cardiac cells, HUVECs, human mesenchymal stem cells, murine 3T3 cell line, murine intestinal cells.
Culture duration post-assembly	From a few hours to several weeks Up to 60 days with hiPSCs	From a few days to several weeks	Short term	Short term	Short term	Mostly a few days, up to two weeks	Up to three weeks
Spheroid handling	Contact	Non-contact	Non-contact	Non-contact	Non-contact	Contact	Contact
Advantages	Rapid tissue assembly Flexibility over the use of different spheroid types Controllable optical mapping Suitable for matrix rich tissues (bone, cartilage)	Compatible with hydrogel embedding Control of spheroid positioning inside complex patterns Possible stacking of multiple spheroids layers to generate 3D tissue	Fine control over microenvironment t 3D culture perfusion Compatible with drug screening purpose	Combinatorial approach Flexibility over the use of different spheroid types	High control of spheroid positioning Quality control for the generation of droplets loaded with individual spheroids Possibility to engineer self-folding droplets	High control of spheroid positioning Combinatorial approach Mechanical stability provided during tissue formation by the needles array	High control of spheroid positioning Microvasculature fabrication using sacrificial material Promotion of microtissue survival by scaffold-based approaches
Limitations	Low reproducibility Limited control over pattern geometry	Long-term presence of magnetic particles Potential cytotoxic effects	Poor control over 3D architecture Difficult to standardize and scale up for multicellular systems	Poor control over 3D architecture Low reproducibility Limited long-term maintenance with necrotic core formation	Non-physiological cell density Limited performance for complex 3D structuration	Low flexibility Not suitable for large aggregates Time-consuming Possible low cohesion of the bio-construct after micro-needle array removal low reproducibility	Low printing velocity due to sequential handling of spheroids Challenging maintenance of mechanical stability when associated with sacrificial material
3D Positional accuracy	Low	Medium	Low	Low	High	High	High
Scalability	Low	High	Difficult for multi-cellular system	Low	Medium	Low	Reduced by printing velocity
Comments		Ongoing developments to reduce particle cytotoxicity	Requires further developments for the evolution of spheroid assemblies towards forming a microtissue	Ongoing studies to increase the diffusion of oxygen and nutrients	Requires careful control over the synchronization of spheroid printing and the movement of the printing nozzle	Ongoing development of tailoring micromanipulators that can match spheroid dimensions	Requires careful attention of the choice of supporting hydrogel
References	[25–27]	[28–31]	[32]	[33–35]	[36,37]	[38–46]	[22,47–50]

2.1. Directed Assembly of Spheroids and Organoids

Self-assembly is usually defined as the autonomous organization of mobile objects into complex architectures [51,52]. Directed assembly involves the introduction of driving forces such as chemical bonding, physical interactions, geometrical confinement, or biological adhesion that can be tuned to orient the assembly into a desired structure or configuration [53]. This concept has been recognized as an efficient approach to ordering large numbers of mobile objects (e.g., microparticles, cells) in a parallel way and has been recently extended to spheroids. Kim et al. (2018) generated scaffold-free 3D cardiac microtissues composed of multicellular spheroids used as building blocks and arranged in different configurations such as homotypic or heterotypic pairs and elongated structures (Figure 2A). Using a construction strategy based on the confinement of spheroids within topographically patterned templates the authors demonstrated the construction of fused heterocellular cardiac tissue with interconnected morphologies [25]. Birey et al. (2017) applied the same method for the fusion of two forebrain organoids (Figure 2B) to mimic human brain development and demonstrate inter-neuronal migration [26].

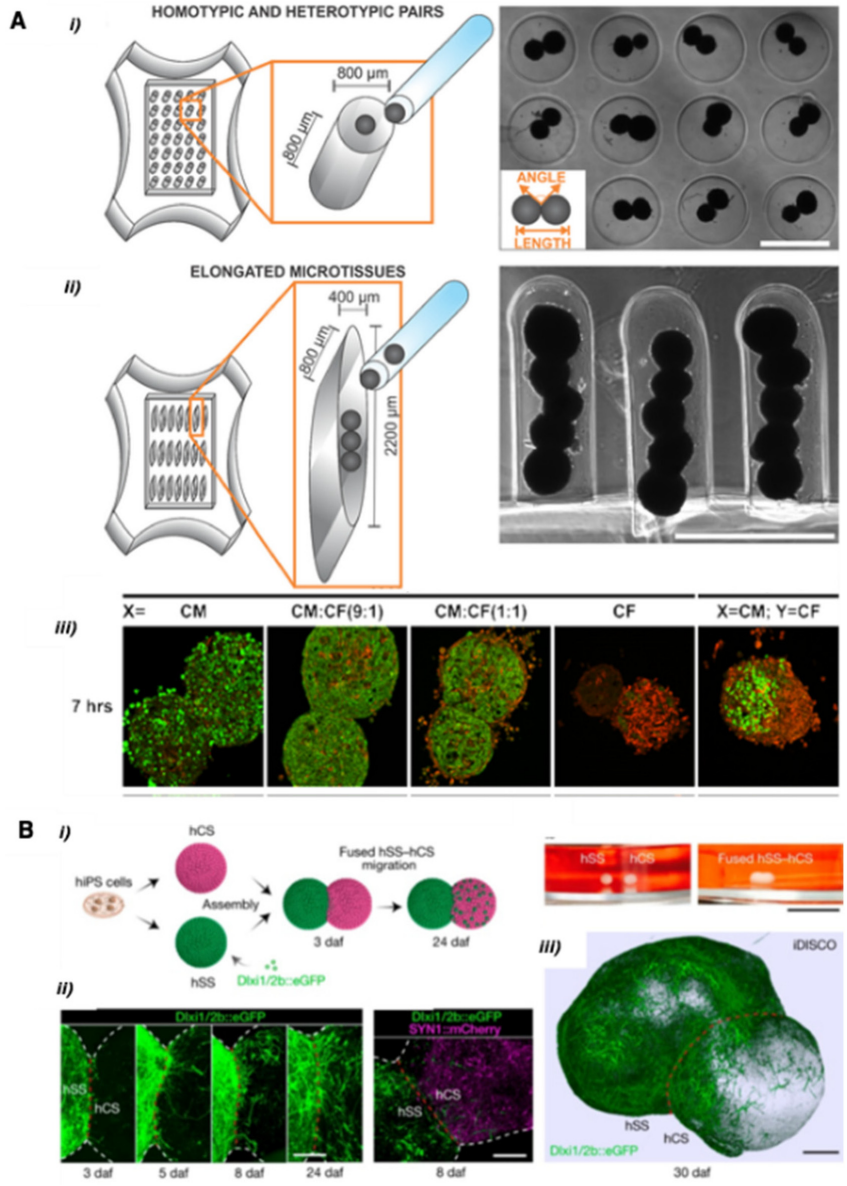

Figure 2. Directed assembly approaches. (**A**) Formation of cardiac spheroid pairs, and elongated microtissues. Cardiac fibroblasts (CF) and cardiomyocytes (CM) in suspension were co-seeded to the center of the hydrogel. (i) cylindrical microwells containing homotypic or heterotypic spheroid pairs

(ii) elongated molds to form a larger building block. Scale bars: 800 µm. (iii) Cryosections of spheroids stained with antibodies recognizing α-sarcomeric actinin and vimentin for the CMs (green) and CFs (red), respectively. Scale bar: 50 µm. Reprinted from Ref. [25]. (**B**) Spheroid fusion of human cortical spheroids (hCS) and human subpallium spheroids (hSS). (i) Scheme of spheroid assembly and morphology of the spheroids before and after assembly. (ii) Time-lapse of migration from hSS into hCS (daf: days after fusion). (iii) 3D image of hybrid cerebral microtissue. Scale bar: 200 µm. Reprinted with permission from Ref. [26]. Copyright 2017, Springer Nature.

Another report by Schuurman et al. (2016) investigated the placement of cartilage multicellular spheroids inside an amphiphilic poly(ethyleneglycol)-terephthalate/poly(butyleneterephthalate) (PEGT-PBT) scaffold. The spheroids were assembled to produce a large-scale cellular 3D construct [27]. The zonal cell distribution pattern was not preserved after 31 days of culture; however, the authors evidenced some lateral spheroid fusion resulting in abundant cartilaginous tissue formation [51].

This method provides considerable flexibility in using different multicellular spheroids and controlling their relative proportion [54,55]. This characteristic might be advantageous for rapid and parallel tissue assembly but one of the major obstacles is the lack of flexibility for the creation of arbitrary pattern geometries, in particular when targeting complex or sparse 3D architectures.

2.2. Magnetic Assisted Assembly

Magnetic-driven positioning is a non-contact method to assemble spheroids. The inclusion of magnetic nano/microparticles is required in order to manipulate and position cell aggregates in levitation. The magnetic forces are involved to create specific attractive forces with templates of magnets that can be designed by computer-assisted methods (Figure 3). The organization can be obtained by labeling the cells with magnetic particles or by adding these particles to the cell culture medium [28,56,57]. The magnetic forces are used to maintain the formed 3D architecture while the fusion of the cellular building blocks occurs [29]. Magnetic assisted assembly can be easily upscaled, and combined with other methods such as hydrogel photopatterning [30], but it remains limited by the long-term presence of magnetic particles within the tissue. In a recent study conducted at the International Space Station, undesirable cytotoxic effects of the particles were reduced by using low-toxicity Gd^{3+} salts and performing the assembly in microgravity. The latter was successfully reported by Parfenov et al. (2020) in constructing 3D cartilage tissue incorporating human chondrocytes. The fusion of chondrospheres was observed in a non-toxic paramagnetic Gd^{3+} cell culture medium overcoming the gravitational force constraint [31]. This method is also useful for positioning spheroids on complex patterns with a possible stacking and 3D tissue generation [58,59].

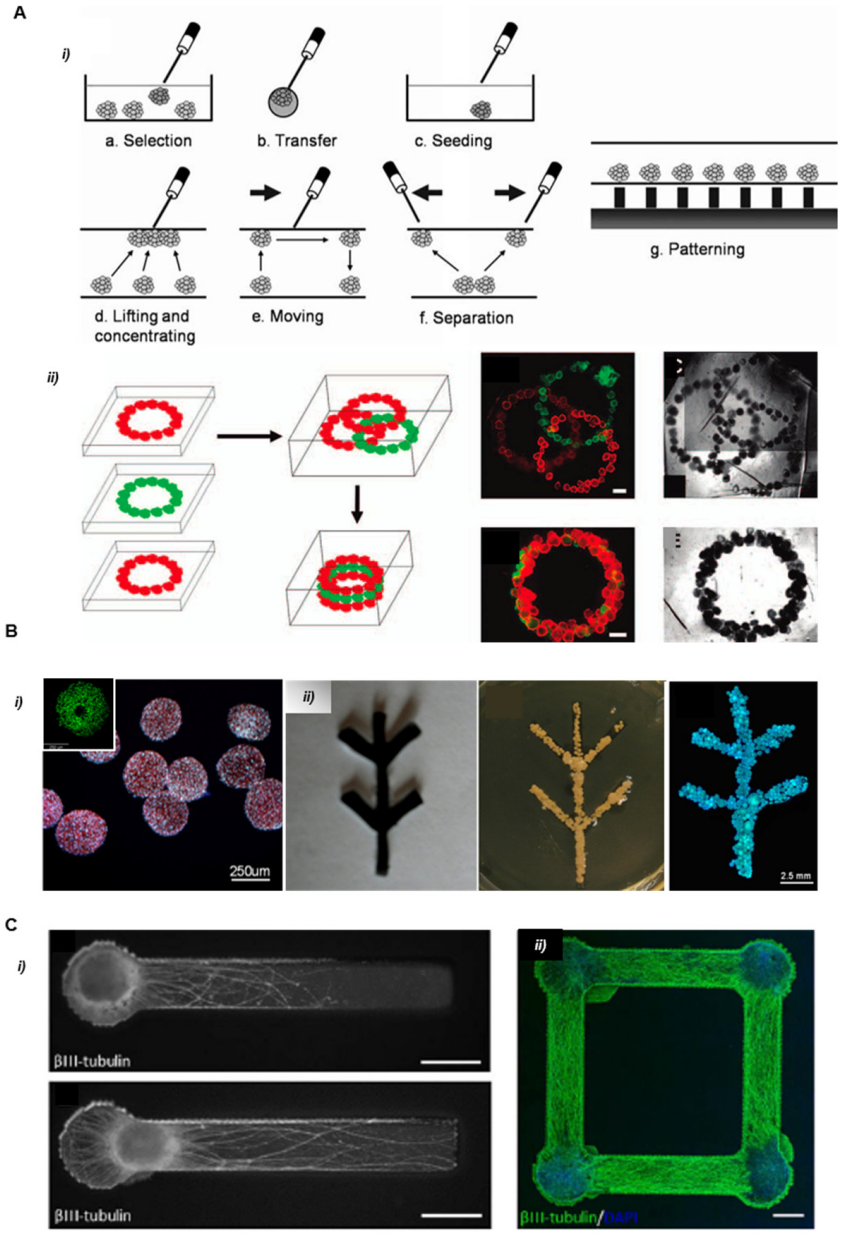

Figure 3. Manipulation of spheroids using a magnetic force. (**A**) (i) Schematic demonstration of spheroid manipulations that can be achieved by using a magnetic force. (ii) The scheme of layer-by-layer tissue reconstruction. Three pieces of human microvascular endothelial cell spheroids in Mebiol gel were stacked into an overlapped or aligned three-layered structure. Scale bars, 500 mm. Reprinted with permission from Ref. [29]. Copyright 2008, Mary Ann Liebert. (**B**) Patterning using paramagnetic particles (i) Size distribution and viability (inset) of superparamagnetic iron oxide nanoparticles (SPION) loaded endothelial cell spheroids. (ii) Light microscopy of magnetic template for the fusion of the spheroids (left panel). Magnetic assisted assembly of the spheroids at 48 h (middle panel). Confocal microscopy of preliminary fusion spheroids at Day 10 (right panel). Scale bar 2.5 mm. Reprinted with permission from Ref. [28]. Copyright 2013, John Wiley and Sons. (**C**) Magnetic assembly of central nervous system (CNS) spheroids. (i) Phase images of neural constructs (βIII-tubulin, white) indicate that the positioning of spheroids in constructs is more accurate with magnetic bioprinting (top panel) than manual placement with pipet alone (bottom panel). Scale bar 500 µm. (ii) Confocal imaging showing localized cell bodies (blue) and extending neurites (green) demonstrating the accurate positioning of multiple spheroids in the same construct using a multi-magnet tool. Scale bar 200 µm. Reprinted with permission from Ref. [30]. Copyright 2009, IOP Publishing.

2.3. Microfluidic Handling

Microfluidics has emerged as a powerful tool for the controlled fabrication and programmed assembly of living building blocks [60]. In particular, the use of convective flow in confined geometries provides a simple and easily parallelized route toward the assembly of mobile objects in a suspension. This approach has first been applied to the construction of spheroids or organoids starting from individual cell suspensions. More recently this approach was extended to multi-spheroid constructs. In that respect, Ong et al. (2017) proposed a microfluidic cell culture device capable of directly immobilizing and maintaining the viability and functionality of 3D multicellular spheroids [32] (Figure 4). Patient-derived parental and metastatic oral squamous cell carcinoma OSCC tumor and human HepG2 hepatocyte spheroids were assembled and cultivated for up to 72 h with good viability and functionality. Whereas the evolution of the spheroid assemblies towards a microtissue could not be demonstrated, the metabolic activities of HepG2 spheroids cultured in the 3D printed device were significantly higher than those of static 2D, which were consistent with previous reports that 3D perfusion cultures enhance the liver-specific functions of hepatocytes [32]. These results also demonstrated the advantages of microfluidic culture systems for drug screening purposes or improving culture conditions toward tissue implantation and regeneration.

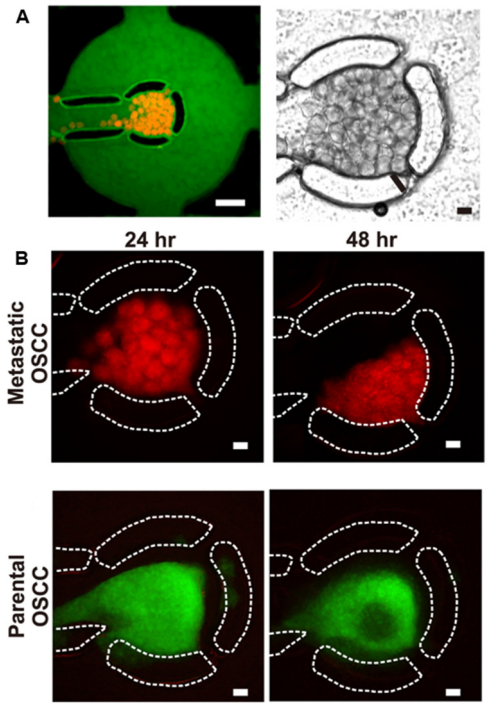

Figure 4. Visualization of metastatic oral squamous cell carcinoma (OSCC) spheroids immobilized within the cell culture chamber by (**A**) fluorescence (left) and light transmission (right) imaging. Culture medium was spiked with FITC-tagged BSA to visualize the cell culture chamber. Scale bar = 500 μm. (**B**) Fluorescent images of metastatic and parental HN137 OSCC spheroids in the microfluidic device after 24 h and 48 h of perfusion culture. Scale bar 100 μm. Reprinted with permission from Ref. [32]. Copyright 2009, IOP Publishing.

2.4. Programmable Assembly in Hanging Droplets

A straightforward approach to the formation of a spheroid is the hanging-drop method. Cells are suspended in droplets of the medium, where they develop into coherent 3D aggregates. In addition to being simple, the method eliminates surface interactions with an underlying substratum, requires only a few starting cells, and is highly scalable and reproducible. For the same reasons, this method has been applied to the co-cultivation of mixed cell populations and the fusion of cell aggregates.

In a recent article, Sloan et al. (2018) demonstrated the ability to generate region-specific spheroid models to study human brain development [33]. The authors have produced subdomain-specific forebrain spheroids from human pluripotent stem cells (hPSCs) and shown how to combine the neural spheroids (human cortical spheroids (hCSs) and human subpallial spheroids (hSSs)) in vitro to assemble forebrain assembloids that recapitulate the interactions of glutamatergic and GABAergic neurons seen in vivo and form physiologically relevant connections when assembled together. For that purpose, spheroids were fused by confinement in the bottom of a 1.5-mL Eppendorf tube, providing a simple and highly parallelized method for the creation of neural assembloids. Using a similar approach, Andersen et al. (2020) have demonstrated the assembly of derived organoids resembling the cerebral cortex or the hindbrain/spinal cord with human skeletal muscle spheroids to generate 3D cortico-motor assembloids [34]. The authors envision that his three-way system could develop a human cellular model of spinal cord injury (SCI) or be applied to assembloids of various parts of the central nervous system to bring insights into understanding its underlying developmental mechanisms into identifying therapeutic strategies.

More recently, Cui et al. (2021) have developed a droplet microarray (DMA) platform that enables the parallel generation of cell spheroids using hanging drop methods [35]. From the conceptual point of view, this approach is similar to conventional strategies used for spheroid preparation that provide geometrical confinement in a cell suspension thanks to the shape of the drop interface. The authors advantageously combined this strategy with the planar arrays of hydrophilic patches that permit to generate, where the drops were developed and were used as anchoring structures separated by superhydrophobic barriers. Spheroids were generated by dispensing suspended cells in 50 to 300 nL liquid volumes and exploiting the gravity-driven aggregation process occurring at the droplet-air interface. By engineering specific DMA with controlled size and distances, it is then possible to add controlled volumes of the medium into neighboring droplets to selectively induce a spontaneous merging. Finally, the two initially separated spheroids were confined at the droplet base to promote their fusion. The combinatorial capacity of this method has allowed the creation of binary, ternary and quaternary assemblies (Figure 5). The method was applied to the study of the fusion of HepG2 spheroids or to the study of Wnt signaling propagation between 3D spheroids with varying cell compositions (HepG2, HeLa, and HEK 293T) first on double and further on triple spheroid complexes [35]. This method opens the way for high throughput and combinatorial investigations for rare and limited cell types such as primary patient-derived cells. It is an open droplet microarray platform that enables the structure of interest to be easily retrieved during experiments. However, it is poorly adapted to the creation of larger dimension multi-spheroid assemblies with controlled 3D architectures due to the formation of necrotic core induced by the limited diffusion of oxygen and nutrients.

2.5. Bioprinting

Bioprinting is an additive construction process used to deliver and spatially organize cells by stacking and assembling them into 3D architectures through different methods. This process is applicable to individual cells, cell aggregates, and spheroids with or without a supporting biomaterial. The process can be automated, thus allowing it to handle large quantities of biological materials and to create 3D arrangements with a resolution down to the cell level with high reproducibility [22,61,62].

Current conventional cell printing systems (extrusion, inkjet, or laser-assisted method) offer a resolution below 50 µm, but they imply laborious multi-material printing strategies and lack the possibility of handling large cellular constructs such as cell aggregates, organoids, or spheroids. The concept of printing tissue spheroids was first introduced in 2008 [63–65]. Forgacs et al. (2008) precisely positioned multicellular spheroids by bioprinting onto a layer of collagen, known as a biopaper [65]. Since then, many reports have been detailing new automated methodologies for spheroid printing based on drop dispensing or

on dedicated microgrippers [13,66–68]. In bioprinting technologies, homogeneity in the size distribution of spheroids is a critical parameter to make them processable or dispensable through a bioprinter head to prevent damage or clogging. Therefore, standardization of the spheroid dimension is largely desirable for continuous dispensing.

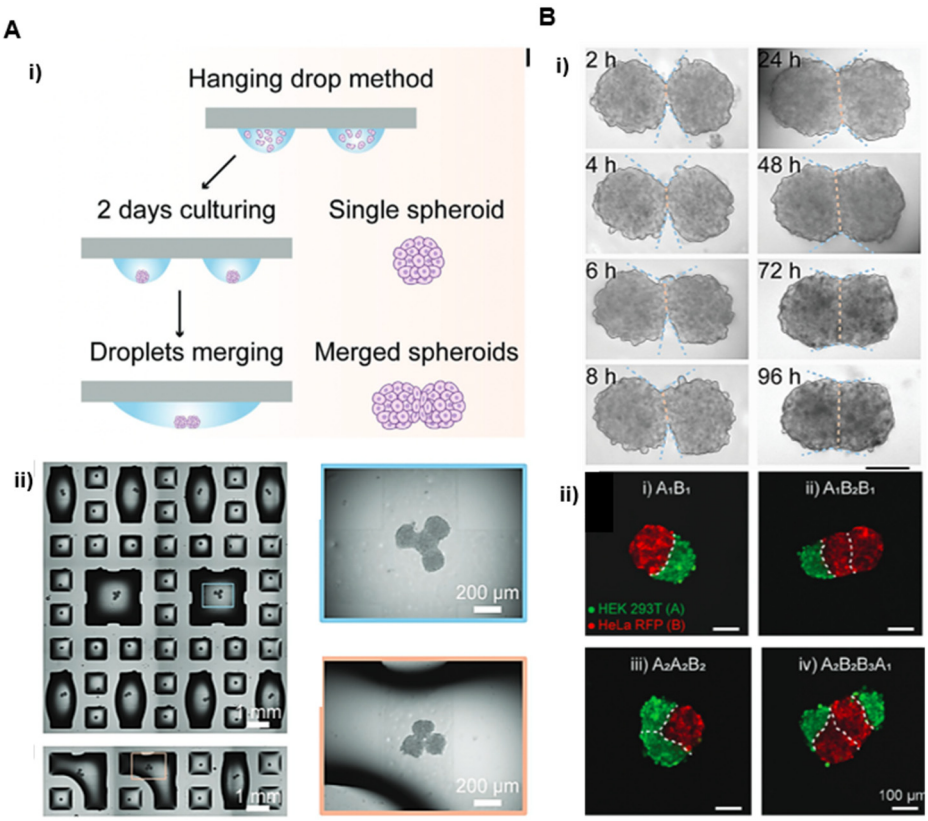

Figure 5. Programmable hanging drop method to form arrays of spheroids Reprinted with permission from Ref. [35]. Copyright 2020, John Wiley and Sons. (**A**) Merging of adjacent droplets. (i) Schematic of the hanging drop method to form arrays of cell spheroids using hydrophilic spots divided by superhydrophobic borders (ii) Micrograph of an array containing 2, 3, and 4 merged droplets (left side) and enlarged images of fused spheroids in merged droplets after 24 h (right side). (**B**) Examples of multi-spheroid architectures formed by this method. (i) Micrographs of two HepG2 spheroids fusing step by step over 96 h. (ii) Fluorescence microscopy images of hetero-spheroid architectures built from two different cell lines (HeLa cells expressing RFP and HEK 293T stained with green 24 h post merging. Scale bars 100 μm.

2.5.1. Drop Based Printing

Droplet-based bioprinting uses methods similar to those involved in inkjet printers [68]. A single spheroid is loaded into a droplet of a bio-ink, which is used as a carrier for the printing and positioning of spheroids on surfaces (Figure 6). The key elements of drop-based bioprinting are the physical properties of the ink, the volume of the droplet, and the frequency of deposition, which are monitored by the dispensing head of the printer. Careful control has to be provided for the synchronization of the spheroid printing together with the movement of the printing nozzle. This method allows the fabrication of layers made of spheroids [12] together with more complex 3D structures (Figure 6A) [36]. More recently, Gutzweiler et al., (2017), adapted this scaffold-free bioprinting technique to automatically generate HUVEC spheroids via the hanging drop method [37]. The authors demonstrated a controlled deposition of single spheroids by drop-on-demand printing with interesting capabilities (1 μL droplet volumes and assembly of around 1500 HUVEC spheroids on a fibrin surface). The authors reported a spheroid printing efficiency of 97% (Figure 6B). The efforts devoted to the automation of the printing process have yielded a

significant improvement in resolution, processing speed, and material saving that makes this technology upscalable. However, this method has limited performance in creating vertical or 3D complex structures and still does not provide cell densities mimicking native tissues.

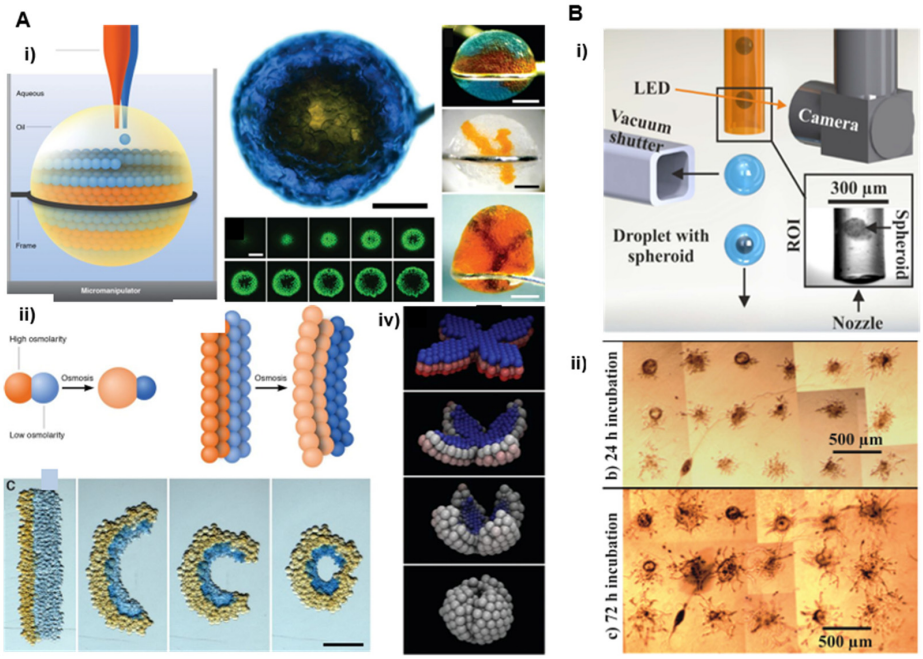

Figure 6. Droplet-based bioprinting. (**A**) Based on osmolarity gradients Reprinted with permission from Ref. [36]. Copyright 2013, The American Association for the Advancement of Science. (i) Droplet networks printed in bulk aqueous solution. The principle of aqueous droplets is dispensing into a drop of oil suspended in bulk aqueous solution (left side). Top view of a network printed in aqueous solution. A core of orange droplets is surrounded by a shell of blue droplets containing fluorescent pyranine (top middle). Confocal microscopy of the network in horizontal sections showing the fluorescent shell of droplets around the nonfluorescent core (bottom middle). Different types of networks printed in bulk aqueous solution (right side). Scale bars 400 µm. (ii) Principle of osmolarity gradients. (iii) Schematic of two droplets of different osmolarities joined by a lipid bilayer. The water flow through the bilayer causes the droplets to swell or shrink. (iv) Frames from a folding simulation of a network with a similar initial geometry Blue and red represent the lowest and highest initial osmolarities, respectively. White indicates the average of the two. (**B**) Single spheroid deposition setup Reprinted with permission from Ref. [37]. Copyright 2009, IOP Publishing: (i) Protruding transparent nozzle of a dispenser is primed with the spheroid solution. The generated droplet containing the spheroid can be dispensed onto a substrate if a spheroid is optically detected at the nozzle exit. If no single spheroid is detected, the droplet is aspirated by a vacuum shutter system. (ii) HUVEC spheroids were dispensed to defined positions and cultured for 24 h (top image) and 72 h (bottom image).

2.5.2. Bioprinting with Microneedle Arrays

The use of removable scaffolds for the assembly of the multi-spheroid construct was first reported by Itoh et al. in 2015 [38]. This method is inspired by the Japanese traditional art Ikebana and uses arrays of needles as a temporary scaffold in which spheroids are immobilized by a robotic arm. This biomaterial-free method enables the accurate spatial organization of the spheroids or organoids in complex tissues analogs of practically any composition and organization [39–41]. The mechanical stability provided by the scaffold favors cell interaction, matrix secretion, and the formation of cohesive and functional tissue. The absence of biomaterials is also advantageous for implantation experiments, as it reduces the potential immune response. Itoh et al. used this method to produce models

of the artificial aorta and implanted the resulting models in rats. The authors reported an endothelial network formation covering the inner surface of the tubular tissue after 5 days of implantation. Demonstrations of the printing and assembly of multicellular spheroids composed of human umbilical vein endothelial cells, human aortic smooth muscle cells, and human dermal fibroblasts were successfully achieved into scaffold-free small diameter tubular tissue (Figure 7A). This method provides a high accuracy thanks to the geometrical confinement permitted by the needle array. However, it imposes certain limitations regarding spheroid size to fit in the needle tip and gap between needles.

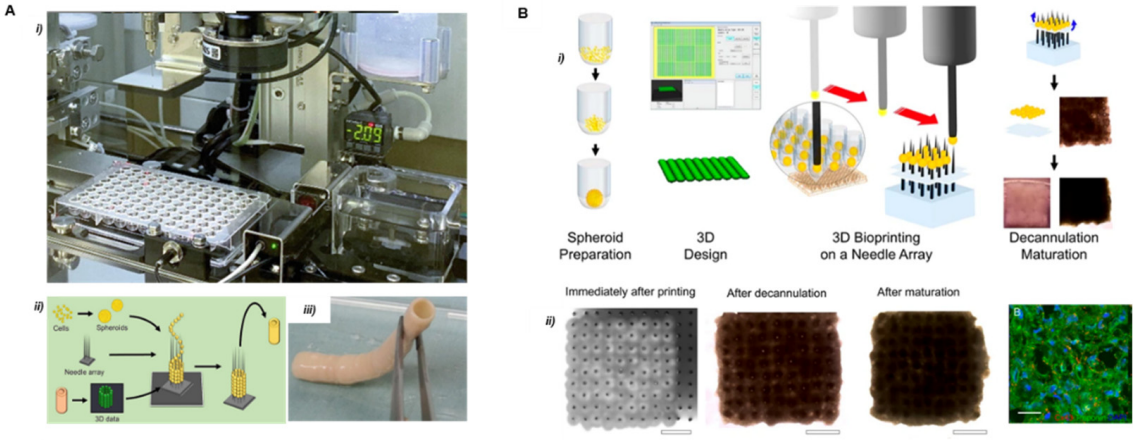

Figure 7. Principles of the Kenzan method. (**A**) Main components of the Kenzan bioprinting automated platform Reprinted with permission from Ref. [40]. Copyrihgt 2021, Springer Nature. (i) Robotic system. (ii) Illustration of methodology to create a scaffold-free cell-based vascular graft. (iii) A ready to implant cell-based vascular graft (diameter 5 mm × length 5 cm). (**B**) Bioprinting of cardiac patches using microneedle array principle Reprrinted from Ref. [46] (i) Schematic overview of biomaterial-free cardiac bioprinting process. (ii) Optical microscopy images at different steps and confocal microscopy of resulting cardiac patches. Scale bars 40 µm and 20 µm, respectively.

Moreover, needle-based bioprinting techniques are usually time-consuming and may not be adapted to build scalable constructs. The removal of the microneedle array is a critical step, especially if the mechanical cohesion of the cell is low. This difficulty results in low reproducibility and accuracy [38,41–45]

In 2017, Ong et al. demonstrated the bioprinting of spontaneously beating cardiac patches from multicellular cardiac spheroids using the microneedle array method (Figure 7B) [46]. The handling system was based on a bioprinting platform allowing the sequential manipulation of an individual spheroid by vacuum suction and delivery. It allows for the selection of spheroids with the desired dimension, for example, between 450 µm to 550 µm in diameter for micromanipulation, and rejects the use of all others that do not fit these criteria. This method provides more than 90% cell viability in a single-layered patch. Severe limitations were observed for the construction of multi-layer thick patches that reveal slow conduction velocity and a decrease in cell viability due to a lack of vascularization in the tissue. Moreover, the weak mechanical properties of the 3D bioprinted patches and their fragility during decannulation turned out to be a limitation for implantation applications.

It is interesting to notice that the methods presented here rely on the use of robotic handling to manipulate spheroids selectively and assemble them at precise locations. While most demonstrations rely on aspiration-based principles using pipetting platforms or bioprinters, this application has attracted a large interest in the field of robotic handling. Recent micromanipulation approaches have demonstrated their flexibility and accuracy for the handling of living objects such as cells, spheroids, and embryos while preserving their viability and integrity. In their recent work, Kozaki et al. (2020) developed a micromanipulator through high-resolution micro stereolithography that can capture and release a spheroid

with minimal damage [69]. Spheroids were captured from the culture medium and trapped in a droplet of culture medium inside the cage-like microfingers. Injection of air through the fingers with controlled pressure was then involved in releasing the spheroid at the desired position, thanks to the elastic deformation of the fingers. This method allows the adaptation of the micromanipulator to match the dimensions and mechanical properties of the spheroid to be handled [69,70].

2.5.3. Pressure Driven Bioprinting

Improving the physiological relevance of bioprinting and promoting vascularization and survival of the microtissue over long periods of time are key features in the perspective of tissue function and reimplantation. In this respect, a novel spheroid aspiration method was proposed and successfully tested on osteogenic spheroids. Ayan et al. (2020) developed an original assembly method using aspiration forces and high precision positioning onto hydrogel substrates [47,48]. The authors demonstrated vascular network formation by studying angiogenic sprouting of spheroids and osteogenic tissue engineering (Figure 8A). This method is compatible with a wide range of spheroid dimensions and is applicable to both scaffold-based and scaffold-free configurations. It provides a micrometric precision in spheroid placement in controlled architectures and is compatible with multi-spheroid construction. As previously mentioned, the biggest challenge of this kind of method is linked to the low speed imposed by the sequential handling of spheroids. Moreover, limitations arise for the assembly of complex 3D architecture that requires an external scaffold or sacrificial material to maintain the mechanical stability of the construct during printing. It is worth mentioning that the choice of supporting hydrogel (e.g., Coll-I or GelMA) around the spheroid is essential to promote adhesion and tissue integrity.

Another remarkable report by Daly et al. (2021) described a method using a supporting hydrogel to form high cell density microtissues by controlled spheroid fusion [49]. The properties of the supporting hydrogel enable precise positioning and holding of spheroids and high spheroid viability after printing (Figure 8B). The viscoelastic and non-adhesive nature of the hydrogel facilitates the fusion between adjacent spheroids into prescribed, stable structures. By mixing spheroids of different cell compositions, iPSC-derived cardiomyocytes, or primary human cardiac fibroblasts, the authors reported a model of focal cardiac fibrosis that replicates post-myocardial infarction pathologies with reduced contractile output and electrical synchronization.

The same kind of method has been implemented to manufacture thick tissues. Skylar-Scott et al. (2019) produced multicellular cardiac tissue (HUVEC cells and human iPSC-derived cardiac spheroids derived organoids) with engineered ECMs and embedded vasculature through bioprinting of a sacrificial bio-ink [50]. The developed method manipulates hundreds of thousands of organ building blocks (OBB) into tissular matrices with high cellular density (Figure 8C), in which hierarchical vascular channels can be introduced. Despite the need for large-scale production of organoids (~10^8 cells/mL), this method enables the fabrication of perfusable organ-specific tissues of arbitrary volume and shape in a scalable manner.

The bioprinting strategy also offers the possibility to print multiple cell types in the form of the concentrated cell suspension or cell aggregates obtained from dissociated organoids. Compared to spheroid printing, the reduced size of such aggregates prevents the risk of necrotic core formation and provides more flexibility for the cells to interact and evolve spontaneously towards a 3D architecture and functional tissue. Recently, Brassard et al. (2020) introduced a bioprinting concept adapted to the delivery of high density of stem cells or cell aggregates directly into extracellular matrices with a resolution down to the single line-level [22]. The authors showed the spontaneous evolution of printed intestinal stem cells (ISC) or mesenchymal stem cells (MSC) towards a tubular-shaped tissue reproducing the luminal morphology of the intestine. This extrusion-based system was also used for the organization of centimeter-scale tissues that comprise features such as lumens or branched vasculature. Morphogenesis could also be modulated by sequential deposition of the supporting epithelial cells and the organ boundaries of the gastrointestinal tract (Figure 9). Sachs et al. (2017) also used the fusion

of intestinal organoids to generate centimeter-scale interconnected 'mini guts.' The authors generated macroscopic size intestinal tubes from small cystic organoids by embedding them in a floating collagen hydrogel to allow the spheroids containing stem cells to align and self-organize [71]. These two methods are inspiring examples of direct bioprinting in hydrogels allowing self-organization of the cell aggregates from millimeter to centimeter scales.

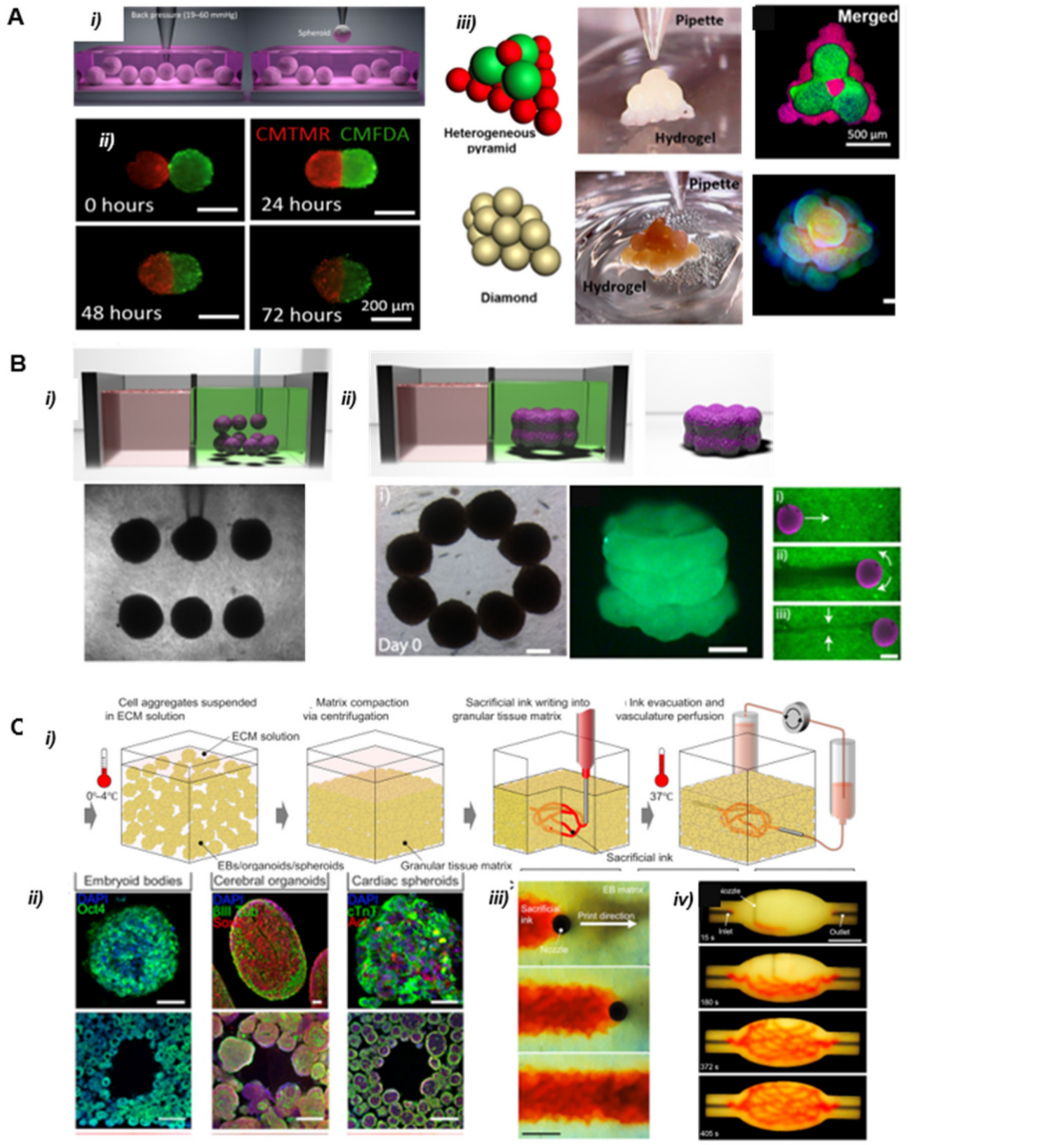

Figure 8. (**A**) Bioprinting of spheroids by a pressure-driven method Reprinted from Ref. [47]. (i) Illustration of the picking of individual spheroids by aspiration. (ii) Time-lapse images of the self-assembly process after bioprinting of 3T3 spheroids at different time points. (iii) Illustrations and micrographs of different shaped 3D printed structures with HUVEC and MSC spheroids represented in red and green, respectively. Dapi (blue) was used for staining of nucleus. (**B**) 3D bioprinting spheroids in supporting hydrogels Reprinted from Ref. [49]. (i) Spheroid deposition. (ii) Spheroid fusion in and removal of the structure from the gel after 4 days of culture. Scale bars 200 µm. (**C**) Sacrificial writing into a tissular matrix based on extrusion bioprinting Reprinted from Ref. [50]. (i) Illustration of the process. (ii) Examples of cellular construction for different OBB (organ building block) based matrices composed of embryoid bodies, cerebral organoids, and cardiac spheroids. (iii) Time-lapse of sacrificial ink (red) writing within a tissular matrix. (iv) Embedded 3D printing of a branched, hierarchical vascular network within a tissue matrix connected to inlet and outlet tubes, scale bar 10 mm.

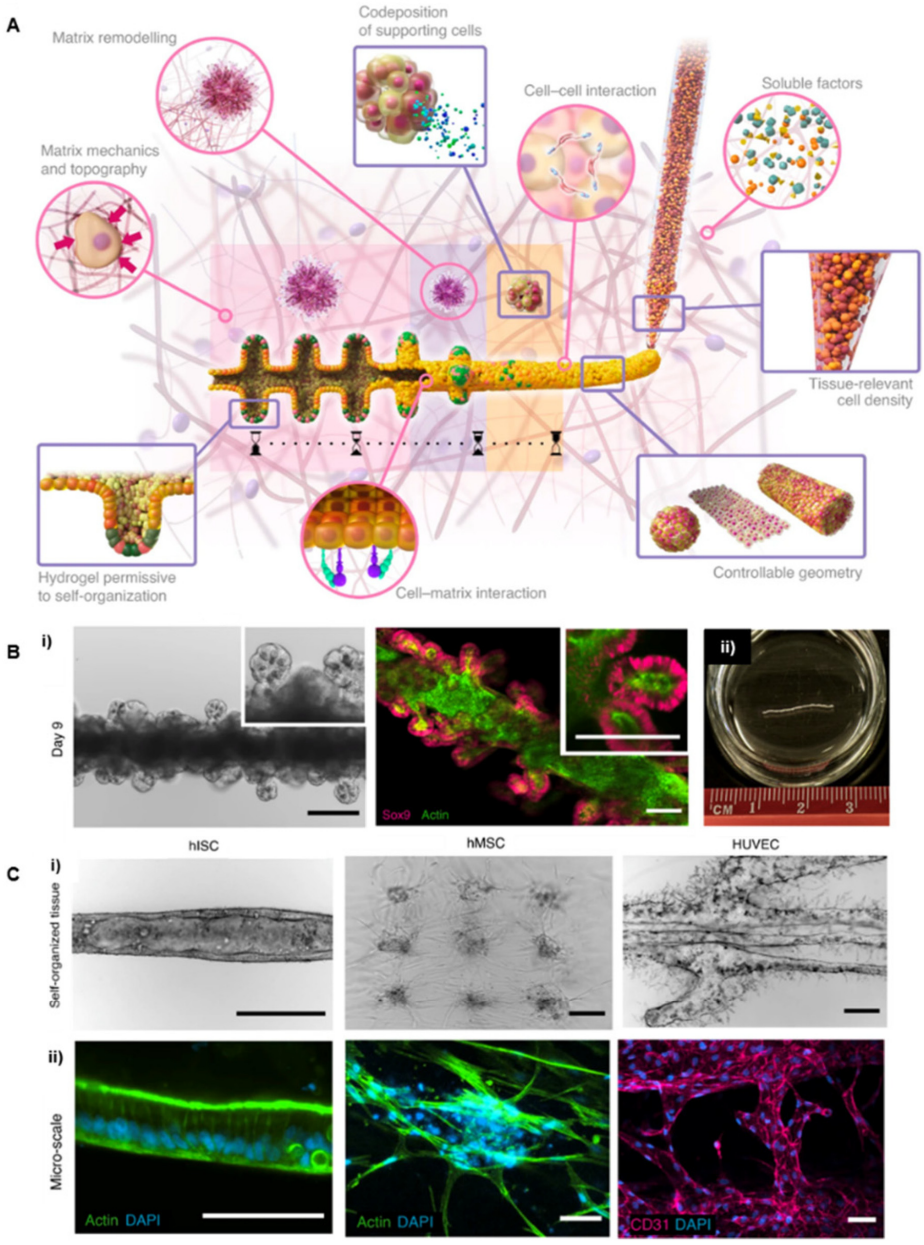

Figure 9. Bioprinting high cellular densities inside hydrogels. Reprinted with permission from Ref. [22]. Copyright 2020, Springer Nature. (**A**) Macroscopic intestinal printing principle. Multicellular self-organization was achieved directly inside the hydrogel environment. (**B**) (i) Bright-field and confocal microscopy of the intestinal tube showing stem cells forming the crypts on Day 9. Scale bars, 200 µm (left), 100 µm (right). (ii) Image of a centimetric intestinal tube. (**C**) Bright-field and confocal microscopy of the embedded patterns of hISC, hMSC, and HUVEC cells. (i) Bright-field images. Scale bars, 500 µm. (ii) Cells were labeled with DAPI (blue) and F-actin (green) or CD31 (pink). Scale bars, 250 µm (left) and 75 µm (right).

3. Conclusions and Future Perspectives

All the technological developments and related instruments presented in this review are highly encouraging. They suggest that manipulating and assembling building blocks such as spheroids or organoids is a possible route for generating relevant pieces of tissues that exhibit overall dimensions compatible with their use as advanced physiological models. Compared to the assembly of individual cell suspension at low concentrations, 3D cell aggregates provide cellular building blocks promoting cell-cell interactions, ECM secretion,

cell differentiation, and tissue vascularization, thus leading to culture models that can better recapitulate the structure and function of native tissues.

This field of research activity is expanding, driven by the demand for the reduction of animal testing in agreement with the current guidelines and legislation recommending following the "3R" principles: "Replace, Reduce, and Refine" [72,73]. Fundamental studies of various biological mechanisms linked to specific functions of tissues, pharmacological drug testing, and toxicology, precision medicine or regenerative therapies represent examples of the broad spectrum of the possible end-users of this kind of technology. The current state of the art of this kind of method clearly shows that the field is in an exploratory phase mainly focused on the handling and patterning of cells and spheroids. Up to now, little attention has been paid to the collective behavior of cells and their adequate supply of oxygen and substrates according to the chosen technology, whereas the issue of necrotic core and the poor perfusion of the inner cell mass is clearly established [22,54,62]. Pending more complete experimental data, it is reasonable to speculate that the aggregation in macrostructure without a "technological" help to improve the providing in substrates will lead to this kind of limits in long term culture. At this level of the domain's infancy, it is difficult to predict if a standardized method combining reproducibility, throughput, and versatility to all kinds of tissue constructs will emerge. We feel that according to the targeted tissue model (skin, brain, adipose tissue, bone, liver, intestine ...), the topological constraints required to mimic the physiological situation will select different methods to adapt to the final target (in vitro bioassay or transplantation). The process of building cannot be distinguished from the final goal again. Indeed, the field is not limited by a lack of technological solutions: automation methods and microfabrication techniques provide a large reservoir of processes that can be implemented for building 3D multicellular building blocks while preserving cell viability. The main objective of the domain is rather to combine the engineering process together with the biological evolution of the cells inside the constructs that need to be favored as a functionality of the tissue. Successful methods will be those combining top-down (engineering) and bottom-up (biology) processes in such a way that the evolution of the living entities is guided efficiently towards a directed architecture exhibiting the key functional features of the physiological counterpart. In other words, the expectation from the technological process of assembling is not the generation of a final functional structure but rather the construction of a scenario of cell evolution in 3D where the engineered structure triggers the evolution of the multicellular spheroids leading to the emergence of a function. In such a vision, the time evolution of the produced construct is as important as its design, while careful attention has to be paid to the conditions of long-term culture to allow maintenance and self-organization of multiple cell types. Future progress in the field is therefore linked to the development of simulation tools capable of modeling the evolution of the spheroids and cell populations during long-term culture. The results of these simulations will be crucial for guiding the selection of the cells to be incorporated inside the manipulated spheroids and for guiding the design of the construct during the assembling process.

Future works for researchers in the field need to address some common objectives for all kinds of tissue constructs: (i) improve the capacities in the manipulation and organization of the spheroids in higher quantities and with a better spatial resolution. (ii) increase the efficiency (assembling or writing speeds) in terms of the ability to work with a substantial number of spheroids to mimic macro-scale tissues (iii) meet the multicellular need, which is mandatory in tissue engineering; and, finally, (iv) develop simulation tools for guiding the design of the architecture to reach functionality upon time self-evolution.

Funding: This work was partly supported as part of the HoliFAB project funded by the European Union's Horizon 2020 research and innovation program (grant agreement no. 760927) and as part of the MultiFAB project funded by FEDER European Regional Funds and French Région Occitanie (grant agreement number 16007407/MP0011594). This work also received support from the French National Agency for Research (hiPS-Adipospheres ANR-18-CE 18-0006 and Printiss ANR-21-CE19-0041-01). This work was also partly supported by the French RENATECH network.

Conflicts of Interest: The authors declare no conflict of interest.

References

1. Takebe, T.; Sekine, K.; Enomura, M.; Koike, H.; Kimura, M.; Ogaeri, T.; Zhang, R.-R.; Ueno, Y.; Zheng, Y.-W.; Koike, N.; et al. Vascularized and Functional Human Liver from an IPSC-Derived Organ Bud Transplant. *Nature* **2013**, *499*, 481–484. [CrossRef] [PubMed]
2. Yap, K.K.; Dingle, A.M.; Palmer, J.A.; Dhillon, R.S.; Lokmic, Z.; Penington, A.J.; Yeoh, G.C.; Morrison, W.A.; Mitchell, G.M. Enhanced Liver Progenitor Cell Survival and Differentiation in Vivo by Spheroid Implantation in a Vascularized Tissue Engineering Chamber. *Biomaterials* **2013**, *34*, 3992–4001. [CrossRef] [PubMed]
3. Rossen, N.S.; Anandakumaran, P.N.; zur Nieden, R.; Lo, K.; Luo, W.; Park, C.; Huyan, C.; Fu, Q.; Song, Z.; Singh-Moon, R.P.; et al. Injectable Therapeutic Organoids Using Sacrificial Hydrogels. *iScience* **2020**, *23*, 101052. [CrossRef]
4. Mekhileri, N.V.; Lim, K.S.; Brown, G.C.J.; Mutreja, I.; Schon, B.S.; Hooper, G.J.; Woodfield, T.B.F. Automated 3D Bioassembly of Micro-Tissues for Biofabrication of Hybrid Tissue Engineered Constructs. *Biofabrication* **2018**, *10*, 024103. [CrossRef] [PubMed]
5. Karolak, A.; Markov, D.A.; McCawley, L.J.; Rejniak, K.A. Towards Personalized Computational Oncology: From Spatial Models of Tumour Spheroids, to Organoids, to Tissues. *J. R. Soc. Interface* **2018**, *15*, 20170703. [CrossRef] [PubMed]
6. Panoutsopoulos, A.A. Organoids, Assembloids, and Novel Biotechnology: Steps Forward in Developmental and Disease-Related Neuroscience. *Neuroscientist* **2021**, *27*, 463–472. [CrossRef]
7. Gilazieva, Z.; Ponomarev, A.; Rutland, C.; Rizvanov, A.; Solovyeva, V. Promising Applications of Tumor Spheroids and Organoids for Personalized Medicine. *Cancers* **2020**, *12*, 2727. [CrossRef]
8. Gunti, S.; Hoke, A.T.K.; Vu, K.P.; London, N.R. Organoid and Spheroid Tumor Models: Techniques and Applications. *Cancers* **2021**, *13*, 874. [CrossRef]
9. Ryu, N.E.; Lee, S.H.; Park, H. Spheroid Culture System Methods and Applications for Mesenchymal Stem Cells. *Cells* **2019**, *8*, 1620. [CrossRef]
10. Datta, P.; Ayan, B.; Ozbolat, I.T. Bioprinting for Vascular and Vascularized Tissue Biofabrication. *Acta Biomater.* **2017**, *51*, 1–20. [CrossRef]
11. De Moor, L.; Merovci, I.; Baetens, S.; Verstraeten, J.; Kowalska, P.; Krysko, D.V.; de Vos, W.H.; Declercq, H. High-Throughput Fabrication of Vascularized Spheroids for Bioprinting. *Biofabrication* **2018**, *10*, 035009. [CrossRef] [PubMed]
12. Cui, X.; Boland, T. Human Microvasculature Fabrication Using Thermal Inkjet Printing Technology. *Biomaterials* **2009**, *30*, 6221–6227. [CrossRef]
13. Ouyang, L.; Armstrong, J.P.K.; Salmeron-Sanchez, M.; Stevens, M.M. Assembling Living Building Blocks to Engineer Complex Tissues. *Adv. Funct. Mater.* **2020**, *30*, 1909009. [CrossRef]
14. Nichol, J.W.; Khademhosseini, A. Modular Tissue Engineering: Engineering Biological Tissues from the Bottom Up. *Soft Matter* **2009**, *5*, 1312–1319. [CrossRef] [PubMed]
15. Ranga, A.; Gobaa, S.; Okawa, Y.; Mosiewicz, K.; Negro, A.; Lutolf, M.P. 3D Niche Microarrays for Systems-Level Analyses of Cell Fate. *Nat. Commun.* **2014**, *5*, 4324. [CrossRef] [PubMed]
16. Atala, A.; Kasper, F.K.; Mikos, A.G. Engineering Complex Tissues. *Sci. Transl. Med.* **2012**, *4*, 160rv12. [CrossRef]
17. Baraniak, P.R.; McDevitt, T.C. Scaffold-Free Culture of Mesenchymal Stem Cell Spheroids in Suspension Preserves Multilineage Potential. *Cell Tissue Res.* **2011**, *347*, 701–711. [CrossRef]
18. Wimmer, R.A.; Leopoldi, A.; Aichinger, M.; Wick, N.; Hantusch, B.; Novatchkova, M.; Taubenschmid, J.; Hämmerle, M.; Esk, C.; Bagley, J.A.; et al. Human Blood Vessel Organoids as a Model of Diabetic Vasculopathy. *Nature* **2019**, *565*, 505–510. [CrossRef]
19. Fedorovich, N.E.; Schuurman, W.; Wijnberg, H.M.; Prins, H.-J.; van Weeren, P.R.; Malda, J.; Alblas, J.; Dhert, W.J.A. Biofabrication of Osteochondral Tissue Equivalents by Printing Topologically Defined, Cell-Laden Hydrogel Scaffolds. *Tissue Eng. Part C Methods* **2011**, *18*, 33–44. [CrossRef]
20. Lee, Y.B.; Polio, S.; Lee, W.; Dai, G.; Menon, L.; Carroll, R.S.; Yoo, S.S. Bio-Printing of Collagen and VEGF-Releasing Fibrin Gel Scaffolds for Neural Stem Cell Culture. *Exp. Neurol.* **2010**, *223*, 645–652. [CrossRef]
21. Eke, G.; Mangir, N.; Hasirci, N.; Macneil, S.; Hasirci, V. Development of a UV Crosslinked Biodegradable Hydrogel Containing Adipose Derived Stem Cells to Promote Vascularization for Skin Wounds and Tissue Engineering. *Biomaterials* **2017**, *129*, 188–198. [CrossRef]
22. Brassard, J.A.; Nikolaev, M.; Hübscher, T.; Hofer, M.; Lutolf, M.P. Recapitulating Macro-Scale Tissue Self-Organization through Organoid Bioprinting. *Nat. Mater.* **2020**, *20*, 22–29. [CrossRef]
23. Li, Y.; Kumacheva, E. Hydrogel Microenvironments for Cancer Spheroid Growth and Drug Screening. *Sci. Adv.* **2018**, *4*, eaas8998. [CrossRef]
24. Jauković, A.; Abadjieva, D.; Trivanović, D.; Stoyanova, E.; Kostadinova, M.; Pashova, S.; Kestendjieva, S.; Kukolj, T.; Jeseta, M.; Kistanova, E.; et al. Specificity of 3D MSC Spheroids Microenvironment: Impact on MSC Behavior and Properties. *Stem Cell Rev. Rep.* **2020**, *16*, 853–875. [CrossRef]
25. Kim, T.Y.; Kofron, C.M.; King, M.E.; Markes, A.R.; Okundaye, A.O.; Qu, Z.; Mende, U.; Choi, B.-R. Directed Fusion of Cardiac Spheroids into Larger Heterocellular Microtissues Enables Investigation of Cardiac Action Potential Propagation via Cardiac Fibroblasts. *PLoS ONE* **2018**, *13*, e0196714. [CrossRef]
26. Birey, F.; Andersen, J.; Makinson, C.D.; Islam, S.; Wei, W.; Huber, N.; Fan, H.C.; Metzler, K.R.C.; Panagiotakos, G.; Thom, N.; et al. Assembly of Functionally Integrated Human Forebrain Spheroids. *Nature* **2017**, *545*, 54–59. [CrossRef]

27. Schuurman, W.; Harimulyo, E.B.; Gawlitta, D.; Woodfield, T.B.F.; Dhert, W.J.A.; van Weeren, P.R.; Malda, J. Three-Dimensional Assembly of Tissue-Engineered Cartilage Constructs Results in Cartilaginous Tissue Formation without Retainment of Zonal Characteristics. *J. Tissue Eng. Regen. Med.* **2016**, *10*, 315–324. [CrossRef]
28. Whatley, B.R.; Li, X.; Zhang, N.; Wen, X. Magnetic-Directed Patterning of Cell Spheroids. *J. Biomed. Mater. Res. Part A* **2014**, *102*, 1537–1547. [CrossRef]
29. Lin, R.-Z.; Chu, W.-C.; Chiang, C.-C.; Lai, C.-H.; Chang, H.-Y. Magnetic Reconstruction of Three-Dimensional Tissues from Multicellular Spheroids. *Tissue Eng. Part C Methods* **2008**, *14*, 197–205. [CrossRef]
30. Bowser, D.A.; Moore, M.J. Biofabrication of Neural Microphysiological Systems Using Magnetic Spheroid Bioprinting. *Biofabrication* **2019**, *12*, 015002. [CrossRef]
31. Parfenov, V.A.; Khesuani, Y.D.; Petrov, S.V.; Karalkin, P.A.; Koudan, E.V.; Nezhurina, E.K.; das Pereira, F.; Krokhmal, A.A.; Gryadunova, A.A.; Bulanova, E.A.; et al. Magnetic Levitational Bioassembly of 3D Tissue Construct in Space. *Sci. Adv.* **2020**, *6*, eaba4174. [CrossRef]
32. Ong, L.J.Y.; Islam, A.; DasGupta, R.; Iyer, N.G.; Leo, H.L.; Toh, Y.-C. A 3D Printed Microfluidic Perfusion Device for Multicellular Spheroid Cultures. *Biofabrication* **2017**, *9*, 045005. [CrossRef]
33. Sloan, S.A.; Andersen, J.; Paşca, A.M.; Birey, F.; Pașca, S.P. Generation and Assembly of Human Brain Region–Specific Three-Dimensional Cultures. *Nat. Protoc.* **2018**, *13*, 2062–2085. [CrossRef]
34. Andersen, J.; Revah, O.; Miura, Y.; Thom, N.; Amin, N.D.; Kelley, K.W.; Singh, M.; Chen, X.; Thete, M.V.; Walczak, E.M.; et al. Generation of Functional Human 3D Cortico-Motor Assembloids. *Cell* **2020**, *183*, 1913–1929.e26. [CrossRef] [PubMed]
35. Cui, H.; Wang, X.; Wesslowski, J.; Tronser, T.; Rosenbauer, J.; Schug, A.; Davidson, G.; Popova, A.A.; Levkin, P.A. Assembly of Multi-Spheroid Cellular Architectures by Programmable Droplet Merging. *Adv. Mater.* **2021**, *33*, 2006434. [CrossRef] [PubMed]
36. Villar, G.; Graham, A.D.; Bayley, H. A Tissue-like Printed Material. *Science* **2013**, *340*, 48–52. [CrossRef] [PubMed]
37. Gutzweiler, L.; Kartmann, S.; Troendle, K.; Benning, L.; Finkenzeller, G.; Zengerle, R.; Koltay, P.; Stark, G.B.; Zimmermann, S. Large Scale Production and Controlled Deposition of Single HUVEC Spheroids for Bioprinting Applications. *Biofabrication* **2017**, *9*, 025027. [CrossRef]
38. Itoh, M.; Nakayama, K.; Noguchi, R.; Kamohara, K.; Furukawa, K.; Uchihashi, K.; Toda, S.; Oyama, J.; Node, K.; Morita, S. Scaffold-Free Tubular Tissues Created by a Bio-3D Printer Undergo Remodeling and Endothelialization When Implanted in Rat Aortae. *PLoS ONE* **2015**, *10*, e0136681. [CrossRef]
39. Mukae, Y.; Itoh, M.; Noguchi, R.; Furukawa, K.; Arai, K.-I.; Oyama, J.-I.; Toda, S.; Nakayama, K.; Node, K.; Morita, S. The Addition of Human IPS Cell-Derived Neural Progenitors Changes the Contraction of Human IPS Cell-Derived Cardiac Spheroids. *Tissue Cell* **2018**, *53*, 61–67. [CrossRef]
40. Itoh, M. Scaffold-Free Autologous Cell-Based Vascular Graft for Clinical Application. In *Kenzan Method for Scaffold-Free Biofabrication*; Springer: Cham, Switzerland, 2021; pp. 117–125. [CrossRef]
41. Arai, K.; Murata, D.; Takao, S.; Nakamura, A.; Itoh, M.; Kitsuka, T.; Nakayama, K. Drug Response Analysis for Scaffold-Free Cardiac Constructs Fabricated Using Bio-3D Printer. *Sci. Rep.* **2020**, *10*, 8972. [CrossRef]
42. Ong, C.S.; Fukunishi, T.; Nashed, A.; Blazeski, A.; Zhang, H.; Hardy, S.; DiSilvestre, D.; Vricella, L.; Conte, J.; Tung, L.; et al. Creation of Cardiac Tissue Exhibiting Mechanical Integration of Spheroids Using 3D Bioprinting. *J. Vis. Exp. JoVE* **2017**, *125*, e55438. [CrossRef]
43. Murata, D.; Tokunaga, S.; Tamura, T.; Kawaguchi, H.; Miyoshi, N.; Fujiki, M.; Nakayama, K.; Misumi, K. A Preliminary Study of Osteochondral Regeneration Using a Scaffold-Free Three-Dimensional Construct of Porcine Adipose Tissue-Derived Mesenchymal Stem Cells. *J. Orthop. Surg. Res.* **2015**, *10*, 35. [CrossRef]
44. Noguchi, R.; Nakayama, K.; Itoh, M.; Kamohara, K.; Furukawa, K.; Oyama, J.I.; Node, K.; Morita, S. Development of a Three-Dimensional Pre-Vascularized Scaffold-Free Contractile Cardiac Patch for Treating Heart Disease. *J. Heart Lung Transplant.* **2016**, *35*, 137–145. [CrossRef]
45. Moldovan, N.I.; Hibino, N.; Nakayama, K. Principles of the Kenzan Method for Robotic Cell Spheroid-Based Three-Dimensional Bioprinting. *Tissue Eng. Part B Rev.* **2017**, *23*, 237–244. [CrossRef] [PubMed]
46. Ong, C.S.; Fukunishi, T.; Zhang, H.; Huang, C.Y.; Nashed, A.; Blazeski, A.; DiSilvestre, D.; Vricella, L.; Conte, J.; Tung, L.; et al. Biomaterial-Free Three-Dimensional Bioprinting of Cardiac Tissue Using Human Induced Pluripotent Stem Cell Derived Cardiomyocytes. *Sci. Rep.* **2017**, *7*, 4566. [CrossRef]
47. Ayan, B.; Heo, D.N.; Zhang, Z.; Dey, M.; Povilianskas, A.; Drapaca, C.; Ozbolat, I.T. Aspiration-Assisted Bioprinting for Precise Positioning of Biologics. *Sci. Adv.* **2020**, *6*, eaaw5111. [CrossRef] [PubMed]
48. Ayan, B.; Wu, Y.; Karuppagounder, V.; Kamal, F.; Ozbolat, I.T. Aspiration-Assisted Bioprinting of the Osteochondral Interface. *Sci. Rep.* **2020**, *10*, 13148. [CrossRef]
49. Daly, A.C.; Davidson, M.D.; Burdick, J.A. 3D Bioprinting of High Cell-Density Heterogeneous Tissue Models through Spheroid Fusion within Self-Healing Hydrogels. *Nat. Commun.* **2021**, *12*, 753. [CrossRef]
50. Skylar-Scott, M.A.; Uzel, S.G.M.; Nam, L.L.; Ahrens, J.H.; Truby, R.L.; Damaraju, S.; Lewis, J.A. Biomanufacturing of Organ-Specific Tissues with High Cellular Density and Embedded Vascular Channels. *Sci. Adv.* **2019**, *5*, eaaw2459. [CrossRef]
51. Whitesides, G.M.; Grzybowski, B. Self-Assembly at All Scales. *Science* **2002**, *295*, 2418–2421. [CrossRef]
52. Athanasiou, K.A.; Eswaramoorthy, R.; Hadidi, P.; Hu, J.C. Self-Organization and the Self-Assembling Process in Tissue Engineering. *Annu. Rev. Biomed. Eng.* **2013**, *15*, 115–136. [CrossRef]

53. Bulanova, E.A.; Koudan, E.V.; Degosserie, J.; Heymans, C.; das Pereira, F.; Parfenov, V.A.; Sun, Y.; Wang, Q.; Akhmedova, S.A.; Sviridova, I.K.; et al. Bioprinting of a Functional Vascularized Mouse Thyroid Gland Construct. *Biofabrication* **2017**, *9*, 034105. [CrossRef]
54. Ovsianikov, A.; Khademhosseini, A.; Mironov, V. The Synergy of Scaffold-Based and Scaffold-Free Tissue Engineering Strategies. *Trends Biotechnol.* **2018**, *36*, 348–357. [CrossRef]
55. Schon, B.S.; Schrobback, K.; van der Ven, M.; Stroebel, S.; Hooper, G.J.; Woodfield, T.B.F. Validation of a High-Throughput Microtissue Fabrication Process for 3D Assembly of Tissue Engineered Cartilage Constructs. *Cell Tissue Res.* **2012**, *347*, 629–642. [CrossRef]
56. Jafari, J.; Han, X.L.; Palmer, J.; Tran, P.A.; O'Connor, A.J. Remote Control in Formation of 3D Multicellular Assemblies Using Magnetic Forces. *ACS Biomater. Sci. Eng.* **2019**, *5*, 2532–2542. [CrossRef]
57. Parfenov, V.A.; Petrov, S.V.; Pereira, F.D.A.S.; Levin, A.A.; Koudan, E.V.; Nezhurina, E.K.; Karalkin, P.A.; Vasiliev, M.M.; Petrov, O.F.; Komlev, V.S.; et al. Scaffold-Free, Label-Free, and Nozzle-Free Magnetic Levitational Bioassembler for Rapid Formative Biofabrication of 3D Tissues and Organs. *Int. J. Bioprinting* **2020**, *6*, 110–119. [CrossRef]
58. Chen, C.; Tang, S.; Hu, K. Magnetic Hydrogel Based on Magnetic Nanoparticle Assemblies Providing a Platform for Multicellular Spheroids with High Expression of Glioma Tumor Stem Cell Related Markers. *Nanosci. Nanotechnol. Lett.* **2017**, *9*, 77–80. [CrossRef]
59. Abdel Fattah, A.R.; Meleca, E.; Mishriki, S.; Lelic, A.; Geng, F.; Sahu, R.P.; Ghosh, S.; Puri, I.K. In Situ 3D Label-Free Contactless Bioprinting of Cells through Diamagnetophoresis. *ACS Biomater. Sci. Eng.* **2016**, *2*, 2133–2138. [CrossRef]
60. Chung, S.E.; Park, W.; Shin, S.; Lee, S.A.; Kwon, S. Guided and fluidic self-assembly of microstructures using railed microfluidic channels. *Nature Mater.* **2008**, *7*, 581–587. [CrossRef]
61. Nikolaev, M.; Mitrofanova, O.; Broguiere, N.; Geraldo, S.; Dutta, D.; Tabata, Y.; Elci, B.; Brandenberg, N.; Kolotuev, I.; Gjorevski, N.; et al. Homeostatic Mini-Intestines through Scaffold-Guided Organoid Morphogenesis. *Nature* **2020**, *585*, 574–578. [CrossRef]
62. Ranga, A.; Girgin, M.; Meinhardt, A.; Eberle, D.; Caiazzo, M.; Tanaka, E.M.; Lutolf, M.P. Neural Tube Morphogenesis in Synthetic 3D Microenvironments. *Proc. Natl. Acad. Sci. USA* **2016**, *113*, E6831–E6839. [CrossRef]
63. Mironov, V.; Visconti, R.P.; Kasyanov, V.; Forgacs, G.; Drake, C.J.; Markwald, R.R. Organ Printing: Tissue Spheroids as Building Blocks. *Biomaterials* **2009**, *30*, 2164–2174. [CrossRef]
64. Dababneh, A.B.; Ozbolat, I.T. Bioprinting Technology: A Current State-of-the-Art Review. *J. Manuf. Sci. Eng.* **2014**, *136*, 061016. [CrossRef]
65. Jakab, K.; Norotte, C.; Damon, B.; Marga, F.; Neagu, A.; Besch-Williford, C.L.; Kachurin, A.; Church, K.H.; Park, H.; Mironov, V.; et al. Tissue Engineering by Self-Assembly of Cells Printed into Topologically Defined Structures. *Tissue Eng.-Part A* **2008**, *14*, 413–421. [CrossRef]
66. Leberfinger, A.N.; Dinda, S.; Wu, Y.; Koduru, S.V.; Ozbolat, V.; Ravnic, D.J.; Ozbolat, I.T. Bioprinting Functional Tissues. *Acta Biomater.* **2019**, *95*, 32–49. [CrossRef]
67. Agarwal, T.; Banerjee, D.; Konwarh, R.; Esworthy, T.; Kumari, J.; Onesto, V.; Das, P.; Lee, B.H.; Wagener, F.A.D.T.G.; Makvandi, P.; et al. Recent Advances in Bioprinting Technologies for Engineering Hepatic Tissue. *Mater. Sci. Eng. C* **2021**, *123*, 112013. [CrossRef]
68. Gudapati, H.; Dey, M.; Ozbolat, I. A Comprehensive Review on Droplet-Based Bioprinting: Past, Present and Future. *Biomaterials* **2016**, *102*, 20–42. [CrossRef]
69. Kozaki, S.; Moritoki, Y.; Furukawa, T.; Akieda, H.; Kageyama, T.; Fukuda, J.; Maruo, S. Additive Manufacturing of Micromanipulator Mounted on a Glass Capillary for Biological Applications. *Micromachines* **2020**, *11*, 174. [CrossRef]
70. Moritoki, Y.; Furukawa, T.; Sun, J.; Yokoyama, M.; Shimono, T.; Yamada, T.; Nishiwaki, S.; Kageyama, T.; Fukuda, J.; Mukai, M.; et al. 3D-Printed Micro-Tweezers with a Compliant Mechanism Designed Using Topology Optimization. *Micromachines* **2021**, *12*, 579. [CrossRef]
71. Sachs, N.; Tsukamoto, Y.; Kujala, P.; Peters, P.J.; Clevers, H. Intestinal Epithelial Organoids Fuse to Form Self-Organizing Tubes in Floating Collagen Gels. *Development* **2017**, *144*, 1107–1112. [CrossRef]
72. Buchanan, K.; Burt de Perera, T.; Carere, C.; Carter, T.; Hailey, A.; Hubrecht, R.; Jennings, D.; Metcalfe, N.; Pitcher, T.; Peron, F.; et al. Guidelines for the Treatment of Animals in Behavioural Research and Teaching. *Anim. Behav.* **2012**, *83*, 301–309. [CrossRef]
73. Sneddon, L.U.; Halsey, L.G.; Bury, N.R. Considering Aspects of the 3Rs Principles within Experimental Animal Biology. *J. Exp. Biol.* **2017**, *220*, 3007–3016. [CrossRef] [PubMed]

Additive Manufacturing 72 (2023) 103629

Contents lists available at ScienceDirect

Additive Manufacturing

journal homepage: www.elsevier.com/locate/addma

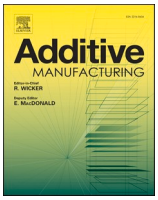

Research paper

A microfluidics-assisted photopolymerization method for high-resolution multimaterial 3D printing

Victor Fournié [a,c,*], Bastien Venzac [a], Emmanuelle Trevisiol [b], Julie Foncy [a], Julien Roul [a], Sandrine Assie-Souleille [a], Mélanie Escudero [d], Pierre Joseph [a], Arnaud Reitz [c], Laurent Malaquin [a,*]

[a] Laboratoire d'analyse et d'architecture des systèmes-CNRS, Toulouse 31400, France
[b] Toulouse Biotechnology Institute-INSA-CNRS, Toulouse 31400, France
[c] Fluigent SA, Kremlin-bicètre 94270, France
[d] RESTORE Research Center, Université de Toulouse, INSERM 1301, CNRS 5070, EFS, ENVT, 31100 Toulouse, France

ARTICLE INFO

Keywords:
Additive manufacturing
Multimaterial 3D printing
High-resolution 3D printing
Photopolymerization
Microfluidics

ABSTRACT

3D printing and bioprinting are recognized as key technologies for the construction of complex micro-devices, micro-environments, and culture models. Thanks to their potential to produce precisely heterogeneous and 3D architectures, multimaterial printing methods, which enable the production of functional 3D structures integrating multiple materials, have attracted specific attention. Nevertheless, combining multimaterial and high-resolution printing is still a major challenge, and the available technologies do not provide simultaneously the resolution and multiplexing capabilities required to create heterogeneous 3D environments. In this work, we introduce the 3D-FlowPrint concept, which involves an opto-microfluidic printhead immersed in a liquid and moved above a surface. This technology combines the convenience of microfluidics in terms of the handling and delivery of small volumes of materials with the resolution provided by laser lithography. Delivered materials are hydrodynamically confined under the printhead owing to controlled aspiration of the injected material, ensuring a continuous supply of material and avoiding cross-contamination issues. Combining microfluidics with photopolymerization provides unique advantages as it separates the polymerization process from the material delivery, permitting high-resolution polymerization (down to 10 μm) and multimaterial handling (switching time below 60 s). We present a first proof-of-concept using poly(ethylene glycol) diacrylate (PEGDA)-based hydrogels as a photosensitive material model, along with a detailed investigation of the influence of exposure parameters, printhead velocity, and hydrodynamic parameters on the fabrication of 2D and 3D heterogeneous structures. 3D-FlowPrint allows the creation of sub-millimetric to millimetric scale objects with multimaterial designs. A first validation was performed to show the potential of the approach in biology for the creation of engineered microenvironments for cell culture.

1. Introduction

Additive manufacturing is the state-of-the-art for the fabrication of complex three-dimensional (3D) structures. Recent advances have enabled 3D printing of biocompatible materials, cells, and supporting components to create 3D scaffolds or 3D models of functional living tissues [1].

Typically, these models contain several cell types in close proximity (<100 μm) and at various densities encapsulated inside hydrogels having a large range of mechanical properties and biochemical compositions. The ability to print one construct with different hydrogels, each containing (or not) different cell types or the same cells at different

Abbreviations and variables: V, printhead velocity; Z_{gap}, gap between the substrate and the printhead, measured at the closest point under the PDMS dome in the polymerization area; φ_{in}, φ_{out}, Injection and aspiration flowrates; $R\varphi = \varphi_{out}/\varphi_{in}$, flowrate ratio; μ_{mat}, μ_{med}, dynamic viscosities of the injected material and of the medium respectively; HFC, Hydrodynamic flow confinement; Rr, Retrieval rate, defines the mass ratio between the injected and retrieved material when reaching steady state regime.

* Correspondence to: Laboratoire d'analyse et d'architecture des systèmes-CNRS, 7 avenue du colonel Roche, Toulouse 31400, France.
E-mail addresses: vfournie@laas.fr (V. Fournié), lmalaqui@laas.fr (L. Malaquin).

https://doi.org/10.1016/j.addma.2023.103629
Received 15 February 2023; Received in revised form 5 May 2023; Accepted 24 May 2023
Available online 25 May 2023

densities with resolutions close to tens-of-micrometers is a key enabling feature for the creation of relevant models [2–6]. However, few concepts have managed to combine a simple method for multimaterial printing with such resolution. Traditional micro-extrusion [7] or inkjet printing [5] are well recognized as efficient techniques to create multimaterial structures, but they still present some issues in terms of resolution, mainly driven by the size of the extrusion system or the dimensions of the generated droplets. Laser-assisted techniques [8,9] enable higher resolution, but the photopolymerization process usually takes place in a vat containing one single material, making it challenging to print multimaterial objects.

Photolithography-based methods have been widely investigated for additive manufacturing and bioprinting [10]. They show promise in terms of resolution as they allow the separation of the mass transport mechanism from structuration aspects and thus high-resolution at the sub-micrometer scale [11]. The development of multimaterial approaches combined with photolithography has naturally attracted huge interest in recent years. Compared with traditional extrusion printing, where cylindrical filaments of liquid or shear-thinning bioinks are physically deposited with a moving nozzle, stereolithography (SLA) [12,13] uses controlled illumination to selectively photocrosslink liquid bioinks into solid features, offering superior spatial resolution to that of extrusion or inkjet printers. However, conventional SLA systems are almost exclusively designed to print hard plastic materials for non-biological applications and few offer multimaterial capability [6]. Combining the resolution of laser-based 3D printing methods with the capacity of printing heterogeneous structures starting from a material library has attracted huge interest in bioprinting, among other fields [14]. A straightforward and common approach is to perform sequential printing processes where the samples are moved into different vats to perform successive development and material immersion steps [15–17]. This gives rise to efficient but tedious manipulations that hinder the global printing throughput. From the perspective of developing more straightforward processes, Grigoryan et al. proposed a multi-material SLA bioprinter involving a motorized sled allowing nascent structures to interface with separate bioinks of variable chemical or cellular compositions [18]. This method has proven to be compatible with photoresists and hydrogel materials adapted to bioprinting. However, the authors acknowledged certain limitations of the printing system with respect to scale, resolution, automation, and material selection. Beyond the feature-size limitations inherent to projection SLA, the construction of large structures with complex internal heterogeneity would require numerous rinsing and material-change steps making this technique laborious. Peng et al. [19] have proposed in 2021 an interesting combination of micro-extrusion, for functional materials, and photolithography, for high speed and high-resolution printing. This hybrid method is versatile but certain limitations due to the rheology of extruded materials and the corresponding printing resolution may impede applications in the field of cell culture and tissue engineering.

The integration of fluidic control to ensure automated injection has attracted huge interest over the last few years. In 2018, Miri et al. developed a microfluidic chip with sequential injection allowing the printing of multimaterial structures [20]. A Z platform deforming a flexible PDMS membrane allowed the fabrication of 3D objects. Despite the ingenuity of the system, several drawbacks were presented, such as size limitations in the XY plane and the Z direction as well as stress on the PDMS membrane and the structure due to the movement of the Z platform. On a larger scale, Han et al. have proposed a micro-SLA method based on the integration of a microfluidic cell surrounding the sample that permits a fast and sequential injection of different materials with viscosities up to 58 mPa.s [21]. The authors have shown the injection of several material with fast switching times but relatively high flowrate of ~1 mL/s that could be detrimental for soft material applications. A similar concept was also successfully applied to multiphoton lithography in the work of Mayer et al. [22]. By optimization of the microfluidic circuitry, the authors demonstrated multimaterial capacity with a reduction of the swept volumes to 500 µL. However, due to specific constraints imposed by the objective, the geometry of the chamber limits the height of the printed samples to 100 µm. More recently, Lipkowitz et al. proposed an alternative approach that uses the active control of mass transport combined with continuous liquid interface printing [23]. This approach permits multimaterial injection and delivery in the exposure area to allow rapid printing of multiple different resins simultaneously at varying scales. However, this method relies on the integration of the fluidic injection channels directly in the fabricated structures and is subject to potential issues related to material recovery and subsequent contamination.

Several of these methods profit from the miniaturization of 3D printing concepts into microfluidic devices and present the possibility of reducing the volumes of liquid and providing better control and reproducibility of flowrates. Microfluidics provides parallelization and multiplexing capacities that are essential to mix and accurately tune the composition of the materials thanks to an integrated microfluidic circuitry. Skylar-Scott et al. demonstrated the integration of microfluidics in the printhead in the context of extrusion printing [24]. The authors reported the design and fabrication of voxelated matter using multimaterial multinozzle 3D (MM3D) printing. Simple or multi-photon approaches have also been reported for enclosed microfluidic devices for the fabrication of small (<1 mm) 3D objects or particles through continuous flow lithography [25,26]. However, such methods impose a Z limitation on the objects between the two planes of the microfluidic chip, and this prevents or complicates the creation of 3D objects. Clearly, despite certain inherent limitations induced by either large material consumption, design limitations, or contamination issues, all these approaches demonstrate the opportunities provided by laser-assisted methods and/or fluidic systems for multimaterial printing as they decouple mass transport and material delivery from the writing mechanism, i.e., photopolymerization.

Here, we propose the 3D-FlowPrint concept (Fig. 1, [27]), an original printhead design with hydrodynamic confinement that provides fast and efficient microfluidic injection in the printing area. The use of both aspiration and injection systems with controllable pressures allows efficient recovery of excess injected material in the printing area, thus limiting the risk of contamination in the surrounding media. From a conceptual point of view, this device borrows some of the aspects of the microfluidic probe concept first proposed by D. Juncker and E. Delamarche [28–30]. However, 3D-FlowPrint relies on a different design allowing the injection of viscous materials and the possibility to work at long distances (>500 µm) from a substrate. Furthermore, an optical fiber is integrated in the printhead to photopolymerize the material during material injection. Unlike most applications, the light does not cross the material container layer but is directly provided in the printhead close to the fluidic delivery system. To our knowledge, the integration of a light source within such a device to precisely photopolymerize hydrogels has not been reported. The combination of an open microfluidic device with integrated optics opens a new field of research for the 3D structuring of materials. Contrary to previous works, our approach provides the ability to control spatially the composition of the structures with multiple materials and enable the fabrication of multiscale 3D objects.

In this article, the printhead fabrication protocol, including its 3D SLA printing and assembly, is presented. We describe hydrodynamic aspects of the system, its optimization through Comsol simulations, and its operative regime. The in-flow photopolymerization is explained and analyzed. Finally, we present 3D pieces with precise evaluation of XYZ attributes as well as details of their multimaterial characteristics and their use in the study of spheroid/cell cultures on structured materials.

2. Materials and methods

2.1. Materials and chemicals

Poly-(ethylene glycol) diacrylate (PEGDA) Mw = 700 g/mol,

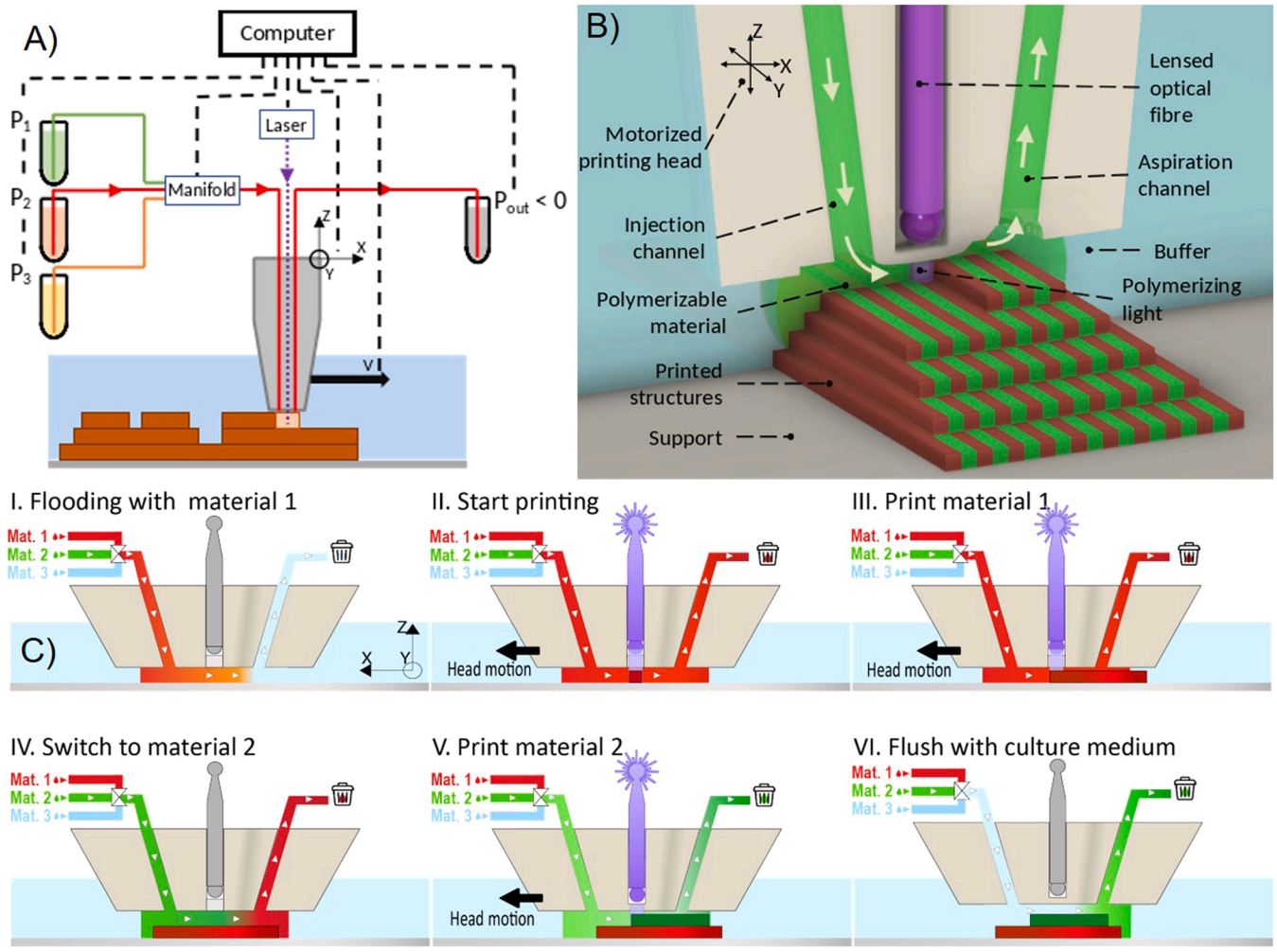

Fig. 1. 3D Illustration of the 3D-FlowPrint concept. (A) Planar schematics showing the setup of the instrument (B) Schematic of the opto-fluidic processes with a XZ cross-section of the head. (C) Multimaterial printing workflow.

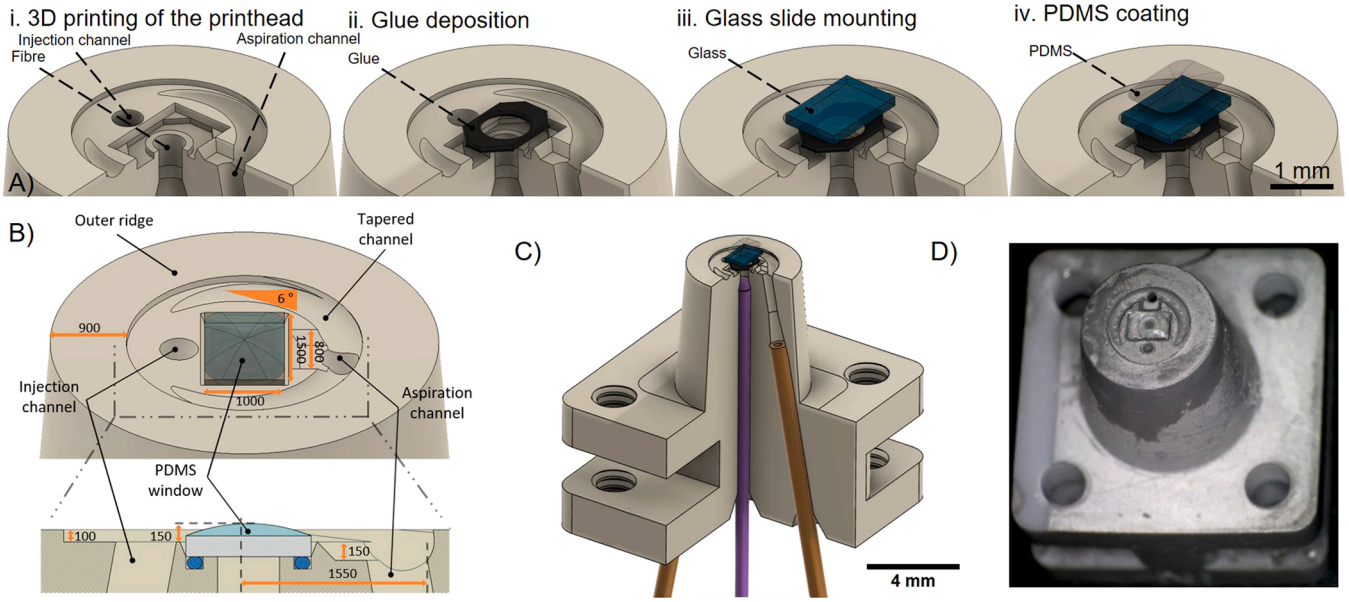

Fig. 2. Printhead fabrication protocol. (A) Design of the printhead obtained by SLA 3D printing (i). A glass slide is bound to the printhead (ii–iii) and protected with a PDMS coating (iv). (B) Top view and cross cut image of the printhead structures and dimensions (values are given in μm). (C) Overall view of the printhead showing the structure of the injection and aspiration channels (orange) and the insertion of an optical fibre (purple). (D) Optical micrograph of an assembled printing head.

lithium-2,4,6-trimethylbenzoylphosphinate (LAP), Rhodamine B, 3-methacryloxypropyltrimethoxysilane (MAPTMS), phosphate-buffered saline (PBS), polydimethylsiloxane (PDMS) Sylgard 184 (Dow Corning) were purchased from Sigma-Aldrich. Fluorescent carboxylate-modified particles (FluoSpheres™ D = 200 nm and Fluoro-Max™ D = 300 nm or D = 5 μm) were purchased from Thermo Fischer. Epotek 301 glue was purchased from FTpolymers. If not mentioned otherwise, all hydrogel solutions were prepared with 40 v/v% PEGDA and 60 v/v% deionized water (Millipore), 0.01 w/v% LAP (diluted in Millipore deionized water). For imaging, GFP or mCherry fluorescent particles (200 nm, 300 nm, or 5 μm) were added at a concentration of 0.01 v/v% (or $\approx 7 \times 10^9$ nanoparticles of 300 nm per mL. All solutions were prepared at room temperature (RT) and magnetically stirred for 2 h. Sterilization of the hydrogel solutions was performed by filtering through a 200-nm filter before printing (Millex-GS Syringe Filter Unit, 0.22 μm).

2.2. Printhead fabrication process

The design and fabrication of the 3D printheads are illustrated in Fig. 2.A. The printhead body was fabricated with a commercial SLA 3D printer (DWS 29 J+, DWS, Italy) offering a 40-μm XY resolution combined with a tunable 10 to 100 μm Z resolution, wavelength = 405 nm. We selected DL260 composite photosensitive resist (composite urethane-acrylate resist, Young's modulus ≈ 2 GPa, DWS Systems, Italy) as a base material. Batches of eight printheads were produced simultaneously using a printing speed of 5800 mm/s and slicing/hatching distances of 30 μm (corresponding to 1.1 kJ/cm^2; Fig. 2.A.I.). The printing proceeded for 3 h per batch. Once printed, the parts were developed by immersion in acetone at RT for at least 5 min in an ultrasonic bath (Elma S100H).

Protection and sealing of the optical fiber insert were performed using a 1 mm × 1.5 mm borosilicate glass slide obtained by dicing a 170-μm thick glass slide using a DAO321 system. Prior to glass slide integration, a small volume (50 nL) of glue (bicomponent epoxy adhesive Epotek 301, Ftpolymers) was delivered into the cavity surrounding the optical fiber aperture (Fig. 2.A.II.). The glass slide was further mounted on the printhead (Fig. 2.A.III.). Both glue and glass slides were bonded on the printhead with a microelectronic assembling machine (Tresky 3000). Bonding was performed at 70 °C for 1 h.

Finally, a PDMS layer was added to the top of the glass slide. This layer acts as a non-adhesive coating, as oxygen-based inhibition near the PDMS surface allows for hydrogel crosslinking while preventing attachment to the printing head during motion [25,31]. We deposited an approximately 77-nL drop of PDMS (Sylgard 184; Fig. 2.A.IV) to obtain a dome with a 150-μm thickness. PDMS has good transparency at 405 nm, which prevents energy loss and provides an optical index that preserves the laser beam size. A ball-lensed optical fiber (BL-5 on high power single mode 405 nm fiber from WT&T) with focus distances between 200 and 3000 μm and a waist diameter of 7 μm was inserted in the printhead. As the printheads are produced in a fast and reproducible manner, they were considered disposable and thus replaced before each experiment to prevent any risk of contamination.

2.3. Photo-polymerization control

The optical fiber was coupled to a 405-nm monomodal laser (Laserboxx from Oxxius) with adjustable power (P_{in}) ranging from 5 to 120 mW. To provide more accurate control of the beam intensity and compensate for the non-linear response of the laser intensity at low or high power, the laser driver was triggered with a function generator with 1 kHz square signals and a variable duty cycle to further modulate the intensity by a factor DC_{FG}. The effective output power was measured by positioning a Thorlabs S170C probe with PM200 power meter at 1 cm from the printhead apex.

To achieve different beam sizes, we modified the vertical position of the fiber in order to modulate the polymerization area by defocusing (Suppl. Fig. 1). In high-resolution mode (HR, FWHM = 7–20 μm), the fiber was positioned to align the focus point at the printhead surface (PDMS dome) while in low-resolution mode (LR, FWHM = 50–100 μm), the fiber was positioned 400 μm above in order to enlarge the beam profile in the polymerization area. For a given laser intensity, displacing the fiber induces a variation of spatial distribution of light. Compensation of the dose was performed by dynamically adapting the laser input power (P_{in}) or the function generator duty cycle (DC_{FG}). For one isolated line, the surface dose was approximated as: $dose = P_{output}/(D_{spot} \bullet V)$ (1), where P_{output} ($P_{output} = P_{input} \bullet k_{transmission} \bullet DC_{FG}$ (2)) is the laser power at the printhead apex, D_{spot} is the FWHM of the spot, P_{input} is the nominal input power, and $K_{transmission}$ is the light transmission factor between the laser emitter and printhead apex. By tuning both the FG duty cycle (0.1–100%) and the input power (15–120 mW), we achieved an output power range from 0.7 μW to 21 mW, or 194 kW/m^2 to 584 MW/m^2 with $R_{spot} = 6$ μm.

Certain experiments (e.g., Fig. 5.E) were carried out using a dual fiber printhead (Suppl. Fig. 1. A). The printhead design was adapted to integrate two optical fibers. A computer-driven fiber switch (FFSW-122000323-MD, Laser Components) was integrated between the laser source and the fibers to switch between high-resolution and low-resolution modes.

2.4. Control of microfluidic injection

Buffer medium and photopolymerizable materials were introduced to 15-mL falcon tubes. Each tube was connected to a M-switch 10-to-1 microfluidic valve (Fluigent, France) allowing selection of the solution to be injected. The aspiration channel was connected to a 50-mL falcon tube. A Fluigent Flow-EZ air pressure controller was used to generate a positive pressure relative to P_{atm} in the injection tubes to drive fluids, while a Fluigent Push-Pull air pressure controller imposed a negative pressure (relative to P_{atm}) in order to promote fluid aspiration to the aspiration channel. The Flow EZ system was coupled to flowrate sensors (Fluigent Flow unit Medium ± 80 μL/min or Large ± 1 mL/min) allowing feedback control of flowrate in both the injection and aspiration channels. To favor HFC and prevent cross-contamination of the injected material in the medium surrounding the printing area, the flowrate ratio between aspiration and injection was adjusted according to the printing speed, material viscosity, and distance between the gap and surface (Z_{gap}), as discussed in part 3.2.

2.5. Printhead design

STL printhead designs were generated using Fusion360 (Autodesk, San Fransisco, USA). Hydrodynamic optimization and characterization of the printhead design was carried out through Comsol simulations (v5.5 Comsol Multiphysics, COMSOL AB, Sweden). The printhead consists of a conical device integrating one cylindrical port (diameter 550 μm) for optical fiber insertion as well as injection and aspiration channels for material delivery and recovery (Fig. 2. C). Guiding microfluidics structures were integrated at the apex of the printhead to control the spatial distribution of hydrodynamic resistance and material flow during injection (Fig. 2. B). In particular, a circular tapered channel with increasing depth (R = 1.3 mm, r = 0.5 mm, maximum depth = 250 μm, angle = 6°) was integrated to guide the flow of injected material toward the printing area. An additional ditch (width = 600 μm, length = 800 μm, height = 150 μm) was placed near the aspiration channel in the axis of the polymerization point to guide the injected material toward the polymerization point. To further increase material recovery, a 900-μm wide and 100-μm high ridge was integrated at the periphery of the printhead to help isolate the injection and aspiration ports from the outer environment.

2.6. CFD Comsol simulations

CFD simulations were performed using the commercial finite element software Comsol Multiphysics. Numerical simulations involved both "*laminar flow*" and "*transport of diluted species*" modules through "*time dependent*" studies. The model 3D geometry was built in Comsol using the above specifications. The viscosity of the environmental solution (μ_{med}) was set to 1 mPa.s, as water, and if not specified otherwise, μ_{mat} was set to 8.5 mPa.s, which is the viscosity of a solution of 40% PEGDA 700% and 60% DI-water [32]. Printhead velocity is defined by slip boundary conditions on the printed structures (if present), exterior box, and support. The software calculates each point viscosity by linear evaluation depending on the point concentration of the injected and environmental material.

2.7. Instrumental platform and control software

The printing platform was integrated on a fluorescence microscope (IX71, Olympus) equipped with an XY-stage (MS-2000, ASI) with a range of 120 × 110 mm and a 1-μm repeatability. The printhead was mounted on a translation stage (LTA-HL, Newport) providing control of the Z position with 25-mm maximum displacement and a 3-μm repeatability. The Z stage was mounted on the microscope frame, thus allowing movement of the sample in the XY plane independently while maintaining the position of the printhead. The whole setup was integrated in a temperature-controlled enclosure (H201-T-unit-BL from Okolab).

All hardware components (XY-stage, Z-stage, pressure controllers, fluidic valve, laser, FG, fiber switch) were driven with a homemade LabVIEW (National Instruments) interface. The software was designed to process Gcode (all required actions of the printer combined into a script) and transform coordinates in a list of trajectory vectors, including {moving speed, X movement, Y movement, Z height, laser state, material to be printed, flowrates, high/low resolution boolean, delay}.

2.8. Slicer development

The development of a multimaterial and multiresolution 3D printing process requires synchronizing the material injection, the adaptation of the laser beam, and the printing trajectories according to the features of the design. For those reasons, we developed a dedicated slicer software with Python. The vectorization was performed in five steps (Suppl. Fig. 2): i) slicing of the STL objects in the Z-axis; ii) selection of the material and optimum resolution for each slice; iii) filling of the design features according to hatching and velocity; iv) vector sorting depending on the printing strategy; and v) export of vectors dataset in specific Gcode format.

2.9. Substrate preparation

Printing was performed on 24 mm × 32 mm × 170 μm glass slides (Menzel purchased from Fisher Scientific), treated with MAPTMS (Sigma Aldrich) for adhesion of the printed hydrogel. The glass slides were first washed with acetone, deionized water, and ethanol, then dried under a nitrogen stream. Then, the slides were activated using air-plasma treatment for 5 min (Diener PICO, 0.5 mBar, 40 kHz, 50 W). A solution of 1% MAPTMS and 0.3% acetic acid in DI water and 98.7% ethanol was prepared. The glass slides were immersed for 5 min, then rinsed with ethanol, dried with nitrogen, and stored under vacuum.

The glass slides were mounted on 75 mm × 50 mm microscope glass slides (Sigma Aldrich: 2947) using synthetic double-sided rubber, from which we can recover the glass slide after the printing (Tesa tape purchased from RadioSpare). On the perimeter of the larger glass slide, a rectangular PMMA frame with a thickness of 8 mm, fixed by double-sided tape, created a wall containing the buffer medium, for immersed printing.

2.10. Cell-culture and labelling

For the cell seeding experiments, substrates, tubes, and the environment were first sterilized with a 70% ethanol solution. PC3-GFP prostate cancer cells were seeded at a concentration of 10,000 cells/cm^2 and cultured for 3 days in 5 mL of medium (RPMI, 10% fetal bovine serum, 1% penicillin-streptomycin-G418) at 37 °C under 5% CO_2. After 3 days, the cells were fixed with 4% formalin for 20 min and permeabilized in 0,2% tritonX-100. The cell nuclei were stained with DAPI solution at 0.02 mg/mL for 5 min. After staining, the samples were stored in PBS solution at 4 °C.

For the spheroids experiments, human adipose derived stem cells (hASCs) were isolated from abdominal dermolipectomy waste (Plastic Surgery Department, CHU Toulouse, France) from female donors, as previously described [33]. The experimental protocols were approved by the French Research Ministry's institutional ethics committee (N°: DC-2015–23–49) and informed consent was obtained from all subjects in accordance with institutional guidelines on human tissue handling and use. hASCs were plated and amplified in endothelial cell growth medium-2 (EGM2, Promocell) containing 0.1% (v/v) amphotericin B (Life-Technologies) and 1% (v/v) streptomycin/penicillin (Life--Technologies). The medium was changed every 2–3 days. When the cells reached 80% confluency, they were harvested and hASC spheroids were generated by seeding 50,000 cells in 50 μL of EGM2 medium in ultra-low attachment (ULA) 96-well round-bottom plates (Corning Incorporated Life Sciences) and maintained overnight under stirring (150 rpm). Cells were kept in EGM2 (150 μL added at day 1) medium until spheroid formation, i.e., 1–2 days after seeding. Spheroids of hASCs were individually handled and deposited in each cavity of the PEGDA structure on fibronectin-coated glass coverslips (solution at 10 μg/mL fibronectin, 37 °C overnight and washed with PBS) in a minimal volume of EGM2 medium to cover the entire structure. The spheroids were allowed to settle for several hours at 37 °C to promote attachment of the spheroids to the glass surface before further addition of EGM2 medium. The spheroids were maintained for 3–6 days and the EGM2 medium was changed every 2–3 days. After culture, PEGDA structures containing spheroids were washed in PBS and fixed with 4% paraformaldehyde overnight at RT. Samples were then permeabilized and blocked in PBS solution containing 1% Triton X-100 (Sigma) and 3% horse serum (Jackson Immunoresearch) for 3 h at RT. Next, samples were incubated with Alexa Fluor™ 488 Phaloïdin (1/500) in PBS containing 1% Triton X-100% and 1% horse serum for 3 h at RT. After PBS washing, nuclei were stained with 2 μg/mL DAPI for 1 h at RT (Sigma, USA).

2.11. Imaging

Scanning electron microscopy (SEM) imaging was performed with a Hitachi S-3700 N for printheads and hydrogel structures (dried under standard atmosphere for vacuum imaging). Images 3.A, 5.C-F, 7.B, 8.A-C, 9.A/E, graphical abstract, Suppl. images 2.G and 3., and Suppl. Video 1 were taken with an inverted microscope IX71 Olympus, DAPI, FITC or mCherry filters and a Nikon DS-Qi1Mc camera. Images 5. A-B, 7. A, 9. B-D/F were taken with a confocal Leica SP8. Image 2.D. was taken with a Dino camera. Images were analyzed with imageJ [34] using the 3D TransformJ plugin [35].

3. Results & Discussion

3.1. Description of the opto-microfluidic printing concept

Similarly to microfluidic probes [28–30], the 3D-Flowprint printhead consists in a microfluidic device with one injection and one aspiration channel for local delivery of a stream onto a surface (Fig. 1). This microfluidic delivery has many advantages, i.e., low volume consumption, multiplexing, local material delivery, and control of material composition. Optimized open microfluidic channels on the surface of the

printhead (see part 2.5) and precise control of the injection and aspiration flowrates (see part 3.2) enable hydrodynamic flow confinement (HFC) of the injected material and prevent cross-contamination in the medium.

To create these open microfluidic channels, the use of 3D printing technologies, in particular SLA, provides unique advantages for the prototyping and optimization of the microstructured volume and surface of the printhead (see part 2.2). Moreover, it offers a reliable low-cost and simple approach to the construction of 3D microfluidic devices with resolutions at the micrometric scale [30,36,37] that are largely impossible with standard photolithography or molding approaches.

The hydrogel solutions to be injected inside the printhead are photopolymerizable liquid materials with viscosities relatively close to that of water (μ_{mat} = 8.5 mPa.s for our main solution) [38]. Unlike micro-extrusion or droplet-based techniques, this printer does not require specific material characteristics such as shear-thinning properties or surface tensions adapted for droplet formation [38,39]. We focused our interest on poly(ethylene glycol) diacrylate (PEGDA), which is recognized for the development of hydrogel scaffolds and 3D models of microenvironments [40].

Between the injection and aspiration channels, a closed third channel contains a ball-lensed optical fiber (Fig. 1. B) with a focus waist diameter between 7 and 100 μm. It provides a near-collimated light all the way from the printhead to the previous slice. The illumination activates the photo-initiator lithium phenyl-2,4,6-trimethylbenzoylphosphinate (LAP), which is cleavable at 405 nm, resulting in two radically activated species. The formers initiate a chain reaction on the double carbon bonds of the hydrogel methacrylate groups to create a network, turning the liquid injected solution to a solid at the polymerization spot [41,42]. In this work, we used mainly PEGDA hydrogel and LAP photo-initiator (40% PEGDA 700, 60% PBS, 0.01% LAP), which are both biocompatible at the stated concentrations [40,42,43]. Then, as with most 3D-printing technologies, an XYZ computed itinerary constructs the 3D object vector-by-vector (Suppl. Fig. 3 and Suppl. Video 1). To increase printing speed and to add more versatility to the printer, we also implemented multi-resolutions printing.

3.2. Microfluidic characterization

3.2.1. Hydrodynamic flow confinement

Multimaterial printing systems impose a fast and efficient renewal and removal of material in the printing area to prevent contamination of the surrounding medium with unpolymerized material. Here, the small gap between the printhead and the printing substrate induces high hydrodynamic resistance between the injection and aspiration ports that limits the flow of material in the printing area and favors its spreading outside the printhead. A careful optimization of the printhead design to limit such spreading and control the distribution of flows was performed using hydrodynamic simulations and subsequently validated experimentally.

As shown in Fig. 3, the printhead geometry was designed to ensure a continuous flow of material in the exposure area and the confinement of the injected material in the printing area. The injection channel was placed at the nearest point to the PDMS dome to (i) decrease the distance between the injection channel and the polymerization point; (ii) decrease the distance between the injection and aspiration channels; and (iii) increase the distance between the injection channel and the surrounding medium. In order to further enhance the hydrodynamic confinement, the printhead integrates a buried structure at its periphery that is composed of a circular tapered channel that connects the injection port to the aspiration port, with increasing depth toward the latter (Fig. 2. B). The hydrodynamic resistance and pressure drop induced along this structure favors the orientation of the flow towards the aspiration channel and through the exposure area. In order to further enhance this confinement effect, a 900-μm-wide and 100-μm-high ridge at the periphery of the printhead helps isolate the injection and aspiration ports from the outer environment.

Fig. 3 A and 3. B provide a comparative study between experimental characterization and computer fluid dynamics (CFD) simulation of the hydrodynamic flow distribution in the printing area. In this experiment, the distance Z_{gap} between the printhead and surface was set to 100 μm. A suspension of 5 μm fluorescent particles (at 0.01% v/v) was added to our standard PEGDA 700 solution, which was used to monitor the flow distribution of the injected material. In this first series of experiments,

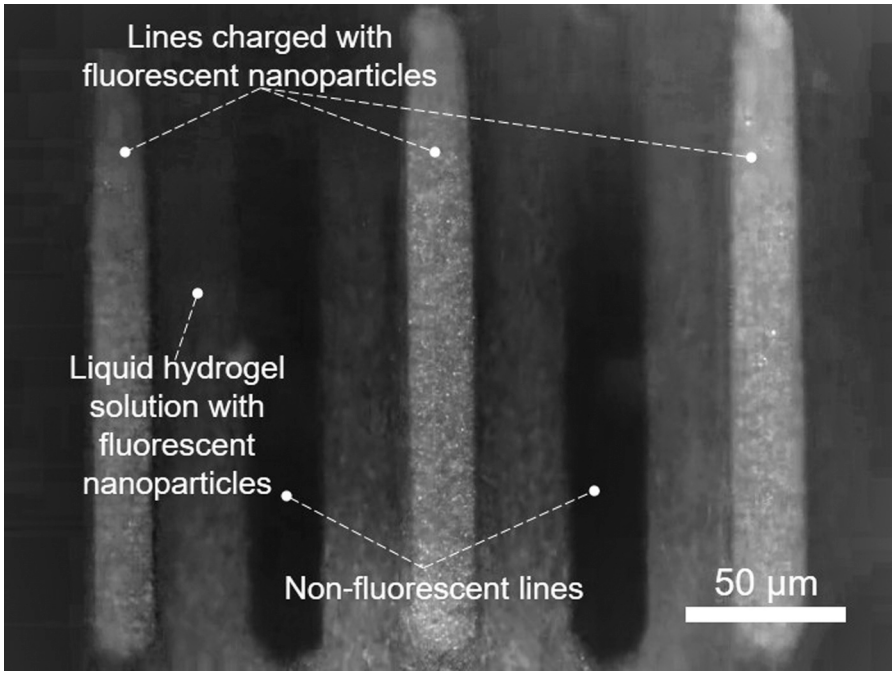

Video S1. A video clip is available online. Supplementary material related to this article can be found online at doi:10.1016/j.addma.2023.103629.

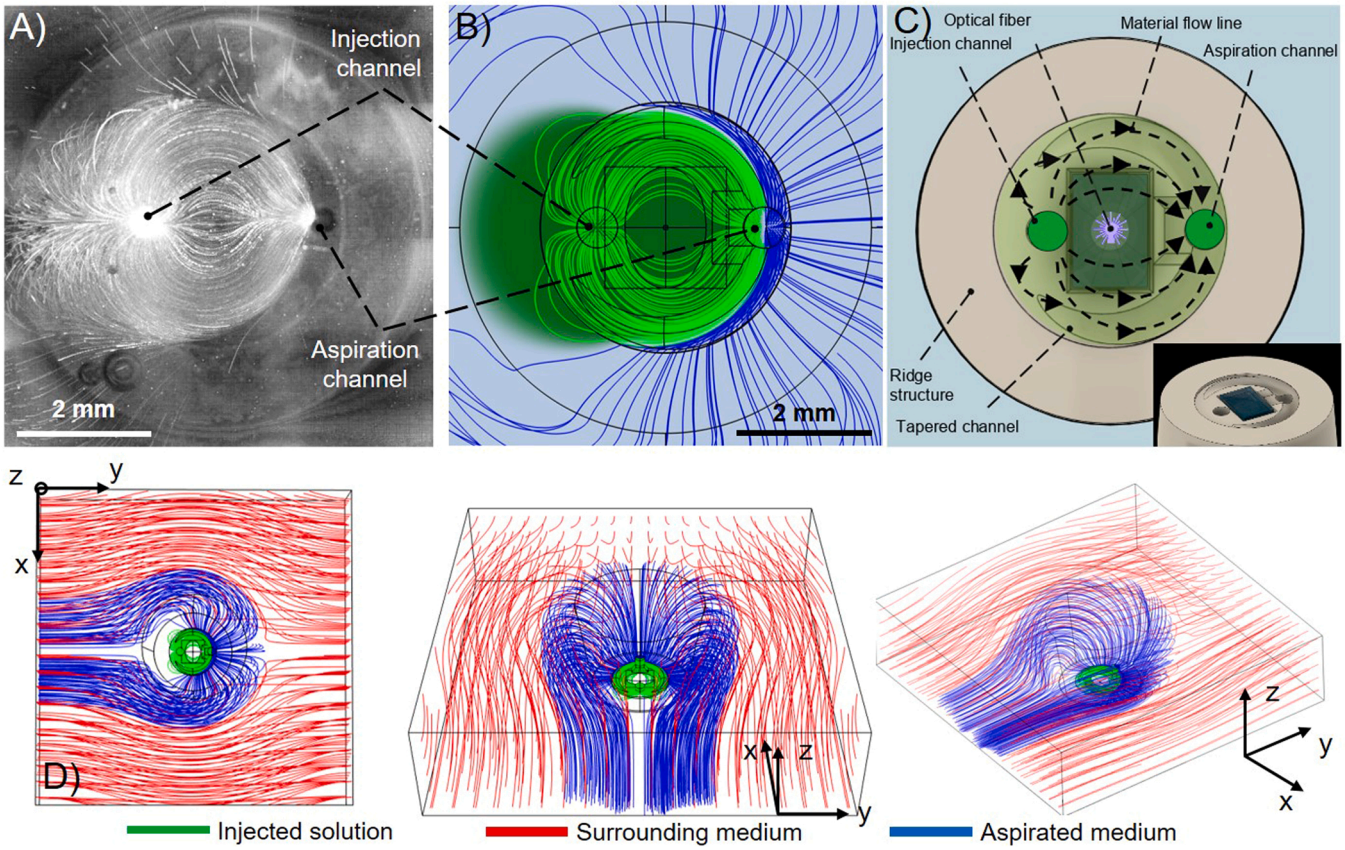

Fig. 3. Characterization of flow distribution around the printhead. (A) Experimental analysis showing the simultaneous injection and aspiration of a suspension of fluorescent particles. (B) Comsol simulations performed according to experimental parameters. (C) Schematic of the structure and topography of the printhead: A tapered microchannel associated to a circular ridge structure are used to induce hydrodynamic confinement of the injected material. (D) Three views showing the 3D distribution of flow obtained from Comsol simulations. (A-B-D) Parameters: V = + 0.1 mm/s, Z_{gap} = 100 μm, μ_{mat} = 8.5 mPa.s, μ_{med} = 1 mPa.s, φ_{in} = 25 μL/min, Rφ = 5. (B-D) Green, blue and red flow lines represent the flow distribution of respectively the injected material, the aspirated medium and the surrounding medium.

the printhead was kept immobile to better analyze the effect of the printhead topology on the flow distribution. The injection flowrate was set to 25 μL/min while the aspiration channel flowrate was set to 125 μL/min. The pictures in Fig. 3. A-B describe the flow trajectories along the plane XY, seen through the substrate. For Fig. 3. A, a video was taken, and frame intensity maxima, indicating the position of nanoparticles in each frame, have been extracted and summed to obtain the nanoparticles paths. As can be seen in Fig. 3. A, a cardioid-like flow distribution pattern is observed. Fig. 3.B. shows the distribution of hydrodynamic flow lines during material injection (in green for the injected material and in blue for the surrounding medium). There is a qualitative agreement in flow-line distribution between the experimental results and numerical studies. All visible flow lines associated with the material injection are directed towards the aspiration port. Moreover, a significant fraction of the flow lines directed towards the aspiration port is associated with the surrounding medium. These flow lines surround the limits of the injection area and confirm the confinement of the material within the printhead footprint.

On the left of Fig. 3. A, some nanoparticles can be seen, at low speed, on the external edge of the confined area. By varying the hydrodynamics parameters, this phenomenon might lead to notable material loss and potential cross-contamination. The parameters influencing this phenomenon are investigated in the next section.

3.2.2. *Influence of Z_{gap}, flowrate ratio, and V on flow confinement*

Estimation of the retrieval rate Rr (Rr = collection of the polymerizable material over injection) was measured through numerical simulations to study this phenomenon quantitatively. An exhaustive analysis of the evolution of the Rr depending on printhead velocity V, Z_{gap} and flowrate ratio ($R\varphi = \varphi_{out}/\varphi_{in}$) was performed through Comsol simulations (Fig. 4). At time t = 0 s, the entire system is filled with the first solution (in blue), representing the medium with μ_{med} = 1 mPa.s. Then, during the study, a continuous inflow of a second material with μ_{mat} = 8.5 mPa.s (in green) was applied on the injection channel at φ_{in} = 25 μL/min. A similar flowrate-controlled outflow was applied to the aspiration channel at the value $\varphi_{out} = -R\varphi^* \varphi_{in}$ (typical flowrate ratio was Rφ = 5). The simulations ran until t = 50 s (which is beyond equilibrium when HFC is maintained). The in-plane printhead velocity V is represented by adding a flow-condition on the support and the exterior box, with typical value V = +0.1 mm/s. The images are top-view, and the black lines represent the outline of the printhead geometry.

As seen in Fig. 4. B–C, for Z_{gap} < 200 μm, the flow confinement is improved (higher Rr) when drawing closer to the surface due to the increasing influence of the printhead surface structure. The hydrodynamic confinement induced by the printhead architecture increases significantly as the distance between the printhead and the surface decreases to the order of magnitude of the ridge and the other surface structures. Lower Z_{gap} is favorable to the printing of thin structures, yet HFC is still attainable at higher Z_{gap} up to 500 μm (with an appropriate flowrate ratio, as seen in Fig. 4. C), presenting the possibility of printing of high structures. Increasing the printhead velocity along the positive X-axis favors material recovery as this contributes to the motion of material towards the aspiration channel. For example, with Z_{gap} = 100 μm and Rφ = 5, Rr is 88%, 98%, and 100% (Fig. 4. E), respectively, at V = 0 mm/s, 0.1 mm/s, and 0.3 mm/s. Conversely, moving the printhead backward contributes to the spreading of the material outside the

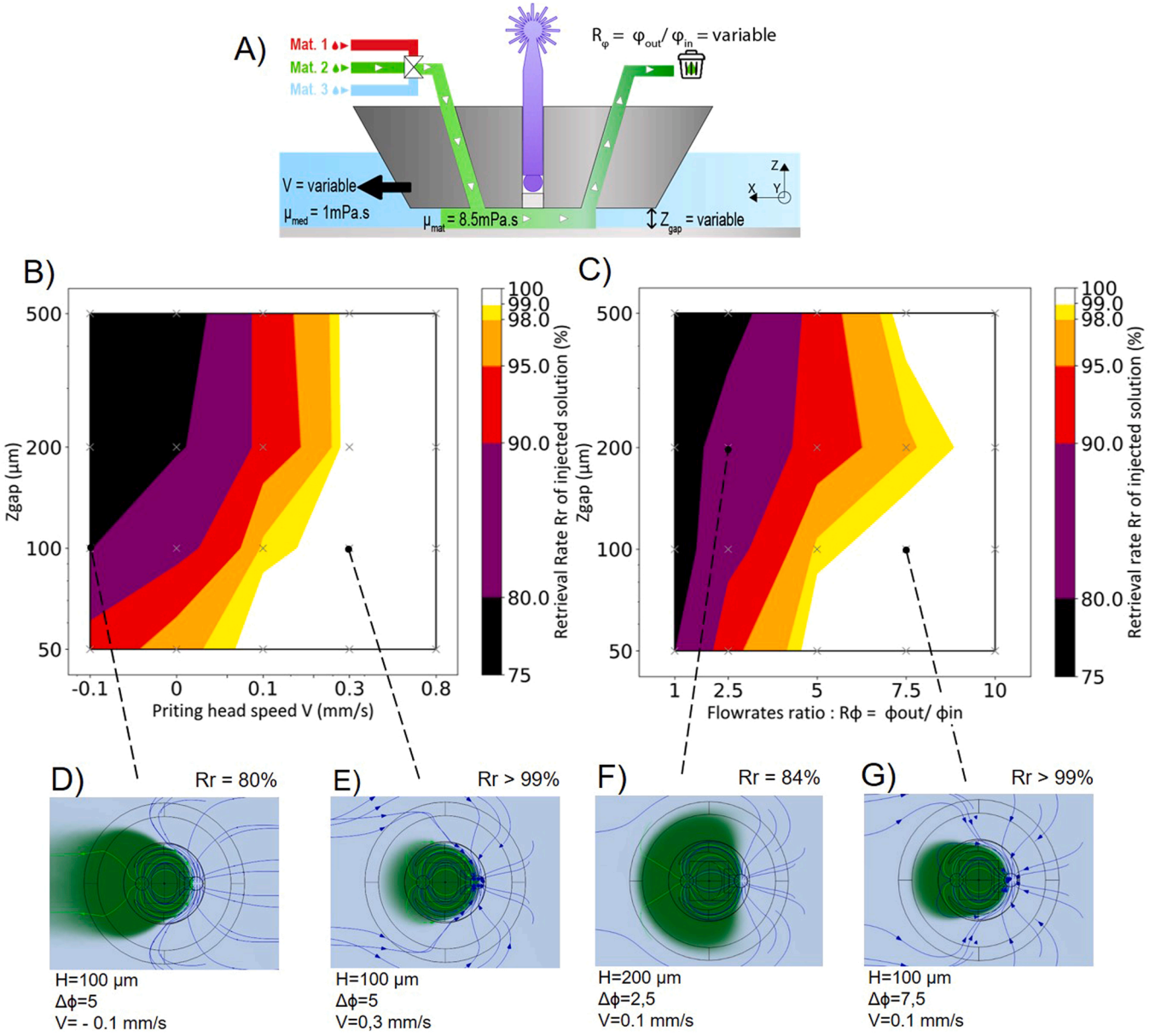

Fig. 4. Numerical simulations (Comsol) showing the influence of flowrate ratio Rφ, printhead velocity V and Z_{gap} on hydrodynamic flow confinement (HFC) (μ_{mat} = 1 mPa.s and μ_{med} = 8.5 mPa.s). (A) Schematic illustration of the main parameters investigated in this study. (B) Diagram showing the impact of V and Z_{gap} on the HFC. Rφ = 5. (C) Diagram showing the impact of Rφ and Z_{gap} on the HFC. V = 0.1 mm/s. (B–C) Grey crosses show data points obtained through Comsol simulations. Color codes were generated by interpolation between data points. (D-E-F-G) Images are Comsol top-view cross-sections (at mid-Z_{gap}) for injection of green material in blue medium with the conditions listed below. Images (E) and (G) illustrate typical low-confinement situations giving rise to material loss in the surrounding medium.

printhead area, thus reducing HFC. As an example, Rφ = 5 is not sufficient to maintain HFC with backward motion V = −0.1 mm/s for all Z_{gap} (Fig. 4. D).

Fig. 4. C confirms the expected influence of Rφ on the HFC, demonstrating that higher Rφ leads to better confinement for every Z_{gap}. We observed that Rr > 99% can be obtained at low Rφ (Rφ = 5) with Z_{gap} = 50 µm while Rφ has to be increased (Rφ ≥7.5) to reach the same level of recovery when increasing Z_{gap} above 100 µm (Fig. 4. G) to avoid cross-contamination, as seen in Fig. 4.F.

3.2.3. *Influence of material viscosity*

When compared with the surrounding medium (typically a water-based medium with viscosity (μ_{med}) = 1 mPa.s), injected materials with different viscosities (μ_{mat}) may modify the flow distribution and therefore Rr. Numerical simulations were performed with different values of μ_{mat} ranging from 1 to 10 mPa.s while keeping μ_{med} at 1 mPa.s (V = 0.1 mm/s, Z_{gap} = 50 µm, Rφ= 2.5). The HFC decreases because a more viscous material tends to be less aspirated, leading to the environmental solution taking over in the aspiration channel. By increasing the viscosity by a factor of 10, Rr only decreases from 100% to 92% (Suppl. Fig. 4), meaning that the viscosity of the injected material has a low impact on the flow distribution.

3.2.4. *Multimaterial injection and flushing*

Sequentially flushing and injecting different materials is essential for multimaterial printing, with fast and complete removal of the previous material required to avoid cross-contamination. The printhead was designed as an integrated microfluidic device connected to a library of materials through a manifold and rotating valve (see part 2.4), allowing switching during printing from one material to another. We investigated

this protocol first by the replacement of PEGDA 700 ($\mu = 8.5$ mPa.s) loaded with green fluorescent 300-nm particles with PEGDA 700 loaded with red fluorescent particles using typical flowrates ($\varphi_{in} = 30$ µL/min, $R\varphi = 5$, $V = 0$, and $Z_{gap} = 100$ µm). After 60 s, more than 90% of the first material was removed and replaced (Suppl. Fig. 5. A). This measure integrates the time required for the solution to fill the dead volumes between the valve and the printhead and considers Taylor diffusion. Then, the flushing of the PEGDA 700 material by a less viscous buffer medium ($\mu = 1$ mPa.s) was performed at the same typical flow rate and at higher flowrates ($\varphi_{in} = 60$ µL/min, $R\varphi = 5$). The results suggest a quasi-linear influence of the flushing time with flowrate, with a replacement ratio of 90% at 15 s and 30 s, respectively, for high and typical flowrates (Suppl. Fig. 5. B).

3.3. Material photopolymerization during injection

3.3.1. General concept of the opto-fluidic polymerization

Our initial experimental and numerical studies demonstrated the possibility of dynamic control of the confinement and sequential injection of photopolymerizable materials in the exposure area. Our next studies were devoted to demonstrating the photopolymerization of the materials during injection and to the characterization of the printing

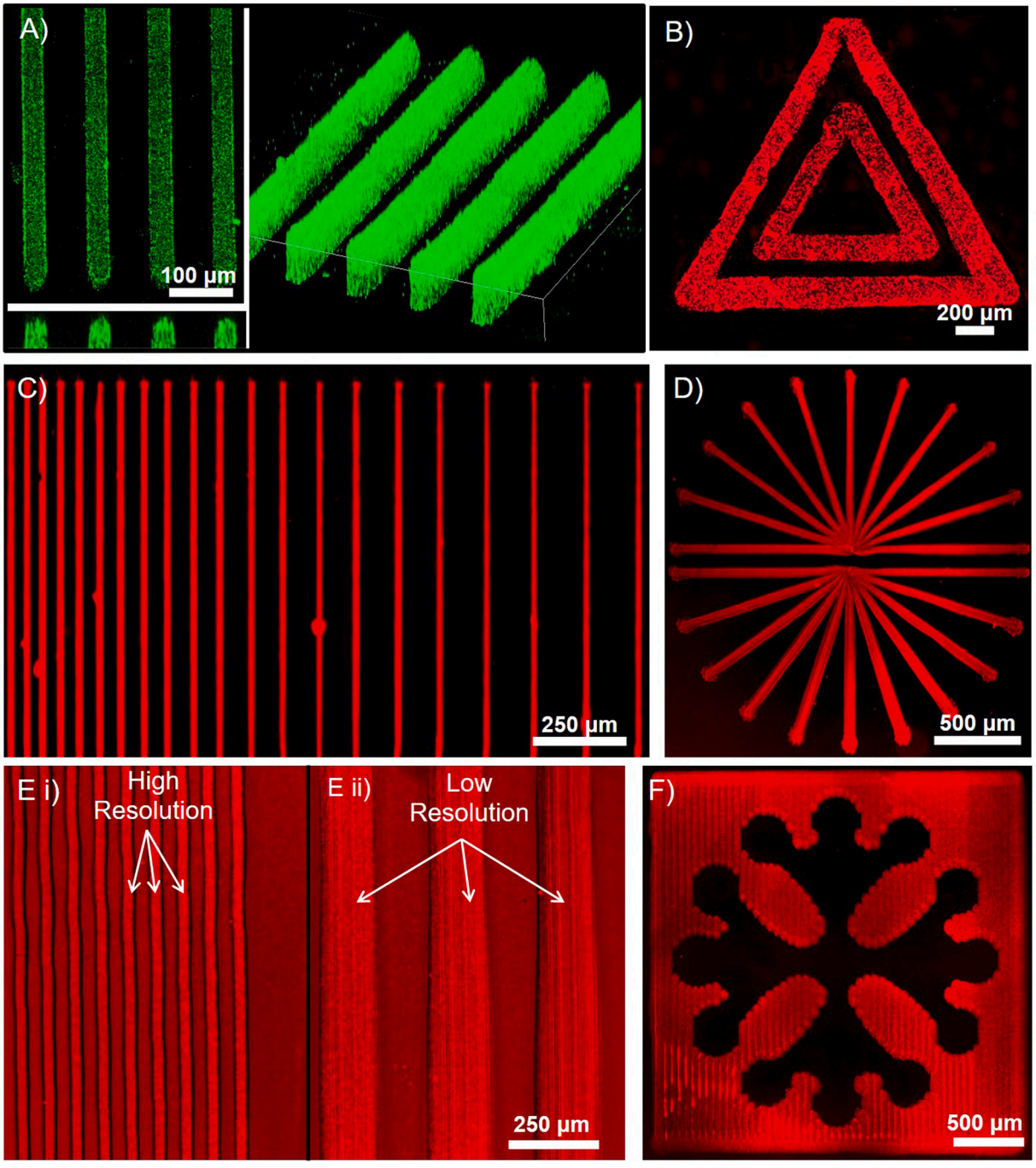

Fig. 5. Images of single-layer PEGDA structures. Suspension of 200 nm GFP (A) or 300-nm mCherry (B-F) particles were added to the material for better visualization. (A) Array of lines with constant spacing (top view, cross-section, and 3D view). (B) Intricated triangular structures. (C) Array of lines with varying spacing (30–150 µm). (D) and varying printing orientation). (E) Multiresolution printing of lines with two optical fibre configurations leading to different line widths of 35 and 160 µm. (F) Printing of a large-scale cross structure. (A-B) Confocal images. (C-D-E-F) Fluorescence images.

process. Contrary to conventional SLA or 2PP methods, in which the photosensitive material is processed under static conditions, the material here is in movement during the photopolymerization process, reminiscent of continuous flow lithography [26,44] where a flow of material is polymerized while flowing in a confined microfluidic channel. With such a process, as demonstrated in these studies, a careful investigation of the coupling between of the laser power and printhead velocity is required to determine the impact of the hydrodynamic flow on the polymerization process and resolution.

Our first validations were performed by the printing of line arrays (such as in Fig. 5. A) using PEGDA solutions. Fig. 5 shows typical examples of PEGDA features printed for a Z_{gap} value of 50 μm and observed through confocal and bright field or fluorescence imaging. Fig. 5. C shows lines of 10 μm with decreasing distances between them until 30 μm. Most printings were realized in the positive X-axis direction, yet it is possible to print in any direction, as shown in Fig. 5. B/D. Overtime, some nanoparticles aggregation might occur explaining the grainy aspect of the fluorescence images. Nevertheless, SEM images (such as in Fig. 7. C-D) confirmed the homogeneity of the hydrogel material in the printed structures.

These results confirmed that the effect of laser pulse time (blinking with a square signal at $DC_{FG} = 1$ kHz, see part 2.3) on the polymerization process is not noticeable. The distance traveled by the printhead between two pulses ($d_{pulse} = V/DC_{FG}$) in the common velocity range 0.05–0.8 mm/s varies between 0.05 and 0.8 μm, which can be considered negligible compared to the laser spot size.

We also investigated experimentally the spatial distribution of light intensity provided by the optical fibers coupled to the 405 nm laser source (see part 2.3). Sliding the fibers in the printhead indeed induces a defocusing effect that modifies the intensity distribution and controls the spot size (Suppl. Fig. 1). For example, Suppl. Fig. 1.B. shows the spatial distribution of light intensity in the exposure area for two optical configurations that were obtained by adjusting the vertical position of the fibers in the printhead (0 and 600 μm). In this configuration, the laser spots were estimated to be around 6 and 17 μm (FWHM measured with $Z_{gap} = 50$ μm). The profile of the energy distribution shows a good homogeneity over large Z distances (>200 μm) allowing the processing of thick material layers. The optical fibers and printheads are easily changed, allowing different spot sizes and widths of printed lines across experiments. A small spot size (6–40 μm) was mainly used to benefit high-resolution printing (i.e., Fig. 5. C/E.i, Fig. 6), while a larger spot size (up to 200 μm, i.e., Fig. 5. B/E.ii, Fig. 7. A) was favorable for stability and quicker printing.

3.3.2. *Influence of printhead velocity and output power during photopolymerization*

In-flow photopolymerization was investigated through systematic modulation of the output power P_{out} and printhead velocity V by measuring the printing resolution. To be consistent with the hydrodynamic studies performed earlier, we investigated V in the range 0.05–0.8 mm/s, which is known to be compatible with hydrodynamic confinement conditions ($R\varphi = 7.5$, $\varphi in = 25$ μL/min), and we varied P_{out} in the range 0.0525–0.4 mW. For each P_{out} and V combination, the minimum dose required to create stable structures was estimated and the line width were vertically measured with an inversed fluorescence microscope (Fig. 6. A). The minimum line width obtained experimentally was 20 μm for several combinations of P_{out} and V corresponding to a threshold dose of 3750 mJ/cm^2 (see part 2.3 and eq. 1) and can be associated with a ratio $P/V = 0.74$ mJ/mm. As expected, the line width value increases with dose up to a value close to 160 μm. The results reveal a logarithmic dependence of line width on P_{out}/V (Suppl. Fig. 6). We could fit the curves to Eq. 3:

$$Width(P_{out}, V) = k_1 \bullet \ln(k_2 \bullet P_{out}/V) \quad (3)$$

with $k_1 = 44.82$, $k_2 = 2.376$, and $R^2 = 0.9704$.

3.3.3. *Influence of pre-existing structures on the printing process*

The exposure dose is associated with the residence time of the material in the area covered by the laser spot. This residence time correlates with the velocity of the material relative to the optical fiber, resulting both from the velocity of the printhead relative to the substrate and from the velocity of the material relative to the printhead. A question naturally arising when considering material inflow is the impact of preexisting structure at the proximity of the exposure area. Indeed, the printing process occurs in a continuous manner with the motion of the laser spot according to the programmed trajectory. Structures may modify the distribution of velocities, affecting the photopolymerization dose and impeding material supply during printing.

Simulations performed at $\varphi in = 25$ μL/min, $R\varphi = 5$ showed that on

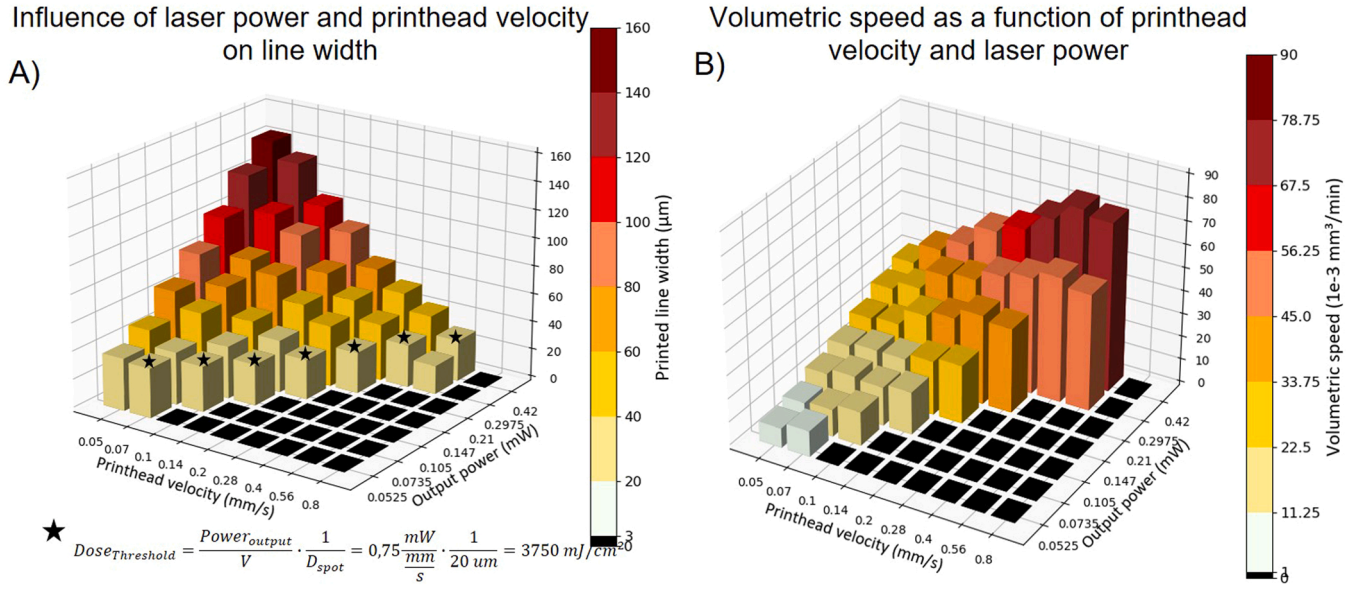

Fig. 6. Study of the in-flow photopolymerization. (A) Influence of the optical output power and printing speed on line width. Experiment realized with h = 75, φ_{in} = 25 μL/min, and Rφ = 5. Dose threshold values correspond to the minimum dose giving rise to stable structures (marked with a *). (B) Volumetric printing speeds based on the data in Fig. 6.A data and eq. 4.

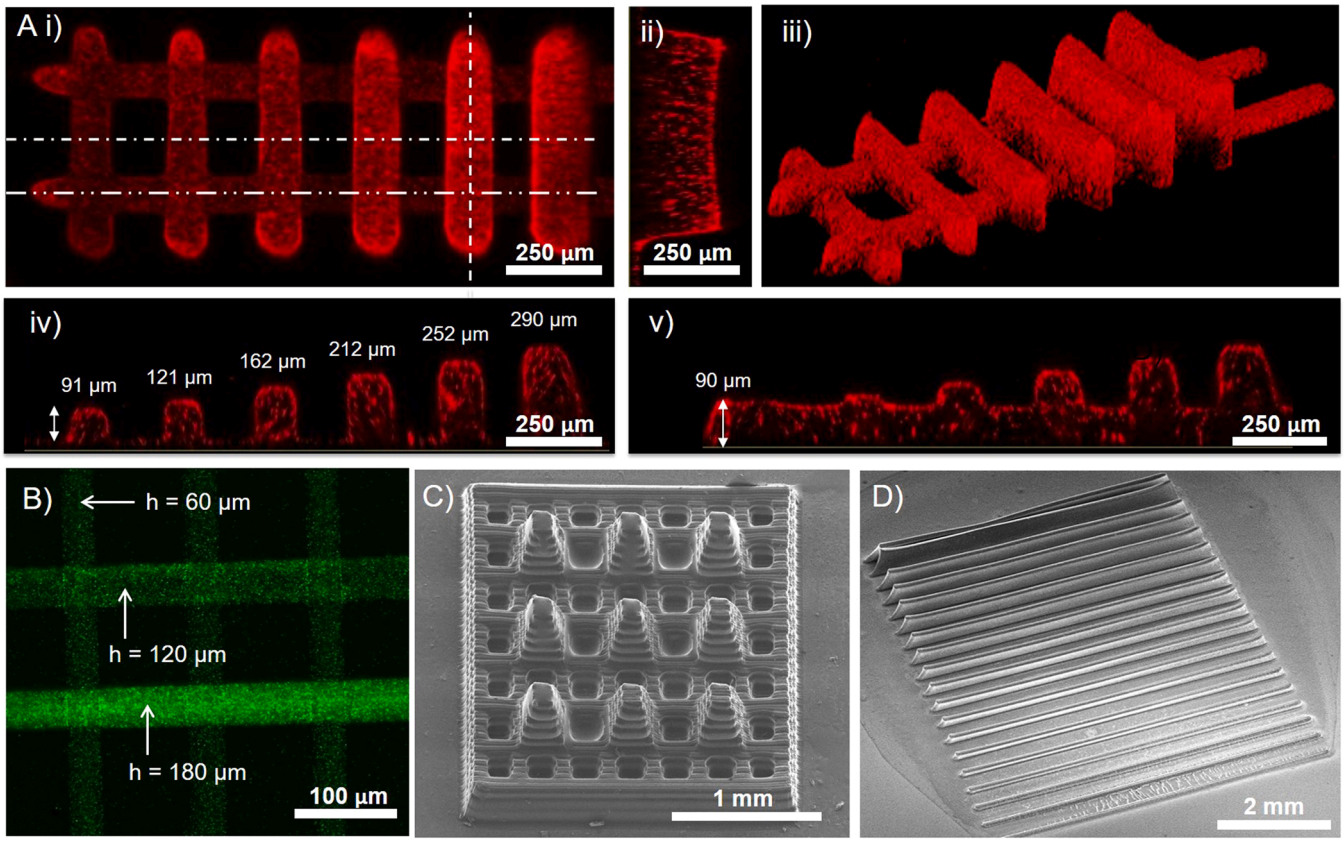

Fig. 7. 2.5D and 3D PEGDA printed structures. (A) Confocal pictures of a ladder structure with segments printed at varying heights (h = 100 or 350 µm). (B) Fluorescence image of crossing lines successively printed with three different printing heights. (C) SEM image of a millimetric 3D structure, including protruding and recessed pyramidal features. (D) SEM image of an array of lines with varying heights (h = 20–400 µm).

flat substrates with no pre-existing printed structures, the velocity of the solution relative to the head is around 0.5 mm/s in the polymerization area (measured at mid-Z_{gap} = 25 µm, Suppl. Fig. 7. A). When considering the presence of structures, simulations confirmed a significant reduction of the material velocity. In the vicinity of a pre-existing printed line, solution velocity drops to 0.1 mm/s (printhead velocity), as can be observed in supplementary figure 7.B. During the printing of a continuous layer (Suppl. Fig. 7.C.), the fluid is also slowed by the previously printed adjacent lines on the side. In both cases, the reduction of material velocity near the printed structures reduces the impact of material inflow and aspiration on the photopolymerization process that propagates progressively in the vicinity of the structure being processed.

The nearly constant width of printed lines in Fig. 6. A when keeping a constant P/V factor confirms that the dose is linked to the velocity of the printhead motion and that the motion due to the injection and aspiration flow is negligible. This observation provides an additional illustration of the decoupling between the photopolymerization and the hydrodynamic aspects (related to mass transport through injection and aspiration). For the start of new lines, no structures are already present, so the speed reduction is not effective. To overcome this limitation, we implemented over-dosing for these circumstances, which was achieved by a pause of 0.2 s before starting the printhead motion.

3.3.4. Printing resolution and correlated printing time

Fig. 6. A shows a minimum line width of 20 µm for a laser spot size of 16 µm (measured as described in part 3.3.2). We observed that printed line width was almost always bigger than the estimated laser spot size. We hypothesize that this effect is due to chemical diffusion of reactive species, light dispersion and over-dosing above the polymerization threshold.

Fig. 6. B shows the evolution of the volumetric printing speed according to the printhead velocity and output power in the same range of values as shown in Fig. 6. A for Z_{gap} = 75 µm. The volumetric printing speed is given by $V^{xyz}_{printing} = V \bullet width \bullet height$ (4). We observed a logarithmic influence of the printhead velocity on the width (see Eq. 3), meaning that the best strategy for increasing the overall volumetric speed and decrease the printing time is to increase the printhead velocity. The variation of the width by modulation of P_{out} and V is advantageous as it allows tuning the width of printed features. From this perspective, increasing the laser spot size by switching to a larger spot size configuration should be preferable as compared to increasing the output power. Fig. 5.E. demonstrates this capacity by the printing of two line arrays using a dual fiber head (high-resolution fiber on the left and lower-resolution fiber on the right). This feature could also be used to adjust the overlap between adjacent lines when considering the printing of merged lines to create a bulk object [45]. Using two fibers inside the printhead could also allow multi-wavelength printing for more specific multimaterial printing, such as that proposed by Ravanbakhsh in 2021 [6].

3.4. Processing multilayered and multimaterial 3D structures

3.4.1. Control of layer thickness

The creation of 3D structures through additive manufacturing processes requires accurate and reproducible control of the thickness of each printed layer. With 3D-FlowPrint technology, the layer thickness is defined by the geometrical confinement between the PDMS window and the support, i.e., the Z_{gap} value. Consequently, the Z_{gap} value is directly associated with the layer thickness as provided by the slicing software (see part 2.8). Fig. 7. B shows an example of structures obtained for V = 0.1 mm/s at three different programmed heights (60, 80, and

120 μm). Each line was printed in a single passage, programming Z_{gap} to the desired thickness value. Interestingly, the three structures show almost constant lateral dimensions (~30 μm), demonstrating the low influence of Z_{gap} on lateral feature dimensions, and thus a limited spreading of light distribution in the layer. We performed a more systematic study of the correlation between the vertical position of the printhead and the resulting structure thickness for values up to 350 μm. We implemented a fiber with large spot size (100 μm) resulting in an enlargement of the lines up to 150 μm. The dose was maintained constant during the experiment. Fig. 7. A shows a ladder structure with programmed heights varying from 100 to 350 μm in 50-μm increments. Each segment of the structure was printed in a single passage by adjusting Z_{gap} to the target thickness. Confocal observations revealed a 16% shrinking of the structure in the Z-axis. In the cross-section shown in Fig. 7.A.iv., orthogonally to the lines, we can see the accurate shape, while slight slopes (5°) are visible at the beginning and the end of lines in Fig. 7.A.ii due to shrinkage.

This experiment demonstrates the ability to produce, independently from the printhead velocity and output power, structures with a wide range of thicknesses. This observation first confirms the low light absorption in the polymerization layer, which is negligible in the range of dimensions investigated. This is made possible by the transparency of the injected PEGDA-based material. The hydrogel solutions indeed exhibit a low absorbance coefficient ($\leq 0.01\ m^{-1}$) [46] that allows vertically uniform polymerization of the hydrogel layer. Thus, the polymerization of such PEGDA formulations does not show mechanisms related to front polymerization that may have arisen in absorbing samples [47]. Optimizing the transparency of the material is thus a clear advantage in terms of writing speed when considering the processing of thick material layers. However, this feature underlines one of the limits of the printing system when considering the creation of hollow structures or overhangs that might require careful adjustment of light absorption to benefit from the front polymerization mechanism.

3.4.2. *Raster-printing protocol with positive and negative X velocities*

The printhead was designed to ensure efficient confinement and recovery of the material by creating a preferential pathway, with low hydrodynamic resistance, towards the aspiration channel. This resulted in an asymmetric design that favors the flow of the material along the X direction from the injection port to the aspiration port. However, because of the no-slip boundary conditions, the printhead motion relative to the substrate modifies hydrodynamic flow in the exposure area. As illustrated in Fig. 4. D, moving the printhead in the negative direction may impede hydrodynamic confinement and favor loss of material in the surrounding medium. Even if we could still demonstrate the ability to print in 360° as shown in Fig. 5. D, polymerization was thus preferably performed following the positive X-axis direction. The printing of extended structures was processed using a conventional raster method (Suppl. Fig. 8. B). In each layer, the slicing software decomposes the features in an array of adjacent vectors oriented along the X direction. The trajectory of the printhead follows the first vector with laser on (green). Then, the laser is turned off along the second vector (dashed red) and the printhead is positioned at the beginning of the third vector. According to the expected line width, a 10% overlap between each laser passage was implemented to ensure cohesion of the final structure. In order to further limit potential loss of material during the repositioning of the printhead, the Rφ ratio was dynamically adjusted during the process, i.e., $R\varphi = 5$ during printing and increased up to $R\varphi = 10$ during repositioning (with $V = 0.1$ mm/s and $Z_{gap} = 50$ μm; see Suppl. Fig. 8. B). We could prove the efficiency of our printing method by creating a French Occitan cross, as shown in Fig. 5.F.

We demonstrated the robustness of this printing process for the creation of millimetric-scale multilayered structures, such as that presented in Fig. 7.C. This structure integrates an array of pyramidal features with a 500 μm x 500 μm base and 500 μm height. In this experiment, the printhead velocity was set to 0.5 mm/s while the Z_{gap} value was set to 75 μm and maintained constant for each of the eight layers composing the final structure. The printing was performed in 6 h (Fig. 7.C.). Interestingly, this capacity of printing for long periods demonstrates the stability of the printing process. On the one hand, it shows that all along the printing, the injection and aspiration strategy allows for a continuous supply of photopolymerizable material to the exposure zone, even in the case of high-aspect-ratio structures such as those presented above. On the other hand, the spot size and associated printed voxel width remained stable along the experiment with no visible ageing of the PDMS layer. This result confirms the durability of the printheads..

3.4.3. *Material switching*

An example of material switching while printing is presented in Suppl. Video 1 (at video speed x8). Fig. 8. A-B-C shows several proofs of concept for multimaterial printing using different solutions of PEGDA prepolymer containing suspensions of fluorescent nanoparticles. Even in the case of enclosed structures, such as those presented in Fig. 8.B., we did not observe any impact of the presence of polymerized structures in the exposure area prior to the injection of a second material. The structures show a homogeneous shape, composition, and constant resolution (line width of 50 μm). Similar results were obtained in the case of 3D multilayer structures, such as the helicoïdal structure shown in Fig. 8.C. That structure was obtained using three standard PEGDA solutions (1st with green particles, 2nd with red particles, and 3rd without nanoparticles). This millimeter-scale structure was obtained by stacking five layers with a thickness of 100 μm. For each layer, the systems performed successive injections of materials with $\varphi_{in} = 30$ μL/min, $R\varphi = 5$, and a flushing time of 90 s. Fluorescence imaging confirmed the stability of the printing process. These results also show that, for these conditions, there is no cross-contamination of materials in the printed features, which would indicate insufficient material inflow or flushing time when switching from one material to another. Han et al. achieved a switching time at 90% of 8 s [21]. However, they impose major stress on the printing structures with flowrates of approximately 1 mL/s, which is around 300-times the flowrate we used in this work. A compromise might be determined by the user to balance the advantages of fast switching time and high flowrate.

3.5. *Printing scaffolds for cell patterning and spheroid engineering*

We investigated how a cell colony could be patterned by non-adherent PEGDA printed on a glass surface. Cells (PC3-GFP) were seeded onto arrays of lines (Fig. 9. A), grids (Fig. 9. B), and converging lines (Fig. 9. C). As expected, no cells were detected on the PEGDA structures at day 1, confirming its protein-repellant and non-adherent properties (Fig. 9. A) while some cells can be observed even in the narrow gap separating the lines (gap = 20 μm). Cell division led to cell confluence after day 3 of culture. The 3D-FlowPrint technology allowed us to explore cell development in specific and tuned geometric conditions. Interestingly, we can see the cells starting to grow out of the PEGDA lines (height = 50 μm) at day 3. As shown in Fig. 9. C, cell development proceeded until an accessible distance of 10 μm between two converging lines. The 3D-FlowPrint technology could also be used to probe cell aggregates using a PEGDA grid (Fig. 9. B).

We also investigated how cell migration from human ASC spheroids can be spatially controlled using guiding structures based on differential cell adhesive properties. This printing technology allowed us to generate high-aspect-ratio non-adherent PEGDA patterns delimiting cavities (D = 450 μm, h = 600 μm) surrounded by guiding channels with different widths (100, 150, and 200 μm, Fig. 9. D-F). Cavity size was adjusted to spheroid dimension allowing hosting of the spheroids inside and maintaining them during culture. Cell attachment was observed in the adhesive areas in the first hours of culture. F-actin phalloidin staining revealed that, after 3 days, spheroid sprouting was restricted to the adhesive channels. Cell colonization was only restricted by the PEGDA

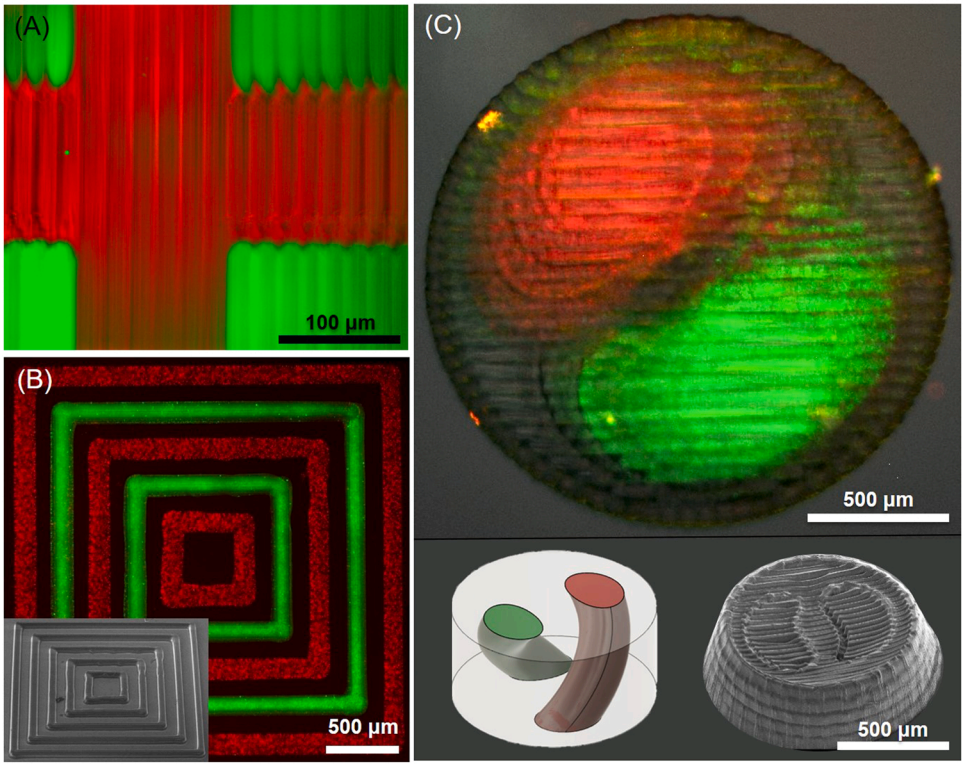

Fig. 8. Demonstration of multimaterial printing. (A) Successive printing of segments showing low cross contamination and alignment resolution, h = 50 µm.(B) Concentric squares printed from larger to smaller, h = 50 µm.(C) Double helicoidal structure, h = 500 µm. Lower left and right corners show a CAD image and a SEM image of the printed structure. (A-B-C) All made from PEGDA solutions (with 300-nm mCherry particles for red, 200-nm GFP particles for green, and no nanoparticles for grey).

geometry independently of channel size. Altogether, these results suggest that this printing approach could be adapted for further characterization of cell confinement and patterning effects on biological processes. This design may be especially useful to study the mechanisms of confined migration, known to promote cancer cell invasion [48]. Moreover, being able to drive spheroid fusion [49] or interconnectivity [50,51] in biomaterials is currently of major interest in the tissue engineering field.

4. Conclusion

Most 3D printing methods reported so far lack the ability to print multimaterial objects in combination with high-resolution. Some have achieved this goal by laborious swapping between reservoirs or by printing inside fluidic chambers. In this article, we proposed a new method to 3D print multimaterial high-resolution objects by combining photopolymerization with a microfluidic printhead. Such a system prints directly in immersion in open media and does not require a tank of material, since the printhead is itself responsible for material supply without cross-contaminating the surrounding environment. By dissociating the polymerization process from the material supply, we were able to reach high-resolution printing (down to 10 µm in the XY plane) with multimaterial ability. Unlike most extrusion systems, the material does not need any specific properties, such as shear thinning, and can have a viscosity close to that of water. This printer also benefits from two-resolution printing to promote overall printing speed. Using a second wavelength with a dual-fiber printhead could be useful for heterogeneous structures with specific materials, as proposed by Ravanbakhsh in 2021 [6].

In this study, we 3D-printed the printhead itself to gain time, cost, and especially versatility. The printhead has been optimized through Comsol simulation by adding or removing structures at the apex in order to enhance the confinement ability and to direct the injected material toward the polymerization point. Similar simulations helped us to demonstrate our capability to confine the injected material in the enclosure below the printhead and the substrate without cross-contamination. This was achieved by choosing the right printing parameters through systematic microfluidic simulations and correlation to experiments. We demonstrated that in-flow photopolymerization was achievable, and we characterized the theoretical dose threshold. We demonstrated the potential of our system to print close, non-touching structures without the issue of dose overlapping in the gap. We presented multiple examples of objects printed with this technology, including high-resolution printing in the XYZ axis, high-aspect-ratio structures, inscribed structures, and multimaterial structures. Finally, we used the 3D-FlowPrint technology to create 2.5D objects to culture cells and spheroids on constrained environments, showing the specific development of the aforementioned elements.

In the future, enlarging the range of printable biomaterials is the main objective. For example, combining PEGDA-based materials with gelatin methacrylate (Gel-MA), methacrylated collagen (Col-MA) or methacrylated hyaluronic acid (HA-MA) appears to be a promising perspective to promote cell adhesion [52] while keeping the hydrodynamic properties close to those of PEGDA. Materials with high contents of HA-MA or Gel-MA would allow introducing cell suspensions directly within the hydrogel formulation and thus opening a path towards 3D bioprinting. From this perspective, the multiplexing and multiresolution capacities of our approach would provide opportunities for the creation of heterogeneous multiscale structures requiring the organization of specific cell populations in complex architectures.

CRediT authorship contribution statement

Fournie Victor: Writing – review & editing, Writing – original draft, Visualization, Software, Methodology, Investigation, Conceptualization. **Malaquin Laurent:** Writing – review & editing, Writing – original draft, Visualization, Validation, Project administration, Methodology, Funding acquisition, Conceptualization. **Reitz Arnaud:** Writing – review & editing, Project administration, Funding acquisition, Conceptualization. **Joseph Pierre:** Writing – review & editing, Conceptualization. **Escudero Melanie:** Writing – original draft, Investigation. **Assie-Souleille Sandrine:** Writing – review & editing, Investigation, Conceptualization.

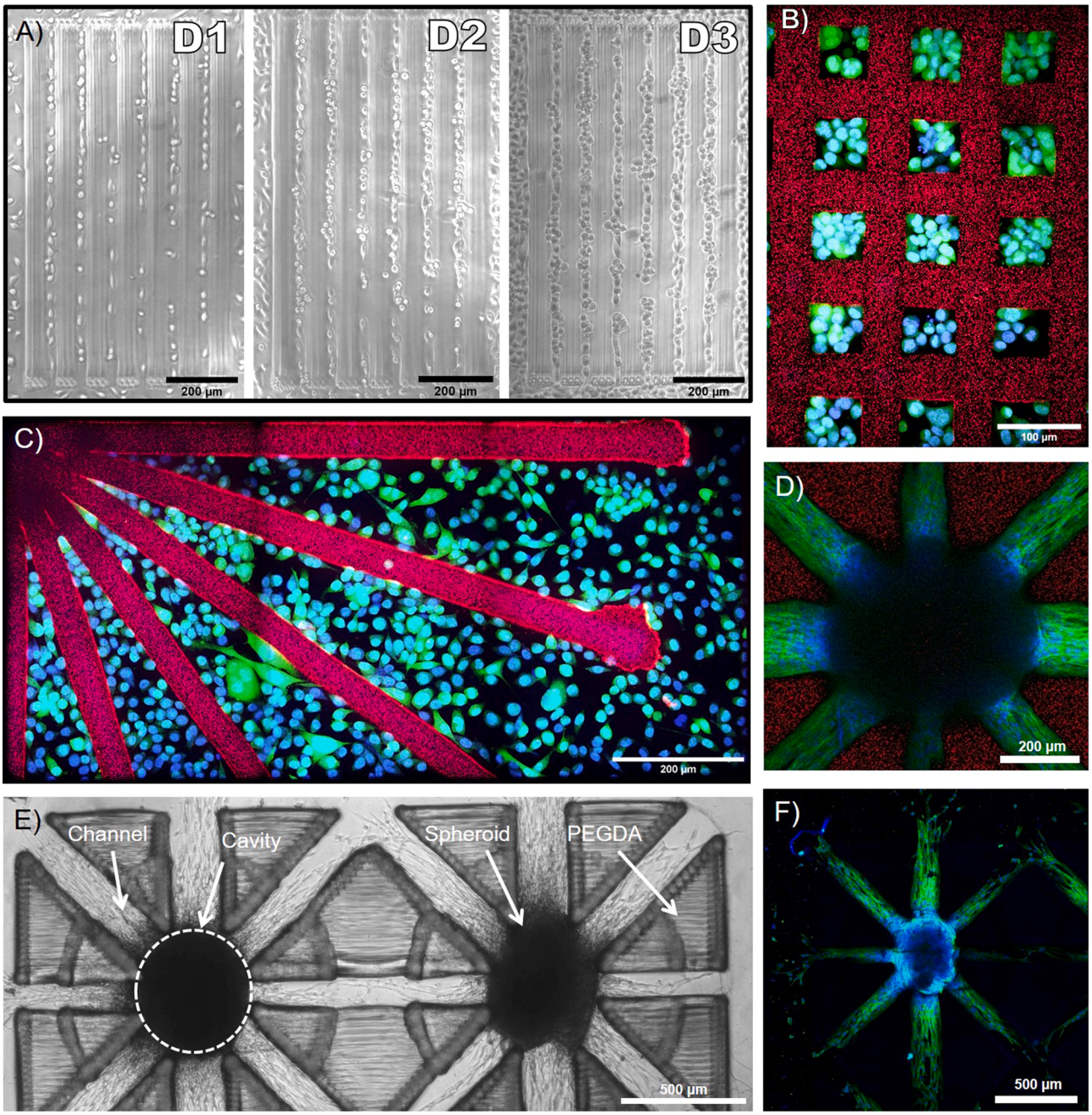

Fig. 9. Illustration of cell and spheroid patterning on PEGDA patterns. (A, B, C) PC3 cells were cultivated on non-adherent PEGDA arrays of lines. (A) Images show a time lapse taken at day 1, 2, and 3. (B,C) PC3 cells after 3 days of culture. (D-E-F) Spheroids generated from hASCs were cultivated on PEGDA channel arrays. Pictures were taken at day 3 for (D-E) and day 6 for (F). (A-E) are bright field images and (B, C, D, F) are confocal images (PEGDA structures can be seen with mCherry nanoparticles (B, C, D), actin is marked in green (B, C, D, F), and nuclei are marked in blue (B, C, D, F)).

Roul Julien: Investigation. **Foncy Julie:** Investigation, Funding acquisition, Conceptualization. **Trevisiol Emmanuelle:** Writing – review & editing. **Venzac Bastien:** Writing – review & editing, Investigation.

Declaration of Competing Interest

The authors declare the following financial interests/personal relationships which may be considered as potential competing interests Victor Fournie reports financial support, administrative support, equipment, drugs, or supplies, and travel were provided by Fluigent. Arnaud Reitz reports financial support and travel were provided by Fluigent. Victor Fournie has patent Printhead of a printer, printer and printing method issued to EP3661754B1. Laurent Malaquin has patent Printhead of a printer, printer and printing method issued to EP3661754B1. Sandrine Assie-Souleille has patent Printhead of a printer, printer and printing method issued to EP3661754B1. Victor Fournie and Arnaud Reitz are employees of Fluigent SA (Kremlin-bicètre, 94270, FRANCE). The remaining authors have no conflicts of interest to declare. L. Malaquin, S. Assie-Souleille and V. Fournie (among other inventors) have patented the 3D-FlowPrint technology (EP3661754 - 2020–06-10).

Data Availability

Data will be made available on request.

Acknowledgements and funding

The authors would like to acknowledge Manon Naudé and Marie-Charline Blatché (LAAS-CNRS, Toulouse, FRANCE) for their support in cell culture experiments, Laurence Vaysse and Louis Casteilla (Restore, UMR 1301 (Inserm) / UMR 5070 (CNRS), Toulouse, FRANCE) for their support in the analysis of biological results, Brice Ronsin (CBD Imaging core facility, TRI Genotoul, Toulouse FRANCE) for his support in confocal imaging and Godefroi Saint-Martin (LAAS-CNRS, Toulouse, FRANCE) for his support in instrumental development. This work was supported by the French RENATECH network. It was partly supported as part of the MultiFAB project funded by FEDER European Regional Funds and French Région Occitanie (16007407/MP0011594), by the HoliFAB project funded by the European Union's H2020 program (760927), by the French national agency for the research (ANR Printiss, ANR21CE1941), and by the French National Agency of Research and Technology (2020/0037).

Appendix A. Supporting information

Supplementary data associated with this article can be found in the online version at doi:10.1016/j.addma.2023.103629.

References

[1] A.C. Daly, M.E. Prendergast, A.J. Hughes, J.A. Burdick, Bioprinting for the Biologist, Cell vol. 184 (1) (2021) 18–32, https://doi.org/10.1016/j.cell.2020.12.002.
[2] S.V. Murphy, A. Atala, 3D bioprinting of tissues and organs, 2014 32:8, Nat. Biotechnol. vol. 32 (8) (2014) 773–785, https://doi.org/10.1038/nbt.2958.
[3] P. Bajaj, R.M. Schweller, A. Khademhosseini, J.L. West, R. Bashir, 3D Biofabrication Strateg. Tissue Eng. Regen. Med. (2014), https://doi.org/10.1146/annurev-bioeng-071813-105155.
[4] I.T. Ozbolat, M. Hospodiuk, Current advances and future perspectives in extrusion-based bioprinting, Biomaterials vol. 76 (2016) 321–343, https://doi.org/10.1016/j.biomaterials.2015.10.076.
[5] H. Gudapati, M. Dey, I. Ozbolat, A comprehensive review on droplet-based bioprinting: Past, present and future, Biomaterials vol. 102 (2016) 20–42, https://doi.org/10.1016/J.BIOMATERIALS.2016.06.012.
[6] H. Ravanbakhsh, V. Karamzadeh, G. Bao, L. Mongeau, D. Juncker, Y.S. Zhang, Emerging Technologies in Multi-Material Bioprinting, Adv. Mater. vol. 33 (49) (2021) 2104730, https://doi.org/10.1002/adma.202104730.
[7] L. Ning, X. Chen, A brief review of extrusion-based tissue scaffold bio-printing, p. 1600671–1600671, Biotechnol. J. vol. 12 (8) (2017), https://doi.org/10.1002/BIOT.201600671.
[8] R. Devillard, et al., Chapter 9 - Cell Patterning by Laser-Assisted Bioprinting (in Micropatterning in Cell Biology Part A), in: M. Piel, M. Théry (Eds.), Methods in Cell Biology, vol. 119, Academic Press, 2014, pp. 159–174, https://doi.org/10.1016/B978-0-12-416742-1.00009-3 (in Micropatterning in Cell Biology Part A).
[9] D. Hakobyan, et al., Laser-Assisted Bioprinting for Bone Repair, in 3D Bioprinting: Principles and Protocols, in: J.M. Crook (Ed.), Methods in Molecular Biology, Springer US, New York, NY, 2020, pp. 135–144, https://doi.org/10.1007/978-1-0716-0520-2_8.
[10] Z. Zheng, D. Eglin, M. Alini, G.R. Richards, L. Qin, Y. Lai, Visible Light-Induced 3D Bioprinting Technologies and Corresponding Bioink Materials for Tissue Engineering: A Review, Engineering vol. 7 (7) (2021) 966–978, https://doi.org/10.1016/j.eng.2020.05.021.
[11] T. Zandrini, S. Florczak, R. Levato, A. Ovsianikov, Breaking the resolution limits of 3D bioprinting: future opportunities and present challenges, Trends Biotechnol. (2022), https://doi.org/10.1016/j.tibtech.2022.10.009.
[12] Q. Ge, et al., Projection micro stereolithography based 3D printing and its applications, Int. J. Extrem. Manuf. vol. 2 (2) (2020), 022004, https://doi.org/10.1088/2631-7990/ab8d9a.
[13] H. Kumar, K. Kim, , Stereolithography 3D Bioprinting, Methods Mol. Biol. vol. 2140 (2020) 93–108, https://doi.org/10.1007/978-1-0716-0520-2_6/COVER.
[14] L. Yang, F. Mayer, U.H.F. Bunz, E. Blasco, M. Wegener, Multi-material multi-photon 3D laser micro- and nanoprinting, gxjzz vol. 2 (3) (2021) 296–312, https://doi.org/10.37188/lam.2021.017.
[15] C. Zhou, Y. Chen, Z. Yang, B. Khoshnevis, Digital material fabrication using mask-image-projection-based stereolithography, Rapid Prototyp. J. vol. 19 (3) (2013) 153–165, https://doi.org/10.1108/13552541311312148/FULL/XML.
[16] Y. Lu, et al., Microstereolithography and characterization of poly(propylene fumarate)-based drug-loaded microneedle arrays, Biofabrication vol. 7 (4) (2015), 045001, https://doi.org/10.1088/1758-5090/7/4/045001.
[17] Z.-C. Ma, et al., Femtosecond laser programmed artificial musculoskeletal systems, Art. no 1, Nat. Commun. vol. 11 (1) (2020), https://doi.org/10.1038/s41467-020-18117-0.
[18] B. Grigoryan et al., Development, characterization, and applications of multi-material stereolithography bioprinting, Scientific Reports, vol. 11, p. 3171–3171, 123apr. J.-C., ⟨doi:10.1038/s41598–021-82102-w⟩.
[19] X. Peng, et al., Integrating digital light processing with direct ink writing for hybrid 3D printing of functional structures and devices, Addit. Manuf. vol. 40 (2021), 101911, https://doi.org/10.1016/j.addma.2021.101911.
[20] A.K. Miri, et al., Microfluidics-enabled multimaterial maskless stereolithographic bioprinting, Adv. Mater. vol. 30 (27) (2018) 1800242, https://doi.org/10.1002/adma.201800242.
[21] D. Han, C. Yang, N.X. Fang, H. Lee, Rapid multi-material 3D printing with projection micro-stereolithography using dynamic fluidic control, Addit. Manuf. vol. 27 (2019) 606–615, https://doi.org/10.1016/J.ADDMA.2019.03.031.
[22] F. Mayer, S. Richter, J. Westhauser, E. Blasco, C. Barner-Kowollik, M. Wegener, Multimaterial 3D laser microprinting using an integrated microfluidic system, Sci. Adv. vol. 5 (2) (2019), https://doi.org/10.1126/SCIADV.AAU9160/SUPPL_FILE/AAU9160_SM.PDF.
[23] G. Lipkowitz, et al., Injection continuous liquid interface production of 3D objects, Sci. Adv. vol. 8 (39) (2022) eabq3917, https://doi.org/10.1126/sciadv.abq3917.
[24] M.A. Skylar-Scott, J. Mueller, C.W. Visser, J.A. Lewis, Voxelated soft matter via multimaterial multinozzle 3D printing, in: Nature 2019 575:7782, vol. 575, 2019, pp. 330–335, https://doi.org/10.1038/s41586-019-1736-8.
[25] D. Dendukuri, D.C. Pregibon, J. Collins, T.A. Hatton, P.S. Doyle, Continuous-flow lithography for high-throughput microparticle synthesis, Art. no 5, Nat. Mater. vol. 5 (5) (2006), https://doi.org/10.1038/nmat1617.
[26] S.C. Laza, M. Polo, A.A.R. Neves, R. Cingolani, A. Camposeo, D. Pisignano, Two-photon continuous flow lithography, Adv. Mater. vol. 24 (10) (2012) 1304–1308, https://doi.org/10.1002/adma.201103357.
[27] L. Malaquin, J.L. Viovy, S. Assie-Souleille, X. Dollat, et V. Fournie, Tête d'impression d'une imprimante, imprimante et procédé d'impression, EP3661754A1, 10 juin 2020 Consulté le: 6 janvier 2023. [En ligne]. Disponible sur: https://patents.google.com/patent/EP3661754A1/fr?oq=EP3661754.
[28] D. Juncker, M. Qasaimeh, A. Mckinney, et A. Hur Queval, Multipurpose microfluidic probe Related papers Microfluidics for Processing Surfaces and Miniat urizing Biological Assays Chamber and microfluidic probe for microperfusion of organot ypic brain slices, 2005, ⟨doi:10.1038/nmat1435.
[29] M.A. Qasaimeh, T. Gervais, D. Juncker, Microfluidic quadrupole and floating concentration gradient, Nat. Commun. 2011 2:1 vol. 2 (1) (2011) 1–8, https://doi.org/10.1038/ncomms1471.
[30] A. Brimmo, P.-A. Goyette, R. Alnemari, T. Gervais, M.A. Qasaimeh, 3D Printed Microfluidic Probes, Art. no 1, Sci. Rep. vol. 8 (1) (2018), https://doi.org/10.1038/s41598-018-29304-x.
[31] K.S. Lim et al., New Visible-Light Photoinitiating System for Improved Print Fidelity in Gelatin-Based Bioinks, 2016, doi:10.1021/acsbiomaterials.6b00149.
[32] J.M. Vuksanović, M.L. Kijevčanin, I.R. Radović, Poly(ethylene glycol) diacrylate as a novel chaotropic compound for design of aqueous biphasic systems, J. Mol. Liq. vol. 261 (2018) 250–264, https://doi.org/10.1016/J.MOLLIQ.2018.04.023.
[33] S. Muller, et al., Human adipose stromal-vascular fraction self-organizes to form vascularized adipose tissue in 3D cultures, Art. no 1, Sci. Rep. vol. 9 (1) (2019), https://doi.org/10.1038/s41598-019-43624-6.
[34] C.A. Schneider, W.S. Rasband, K.W. Eliceiri, NIH Image to ImageJ: 25 years of image analysis, Nat. Methods 2012 9:7 vol. 9 (7) (2012) 671–675, https://doi.org/10.1038/nmeth.2089.
[35] E.H.W. Meijering, W.J. Niessen, M.A. Viergever, Quantitative evaluation of convolution-based methods for medical image interpolation, Med. Image Anal. vol. 5 (2) (2001) 111–126, https://doi.org/10.1016/S1361-8415(00)00040-2.
[36] P. Juskova, A. Ollitrault, M. Serra, J.L. Viovy, L. Malaquin, Resolution improvement of 3D stereo-lithography through the direct laser trajectory programming: application to microfluidic deterministic lateral displacement device, Anal. Chim. Acta vol. 1000 (2018) 239–247, https://doi.org/10.1016/J.ACA.2017.11.062.
[37] M. Babi, et al., Tuning the nanotopography and chemical functionality of 3D printed scaffolds through cellulose nanocrystal coatings, ACS Appl. Bio Mater. vol. 4 (12) (&;;. 2021) 8443–8455, https://doi.org/10.1021/acsabm.1c00970.
[38] N. Paxton, W. Smolan, T. Böck, F. Melchels, J. Groll, T. Jungst, Proposal to assess printability of bioinks for extrusion-based bioprinting and evaluation of rheological properties governing bioprintability, Biofabrication vol. 9 (4) (. 2017), 044107, https://doi.org/10.1088/1758-5090/aa8dd8.
[39] Y. Guo, H.S. Patanwala, B. Bognet, A.W.K. Ma, Inkjet and inkjet-based 3D printing: connecting fluid properties and printing performance, Rapid Prototyp. J. vol. 23 (3) (. 2017) 562–576, https://doi.org/10.1108/RPJ-05-2016-0076.
[40] H. Lin, et al., Application of visible light-based projection stereolithography for live cell-scaffold fabrication with designed architecture, Biomaterials vol. 34 (2) (2013) 331–339, https://doi.org/10.1016/j.biomaterials.2012.09.048.
[41] J.P. Mazzoccoli, Properties of Poly(ethylene glycol) Diacrylate Blends and Acoustically Focused Multilayered Biocomposites Developed for Tissue Engineering Applications, 2008.
[42] B.D. Fairbanks, M.P. Schwartz, C.N. Bowman, K.S. Anseth, Photoinitiated polymerization of PEG-diacrylate with lithium phenyl-2,4,6-trimethylbenzoylphosphinate: polymerization rate and cytocompatibility, Biomaterials vol. 30 (35) (2009) 6702–6707, https://doi.org/10.1016/J.BIOMATERIALS.2009.08.055.
[43] E. Mancha Sánchez, et al., Hydrogels for bioprinting: a systematic review of hydrogels synthesis, bioprinting parameters, and bioprinted structures behavior, Front. Bioeng. Biotechnol. vol. 8 (2020), https://doi.org/10.3389/FBIOE.2020.00776/BIBTEX.

[44] D. Dendukuri, P.S. Doyle, The synthesis and assembly of polymeric microparticles using microfluidics, Adv. Mater. vol. 21 (41) (2009) 4071–4086, https://doi.org/10.1002/adma.200803386.
[45] M. Ziauddin, A.-H. Mourad, S. Khashan, Maskless lithography using negative photoresist material: impact of UV laser intensity on the cured line width, Lasers Manuf. Mater. Process. vol. 5 (2018) 1–10, https://doi.org/10.1007/s40516-018-0058-2.
[46] T. Pelras, S. Glass, T. Scherzer, C. Elsner, A. Schulze, B. Abel, Transparent low molecular weight poly(Ethylene Glycol) diacrylate-based hydrogels as film media for photoswitchable drugs, vol. 9, no 12, p. 639–639, nov. 2017, Polymers Vol. 9 (2017) 639, https://doi.org/10.3390/POLYM9120639.
[47] L. Flach, R.P. Chartoff, A process model for nonisothermal photopolymerization with a laser light source. I: Basic model development, Polym. Eng. Sci. vol. 35 (6) (1995) 483–492, https://doi.org/10.1002/pen.760350605.
[48] D. Fanfone, et al., Confined migration promotes cancer metastasis through resistance to anoikis and increased invasiveness, eLife vol. 11 (2022), e73150, https://doi.org/10.7554/eLife.73150.
[49] A.C. Daly, M.D. Davidson, J.A. Burdick, 3D bioprinting of high cell-density heterogeneous tissue models through spheroid fusion within self-healing hydrogels, Art. no 1, Nat. Commun. vol. 12 (1) (2021), https://doi.org/10.1038/s41467-021-21029-2.
[50] J.J. Kim, M. Jorfi, R.E. Tanzi, D.Y. Kim, P.S. Doyle, D. Irimia, Patterning of interconnected human brain spheroids, Lab Chip vol. 21 (18) (2021) 3532–3540, https://doi.org/10.1039/d0lc01112f.
[51] S. Kim, et al., Spatially arranged encapsulation of stem cell spheroids within hydrogels for the regulation of spheroid fusion and cell migration, Acta Biomater. vol. 142 (2022) 60–72, https://doi.org/10.1016/j.actbio.2022.01.047.
[52] X. Zhan, Effect of matrix stiffness and adhesion ligand density on chondrogenic differentiation of mesenchymal stem cells, J. Biomed. Mater. Res. Part A vol. 108 (3) (2020) 675–683, https://doi.org/10.1002/JBM.A.36847.

Remerciements

Je tiens à exprimer ma profonde gratitude envers les membres de mon jury de thèse pour avoir accepté d'évaluer ce travail. A mes rapporteures **Dr. Joëlle Amédée-Vilamitjana** et **Dr. Julie Dam**, merci pour vos remarques constructives sur le manuscrit et nos discussions enrichissantes durant la soutenance de thèse. A **Dr. Maxime Mahé**, merci d'avoir partagé vos réflexions conceptuelles pendant la soutenance ainsi que vos conseils tout au long de cette thèse en tant que membre de comité de thèse. A **Dr. Nathalie Vergnolles**, merci d'avoir présidé ma soutenance et d'avoir mené nos échanges avec tant de professionnalisme. Vos encouragements avant la soutenance m'accompagneront longtemps.

A **Dr. Christian Dani**, merci pour votre participation à ma soutenance et votre soutien continu. Je vous remercie pour votre ouverture d'esprit et votre envie de partager scientifiquement. Votre collaboration a été inestimable et a grandement contribué à ce travail de thèse.

A **Dr. Nathalie Piccolet d'hann**, membre de mon comité de thèse, merci pour votre contribution à l'avancement de cette thèse et vos précieux conseils tant sur le plan scientifique qu'humain.

A mes directeurs de thèse **Pr. Louis Castilla** et **Dr. Laurent Malaquin** ainsi que ma co-encadrante de thèse, **Dr. Laurence Vaysse**. Merci de m'avoir fait confiance et de m'avoir permis d'intégrer les laboratoires Restore et LAAS-CNRS. Merci à vous trois pour vos conseils, votre aide et vos enseignements tout au long de cette thèse. Louis, merci pour nos nombreuses discussions scientifiques, merci d'avoir toujours essayé de me pousser plus loin dans la réflexion. Je suis souvent sorti de votre bureau avec plus de questions que lorsque j'y étais entré. Je retiendrais qu'il faut se sentir libre intellectuellement et ne pas avoir peur de prendre une nouvelle page blanche. Laurent, merci pour ta patience, ta bienveillance et ta bonne humeur. Merci de m'avoir permis de découvrir le monde de l'ingénierie d'un point de vue pratique. Tu as su me réconcilier avec la biophysique et le "bricolage", ce qui dans un cas comme dans l'autre n'était pas une mince à faire. Je retiendrais qu'il ne faut pas se laisser arrêter par des considérations pratiques, s'il n'y a pas de solutions préexistantes il faut l'inventer. Laurence, merci pour la confiance que tu m'as accordée dès mon stage de Master 2, ouvrant la voie à cette thèse. Merci pour ta détermination et ton envie d'avancée. Je te remercie d'avoir partagé avec moi ton expérience et ta passion pour l'ingénierie tissulaire. Tu m'as enseigné à adopter une plus grande flexibilité dans ma réflexion et de toujours garder en tête la cible terminale.

A **Dr. Audrey Carrière-Pazat**. Je tiens à sincèrement te remercier pour ton soutien scientifique et humain inestimable. Tu as été pour moi le quatrième pilier de mon parcours de thèse. Merci de m'avoir patiemment initié au monde du métabolisme et à son importance. Merci pour ta bienveillance et ton aide qui ont été essentielles, tant dans les moments de doute que dans les phases d'enthousiasme, pour surmonter les défis rencontrés durant ces années de recherche.

Je voudrais adresser mes remerciements à l'ensemble de l'équipe GOT-IT au sein de l'institut RESTORE. Je remercie les chercheurs et les ingénieurs avec qui j'ai eu la chance de pouvoir travailler pour leur temps, leurs commentaires constructifs et leurs suggestions qui ont grandement enrichi ce travail.

Valérie, merci pour ton écoute et ta considération. **Sophie B**, merci pour ta grande participation à ma formation. Merci pour ta gentillesse sans réserve et ton amitié. J'ai énormément apprécié travailler avec toi. **Frédéric**, merci pour tes contributions précieuses et pour ta disponibilité chaque fois que j'ai eu besoin de conseils. **Christophe G.**, merci d'avoir permis la réalisation des expériences *in vivo* qui ont grandement enrichi cette thèse. Merci pour ta bonne humeur constante, ça a toujours été un plaisir de travailler avec toi. **Adeline**, merci pour toutes ces heures de manips passées à tes côtés dans la bonne humeur. Merci pour ton efficacité et toute l'aide que tu as apportée à ce projet. Un grand merci également à **Isabelle** et **Mélissa** pour leur assistance technique en histologie sans laquelle ce travail n'aurait pas été le même. **Philippe**, je te remercie sincèrement pour ta confiance et l'enthousiasme contagieux que tu as partagé avec moi lors de nos échanges. Ta passion pour la recherche et ton dévouement sont une source d'inspiration inestimable. **Corinne**, merci pour ton expertise et ton aide précieuse en imagerie ainsi que tes conseils pour l'avenir.

Merci à l'ensemble des ingénieurs et techniciens de l'équipe pour leur assistance technique, patience et disponibilité, en particulier **Margot, Marion, Selma, Agnès et Emilie**.

Merci à tous les doctorants de l'équipe pour les moments de partage et de solidarité que nous avons vécus ensemble. Je remercie tout particulièrement **Clémence**, **Anastasia** et **Pauline**. Nous avons traversé cette aventure ensemble, votre présence et votre soutien ont été une source de réconfort et de motivation tout au long de ces années. De plus, un merci particulier à **Jeanne**, ma compagne de bureau sur ces derniers mois de thèse. Je suis contente d'avoir pu participer à ta formation et je te souhaite le meilleur pour la suite.

Je tiens également à remercier l'ensemble des membres de l'équipe ELIA pour leur accueil chaleureux, leur implication et leur esprit d'équipe. Bien que mes visites dans votre laboratoire aient été moins fréquentes, je me suis toujours senti accueilli et soutenu par chacun d'entre vous.

Christophe V., merci pour tes remarques enrichissantes et ta réflexion sur l'importance de l'environnement mécanique sur les cellules. **Bastien,** merci pour ta bienveillance, ta positivité et ton aide précieuse. Tu as toujours été présent pour répondre à mes questions.

Un très grand merci à l'ensemble des doctorants et post-doctorants de l'équipe. Je remercie particulièrement **Victor F.** avec qui j'ai eu le plaisir de partager cette aventure. Merci pour ta gentillesse et ton investissement pour créer un espace de recherche sain et convivial. Merci à **Ophélie**, **Elise** et **Ianis** pour m'avoir fait découvrir le fonctionnement du laboratoire et pour avoir toujours été disponibles pour échanger des idées. Merci à **Nicolas** pour son aide précieuse aux côtés d'Elise lors de

ma soutenance de thèse. Merci à **Sandra** d'avoir rejoint le projet. Merci pour ton dynamisme et ta bonne humeur. Je te souhaite de réussir un très beau postdoc.

Enfin un très grand merci aux ingénieurs des plateformes, **Julie**, **Sandrine** et **Daniel** pour leur patience, leur soutien constant et leur implication qui sont essentiels à la bonne avancée des projets.

Je voudrais également remercier tous les autres membres de RESTORE ou du LAAS qui ont contribué de près ou de loin à la réalisation de cette thèse, ainsi qu'à toutes celles et ceux qui m'ont inspiré et soutenu dans cette démarche de recherche. Merci pour les moments de convivialité, les échanges d'idées et les collaborations fructueuses. Travailler à vos côtés a été une expérience enrichissante et inspirante, et je garderai précieusement en mémoire les souvenirs de cette période. Un merci particulier à **Béatrice**, **Philippe V.**, **Yannick**, **Isabelle A.**, **Audrey V.**, **Mélanie G.**, **Nicolas E.**, **Corinne B.**, **Mireille**, **Manue, Lucas, Rémi** et **Clément**.

Merci également à la formidable équipe des doctorants de la *Restore family* pour leur soutien moral constant et leur entraide dans les moments difficiles. Je vous souhaite à chacun le meilleur pour la suite.

Enfin, je dédie ce travail à ma famille et à mes amis, pour leur amour inconditionnel, leur encouragement et leur compréhension pendant les moments de stress et de doute.

Merci à **Delphine**, amie de toujours. Merci d'être infaillible, toujours là pour prêter une oreille attentive à mes soucis, avoir le mot de réconfort ou d'encouragement nécessaire pour me faire retrouver le sourire. Je ne te remercierais jamais assez pour toutes ces années d'amitié.

Merci à mes **grands-parents** de m'avoir soutenu depuis les premiers jours. Merci d'avoir toujours été des exemples de force et de courage et de m'avoir appris à ne jamais me laisser abattre.

Merci à **mes frères et sœurs** pour être l'une des plus grandes sources de joie dans ma vie. Merci de toujours rester fidèles à vous-mêmes. Il n'y avait rien de mieux que de passer une journée avec vous pour se souvenir qu'il y a un monde à côté de la thèse.

Merci à **mes parents** pour leur patience et leur soutien indéfectible. Merci d'avoir toujours cru en moi. Merci de m'avoir écouté radoter sans cesse sur mes cellules. Vous êtes mes piliers, ma réussite est votre réussite car sans vous je n'en serez pas là.

Merci à **Benjamin** pour toutes ces années partagées à tes côtés. Merci pour ton soutien et ta patience sur ces derniers mois de thèse. Merci pour tes certitudes qui savent contrebalancer mes doutes.

References

[1] A. Loewa, J.J. Feng, S. Hedtrich, Human disease models in drug development, Nat. Rev. Bioeng. 1 (2023) 545–559. https://doi.org/10.1038/s44222-023-00063-3.

[2] H.B. van der Worp, D.W. Howells, E.S. Sena, M.J. Porritt, S. Rewell, V. O'Collins, M.R. Macleod, Can animal models of disease reliably inform human studies?, PLoS Med. 7 (2010) e1000245. https://doi.org/10.1371/journal.pmed.1000245.

[3] G.A. Van Norman, Limitations of Animal Studies for Predicting Toxicity in Clinical Trials, JACC Basic Transl. Sci. 5 (2020) 387–397. https://doi.org/10.1016/j.jacbts.2020.03.010.

[4] 112 Executive Board, Human organ and tissue transplantation: report by the Secretariat, (2003) Executive Board 112th session, provisional agenda item 4.3.

[5] N. Barker, S. Bartfeld, H. Clevers, Tissue-Resident Adult Stem Cell Populations of Rapidly Self-Renewing Organs, Cell Stem Cell. 7 (2010) 656–670. https://doi.org/10.1016/j.stem.2010.11.016.

[6] H. Xia, X. Li, W. Gao, X. Fu, R.H. Fang, L. Zhang, K. Zhang, Tissue repair and regeneration with endogenous stem cells, Nat. Rev. Mater. 3 (2018) 174–193. https://doi.org/10.1038/s41578-018-0027-6.

[7] S.E. Iismaa, X. Kaidonis, A.M. Nicks, N. Bogush, K. Kikuchi, N. Naqvi, R.P. Harvey, A. Husain, R.M. Graham, Comparative regenerative mechanisms across different mammalian tissues, NPJ Regen. Med. 3 (2018) 6. https://doi.org/10.1038/s41536-018-0044-5.

[8] J.P. Vacanti, Beyond Transplantation: Third Annual Samuel Jason Mixter Lecture, Arch. Surg. 123 (1988) 545–549. https://doi.org/10.1001/archsurg.1988.01400290027003.

[9] R. Langer, J.P. Vacanti, Tissue engineering, Science. 260 (1993) 920–926. https://doi.org/10.1126/science.8493529.

[10] J.P. Vacanti, R. Langer, Tissue engineering: the design and fabrication of living replacement devices for surgical reconstruction and transplantation, The Lancet. 354 (1999) S32–S34. https://doi.org/10.1016/S0140-6736(99)90247-7.

[11] F. Gattazzo, A. Urciuolo, P. Bonaldo, Extracellular matrix: A dynamic microenvironment for stem cell niche, Biochim. Biophys. Acta. 1840 (2014) 2506–2519. https://doi.org/10.1016/j.bbagen.2014.01.010.

[12] S.J. Morrison, A.C. Spradling, Stem cells and niches: mechanisms that promote stem cell maintenance throughout life, Cell. 132 (2008) 598–611. https://doi.org/10.1016/j.cell.2008.01.038.

[13] J. Barthes, H. Özçelik, M. Hindié, A. Ndreu-Halili, A. Hasan, N.E. Vrana, Cell Microenvironment Engineering and Monitoring for Tissue Engineering and Regenerative Medicine: The Recent Advances, BioMed Res. Int. 2014 (2014) 921905. https://doi.org/10.1155/2014/921905.

[14] Y. Sun, C.S. Chen, J. Fu, Forcing Stem Cells to Behave: A Biophysical Perspective of the Cellular Microenvironment, Annu. Rev. Biophys. 41 (2012) 519–542. https://doi.org/10.1146/annurev-biophys-042910-155306.

[15] K. Nakayama, In Vitro Biofabrication of Tissues and Organs, Biofabrication. (2013) 1–21. https://doi.org/10.1016/B978-1-4557-2852-7.00001-9.

[16] W.S. Harley, C.C. Li, J. Toombs, C.D. O'Connell, H.K. Taylor, D.E. Heath, D.J. Collins, Advances in biofabrication techniques towards functional bioprinted heterogeneous engineered tissues: A comprehensive review, Bioprinting. 23 (2021) e00147. https://doi.org/10.1016/j.bprint.2021.e00147.

[17] Z. Xie, M. Gao, A.O. Lobo, T.J. Webster, 3D Bioprinting in Tissue Engineering for Medical Applications: The Classic and the Hybrid, Polymers. 12 (2020) 1717. https://doi.org/10.3390/polym12081717.

[18] C.D. Devillard, C.A. Marquette, Vascular Tissue Engineering: Challenges and Requirements for an Ideal Large Scale Blood Vessel, Front. Bioeng. Biotechnol. 9 (2021) 721843. https://doi.org/10.3389/fbioe.2021.721843.
[19] E.C. Novosel, C. Kleinhans, P.J. Kluger, Vascularization is the key challenge in tissue engineering, Adv. Drug Deliv. Rev. 63 (2011) 300–311. https://doi.org/10.1016/j.addr.2011.03.004.
[20] F. Lizcano, The Beige Adipocyte as a Therapy for Metabolic Diseases, Int. J. Mol. Sci. 20 (2019) 5058. https://doi.org/10.3390/ijms20205058.
[21] A.M. Singh, L. Zhang, J. Avery, A. Yin, Y. Du, H. Wang, Z. Li, H. Fu, H. Yin, S. Dalton, Human beige adipocytes for drug discovery and cell therapy in metabolic diseases, Nat. Commun. 11 (2020) 2758. https://doi.org/10.1038/s41467-020-16340-3.
[22] M. Kuss, J. Kim, D. Qi, S. Wu, Y. Lei, S. Chung, B. Duan, Effects of tunable, 3D-bioprinted hydrogels on human brown adipocyte behavior and metabolic function, Acta Biomater. 71 (2018) 486–495. https://doi.org/10.1016/j.actbio.2018.03.021.
[23] J.P. Yang, A.E. Anderson, A. McCartney, X. Ory, G. Ma, E. Pappalardo, J. Bader, J.H. Elisseeff, Metabolically Active Three-Dimensional Brown Adipose Tissue Engineered from White Adipose-Derived Stem Cells, Tissue Eng. Part A. 23 (2017) 253–262. https://doi.org/10.1089/ten.TEA.2016.0399.
[24] M.A. Gonzalez Porras, K. Stojkova, F.M. Acosta, C.R. Rathbone, E.M. Brey, Engineering Human Beige Adipose Tissue, Front. Bioeng. Biotechnol. 10 (2022) 906395. https://doi.org/10.3389/fbioe.2022.906395.
[25] O. Wang, L. Han, H. Lin, M. Tian, S. Zhang, B. Duan, S. Chung, C. Zhang, X. Lian, Y. Wang, Y. Lei, Fabricating 3-dimensional human brown adipose microtissues for transplantation studies, Bioact. Mater. 22 (2022) 518–534. https://doi.org/10.1016/j.bioactmat.2022.10.022.
[26] M.H. Barcellos-Hoff, Stroma, in: W. Dubitzky, O. Wolkenhauer, K.-H. Cho, H. Yokota (Eds.), Encycl. Syst. Biol., Springer, New York, NY, 2013: pp. 2017–2019. https://doi.org/10.1007/978-1-4419-9863-7_1384.
[27] C. Frantz, K.M. Stewart, V.M. Weaver, The extracellular matrix at a glance, J. Cell Sci. 123 (2010) 4195–4200. https://doi.org/10.1242/jcs.023820.
[28] M.A. Basson, Signaling in Cell Differentiation and Morphogenesis, Cold Spring Harb. Perspect. Biol. 4 (2012) a008151. https://doi.org/10.1101/cshperspect.a008151.
[29] R. Lehmann, C.M. Lee, E.C. Shugart, M. Benedetti, R.A. Charo, Z. Gartner, B. Hogan, J. Knoblich, C.M. Nelson, K.M. Wilson, Human organoids: a new dimension in cell biology, Mol. Biol. Cell. 30 (2019) 1129–1137. https://doi.org/10.1091/mbc.E19-03-0135.
[30] F. Han, J. Wang, L. Ding, Y. Hu, W. Li, Z. Yuan, Q. Guo, C. Zhu, L. Yu, H. Wang, Z. Zhao, L. Jia, J. Li, Y. Yu, W. Zhang, G. Chu, S. Chen, B. Li, Tissue Engineering and Regenerative Medicine: Achievements, Future, and Sustainability in Asia, Front. Bioeng. Biotechnol. 8 (2020). https://www.frontiersin.org/articles/10.3389/fbioe.2020.00083 (accessed August 21, 2023).
[31] P. Lenas, M. Moos, F.P. Luyten, Developmental Engineering: A New Paradigm for the Design and Manufacturing of Cell-Based Products. Part I: From Three-Dimensional Cell Growth to Biomimetics of In Vivo Development, Tissue Eng. Part B Rev. 15 (2009) 381–394. https://doi.org/10.1089/ten.teb.2008.0575.
[32] J.A. Brassard, M.P. Lutolf, Engineering Stem Cell Self-organization to Build Better Organoids, Cell Stem Cell. 24 (2019) 860–876. https://doi.org/10.1016/j.stem.2019.05.005.
[33] L. Jiménez-Rojo, Z. Granchi, D. Graf, T.A. Mitsiadis, Stem Cell Fate Determination during Development and Regeneration of Ectodermal Organs, Front. Physiol. 3 (2012) 107. https://doi.org/10.3389/fphys.2012.00107.
[34] S. Harmansa, T. Lecuit, Forward and feedback control mechanisms of developmental tissue growth, Cells Dev. 168 (2021) 203750. https://doi.org/10.1016/j.cdev.2021.203750.
[35] E. Scarpa, R. Mayor, Collective cell migration in development, J. Cell Biol. 212 (2016) 143–155. https://doi.org/10.1083/jcb.201508047.

[36] C.J. Chan, C.-P. Heisenberg, T. Hiiragi, Coordination of Morphogenesis and Cell-Fate Specification in Development, Curr. Biol. 27 (2017) R1024–R1035. https://doi.org/10.1016/j.cub.2017.07.010.
[37] R.J. Johnston, C. Desplan, Stochastic Mechanisms of Cell Fate Specification that Yield Random or Robust Outcomes, Annu. Rev. Cell Dev. Biol. 26 (2010) 689–719. https://doi.org/10.1146/annurev-cellbio-100109-104113.
[38] P. Dong, Z. Liu, Shaping development by stochasticity and dynamics in gene regulation, Open Biol. 7 (2017) 170030. https://doi.org/10.1098/rsob.170030.
[39] C. Zechner, E. Nerli, C. Norden, Stochasticity and determinism in cell fate decisions, Development. 147 (2020) dev181495. https://doi.org/10.1242/dev.181495.
[40] M. Mimeault, S.K. Batra, Recent Progress on Tissue-Resident Adult Stem Cell Biology and Their Therapeutic Implications, Stem Cell Rev. 4 (2008) 10.1007/s12015-008-9008–2. https://doi.org/10.1007/s12015-008-9008-2.
[41] N. Perrimon, C. Pitsouli, B.-Z. Shilo, Signaling Mechanisms Controlling Cell Fate and Embryonic Patterning, Cold Spring Harb. Perspect. Biol. 4 (2012) a005975. https://doi.org/10.1101/cshperspect.a005975.
[42] D. Pinheiro, R. Kardos, É. Hannezo, C.-P. Heisenberg, Morphogen gradient orchestrates pattern-preserving tissue morphogenesis via motility-driven unjamming, Nat. Phys. 18 (2022) 1482–1493. https://doi.org/10.1038/s41567-022-01787-6.
[43] E.M. De Robertis, J. Larraín, M. Oelgeschläger, O. Wessely, The establishment of Spemann's organizer and patterning of the vertebrate embryo, Nat. Rev. Genet. 1 (2000) 171–181. https://doi.org/10.1038/35042039.
[44] A. Dekanty, M. Milán, The interplay between morphogens and tissue growth, EMBO Rep. 12 (2011) 1003–1010. https://doi.org/10.1038/embor.2011.172.
[45] L. Lamalice, F. Le Boeuf, J. Huot, Endothelial Cell Migration During Angiogenesis, Circ. Res. 100 (2007) 782–794. https://doi.org/10.1161/01.RES.0000259593.07661.1e.
[46] M. Rodrigues, L.G. Griffith, A. Wells, Growth factor regulation of proliferation and survival of multipotential stromal cells, Stem Cell Res. Ther. 1 (2010) 32. https://doi.org/10.1186/scrt32.
[47] S.G. Ball, C.A. Shuttleworth, C.M. Kielty, Mesenchymal stem cells and neovascularization: role of platelet-derived growth factor receptors, J. Cell. Mol. Med. 11 (2007) 1012–1030. https://doi.org/10.1111/j.1582-4934.2007.00120.x.
[48] T. Rozario, D.W. DeSimone, The Extracellular Matrix In Development and Morphogenesis: A Dynamic View, Dev. Biol. 341 (2010) 126–140. https://doi.org/10.1016/j.ydbio.2009.10.026.
[49] A. Sagner, J. Briscoe, Morphogen interpretation: concentration, time, competence, and signaling dynamics, WIREs Dev. Biol. 6 (2017) e271. https://doi.org/10.1002/wdev.271.
[50] T. Cantz, M.P. Manns, M. Ott, Stem cells in liver regeneration and therapy, Cell Tissue Res. 331 (2008) 271–282. https://doi.org/10.1007/s00441-007-0483-6.
[51] G. Mannino, C. Russo, G. Maugeri, G. Musumeci, N. Vicario, D. Tibullo, R. Giuffrida, R. Parenti, D. Lo Furno, Adult stem cell niches for tissue homeostasis, J. Cell. Physiol. 237 (2022) 239–257. https://doi.org/10.1002/jcp.30562.
[52] D. Zipori, The nature of stem cells: state rather than entity, Nat. Rev. Genet. 5 (2004) 873–878. https://doi.org/10.1038/nrg1475.
[53] P. Pagella, E. Neto, M. Lamghari, T.A. Mitsiadis, Investigation of orofacial stem cell niches and their innervation through microfluidic devices, Eur. Cell. Mater. 29 (2015) 213–223. https://doi.org/10.22203/ecm.v029a16.
[54] S. Malijauskaite, S. Connolly, D. Newport, K. McGourty, Gradients in the in vivo intestinal stem cell compartment and their in vitro recapitulation in mimetic platforms, Cytokine Growth Factor Rev. 60 (2021) 76–88. https://doi.org/10.1016/j.cytogfr.2021.03.002.
[55] J. Zhu, C.B. Thompson, Metabolic regulation of cell growth and proliferation, Nat. Rev. Mol. Cell Biol. 20 (2019) 436–450. https://doi.org/10.1038/s41580-019-0123-5.

[56] K.H. Vining, D.J. Mooney, Mechanical forces direct stem cell behaviour in development and regeneration, Nat. Rev. Mol. Cell Biol. 18 (2017) 728–742. https://doi.org/10.1038/nrm.2017.108.
[57] A.J.M. Santos, Y.-H. Lo, A.T. Mah, C.J. Kuo, The Intestinal Stem Cell Niche: Homeostasis and Adaptations, Trends Cell Biol. 28 (2018) 1062–1078. https://doi.org/10.1016/j.tcb.2018.08.001.
[58] M. Pavel, M. Renna, S.J. Park, F.M. Menzies, T. Ricketts, J. Füllgrabe, A. Ashkenazi, R.A. Frake, A.C. Lombarte, C.F. Bento, K. Franze, D.C. Rubinsztein, Contact inhibition controls cell survival and proliferation via YAP/TAZ-autophagy axis, Nat. Commun. 9 (2018) 2961. https://doi.org/10.1038/s41467-018-05388-x.
[59] B. Zhao, K. Tumaneng, K.-L. Guan, The Hippo pathway in organ size control, tissue regeneration and stem cell self-renewal, Nat. Cell Biol. 13 (2011) 877–883. https://doi.org/10.1038/ncb2303.
[60] M.B. Elowitz, A.J. Levine, E.D. Siggia, P.S. Swain, Stochastic Gene Expression in a Single Cell, Science. 297 (2002) 1183–1186. https://doi.org/10.1126/science.1070919.
[61] F. Paul, Y. Arkin, A. Giladi, D.A. Jaitin, E. Kenigsberg, H. Keren-Shaul, D. Winter, D. Lara-Astiaso, M. Gury, A. Weiner, E. David, N. Cohen, F.K.B. Lauridsen, S. Haas, A. Schlitzer, A. Mildner, F. Ginhoux, S. Jung, A. Trumpp, B.T. Porse, A. Tanay, I. Amit, Transcriptional Heterogeneity and Lineage Commitment in Myeloid Progenitors, Cell. 163 (2015) 1663–1677. https://doi.org/10.1016/j.cell.2015.11.013.
[62] E. Vrieseling, S. Arber, Target-Induced Transcriptional Control of Dendritic Patterning and Connectivity in Motor Neurons by the ETS Gene Pea3, Cell. 127 (2006) 1439–1452. https://doi.org/10.1016/j.cell.2006.10.042.
[63] A. Roorda, D.R. Williams, The arrangement of the three cone classes in the living human eye, Nature. 397 (1999) 520–522. https://doi.org/10.1038/17383.
[64] G.H. Jacobs, J. Nathans, The evolution of Primate color vision, Sci. Am. 300 (2009) 56–63. https://doi.org/10.1038/scientificamerican0409-56.
[65] S. Serizawa, K. Miyamichi, H. Sakano, One neuron-one receptor rule in the mouse olfactory system, Trends Genet. TIG. 20 (2004) 648–653. https://doi.org/10.1016/j.tig.2004.09.006.
[66] P. Ghose, S. Shaham, Cell death in animal development, Dev. Camb. Engl. 147 (2020) dev191882. https://doi.org/10.1242/dev.191882.
[67] E. Hollville, S.E. Romero, M. Deshmukh, Apoptotic Cell Death Regulation in Neurons, FEBS J. 286 (2019) 3276–3298. https://doi.org/10.1111/febs.14970.
[68] M. Affara, B. Dunmore, C. Savoie, S. Imoto, Y. Tamada, H. Araki, D.S. Charnock-Jones, S. Miyano, C. Print, Understanding endothelial cell apoptosis: what can the transcriptome, glycome and proteome reveal?, Philos. Trans. R. Soc. B Biol. Sci. 362 (2007) 1469–1487. https://doi.org/10.1098/rstb.2007.2129.
[69] D.J. Guerin, C.X. Kha, K.A.-S. Tseng, From Cell Death to Regeneration: Rebuilding After Injury, Front. Cell Dev. Biol. 9 (2021) 655048. https://doi.org/10.3389/fcell.2021.655048.
[70] H.V. Wilson, On Some Phenomena of Coalescence and Regeneration in Sponges, J. Elisha Mitchell Sci. Soc. 23 (1907) 161–174.
[71] P.L. Townes, J. Holtfreter, Directed movements and selective adhesion of embryonic amphibian cells, J. Exp. Zool. 128 (1955) 53–120. https://doi.org/10.1002/jez.1401280105.
[72] S.R. Price, N.V.D.M. Garcia, B. Ranscht, T.M. Jessell, Regulation of Motor Neuron Pool Sorting by Differential Expression of Type II Cadherins, Cell. 109 (2002) 205–216. https://doi.org/10.1016/S0092-8674(02)00695-5.
[73] F. Fagotto, Regulation of cell adhesion and cell sorting at embryonic boundaries, Curr. Top. Dev. Biol. 112 (2015) 19–64. https://doi.org/10.1016/bs.ctdb.2014.11.026.
[74] F. Fagotto, The cellular basis of tissue separation, Dev. Camb. Engl. 141 (2014) 3303–3318. https://doi.org/10.1242/dev.090332.
[75] L. Canty, E. Zarour, L. Kashkooli, P. François, F. Fagotto, Sorting at embryonic boundaries requires high heterotypic interfacial tension, Nat. Commun. 8 (2017) 157. https://doi.org/10.1038/s41467-017-00146-x.

[76] F. Fagotto, N. Rohani, A.-S. Touret, R. Li, A Molecular Base for Cell Sorting at Embryonic Boundaries: Contact Inhibition of Cadherin Adhesion by Ephrin/Eph-Dependent Contractility, Dev. Cell. 27 (2013) 72–87. https://doi.org/10.1016/j.devcel.2013.09.004.
[77] D. Duguay, R.A. Foty, M.S. Steinberg, Cadherin-mediated cell adhesion and tissue segregation: qualitative and quantitative determinants, Dev. Biol. 253 (2003) 309–323. https://doi.org/10.1016/S0012-1606(02)00016-7.
[78] J. Jouanneau, J.P. Thiery, Tumor Cell Motility and Invasion, in: J.R. Bertino (Ed.), Encycl. Cancer Second Ed., Academic Press, New York, 2002: pp. 467–473. https://doi.org/10.1016/B0-12-227555-1/00252-5.
[79] E. Theveneau, L. Marchant, S. Kuriyama, M. Gull, B. Moepps, M. Parsons, R. Mayor, Collective chemotaxis requires contact-dependent cell polarity, Dev. Cell. 19 (2010) 39–53. https://doi.org/10.1016/j.devcel.2010.06.012.
[80] J.R. Davis, A. Luchici, F. Mosis, J. Thackery, J.A. Salazar, Y. Mao, G.A. Dunn, T. Betz, M. Miodownik, B.M. Stramer, Inter-cellular forces orchestrate contact inhibition of locomotion, Cell. 161 (2015) 361–373. https://doi.org/10.1016/j.cell.2015.02.015.
[81] D. Cai, S.-C. Chen, M. Prasad, L. He, X. Wang, V. Choesmel-Cadamuro, J.K. Sawyer, G. Danuser, D.J. Montell, Mechanical feedback through E-cadherin promotes direction sensing during collective cell migration, Cell. 157 (2014) 1146–1159. https://doi.org/10.1016/j.cell.2014.03.045.
[82] N.G. Frangogiannis, Transforming growth factor–β in tissue fibrosis, J. Exp. Med. 217 (2020) e20190103. https://doi.org/10.1084/jem.20190103.
[83] C. Ruhrberg, H. Gerhardt, M. Golding, R. Watson, S. Ioannidou, H. Fujisawa, C. Betsholtz, D.T. Shima, Spatially restricted patterning cues provided by heparin-binding VEGF-A control blood vessel branching morphogenesis, Genes Dev. 16 (2002) 2684–2698. https://doi.org/10.1101/gad.242002.
[84] J.C. Boucaut, T. Darribere, Fibronectin in early amphibian embryos. Migrating mesodermal cells contact fibronectin established prior to gastrulation, Cell Tissue Res. 234 (1983) 135–145. https://doi.org/10.1007/BF00217407.
[85] L.A. Davidson, B.G. Hoffstrom, R. Keller, D.W. DeSimone, Mesendoderm extension and mantle closure in Xenopus laevis gastrulation: combined roles for integrin alpha(5)beta(1), fibronectin, and tissue geometry, Dev. Biol. 242 (2002) 109–129. https://doi.org/10.1006/dbio.2002.0537.
[86] M. Ehrbar, A. Sala, P. Lienemann, A. Ranga, K. Mosiewicz, A. Bittermann, S.C. Rizzi, F.E. Weber, M.P. Lutolf, Elucidating the Role of Matrix Stiffness in 3D Cell Migration and Remodeling, Biophys. J. 100 (2011) 284–293. https://doi.org/10.1016/j.bpj.2010.11.082.
[87] T.A. Ulrich, E.M. de Juan Pardo, S. Kumar, The Mechanical Rigidity of the Extracellular Matrix Regulates the Structure, Motility, and Proliferation of Glioma Cells, Cancer Res. 69 (2009) 4167–4174. https://doi.org/10.1158/0008-5472.CAN-08-4859.
[88] C.M. Kraning-Rush, C.A. Reinhart-King, Controlling matrix stiffness and topography for the study of tumor cell migration, Cell Adhes. Migr. 6 (2012) 274–279. https://doi.org/10.4161/cam.21076.
[89] C.-M. Lo, H.-B. Wang, M. Dembo, Y. Wang, Cell Movement Is Guided by the Rigidity of the Substrate, Biophys. J. 79 (2000) 144–152. https://doi.org/10.1016/S0006-3495(00)76279-5.
[90] W.J. Hadden, J.L. Young, A.W. Holle, M.L. McFetridge, D.Y. Kim, P. Wijesinghe, H. Taylor-Weiner, J.H. Wen, A.R. Lee, K. Bieback, B.-N. Vo, D.D. Sampson, B.F. Kennedy, J.P. Spatz, A.J. Engler, Y.S. Choi, Stem cell migration and mechanotransduction on linear stiffness gradient hydrogels, Proc. Natl. Acad. Sci. U. S. A. 114 (2017) 5647–5652. https://doi.org/10.1073/pnas.1618239114.
[91] H. Clevers, Modeling Development and Disease with Organoids, Cell. 165 (2016) 1586–1597. https://doi.org/10.1016/j.cell.2016.05.082.
[92] M. Simian, M.J. Bissell, Organoids: A historical perspective of thinking in three dimensions, J. Cell Biol. 216 (2017) 31–40. https://doi.org/10.1083/jcb.201610056.

[93] M.A. Lancaster, J.A. Knoblich, Generation of cerebral organoids from human pluripotent stem cells, Nat. Protoc. 9 (2014) 2329–2340. https://doi.org/10.1038/nprot.2014.158.
[94] T. Sato, R.G. Vries, H.J. Snippert, M. van de Wetering, N. Barker, D.E. Stange, J.H. van Es, A. Abo, P. Kujala, P.J. Peters, H. Clevers, Single Lgr5 stem cells build crypt-villus structures in vitro without a mesenchymal niche, Nature. 459 (2009) 262–265. https://doi.org/10.1038/nature07935.
[95] M. Hofer, M.P. Lutolf, Engineering organoids, Nat. Rev. Mater. 6 (2021) 402–420. https://doi.org/10.1038/s41578-021-00279-y.
[96] M.A. Lancaster, M. Renner, C.-A. Martin, D. Wenzel, L.S. Bicknell, M.E. Hurles, T. Homfray, J.M. Penninger, A.P. Jackson, J.A. Knoblich, Cerebral organoids model human brain development and microcephaly, Nature. 501 (2013) 373–379. https://doi.org/10.1038/nature12517.
[97] M. Huch, B.-K. Koo, Modeling mouse and human development using organoid cultures, Development. 142 (2015) 3113–3125. https://doi.org/10.1242/dev.118570.
[98] N. Barker, M. Huch, P. Kujala, M. van de Wetering, H.J. Snippert, J.H. van Es, T. Sato, D.E. Stange, H. Begthel, M. van den Born, E. Danenberg, S. van den Brink, J. Korving, A. Abo, P.J. Peters, N. Wright, R. Poulsom, H. Clevers, Lgr5+ve Stem Cells Drive Self-Renewal in the Stomach and Build Long-Lived Gastric Units In Vitro, Cell Stem Cell. 6 (2010) 25–36. https://doi.org/10.1016/j.stem.2009.11.013.
[99] M.Z. Nikolić, O. Caritg, Q. Jeng, J.-A. Johnson, D. Sun, K.J. Howell, J.L. Brady, U. Laresgoiti, G. Allen, R. Butler, M. Zilbauer, A. Giangreco, E.L. Rawlins, Human embryonic lung epithelial tips are multipotent progenitors that can be expanded in vitro as long-term self-renewing organoids, ELife. 6 (2017) e26575. https://doi.org/10.7554/eLife.26575.
[100] E. Gabriel, J. Gopalakrishnan, Generation of iPSC-derived Human Brain Organoids to Model Early Neurodevelopmental Disorders, J. Vis. Exp. JoVE. (2017) 55372. https://doi.org/10.3791/55372.
[101] M. Takasato, P.X. Er, H.S. Chiu, B. Maier, G.J. Baillie, C. Ferguson, R.G. Parton, E.J. Wolvetang, M.S. Roost, S.M. Chuva de Sousa Lopes, M.H. Little, Kidney organoids from human iPS cells contain multiple lineages and model human nephrogenesis, Nature. 526 (2015) 564–568. https://doi.org/10.1038/nature15695.
[102] G. Amadei, C.E. Handford, C. Qiu, J. De Jonghe, H. Greenfeld, M. Tran, B.K. Martin, D.-Y. Chen, A. Aguilera-Castrejon, J.H. Hanna, M.B. Elowitz, F. Hollfelder, J. Shendure, D.M. Glover, M. Zernicka-Goetz, Embryo model completes gastrulation to neurulation and organogenesis, Nature. 610 (2022) 143–153. https://doi.org/10.1038/s41586-022-05246-3.
[103] M. Simunovic, A.H. Brivanlou, Embryoids, organoids and gastruloids: new approaches to understanding embryogenesis, Dev. Camb. Engl. 144 (2017) 976–985. https://doi.org/10.1242/dev.143529.
[104] A.C. Duarte, E.C. Costa, H.A.L. Filipe, S.M. Saraiva, T. Jacinto, S.P. Miguel, M.P. Ribeiro, P. Coutinho, Animal-derived products in science and current alternatives, Biomater. Adv. 151 (2023) 213428. https://doi.org/10.1016/j.bioadv.2023.213428.
[105] N. Ashammakhi, A. GhavamiNejad, R. Tutar, A. Fricker, I. Roy, X. Chatzistavrou, E. Hoque Apu, K.-L. Nguyen, T. Ahsan, I. Pountos, E.J. Caterson, Highlights on Advancing Frontiers in Tissue Engineering, Tissue Eng. Part B Rev. 28 (2022) 633–664. https://doi.org/10.1089/ten.teb.2021.0012.
[106] C. Mason, P. Dunnill, A brief definition of regenerative medicine, Regen. Med. 3 (2008) 1–5. https://doi.org/10.2217/17460751.3.1.1.
[107] Y. Haraguchi, T. Shimizu, M. Yamato, T. Okano, Concise Review: Cell Therapy and Tissue Engineering for Cardiovascular Disease, Stem Cells Transl. Med. 1 (2012) 136–141. https://doi.org/10.5966/sctm.2012-0030.
[108] C.P. Hodgkinson, A. Bareja, J.A. Gomez, V.J. Dzau, Emerging Concepts in Paracrine Mechanisms in Regenerative Cardiovascular Medicine and Biology, Circ. Res. 118 (2016) 95–107. https://doi.org/10.1161/CIRCRESAHA.115.305373.

[109] B. Dhandayuthapani, Y. Yoshida, T. Maekawa, D.S. Kumar, Polymeric Scaffolds in Tissue Engineering Application: A Review, Int. J. Polym. Sci. 2011 (2011) e290602. https://doi.org/10.1155/2011/290602.
[110] A.K. Gaharwar, I. Singh, A. Khademhosseini, Engineered biomaterials for in situ tissue regeneration, Nat. Rev. Mater. 5 (2020) 686–705. https://doi.org/10.1038/s41578-020-0209-x.
[111] R.I. Issa, B. Engebretson, L. Rustom, P.S. McFetridge, V.I. Sikavitsas, The effect of cell seeding density on the cellular and mechanical properties of a mechanostimulated tissue-engineered tendon, Tissue Eng. Part A. 17 (2011) 1479–1487. https://doi.org/10.1089/ten.TEA.2010.0484.
[112] R.L. Mauck, C.C.-B. Wang, E.S. Oswald, G.A. Ateshian, C.T. Hung, The role of cell seeding density and nutrient supply for articular cartilage tissue engineering with deformational loading, Osteoarthritis Cartilage. 11 (2003) 879–890. https://doi.org/10.1016/j.joca.2003.08.006.
[113] S.-J. Shieh, S. Terada, J.P. Vacanti, Tissue engineering auricular reconstruction: in vitro and in vivo studies, Biomaterials. 25 (2004) 1545–1557. https://doi.org/10.1016/S0142-9612(03)00501-5.
[114] C.M. Murphy, F.J. O'Brien, Understanding the effect of mean pore size on cell activity in collagen-glycosaminoglycan scaffolds, Cell Adhes. Migr. 4 (2010) 377–381. https://doi.org/10.4161/cam.4.3.11747.
[115] C.A. Vacanti, L.G. Cima, D. Ratkowski, J. Upton, J.P. Vacanti, Tissue Engineered Growth of New Cartilage in the Shape of a Human Ear Using Synthetic Polymers Seeded with Chondrocytes, MRS Online Proc. Libr. 252 (1991) 367–374. https://doi.org/10.1557/PROC-252-367.
[116] P.T. Brown, A.M. Handorf, W.B. Jeon, W.-J. Li, Stem Cell-based Tissue Engineering Approaches for Musculoskeletal Regeneration, Curr. Pharm. Des. 19 (2013) 3429–3445.
[117] R. Tevlin, G.G. Walmsley, O. Marecic, M.S. Hu, D.C. Wan, M.T. Longaker, Stem and Progenitor Cells: Advancing Bone Tissue Engineering, Drug Deliv. Transl. Res. 6 (2016) 159–173. https://doi.org/10.1007/s13346-015-0235-1.
[118] A. Khademhosseini, N. Ashammakhi, J.M. Karp, S. Gerecht, L. Ferreira, N. Annabi, M.A. Darabi, D. Sirabella, G. Vunjak-Novakovic, R. Langer, Chapter 27 - Embryonic stem cells as a cell source for tissue engineering, in: R. Lanza, R. Langer, J.P. Vacanti, A. Atala (Eds.), Princ. Tissue Eng. Fifth Ed., Academic Press, 2020: pp. 467–490. https://doi.org/10.1016/B978-0-12-818422-6.00027-7.
[119] S. Salemi, J.A. Prange, V. Baumgartner, D. Mohr-Haralampieva, D. Eberli, Adult stem cell sources for skeletal and smooth muscle tissue engineering, Stem Cell Res. Ther. 13 (2022) 156. https://doi.org/10.1186/s13287-022-02835-x.
[120] A.J. Rosenbaum, D.A. Grande, J.S. Dines, The use of mesenchymal stem cells in tissue engineering, Organogenesis. 4 (2008) 23–27.
[121] M.P. Nikolova, M.S. Chavali, Recent advances in biomaterials for 3D scaffolds: A review, Bioact. Mater. 4 (2019) 271–292. https://doi.org/10.1016/j.bioactmat.2019.10.005.
[122] R. Hasanzadeh, T. Azdast, M. Mojaver, M.M. Darvishi, C.B. Park, Cost-effective and reproducible technologies for fabrication of tissue engineered scaffolds: The state-of-the-art and future perspectives, Polymer. 244 (2022) 124681. https://doi.org/10.1016/j.polymer.2022.124681.
[123] R.V. Shevchenko, S.L. James, S.E. James, A review of tissue-engineered skin bioconstructs available for skin reconstruction, J. R. Soc. Interface. 7 (2010) 229–258. https://doi.org/10.1098/rsif.2009.0403.
[124] Y. Ikada, Challenges in tissue engineering, J. R. Soc. Interface. 3 (2006) 589–601. https://doi.org/10.1098/rsif.2006.0124.
[125] T. Schmidt, Y. Xiang, X. Bao, T. Sun, A Paradigm Shift in Tissue Engineering: From a Top–Down to a Bottom–Up Strategy, Processes. 9 (2021) 935. https://doi.org/10.3390/pr9060935.
[126] J.W. Nichol, A. Khademhosseini, Modular Tissue Engineering: Engineering Biological Tissues from the Bottom Up, Soft Matter. 5 (2009) 1312–1319. https://doi.org/10.1039/b814285h.
[127] In search of the Holy Grail: Engineering the stem cell niche, Eur. Pharm. Rev. (n.d.). https://www.europeanpharmaceuticalreview.com/article/6760/in-search-of-the-holy-grail-engineering-the-stem-cell-niche/ (accessed October 6, 2023).

[128] R.D. Abbott, D.L. Kaplan, Engineering Biomaterials for Enhanced Tissue Regeneration, Curr. Stem Cell Rep. 2 (2016) 140–146. https://doi.org/10.1007/s40778-016-0039-3.
[129] L. Wang, C. Wang, S. Wu, Y. Fan, X. Li, Influence of mechanical properties of biomaterials on degradability, cell behaviors and signaling pathways: current progress and challenges, Biomater. Sci. 8 (2020). https://doi.org/10.1039/D0BM00269K.
[130] D. Blondel, M.P. Lutolf, Bioinspired Hydrogels for 3D Organoid Culture, CHIMIA. 73 (2019) 81–81. https://doi.org/10.2533/chimia.2019.81.
[131] D.D. McKinnon, D.W. Domaille, J.N. Cha, K.S. Anseth, Biophysically Defined and Cytocompatible Covalently Adaptable Networks as Viscoelastic 3D Cell Culture Systems, Adv. Mater. 26 (2014) 865–872. https://doi.org/10.1002/adma.201303680.
[132] V. Magno, A. Meinhardt, C. Werner, Polymer Hydrogels to Guide Organotypic and Organoid Cultures, Adv. Funct. Mater. 30 (2020) 2000097. https://doi.org/10.1002/adfm.202000097.
[133] B. Cecen, A. Bal-Ozturk, G. Yasayan, E. Alarcin, P. Kocak, R. Tutar, L.D. Kozaci, S.R. Shin, A.K. Miri, Selection of natural biomaterials for micro-tissue and organ-on-chip models, J. Biomed. Mater. Res. A. 110 (2022) 1147–1165. https://doi.org/10.1002/jbm.a.37353.
[134] K. Yue, G. Trujillo-de Santiago, M.M. Alvarez, A. Tamayol, N. Annabi, A. Khademhosseini, Synthesis, properties, and biomedical applications of gelatin methacryloyl (GelMA) hydrogels, Biomaterials. 73 (2015) 254–271. https://doi.org/10.1016/j.biomaterials.2015.08.045.
[135] D.R. Green, L. Galluzzi, G. Kroemer, Metabolic control of cell death, Science. 345 (2014) 1250256. https://doi.org/10.1126/science.1250256.
[136] S. Ghosh-Choudhary, J. Liu, T. Finkel, Metabolic Regulation of Cell Fate and Function, Trends Cell Biol. 30 (2020) 201–212. https://doi.org/10.1016/j.tcb.2019.12.005.
[137] J. Rouwkema, B. Koopman, C. Blitterswijk, W. Dhert, J. Malda, Supply of nutrients to cells in engineered tissues, Biotechnol. Genet. Eng. Rev. 26 (2010) 163–178. https://doi.org/10.5661/bger-26-163.
[138] H. Abdollahi, L.J. Harris, P. Zhang, S. McIlhenny, T. Tulenko, P.J. DiMuzio, The Role of Hypoxia in Stem Cell Differentiation and Therapeutics, J. Surg. Res. 165 (2011) 112–117. https://doi.org/10.1016/j.jss.2009.09.057.
[139] M. Kapałczyńska, T. Kolenda, W. Przybyła, M. Zajączkowska, A. Teresiak, V. Filas, M. Ibbs, R. Bliźniak, Ł. Łuczewski, K. Lamperska, 2D and 3D cell cultures – a comparison of different types of cancer cell cultures, Arch. Med. Sci. AMS. 14 (2018) 910–919. https://doi.org/10.5114/aoms.2016.63743.
[140] S.P.B. Teixeira, R.M.A. Domingues, M. Shevchuk, M.E. Gomes, N.A. Peppas, R.L. Reis, Biomaterials for Sequestration of Growth Factors and Modulation of Cell Behavior, Adv. Funct. Mater. 30 (2020) 1909011. https://doi.org/10.1002/adfm.201909011.
[141] Z. Wang, Z. Wang, W.W. Lu, W. Zhen, D. Yang, S. Peng, Novel biomaterial strategies for controlled growth factor delivery for biomedical applications, NPG Asia Mater. 9 (2017) e435–e435. https://doi.org/10.1038/am.2017.171.
[142] R.G. Wylie, S. Ahsan, Y. Aizawa, K.L. Maxwell, C.M. Morshead, M.S. Shoichet, Spatially controlled simultaneous patterning of multiple growth factors in three-dimensional hydrogels, Nat. Mater. 10 (2011) 799–806. https://doi.org/10.1038/nmat3101.
[143] K.A. Mosiewicz, L. Kolb, A.J. van der Vlies, M.M. Martino, P.S. Lienemann, J.A. Hubbell, M. Ehrbar, M.P. Lutolf, In situ cell manipulation through enzymatic hydrogel photopatterning, Nat. Mater. 12 (2013) 1072–1078. https://doi.org/10.1038/nmat3766.
[144] M.V. Tsurkan, R. Wetzel, H.R. Pérez-Hernández, K. Chwalek, A. Kozlova, U. Freudenberg, G. Kempermann, Y. Zhang, A.F. Lasagni, C. Werner, Photopatterning of Multifunctional Hydrogels to Direct Adult Neural Precursor Cells, Adv. Healthc. Mater. 4 (2015) 516–521. https://doi.org/10.1002/adhm.201400395.
[145] K.B. Seims, N.K. Hunt, L.W. Chow, Strategies to Control or Mimic Growth Factor Activity for Bone, Cartilage, and Osteochondral Tissue Engineering, Bioconjug. Chem. 32 (2021) 861–878. https://doi.org/10.1021/acs.bioconjchem.1c00090.

[146] X. Wang, Z. Liu, Y. Pang, Concentration gradient generation methods based on microfluidic systems, RSC Adv. 7 (2017) 29966–29984. https://doi.org/10.1039/C7RA04494A.
[147] C.J. Demers, P. Soundararajan, P. Chennampally, G.A. Cox, J. Briscoe, S.D. Collins, R.L. Smith, Development-on-chip: in vitro neural tube patterning with a microfluidic device, Dev. Camb. Engl. 143 (2016) 1884–1892. https://doi.org/10.1242/dev.126847.
[148] Y. Tabata, M.P. Lutolf, Multiscale microenvironmental perturbation of pluripotent stem cell fate and self-organization, Sci. Rep. 7 (2017) 44711. https://doi.org/10.1038/srep44711.
[149] A. Tajeddin, N. Mustafaoglu, Design and Fabrication of Organ-on-Chips: Promises and Challenges, Micromachines. 12 (2021) 1443. https://doi.org/10.3390/mi12121443.
[150] F. Melo-Fonseca, O. Carvalho, M. Gasik, G. Miranda, F.S. Silva, Mechanical stimulation devices for mechanobiology studies: a market, literature, and patents review, Bio-Des. Manuf. 6 (2023) 340–371. https://doi.org/10.1007/s42242-023-00232-8.
[151] T.L. Place, F.E. Domann, A.J. Case, Limitations of Oxygen Delivery to Cells in Culture: An Underappreciated Problem in Basic and Translational Research, Free Radic. Biol. Med. 113 (2017) 311–322. https://doi.org/10.1016/j.freeradbiomed.2017.10.003.
[152] F. Le Pape, L. Cosnuau-Kemmat, G. Richard, F. Dubrana, C. Férec, F. Zal, E. Leize, P. Delépine, HEMOXCell, a New Oxygen Carrier Usable as an Additive for Mesenchymal Stem Cell Culture in Platelet Lysate-Supplemented Media, Artif. Organs. 41 (2017) 359–371. https://doi.org/10.1111/aor.12892.
[153] M. Gholipourmalekabadi, S. Zhao, B.S. Harrison, M. Mozafari, A.M. Seifalian, Oxygen-Generating Biomaterials: A New, Viable Paradigm for Tissue Engineering?, Trends Biotechnol. 34 (2016) 1010–1021. https://doi.org/10.1016/j.tibtech.2016.05.012.
[154] N.S. Selden, M.E. Todhunter, N.Y. Jee, J.S. Liu, K.E. Broaders, Z.J. Gartner, Chemically Programmed Cell Adhesion with Membrane-Anchored Oligonucleotides, J. Am. Chem. Soc. 134 (2012) 765–768. https://doi.org/10.1021/ja2080949.
[155] M. Mueller, S. Rasoulinejad, S. Garg, S.V. Wegner, The Importance of Cell–Cell Interaction Dynamics in Bottom-Up Tissue Engineering: Concepts of Colloidal Self-Assembly in the Fabrication of Multicellular Architectures, Nano Lett. 20 (2020) 2257–2263. https://doi.org/10.1021/acs.nanolett.9b04160.
[156] A. Fatehullah, S.H. Tan, N. Barker, Organoids as an in vitro model of human development and disease, Nat. Cell Biol. 18 (2016) 246–254. https://doi.org/10.1038/ncb3312.
[157] S. Kim, E.M. Kim, M. Yamamoto, H. Park, H. Shin, Engineering Multi-Cellular Spheroids for Tissue Engineering and Regenerative Medicine, Adv. Healthc. Mater. 9 (2020) 2000608. https://doi.org/10.1002/adhm.202000608.
[158] X. Cui, Y. Hartanto, H. Zhang, Advances in multicellular spheroids formation, J. R. Soc. Interface. 14 (2017) 20160877. https://doi.org/10.1098/rsif.2016.0877.
[159] Y.-S. Torisawa, A. Takagi, H. Shiku, T. Yasukawa, T. Matsue, A multicellular spheroid-based drug sensitivity test by scanning electrochemical microscopy, Oncol. Rep. 13 (2005) 1107–1112.
[160] G. Mehta, A.Y. Hsiao, M. Ingram, G.D. Luker, S. Takayama, Opportunities and Challenges for use of Tumor Spheroids as Models to Test Drug Delivery and Efficacy, J. Control. Release Off. J. Control. Release Soc. 164 (2012) 192–204. https://doi.org/10.1016/j.jconrel.2012.04.045.
[161] S. Sohn, M.V. Buskirk, M.J. Buckenmeyer, R. Londono, D. Faulk, Whole Organ Engineering: Approaches, Challenges, and Future Directions, Appl. Sci. 10 (2020) 4277. https://doi.org/10.3390/app10124277.
[162] K.J. Wolf, J.D. Weiss, S.G.M. Uzel, M.A. Skylar-Scott, J.A. Lewis, Biomanufacturing human tissues via organ building blocks, Cell Stem Cell. 29 (2022) 667–677. https://doi.org/10.1016/j.stem.2022.04.012.
[163] A. Persaud, A. Maus, L. Strait, D. Zhu, 3D Bioprinting with Live Cells, Eng. Regen. 3 (2022) 292–309. https://doi.org/10.1016/j.engreg.2022.07.002.
[164] H.C. Ott, T.S. Matthiesen, S.-K. Goh, L.D. Black, S.M. Kren, T.I. Netoff, D.A. Taylor, Perfusion-decellularized matrix: using nature's platform to engineer a bioartificial heart, Nat. Med. 14 (2008) 213–221. https://doi.org/10.1038/nm1684.

[165] C.A. Vacanti, J.P. Vacanti, Bone and cartilage reconstruction with tissue engineering approaches, Otolaryngol. Clin. North Am. 27 (1994) 263–276.
[166] W.S. Kim, J.P. Vacanti, L. Cima, D. Mooney, J. Upton, W.C. Puelacher, C.A. Vacanti, Cartilage engineered in predetermined shapes employing cell transplantation on synthetic biodegradable polymers, Plast. Reconstr. Surg. 94 (1994) 233–237; discussion 238-240.
[167] P.M. Baptista, M.M. Siddiqui, G. Lozier, S.R. Rodriguez, A. Atala, S. Soker, The use of whole organ decellularization for the generation of a vascularized liver organoid, Hepatol. Baltim. Md. 53 (2011) 604–617. https://doi.org/10.1002/hep.24067.
[168] F. Oberpenning, J. Meng, J.J. Yoo, A. Atala, De novo reconstitution of a functional mammalian urinary bladder by tissue engineering, Nat. Biotechnol. 17 (1999) 149–155. https://doi.org/10.1038/6146.
[169] E.A. Sander, K.A. Lynch, S.T. Boyce, Development of the Mechanical Properties of Engineered Skin Substitutes After Grafting to Full-Thickness Wounds, J. Biomech. Eng. 136 (2014) 0510081–0510087. https://doi.org/10.1115/1.4026290.
[170] M.P. Mani, M. Sadia, S.K. Jaganathan, A.Z. Khudzari, E. Supriyanto, S. Saidin, S. Ramakrishna, A.F. Ismail, A.A.M. Faudzi, A review on 3D printing in tissue engineering applications, J. Polym. Eng. 42 (2022) 243–265. https://doi.org/10.1515/polyeng-2021-0059.
[171] P.S. Gungor-Ozkerim, I. Inci, Y.S. Zhang, A. Khademhosseini, M.R. Dokmeci, Bioinks for 3D bioprinting: an overview, Biomater. Sci. 6 (2018) 915–946. https://doi.org/10.1039/c7bm00765e.
[172] G. Eke, L. Vaysse, X. Yao, M. Escudero, A. Carrière, E. Trevisiol, C. Vieu, C. Dani, L. Casteilla, L. Malaquin, Cell Aggregate Assembly through Microengineering for Functional Tissue Emergence, Cells. 11 (2022) 1394. https://doi.org/10.3390/cells11091394.
[173] Y.P. Singh, A. Bandyopadhyay, B.B. Mandal, 3D Bioprinting Using Cross-Linker-Free Silk–Gelatin Bioink for Cartilage Tissue Engineering, ACS Appl. Mater. Interfaces. 11 (2019) 33684–33696. https://doi.org/10.1021/acsami.9b11644.
[174] L. Ruiz-Cantu, A. Gleadall, C. Faris, J. Segal, K. Shakesheff, J. Yang, Multi-material 3D bioprinting of porous constructs for cartilage regeneration, Mater. Sci. Eng. C. 109 (2020) 110578. https://doi.org/10.1016/j.msec.2019.110578.
[175] J.M. Unagolla, A.C. Jayasuriya, Hydrogel-based 3D bioprinting: A comprehensive review on cell-laden hydrogels, bioink formulations, and future perspectives, Appl. Mater. Today. 18 (2020) 100479. https://doi.org/10.1016/j.apmt.2019.100479.
[176] T.J. Hinton, Q. Jallerat, R.N. Palchesko, J.H. Park, M.S. Grodzicki, H.-J. Shue, M.H. Ramadan, A.R. Hudson, A.W. Feinberg, Three-dimensional printing of complex biological structures by freeform reversible embedding of suspended hydrogels, Sci. Adv. 1 (2015) e1500758. https://doi.org/10.1126/sciadv.1500758.
[177] M.E. Kupfer, W.-H. Lin, V. Ravikumar, K. Qiu, L. Wang, L. Gao, D.B. Bhuiyan, M. Lenz, J. Ai, R.R. Mahutga, D. Townsend, J. Zhang, M.C. McAlpine, E.G. Tolkacheva, B.M. Ogle, In Situ Expansion, Differentiation, and Electromechanical Coupling of Human Cardiac Muscle in a 3D Bioprinted, Chambered Organoid, Circ. Res. 127 (2020) 207–224. https://doi.org/10.1161/CIRCRESAHA.119.316155.
[178] A.C. Daly, M.D. Davidson, J.A. Burdick, 3D bioprinting of high cell-density heterogeneous tissue models through spheroid fusion within self-healing hydrogels, Nat. Commun. 12 (2021) 753. https://doi.org/10.1038/s41467-021-21029-2.
[179] B. Ayan, D.N. Heo, Z. Zhang, M. Dey, A. Povilianskas, C. Drapaca, I.T. Ozbolat, Aspiration-assisted bioprinting for precise positioning of biologics, Sci. Adv. 6 (2020) eaaw5111. https://doi.org/10.1126/sciadv.aaw5111.
[180] K. Jakab, B. Damon, F. Marga, O. Doaga, V. Mironov, I. Kosztin, R. Markwald, G. Forgacs, Relating cell and tissue mechanics: implications and applications, Dev. Dyn. Off. Publ. Am. Assoc. Anat. 237 (2008) 2438–2449. https://doi.org/10.1002/dvdy.21684.
[181] R.A. Foty, M.S. Steinberg, The differential adhesion hypothesis: a direct evaluation, Dev. Biol. 278 (2005) 255–263. https://doi.org/10.1016/j.ydbio.2004.11.012.

[182] D.T. Wu, M. Diba, S. Yang, B.R. Freedman, A. Elosegui-Artola, D.J. Mooney, Hydrogel viscoelasticity modulates migration and fusion of mesenchymal stem cell spheroids, Bioeng. Transl. Med. 8 (2022) e10464. https://doi.org/10.1002/btm2.10464.
[183] P.A. Fleming, W.S. Argraves, C. Gentile, A. Neagu, G. Forgacs, C.J. Drake, Fusion of uniluminal vascular spheroids: a model for assembly of blood vessels, Dev. Dyn. Off. Publ. Am. Assoc. Anat. 239 (2010) 398–406. https://doi.org/10.1002/dvdy.22161.
[184] K. Breckwoldt, D. Letuffe-Brenière, I. Mannhardt, T. Schulze, B. Ulmer, T. Werner, A. Benzin, B. Klampe, M.C. Reinsch, S. Laufer, A. Shibamiya, M. Prondzynski, G. Mearini, D. Schade, S. Fuchs, C. Neuber, E. Krämer, U. Saleem, M.L. Schulze, M.L. Rodriguez, T. Eschenhagen, A. Hansen, Differentiation of cardiomyocytes and generation of human engineered heart tissue, Nat. Protoc. 12 (2017) 1177–1197. https://doi.org/10.1038/nprot.2017.033.
[185] J. Andersen, O. Revah, Y. Miura, N. Thom, N.D. Amin, K.W. Kelley, M. Singh, X. Chen, M.V. Thete, E.M. Walczak, H. Vogel, H.C. Fan, S.P. Paşca, Generation of Functional Human 3D Cortico-Motor Assembloids, Cell. 183 (2020) 1913-1929.e26. https://doi.org/10.1016/j.cell.2020.11.017.
[186] L. Liang, Z. Li, B. Yao, J. Enhe, W. Song, C. Zhang, P. Zhu, S. Huang, Extrusion bioprinting of cellular aggregates improves mesenchymal stem cell proliferation and differentiation, Biomater. Adv. 149 (2023) 213369. https://doi.org/10.1016/j.bioadv.2023.213369.
[187] J.A. Reid, P.A. Mollica, R.D. Bruno, P.C. Sachs, Consistent and reproducible cultures of large-scale 3D mammary epithelial structures using an accessible bioprinting platform, Breast Cancer Res. 20 (2018) 122. https://doi.org/10.1186/s13058-018-1045-4.
[188] J.A. Brassard, M. Nikolaev, T. Hübscher, M. Hofer, M.P. Lutolf, Recapitulating macro-scale tissue self-organization through organoid bioprinting, Nat. Mater. 20 (2021) 22–29. https://doi.org/10.1038/s41563-020-00803-5.
[189] C. O'Connor, E. Brady, Y. Zheng, E. Moore, K.R. Stevens, Engineering the multiscale complexity of vascular networks, Nat. Rev. Mater. 7 (2022) 702–716. https://doi.org/10.1038/s41578-022-00447-8.
[190] V. Mastrullo, W. Cathery, E. Velliou, P. Madeddu, P. Campagnolo, Angiogenesis in Tissue Engineering: As Nature Intended?, Front. Bioeng. Biotechnol. 8 (2020). https://www.frontiersin.org/articles/10.3389/fbioe.2020.00188 (accessed August 22, 2023).
[191] Y. Kubota, H.K. Kleinman, G.R. Martin, T.J. Lawley, Role of laminin and basement membrane in the morphological differentiation of human endothelial cells into capillary-like structures, J. Cell Biol. 107 (1988) 1589–1598. https://doi.org/10.1083/jcb.107.4.1589.
[192] N. Koike, D. Fukumura, O. Gralla, P. Au, J.S. Schechner, R.K. Jain, Tissue engineering: creation of long-lasting blood vessels, Nature. 428 (2004) 138–139. https://doi.org/10.1038/428138a.
[193] M. Wanjare, S. Kusuma, S. Gerecht, Perivascular cells in blood vessel regeneration, Biotechnol. J. 8 (2013) 434–447. https://doi.org/10.1002/biot.201200199.
[194] M. Crisan, M. Corselli, W.C.W. Chen, B. Péault, Perivascular cells for regenerative medicine, J. Cell. Mol. Med. 16 (2012) 2851–2860. https://doi.org/10.1111/j.1582-4934.2012.01617.x.
[195] S. Levenberg, J. Rouwkema, M. Macdonald, E.S. Garfein, D.S. Kohane, D.C. Darland, R. Marini, C.A. van Blitterswijk, R.C. Mulligan, P.A. D'Amore, R. Langer, Engineering vascularized skeletal muscle tissue, Nat. Biotechnol. 23 (2005) 879–884. https://doi.org/10.1038/nbt1109.
[196] M.T. Valarmathi, J.W. Fuseler, J.D. Potts, J.M. Davis, R.L. Price, Functional Tissue Engineering: A Prevascularized Cardiac Muscle Construct for Validating Human Mesenchymal Stem Cells Engraftment Potential In Vitro, Tissue Eng. Part A. 24 (2018) 157–185. https://doi.org/10.1089/ten.tea.2016.0539.
[197] T. Takebe, K. Sekine, M. Enomura, H. Koike, M. Kimura, T. Ogaeri, R.-R. Zhang, Y. Ueno, Y.-W. Zheng, N. Koike, S. Aoyama, Y. Adachi, H. Taniguchi, Vascularized and functional human liver from an iPSC-derived organ bud transplant, Nature. 499 (2013) 481–484. https://doi.org/10.1038/nature12271.
[198] R.A. Wimmer, A. Leopoldi, M. Aichinger, N. Wick, B. Hantusch, M. Novatchkova, J. Taubenschmid, M. Hämmerle, C. Esk, J.A. Bagley, D. Lindenhofer, G. Chen, M. Boehm, C.A. Agu,

F. Yang, B. Fu, J. Zuber, J.A. Knoblich, D. Kerjaschki, J.M. Penninger, Human blood vessel organoids as a model of diabetic vasculopathy, Nature. 565 (2019) 505–510. https://doi.org/10.1038/s41586-018-0858-8.

[199] V.M. Ramakrishnan, N.L. Boyd, The Adipose Stromal Vascular Fraction as a Complex Cellular Source for Tissue Engineering Applications, Tissue Eng. Part B Rev. 24 (2018) 289–299. https://doi.org/10.1089/ten.teb.2017.0061.

[200] E.M. Moore, J.L. West, Harnessing Macrophages for Vascularization in Tissue Engineering, Ann. Biomed. Eng. 47 (2019) 354–365. https://doi.org/10.1007/s10439-018-02170-4.

[201] D. Wang, X. Wang, Z. Zhang, L. Wang, X. Li, Y. Xu, C. Ren, Q. Li, L.-S. Turng, Programmed Release of Multimodal, Cross-Linked Vascular Endothelial Growth Factor and Heparin Layers on Electrospun Polycaprolactone Vascular Grafts, ACS Appl. Mater. Interfaces. 11 (2019) 32533–32542. https://doi.org/10.1021/acsami.9b10621.

[202] M.H. Rich, M.K. Lee, K. Baek, J.H. Jeong, D.H. Kim, L.J. Millet, R. Bashir, H. Kong, Material-mediated proangiogenic factor release pattern modulates quality of regenerated blood vessels, J. Control. Release Off. J. Control. Release Soc. 196 (2014) 363–369. https://doi.org/10.1016/j.jconrel.2014.10.020.

[203] N. Yamamura, R. Sudo, M. Ikeda, K. Tanishita, Effects of the mechanical properties of collagen gel on the in vitro formation of microvessel networks by endothelial cells, Tissue Eng. 13 (2007) 1443–1453. https://doi.org/10.1089/ten.2006.0333.

[204] R.G. Mannino, N.K.R. Pandian, A. Jain, W.A. Lam, Engineering “endothelialized” microfluidics for investigating vascular and hematologic processes using non-traditional fabrication techniques, Curr. Opin. Biomed. Eng. 5 (2018) 13–20. https://doi.org/10.1016/j.cobme.2017.11.006.

[205] J. Tien, Microfluidic approaches for engineering vasculature, Curr. Opin. Chem. Eng. 3 (2014) 36–41. https://doi.org/10.1016/j.coche.2013.10.006.

[206] S. Kim, H. Lee, M. Chung, N.L. Jeon, Engineering of functional, perfusable 3D microvascular networks on a chip, Lab. Chip. 13 (2013) 1489–1500. https://doi.org/10.1039/C3LC41320A.

[207] V.A. Liu, S.N. Bhatia, Three-Dimensional Photopatterning of Hydrogels Containing Living Cells, Biomed. Microdevices. 4 (2002) 257–266. https://doi.org/10.1023/A:1020932105236.

[208] P.M. Kharkar, K.L. Kiick, A.M. Kloxin, Designing degradable hydrogels for orthogonal control of cell microenvironments, Chem. Soc. Rev. 42 (2013) 7335–7372. https://doi.org/10.1039/c3cs60040h.

[209] I.K. Zervantonakis, C.R. Kothapalli, S. Chung, R. Sudo, R.D. Kamm, Microfluidic devices for studying heterotypic cell-cell interactions and tissue specimen cultures under controlled microenvironments, Biomicrofluidics. 5 (2011) 13406. https://doi.org/10.1063/1.3553237.

[210] D.B. Kolesky, R.L. Truby, A.S. Gladman, T.A. Busbee, K.A. Homan, J.A. Lewis, 3D Bioprinting of Vascularized, Heterogeneous Cell-Laden Tissue Constructs, Adv. Mater. 26 (2014) 3124–3130. https://doi.org/10.1002/adma.201305506.

[211] M.A. Skylar-Scott, S.G.M. Uzel, L.L. Nam, J.H. Ahrens, R.L. Truby, S. Damaraju, J.A. Lewis, Biomanufacturing of organ-specific tissues with high cellular density and embedded vascular channels, Sci. Adv. 5 (2019) eaaw2459. https://doi.org/10.1126/sciadv.aaw2459.

[212] J.S. Miller, K.R. Stevens, M.T. Yang, B.M. Baker, D.-H.T. Nguyen, D.M. Cohen, E. Toro, A.A. Chen, P.A. Galie, X. Yu, R. Chaturvedi, S.N. Bhatia, C.S. Chen, Rapid casting of patterned vascular networks for perfusable engineered 3D tissues, Nat. Mater. 11 (2012) 768–774. https://doi.org/10.1038/nmat3357.

[213] U.J. Jung, M.-S. Choi, Obesity and Its Metabolic Complications: The Role of Adipokines and the Relationship between Obesity, Inflammation, Insulin Resistance, Dyslipidemia and Nonalcoholic Fatty Liver Disease, Int. J. Mol. Sci. 15 (2014) 6184–6223. https://doi.org/10.3390/ijms15046184.

[214] Global Burden of Disease Collaborative Network, Global Burden of Disease Study 2019 (GBD 2019) Results., (2020). https://vizhub.healthdata.org/gbd-results/.

[215] B. Chong, J. Jayabaskaran, G. Kong, Y.H. Chan, Y.H. Chin, R. Goh, S. Kannan, C.H. Ng, S. Loong, M.T.W. Kueh, C. Lin, V.V. Anand, E.C.Z. Lee, H.S.J. Chew, D.J.H. Tan, K.E. Chan, J.-W. Wang, M.

Muthiah, G.K. Dimitriadis, D.J. Hausenloy, A.J. Mehta, R. Foo, G. Lip, M.Y. Chan, M.A. Mamas, C.W. le Roux, N.W.S. Chew, Trends and predictions of malnutrition and obesity in 204 countries and territories: an analysis of the Global Burden of Disease Study 2019, EClinicalMedicine. 57 (2023). https://doi.org/10.1016/j.eclinm.2023.101850.

[216] B.M. Spiegelman, J.S. Flier, Obesity and the Regulation of Energy Balance, Cell. 104 (2001) 531–543. https://doi.org/10.1016/S0092-8674(01)00240-9.

[217] L. Luo, M. Liu, Adipose tissue in control of metabolism, J. Endocrinol. 231 (2016) R77–R99. https://doi.org/10.1530/JOE-16-0211.

[218] S.D. Parlee, S.I. Lentz, H. Mori, O.A. MacDougald, Quantifying Size and Number of Adipocytes in Adipose Tissue, Methods Enzymol. 537 (2014) 93–122. https://doi.org/10.1016/B978-0-12-411619-1.00006-9.

[219] A.S. Jackson, P.R. Stanforth, J. Gagnon, T. Rankinen, A.S. Leon, D.C. Rao, J.S. Skinner, C. Bouchard, J.H. Wilmore, The effect of sex, age and race on estimating percentage body fat from body mass index: The Heritage Family Study, Int. J. Obes. Relat. Metab. Disord. J. Int. Assoc. Study Obes. 26 (2002) 789–796. https://doi.org/10.1038/sj.ijo.0802006.

[220] R.K. Zwick, C.F. Guerrero-Juarez, V. Horsley, M.V. Plikus, Anatomical, Physiological, and Functional Diversity of Adipose Tissue, Cell Metab. 27 (2018) 68–83. https://doi.org/10.1016/j.cmet.2017.12.002.

[221] A. Sakers, M.K. De Siqueira, P. Seale, C.J. Villanueva, Adipose-tissue plasticity in health and disease, Cell. 185 (2022) 419–446. https://doi.org/10.1016/j.cell.2021.12.016.

[222] S. Gesta, Y.-H. Tseng, C.R. Kahn, Developmental Origin of Fat: Tracking Obesity to Its Source, Cell. 131 (2007) 242–256. https://doi.org/10.1016/j.cell.2007.10.004.

[223] S.M. Jung, J. Sanchez-Gurmaches, D.A. Guertin, Brown Adipose Tissue Development and Metabolism, Handb. Exp. Pharmacol. 251 (2019) 3–36. https://doi.org/10.1007/164_2018_168.

[224] B. Cannon, J. Nedergaard, Brown Adipose Tissue: Function and Physiological Significance, Physiol. Rev. 84 (2004) 277–359. https://doi.org/10.1152/physrev.00015.2003.

[225] A. Fedorenko, P.V. Lishko, Y. Kirichok, Mechanism of Fatty-Acid-Dependent UCP1 Uncoupling in Brown Fat Mitochondria, Cell. 151 (2012) 400–413. https://doi.org/10.1016/j.cell.2012.09.010.

[226] A.M. Cypess, S. Lehman, G. Williams, I. Tal, D. Rodman, A.B. Goldfine, F.C. Kuo, E.L. Palmer, Y.-H. Tseng, A. Doria, G.M. Kolodny, C.R. Kahn, Identification and Importance of Brown Adipose Tissue in Adult Humans, N. Engl. J. Med. 360 (2009) 1509–1517. https://doi.org/10.1056/NEJMoa0810780.

[227] K. Kaikaew, A. Grefhorst, J.A. Visser, Sex Differences in Brown Adipose Tissue Function: Sex Hormones, Glucocorticoids, and Their Crosstalk, Front. Endocrinol. 12 (2021) 652444. https://doi.org/10.3389/fendo.2021.652444.

[228] B. Cannon, J.M.A. de Jong, A.W. Fischer, J. Nedergaard, N. Petrovic, Human brown adipose tissue: Classical brown rather than brite/beige?, Exp. Physiol. 105 (2020) 1191–1200. https://doi.org/10.1113/EP087875.

[229] V. Peirce, S. Carobbio, A. Vidal-Puig, The different shades of fat, Nature. 510 (2014) 76–83. https://doi.org/10.1038/nature13477.

[230] L.Z. Sharp, K. Shinoda, H. Ohno, D.W. Scheel, E. Tomoda, L. Ruiz, H. Hu, L. Wang, Z. Pavlova, V. Gilsanz, S. Kajimura, Human BAT possesses molecular signatures that resemble beige/brite cells, PloS One. 7 (2012) e49452. https://doi.org/10.1371/journal.pone.0049452.

[231] K. Ikeda, P. Maretich, S. Kajimura, The common and distinct features of brown and beige adipocytes, Trends Endocrinol. Metab. TEM. 29 (2018) 191–200. https://doi.org/10.1016/j.tem.2018.01.001.

[232] M.E. Lidell, M.J. Betz, O. Dahlqvist Leinhard, M. Heglind, L. Elander, M. Slawik, T. Mussack, D. Nilsson, T. Romu, P. Nuutila, K.A. Virtanen, F. Beuschlein, A. Persson, M. Borga, S. Enerbäck, Evidence for two types of brown adipose tissue in humans, Nat. Med. 19 (2013) 631–634. https://doi.org/10.1038/nm.3017.

[233] Y. Zhang, R. Proenca, M. Maffei, M. Barone, L. Leopold, J.M. Friedman, Positional cloning of the mouse obese gene and its human homologue, Nature. 372 (1994) 425–432. https://doi.org/10.1038/372425a0.
[234] K. Zorena, O. Jachimowicz-Duda, D. Ślęzak, M. Robakowska, M. Mrugacz, Adipokines and Obesity. Potential Link to Metabolic Disorders and Chronic Complications, Int. J. Mol. Sci. 21 (2020) 3570. https://doi.org/10.3390/ijms21103570.
[235] Y. Deng, P.E. Scherer, Adipokines as novel biomarkers and regulators of the metabolic syndrome, Ann. N. Y. Acad. Sci. 1212 (2010) E1–E19. https://doi.org/10.1111/j.1749-6632.2010.05875.x.
[236] O.A. MacDougald, C.F. Burant, The rapidly expanding family of adipokines, Cell Metab. 6 (2007) 159–161. https://doi.org/10.1016/j.cmet.2007.08.010.
[237] J. Villarroya, R. Cereijo, M. Giralt, F. Villarroya, Secretory Proteome of Brown Adipocytes in Response to cAMP-Mediated Thermogenic Activation, Front. Physiol. 10 (2019) 67. https://doi.org/10.3389/fphys.2019.00067.
[238] J. Villarroya, R. Cereijo, A. Gavaldà-Navarro, M. Peyrou, M. Giralt, F. Villarroya, New insights into the secretory functions of brown adipose tissue, J. Endocrinol. 243 (2019) R19–R27. https://doi.org/10.1530/JOE-19-0295.
[239] T.J. Schulz, Y.-H. Tseng, Emerging Role of Bone Morphogenetic Proteins in Adipogenesis and Energy Metabolism, Cytokine Growth Factor Rev. 20 (2009) 523–531. https://doi.org/10.1016/j.cytogfr.2009.10.019.
[240] A.J. Whittle, S. Carobbio, L. Martins, M. Slawik, E. Hondares, M.J. Vázquez, D. Morgan, R.I. Csikasz, R. Gallego, S. Rodriguez-Cuenca, M. Dale, S. Virtue, F. Villarroya, B. Cannon, K. Rahmouni, M. López, A. Vidal-Puig, BMP8B increases brown adipose tissue thermogenesis through both central and peripheral actions, Cell. 149 (2012) 871–885. https://doi.org/10.1016/j.cell.2012.02.066.
[241] K. Sun, C.M. Kusminski, K. Luby-Phelps, S.B. Spurgin, Y.A. An, Q.A. Wang, W.L. Holland, P.E. Scherer, Brown adipose tissue derived VEGF-A modulates cold tolerance and energy expenditure, Mol. Metab. 3 (2014) 474–483. https://doi.org/10.1016/j.molmet.2014.03.010.
[242] R. Cereijo, A. Gavaldà-Navarro, M. Cairó, T. Quesada-López, J. Villarroya, S. Morón-Ros, D. Sánchez-Infantes, M. Peyrou, R. Iglesias, T. Mampel, J.-V. Turatsinze, D.L. Eizirik, M. Giralt, F. Villarroya, CXCL14, a Brown Adipokine that Mediates Brown-Fat-to-Macrophage Communication in Thermogenic Adaptation, Cell Metab. 28 (2018) 750-763.e6. https://doi.org/10.1016/j.cmet.2018.07.015.
[243] C. Garcia-Beltran, A. Navarro-Gascon, A. López-Bermejo, T. Quesada-López, F. de Zegher, L. Ibáñez, F. Villarroya, Meteorin-like levels are associated with active brown adipose tissue in early infancy, Front. Endocrinol. 14 (2023) 1136245. https://doi.org/10.3389/fendo.2023.1136245.
[244] L. Campderrós, R. Moure, M. Cairó, A. Gavaldà-Navarro, T. Quesada-López, R. Cereijo, M. Giralt, J. Villarroya, F. Villarroya, Brown Adipocytes Secrete GDF15 in Response to Thermogenic Activation, Obes. Silver Spring Md. 27 (2019) 1606–1616. https://doi.org/10.1002/oby.22584.
[245] K.I. Stanford, R.J.W. Middelbeek, K.L. Townsend, D. An, E.B. Nygaard, K.M. Hitchcox, K.R. Markan, K. Nakano, M.F. Hirshman, Y.-H. Tseng, L.J. Goodyear, Brown adipose tissue regulates glucose homeostasis and insulin sensitivity, J. Clin. Invest. 123 (2013) 215–223. https://doi.org/10.1172/JCI62308.
[246] F.J. Ruiz-Ojeda, A. Méndez-Gutiérrez, C.M. Aguilera, J. Plaza-Díaz, Extracellular Matrix Remodeling of Adipose Tissue in Obesity and Metabolic Diseases, Int. J. Mol. Sci. 20 (2019) 4888. https://doi.org/10.3390/ijms20194888.
[247] A. Engin, Adipose Tissue Hypoxia in Obesity and Its Impact on Preadipocytes and Macrophages: Hypoxia Hypothesis, Adv. Exp. Med. Biol. 960 (2017) 305–326. https://doi.org/10.1007/978-3-319-48382-5_13.
[248] E.D. Rosen, B.M. Spiegelman, Adipocytes as regulators of energy balance and glucose homeostasis, Nature. 444 (2006) 847–853. https://doi.org/10.1038/nature05483.

[249] A. Ruban, K. Stoenchev, H. Ashrafian, J. Teare, Current treatments for obesity, Clin. Med. 19 (2019) 205–212. https://doi.org/10.7861/clinmedicine.19-3-205.
[250] M. Chakhtoura, R. Haber, M. Ghezzawi, C. Rhayem, R. Tcheroyan, C.S. Mantzoros, Pharmacotherapy of obesity: an update on the available medications and drugs under investigation, EClinicalMedicine. 58 (2023). https://doi.org/10.1016/j.eclinm.2023.101882.
[251] K. Ziqubu, P.V. Dludla, S.X.H. Mthembu, B.B. Nkambule, S.E. Mabhida, B.U. Jack, T.M. Nyambuya, S.E. Mazibuko-Mbeje, An insight into brown/beige adipose tissue whitening, a metabolic complication of obesity with the multifactorial origin, Front. Endocrinol. 14 (2023). https://www.frontiersin.org/articles/10.3389/fendo.2023.1114767 (accessed August 2, 2023).
[252] A.C. Carpentier, D.P. Blondin, K.A. Virtanen, D. Richard, F. Haman, É.E. Turcotte, Brown Adipose Tissue Energy Metabolism in Humans, Front. Endocrinol. 9 (2018) 447. https://doi.org/10.3389/fendo.2018.00447.
[253] M. Tsoli, M. Moore, D. Burg, A. Painter, R. Taylor, S.H. Lockie, N. Turner, A. Warren, G. Cooney, B. Oldfield, S. Clarke, G. Robertson, Activation of thermogenesis in brown adipose tissue and dysregulated lipid metabolism associated with cancer cachexia in mice, Cancer Res. 72 (2012) 4372–4382. https://doi.org/10.1158/0008-5472.CAN-11-3536.
[254] J. Ni, L. Zhang, Cancer Cachexia: Definition, Staging, and Emerging Treatments, Cancer Manag. Res. 12 (2020) 5597–5605. https://doi.org/10.2147/CMAR.S261585.
[255] L.S. Sidossis, C. Porter, M.K. Saraf, E. Børsheim, R.S. Radhakrishnan, T. Chao, A. Ali, M. Chondronikola, R. Mlcak, C.C. Finnerty, H.K. Hawkins, T. Toliver-Kinsky, D.N. Herndon, Browning of Subcutaneous White Adipose Tissue in Humans after Severe Adrenergic Stress, Cell Metab. 22 (2015) 219–227. https://doi.org/10.1016/j.cmet.2015.06.022.
[256] C.T. Herz, O.C. Kulterer, M. Prager, C. Schmöltzer, F.B. Langer, G. Prager, R. Marculescu, A. Kautzky-Willer, M. Hacker, A.R. Haug, F.W. Kiefer, Active Brown Adipose Tissue is Associated With a Healthier Metabolic Phenotype in Obesity, Diabetes. (2021) db210475. https://doi.org/10.2337/db21-0475.
[257] N.L. Mihalopoulos, J.T. Yap, B. Beardmore, R. Holubkov, M.N. Nanjee, J.M. Hoffman, Cold-Activated Brown Adipose Tissue is Associated with Less Cardiometabolic Dysfunction in Young Adults with Obesity, Obesity. 28 (2020) 916–923. https://doi.org/10.1002/oby.22767.
[258] L. Cheng, J. Wang, H. Dai, Y. Duan, Y. An, L. Shi, Y. Lv, H. Li, C. Wang, Q. Ma, Y. Li, P. Li, H. Du, B. Zhao, Brown and beige adipose tissue: a novel therapeutic strategy for obesity and type 2 diabetes mellitus, Adipocyte. 10 (n.d.) 48–65. https://doi.org/10.1080/21623945.2020.1870060.
[259] C.-H. Wang, Y.-H. Wei, Therapeutic Perspectives of Thermogenic Adipocytes in Obesity and Related Complications, Int. J. Mol. Sci. 22 (2021) 7177. https://doi.org/10.3390/ijms22137177.
[260] A.M. Cypess, L.S. Weiner, C. Roberts-Toler, E.F. Elía, S.H. Kessler, P.A. Kahn, J. English, K. Chatman, S.A. Trauger, A. Doria, G.M. Kolodny, Activation of Human Brown Adipose Tissue by a β3-Adrenergic Receptor Agonist, Cell Metab. 21 (2015) 33–38. https://doi.org/10.1016/j.cmet.2014.12.009.
[261] A.S. Baskin, J.D. Linderman, R.J. Brychta, S. McGehee, E. Anflick-Chames, C. Cero, J.W. Johnson, A.E. O'Mara, L.A. Fletcher, B.P. Leitner, C.J. Duckworth, S. Huang, H. Cai, H.M. Garraffo, C.M. Millo, W. Dieckmann, V. Tolstikov, E.Y. Chen, F. Gao, N.R. Narain, M.A. Kiebish, P.J. Walter, P. Herscovitch, K.Y. Chen, A.M. Cypess, Regulation of Human Adipose Tissue Activation, Gallbladder Size, and Bile Acid Metabolism by a β3-Adrenergic Receptor Agonist, Diabetes. 67 (2018) 2113–2125. https://doi.org/10.2337/db18-0462.
[262] M. Nishio, T. Yoneshiro, M. Nakahara, S. Suzuki, K. Saeki, M. Hasegawa, Y. Kawai, H. Akutsu, A. Umezawa, K. Yasuda, K. Tobe, A. Yuo, K. Kubota, M. Saito, K. Saeki, Production of Functional Classical Brown Adipocytes from Human Pluripotent Stem Cells using Specific Hemopoietin Cocktail without Gene Transfer, Cell Metab. 16 (2012) 394–406. https://doi.org/10.1016/j.cmet.2012.08.001.
[263] C.-H. Wang, M. Lundh, A. Fu, R. Kriszt, T.L. Huang, M.D. Lynes, L.O. Leiria, F. Shamsi, J. Darcy, B.P. Greenwood, N.R. Narain, V. Tolstikov, K.L. Smith, B. Emanuelli, Y.-T. Chang, S. Hagen, N.N.

Danial, M.A. Kiebish, Y.-H. Tseng, CRISPR-engineered human brown-like adipocytes prevent diet-induced obesity and ameliorate metabolic syndrome in mice, Sci. Transl. Med. 12 (2020) eaaz8664. https://doi.org/10.1126/scitranslmed.aaz8664.

[264] S.Y. Min, J. Kady, M. Nam, R. Rojas-Rodriguez, A. Berkenwald, J.H. Kim, H.-L. Noh, J.K. Kim, M.P. Cooper, T. Fitzgibbons, M.A. Brehm, S. Corvera, Human "brite/beige" adipocytes develop from capillary networks, and their implantation improves metabolic homeostasis in mice, Nat. Med. 22 (2016) 312–318. https://doi.org/10.1038/nm.4031.

[265] X. Liu, S. Wang, Y. You, M. Meng, Z. Zheng, M. Dong, J. Lin, Q. Zhao, C. Zhang, X. Yuan, T. Hu, L. Liu, Y. Huang, L. Zhang, D. Wang, J. Zhan, H. Jong Lee, J.R. Speakman, W. Jin, Brown Adipose Tissue Transplantation Reverses Obesity in Ob/Ob Mice, Endocrinology. 156 (2015) 2461–2469. https://doi.org/10.1210/en.2014-1598.

[266] D. Estève, N. Boulet, C. Belles, A. Zakaroff-Girard, P. Decaunes, A. Briot, Y. Veeranagouda, M. Didier, A. Remaury, J.C. Guillemot, S. Ledoux, C. Dani, A. Bouloumié, J. Galitzky, Lobular architecture of human adipose tissue defines the niche and fate of progenitor cells, Nat. Commun. 10 (2019) 2549. https://doi.org/10.1038/s41467-019-09992-3.

[267] J.A. Aronowitz, R.A. Lockhart, C.S. Hakakian, Mechanical versus enzymatic isolation of stromal vascular fraction cells from adipose tissue, SpringerPlus. 4 (2015) 713. https://doi.org/10.1186/s40064-015-1509-2.

[268] S. Lecoutre, M. Lambert, K. Drygalski, I. Dugail, S. Maqdasy, M. Hautefeuille, K. Clément, Importance of the Microenvironment and Mechanosensing in Adipose Tissue Biology, Cells. 11 (2022) 2310. https://doi.org/10.3390/cells11152310.

[269] E.C.M. Mariman, P. Wang, Adipocyte extracellular matrix composition, dynamics and role in obesity, Cell. Mol. Life Sci. 67 (2010) 1277–1292. https://doi.org/10.1007/s00018-010-0263-4.

[270] V. Pellegrinelli, E. Figueroa-Juárez, I. Samuelson, M. U-Din, S. Rodriguez-Fdez, S. Virtue, J. Leggat, C. Çubuk, V.J. Peirce, T. Niemi, M. Campbell, S. Rodriguez-Cuenca, J.D. Blázquez, S. Carobbio, K.A. Virtanen, A. Vidal-Puig, Defective extracellular matrix remodeling in brown adipose tissue is associated with fibro-inflammation and reduced diet-induced thermogenesis, Cell Rep. 42 (2023) 112640. https://doi.org/10.1016/j.celrep.2023.112640.

[271] Y. Wang, L. Ye, Somatosensory innervation of adipose tissues, Physiol. Behav. 265 (2023) 114174. https://doi.org/10.1016/j.physbeh.2023.114174.

[272] A. Géloën, A.J. Collet, G. Guay, L.J. Bukowiecki, Beta-adrenergic stimulation of brown adipocyte proliferation, Am. J. Physiol. 254 (1988) C175-182. https://doi.org/10.1152/ajpcell.1988.254.1.C175.

[273] G. Bronnikov, J. Houstěk, J. Nedergaard, Beta-adrenergic, cAMP-mediated stimulation of proliferation of brown fat cells in primary culture. Mediation via beta 1 but not via beta 3 adrenoceptors, J. Biol. Chem. 267 (1992) 2006–2013.

[274] Md.S. Rahman, H. Jun, The Adipose Tissue Macrophages Central to Adaptive Thermoregulation, Front. Immunol. 13 (2022) 884126. https://doi.org/10.3389/fimmu.2022.884126.

[275] J. Herold, J. Kalucka, Angiogenesis in Adipose Tissue: The Interplay Between Adipose and Endothelial Cells, Front. Physiol. 11 (2020) 624903. https://doi.org/10.3389/fphys.2020.624903.

[276] P. Marzola, F. Boschi, F. Moneta, A. Sbarbati, C. Zancanaro, Preclinical In vivo Imaging for Fat Tissue Identification, Quantification, and Functional Characterization, Front. Pharmacol. 7 (2016) 336. https://doi.org/10.3389/fphar.2016.00336.

[277] C. Sztalryd, D.L. Brasaemle, The perilipin family of lipid droplet proteins: Gatekeepers of intracellular lipolysis, Biochim. Biophys. Acta. 1862 (2017) 1221–1232. https://doi.org/10.1016/j.bbalip.2017.07.009.

[278] L. Casteilla, B. Cousin, M. Carmona, PPARs and Adipose Cell Plasticity, PPAR Res. 2007 (2007) 68202. https://doi.org/10.1155/2007/68202.

[279] S. Al-Ghadban, M. Artiles, B.A. Bunnell, Adipose Stem Cells in Regenerative Medicine: Looking Forward, Front. Bioeng. Biotechnol. 9 (2022) 837464. https://doi.org/10.3389/fbioe.2021.837464.

[280] S.-N. Li, J.-F. Wu, TGF-β/SMAD signaling regulation of mesenchymal stem cells in adipocyte commitment, Stem Cell Res. Ther. 11 (2020) 41. https://doi.org/10.1186/s13287-020-1552-y.
[281] D. Estève, N. Boulet, F. Volat, A. Zakaroff-Girard, S. Ledoux, M. Coupaye, P. Decaunes, C. Belles, F. Gaits-Iacovoni, J.S. Iacovoni, A. Rémaury, B. Castel, P. Ferrara, C. Heymes, M. Lafontan, A. Bouloumié, J. Galitzky, Human White and Brite Adipogenesis is Supported by MSCA1 and is Impaired by Immune Cells, STEM CELLS. 33 (2015) 1277–1291. https://doi.org/10.1002/stem.1916.
[282] A.W. Ferrante, The Immune Cells in Adipose Tissue, Diabetes Obes. Metab. 15 (2013) 34–38. https://doi.org/10.1111/dom.12154.
[283] P.-C. Chan, P.-S. Hsieh, P.-C. Chan, P.-S. Hsieh, The Role of Adipocyte Hypertrophy and Hypoxia in the Development of Obesity-Associated Adipose Tissue Inflammation and Insulin Resistance, in: Adiposity - Omics Mol. Underst., IntechOpen, 2017. https://doi.org/10.5772/65458.
[284] K.D. Nguyen, Y. Qiu, X. Cui, Y.P.S. Goh, J. Mwangi, T. David, L. Mukundan, F. Brombacher, R.M. Locksley, A. Chawla, Alternatively activated macrophages produce catecholamines to sustain adaptive thermogenesis, Nature. 480 (2011) 104–108. https://doi.org/10.1038/nature10653.
[285] K. Fischer, H.H. Ruiz, K. Jhun, B. Finan, D.J. Oberlin, V. van der Heide, A.V. Kalinovich, N. Petrovic, Y. Wolf, C. Clemmensen, A.C. Shin, S. Divanovic, F. Brombacher, E. Glasmacher, S. Keipert, M. Jastroch, J. Nagler, K.-W. Schramm, D. Medrikova, G. Collden, S.C. Woods, S. Herzig, D. Homann, S. Jung, J. Nedergaard, B. Cannon, M.H. Tschöp, T.D. Müller, C. Buettner, Alternatively activated macrophages do not synthesize catecholamines or contribute to adipose tissue adaptive thermogenesis, Nat. Med. 23 (2017) 623–630. https://doi.org/10.1038/nm.4316.
[286] Y.-N. Wang, Y. Tang, Z. He, H. Ma, L. Wang, Y. Liu, Q. Yang, D. Pan, C. Zhu, S. Qian, Q.-Q. Tang, Slit3 secreted from M2-like macrophages increases sympathetic activity and thermogenesis in adipose tissue, Nat. Metab. 3 (2021) 1536–1551. https://doi.org/10.1038/s42255-021-00482-9.
[287] M.A. Ambele, P. Dhanraj, R. Giles, M.S. Pepper, Adipogenesis: A Complex Interplay of Multiple Molecular Determinants and Pathways, Int. J. Mol. Sci. 21 (2020) 4283. https://doi.org/10.3390/ijms21124283.
[288] S. Modica, L.G. Straub, M. Balaz, W. Sun, L. Varga, P. Stefanicka, M. Profant, E. Simon, H. Neubauer, B. Ukropcova, J. Ukropec, C. Wolfrum, Bmp4 Promotes a Brown to White-like Adipocyte Shift, Cell Rep. 16 (2016) 2243–2258. https://doi.org/10.1016/j.celrep.2016.07.048.
[289] B. Gustafson, A. Hammarstedt, S. Hedjazifar, J.M. Hoffmann, P.-A. Svensson, J. Grimsby, C. Rondinone, U. Smith, BMP4 and BMP Antagonists Regulate Human White and Beige Adipogenesis, Diabetes. 64 (2015) 1670–1681. https://doi.org/10.2337/db14-1127.
[290] I.A. Darby, B. Laverdet, F. Bonté, A. Desmoulière, Fibroblasts and myofibroblasts in wound healing, Clin. Cosmet. Investig. Dermatol. 7 (2014) 301–311. https://doi.org/10.2147/CCID.S50046.
[291] M.K. DeBari, R.D. Abbott, Adipose Tissue Fibrosis: Mechanisms, Models, and Importance, Int. J. Mol. Sci. 21 (2020) 6030. https://doi.org/10.3390/ijms21176030.
[292] H. Pan, Y. Xie, Z. Zhang, K. Li, D. Hu, X. Zheng, Q. Fan, T. Tang, YAP-mediated mechanotransduction regulates osteogenic and adipogenic differentiation of BMSCs on hierarchical structure, Colloids Surf. B Biointerfaces. 152 (2017) 344–353. https://doi.org/10.1016/j.colsurfb.2017.01.039.
[293] P. Mallikarjuna, Y. Zhou, M. Landström, The Synergistic Cooperation between TGF-β and Hypoxia in Cancer and Fibrosis, Biomolecules. 12 (2022) 635. https://doi.org/10.3390/biom12050635.
[294] A. Ibrahimi, F. Bonino, S. Bardon, G. Ailhaud, C. Dani, Essential role of collagens for terminal differentiation of preadipocytes, Biochem. Biophys. Res. Commun. 187 (1992) 1314–1322. https://doi.org/10.1016/0006-291x(92)90446-r.
[295] N. Zöller, S. Schreiner, L. Petry, S. Hoffmann, K. Steinhorst, J. Kleemann, M. Jäger, R. Kaufmann, M. Meissner, S. Kippenberger, Collagen I Promotes Adipocytogenesis in Adipose-Derived Stem Cells In Vitro, Cells. 8 (2019) 302. https://doi.org/10.3390/cells8040302.

[296] J. Mauney, V. Volloch, Human bone marrow-derived stromal cells show highly efficient stress-resistant adipogenesis on denatured collagen IV matrix but not on its native counterpart: implications for obesity, Matrix Biol. J. Int. Soc. Matrix Biol. 29 (2010) 9–14. https://doi.org/10.1016/j.matbio.2009.09.002.
[297] W. Wang, P. Seale, Control of brown and beige fat development, Nat. Rev. Mol. Cell Biol. 17 (2016) 691–702. https://doi.org/10.1038/nrm.2016.96.
[298] M. Shao, Q. Zhang, A. Truong, B. Shan, L. Vishvanath, L. Li, P. Seale, R.K. Gupta, ZFP423 controls EBF2 coactivator recruitment and PPARγ occupancy to determine the thermogenic plasticity of adipocytes, Genes Dev. 35 (2021) 1461–1474. https://doi.org/10.1101/gad.348780.121.
[299] P. Seale, B. Bjork, W. Yang, S. Kajimura, S. Chin, S. Kuang, A. Scimè, S. Devarakonda, H.M. Conroe, H. Erdjument-Bromage, P. Tempst, M.A. Rudnicki, D.R. Beier, B.M. Spiegelman, PRDM16 controls a brown fat/skeletal muscle switch, Nature. 454 (2008) 961–967. https://doi.org/10.1038/nature07182.
[300] C. Lepper, C.-M. Fan, Inducible lineage tracing of Pax7-descendant cells reveals embryonic origin of adult satellite cells, Genes. N. Y. N 2000. 48 (2010) 424–436. https://doi.org/10.1002/dvg.20630.
[301] T. Shan, X. Liang, P. Bi, P. Zhang, W. Liu, S. Kuang, Distinct populations of adipogenic and myogenic Myf5-lineage progenitors in white adipose tissues, J. Lipid Res. 54 (2013) 2214–2224. https://doi.org/10.1194/jlr.M038711.
[302] J. Sanchez-Gurmaches, D.A. Guertin, Adipocyte lineages: tracing back the origins of fat, Biochim. Biophys. Acta. 1842 (2014) 340–351. https://doi.org/10.1016/j.bbadis.2013.05.027.
[303] F. Wassermann, The development of adipose tissue, in: Compr. Physiol., John Wiley & Sons, Ltd, 2011: pp. 87–100. https://doi.org/10.1002/cphy.cp050110.
[304] W. Tang, D. Zeve, J.M. Suh, D. Bosnakovski, M. Kyba, R.E. Hammer, M.D. Tallquist, J.M. Graff, White Fat Progenitors Reside in the Adipose Vasculature, Science. 322 (2008) 583–586. https://doi.org/10.1126/science.1156232.
[305] Z. Gao, A.C. Daquinag, F. Su, B. Snyder, M.G. Kolonin, PDGFRα/PDGFRβ signaling balance modulates progenitor cell differentiation into white and beige adipocytes, Dev. Camb. Engl. 145 (2018) dev155861. https://doi.org/10.1242/dev.155861.
[306] E.D. Rosen, B.M. Spiegelman, What We Talk About When We Talk About Fat, Cell. 156 (2014) 20–44. https://doi.org/10.1016/j.cell.2013.12.012.
[307] Z. Zhang, D. Yang, J. Xiang, J. Zhou, H. Cao, Q. Che, Y. Bai, J. Guo, Z. Su, Non-shivering Thermogenesis Signalling Regulation and Potential Therapeutic Applications of Brown Adipose Tissue, Int. J. Biol. Sci. 17 (2021) 2853–2870. https://doi.org/10.7150/ijbs.60354.
[308] F.R. Jornayvaz, G.I. Shulman, Regulation of mitochondrial biogenesis, Essays Biochem. 47 (2010) 10.1042/bse0470069. https://doi.org/10.1042/bse0470069.
[309] M.L. Bonet, J. Ribot, A. Palou, Lipid metabolism in mammalian tissues and its control by retinoic acid, Biochim. Biophys. Acta. 1821 (2012) 177–189. https://doi.org/10.1016/j.bbalip.2011.06.001.
[310] W.W. Yau, P.M. Yen, Thermogenesis in Adipose Tissue Activated by Thyroid Hormone, Int. J. Mol. Sci. 21 (2020) 3020. https://doi.org/10.3390/ijms21083020.
[311] R. Alvarez, J. de Andrés, P. Yubero, O. Viñas, T. Mampel, R. Iglesias, M. Giralt, F. Villarroya, A Novel Regulatory Pathway of Brown Fat Thermogenesis: RETINOIC ACID IS A TRANSCRIPTIONAL ACTIVATOR OF THE MITOCHONDRIAL UNCOUPLING PROTEIN GENE (∗), J. Biol. Chem. 270 (1995) 5666–5673. https://doi.org/10.1074/jbc.270.10.5666.
[312] T. Teruel, R. Hernandez, M. Benito, M. Lorenzo, Rosiglitazone and retinoic acid induce uncoupling protein-1 (UCP-1) in a p38 mitogen-activated protein kinase-dependent manner in fetal primary brown adipocytes, J. Biol. Chem. 278 (2003) 263–269. https://doi.org/10.1074/jbc.M207200200.
[313] J. Zhao, L. Unelius, T. Bengtsson, B. Cannon, J. Nedergaard, Coexisting beta-adrenoceptor subtypes: significance for thermogenic process in brown fat cells, Am. J. Physiol. 267 (1994) C969-979. https://doi.org/10.1152/ajpcell.1994.267.4.C969.

[314] D.P. Blondin, S. Nielsen, E.N. Kuipers, M.C. Severinsen, V.H. Jensen, S. Miard, N.Z. Jespersen, S. Kooijman, M.R. Boon, M. Fortin, S. Phoenix, F. Frisch, B. Guérin, É.E. Turcotte, F. Haman, D. Richard, F. Picard, P.C.N. Rensen, C. Scheele, A.C. Carpentier, Human Brown Adipocyte Thermogenesis Is Driven by β2-AR Stimulation, Cell Metab. 32 (2020) 287-300.e7. https://doi.org/10.1016/j.cmet.2020.07.005.

[315] C. Cero, H.J. Lea, K.Y. Zhu, F. Shamsi, Y.-H. Tseng, A.M. Cypess, β3-Adrenergic receptors regulate human brown/beige adipocyte lipolysis and thermogenesis, JCI Insight. 6 (n.d.) e139160. https://doi.org/10.1172/jci.insight.139160.

[316] M.J. Riis-Vestergaard, B. Richelsen, J.M. Bruun, W. Li, J.B. Hansen, S.B. Pedersen, Beta-1 and Not Beta-3 Adrenergic Receptors May Be the Primary Regulator of Human Brown Adipocyte Metabolism, J. Clin. Endocrinol. Metab. 105 (2020) dgz298. https://doi.org/10.1210/clinem/dgz298.

[317] S.W. Ma, D.O. Foster, Uptake of glucose and release of fatty acids and glycerol by rat brown adipose tissue in vivo, Can. J. Physiol. Pharmacol. 64 (1986) 609–614. https://doi.org/10.1139/y86-101.

[318] S. Corvera, J. Solivan-Rivera, Z. Yang Loureiro, Angiogenesis in adipose tissue and obesity, Angiogenesis. 25 (2022) 439–453. https://doi.org/10.1007/s10456-022-09848-3.

[319] A. Miranville, C. Heeschen, C. Sengenès, C.A. Curat, R. Busse, A. Bouloumié, Improvement of postnatal neovascularization by human adipose tissue-derived stem cells, Circulation. 110 (2004) 349–355. https://doi.org/10.1161/01.CIR.0000135466.16823.D0.

[320] A. Ghosh, L. Gao, A. Thakur, P.M. Siu, C.W.K. Lai, Role of free fatty acids in endothelial dysfunction, J. Biomed. Sci. 24 (2017) 50. https://doi.org/10.1186/s12929-017-0357-5.

[321] W. Hu, M.A. Lazar, Modelling metabolic diseases and drug response using stem cells and organoids, Nat. Rev. Endocrinol. 18 (2022) 744–759. https://doi.org/10.1038/s41574-022-00733-z.

[322] A.S. Karanfil, F. Louis, M. Matsusaki, Biofabrication of vascularized adipose tissues and their biomedical applications, Mater. Horiz. 10 (2023) 1539–1558. https://doi.org/10.1039/D2MH01391F.

[323] S. Gesta, K. Lolmède, D. Daviaud, M. Berlan, A. Bouloumié, M. Lafontan, P. Valet, J.S. Saulnier-Blache, Culture of human adipose tissue explants leads to profound alteration of adipocyte gene expression, Horm. Metab. Res. Horm. Stoffwechselforschung Horm. Metab. 35 (2003) 158–163. https://doi.org/10.1055/s-2003-39070.

[324] I. Samuelson, A. Vidal-Puig, Studying Brown Adipose Tissue in a Human in vitro Context, Front. Endocrinol. 11 (2020) 629. https://doi.org/10.3389/fendo.2020.00629.

[325] S.E. Seiler, D. Xu, J.-P. Ho, K.A. Lo, B.M. Buehrer, Y.J.W. Ludlow, J.-P. Kovalik, L. Sun, Characterization of a primary brown adipocyte culture system derived from human fetal interscapular fat, Adipocyte. 4 (2015) 303–310. https://doi.org/10.1080/21623945.2015.1042192.

[326] V. Zilberfarb, F. Piétri-Rouxel, R. Jockers, S. Krief, C. Delouis, T. Issad, A.D. Strosberg, Human immortalized brown adipocytes express functional beta3-adrenoceptor coupled to lipolysis, J. Cell Sci. 110 (Pt 7) (1997) 801–807. https://doi.org/10.1242/jcs.110.7.801.

[327] L.K. Markussen, M.S. Isidor, P. Breining, E.S. Andersen, N.E. Rasmussen, L.I. Petersen, S.B. Pedersen, B. Richelsen, J.B. Hansen, Characterization of immortalized human brown and white pre-adipocyte cell models from a single donor, PLOS ONE. 12 (2017) e0185624. https://doi.org/10.1371/journal.pone.0185624.

[328] M. Crisan, L. Casteilla, L. Lehr, M. Carmona, A. Paoloni-Giacobino, S. Yap, B. Sun, B. Léger, A. Logar, L. Pénicaud, P. Schrauwen, D. Cameron-Smith, A.P. Russell, B. Péault, J.-P. Giacobino, A reservoir of brown adipocyte progenitors in human skeletal muscle, Stem Cells Dayt. Ohio. 26 (2008) 2425–2433. https://doi.org/10.1634/stemcells.2008-0325.

[329] T. Kishida, A. Ejima, K. Yamamoto, S. Tanaka, T. Yamamoto, O. Mazda, Reprogrammed Functional Brown Adipocytes Ameliorate Insulin Resistance and Dyslipidemia in Diet-Induced

Obesity and Type 2 Diabetes, Stem Cell Rep. 5 (2015) 569–581. https://doi.org/10.1016/j.stemcr.2015.08.007.
[330] Y. Takeda, Y. Harada, T. Yoshikawa, P. Dai, Direct conversion of human fibroblasts to brown adipocytes by small chemical compounds, Sci. Rep. 7 (2017) 4304. https://doi.org/10.1038/s41598-017-04665-x.
[331] P.-I. Huang, Y.-C. Chen, L.-H. Chen, C.-C. Juan, H.-H. Ku, S.-T. Wang, S.-H. Chiou, G.-Y. Chiou, C.-W. Chi, C.-C. Hsu, H.-C. Lee, L.-K. Chen, C.-L. Kao, PGC-1α mediates differentiation of mesenchymal stem cells to brown adipose cells, J. Atheroscler. Thromb. 18 (2011) 966–980. https://doi.org/10.5551/jat.7401.
[332] C. Elabd, C. Chiellini, M. Carmona, J. Galitzky, O. Cochet, R. Petersen, L. Pénicaud, K. Kristiansen, A. Bouloumié, L. Casteilla, C. Dani, G. Ailhaud, E.-Z. Amri, Human multipotent adipose-derived stem cells differentiate into functional brown adipocytes, Stem Cells Dayt. Ohio. 27 (2009) 2753–2760. https://doi.org/10.1002/stem.200.
[333] A. Rashnonejad, G. Ercan, C. Gunduz, A. Akdemir, Y.O. Tiftikcioglu, Comparative analysis of human UCB and adipose tissue derived mesenchymal stem cells for their differentiation potential into brown and white adipocytes, Mol. Biol. Rep. 45 (2018) 233–244. https://doi.org/10.1007/s11033-018-4156-1.
[334] T. Ahfeldt, R.T. Schinzel, Y.-K. Lee, D. Hendrickson, A. Kaplan, D.H. Lum, R. Camahort, F. Xia, J. Shay, E.P. Rhee, C.B. Clish, R.C. Deo, T. Shen, F.H. Lau, A. Cowley, G. Mowrer, H. Al-Siddiqi, M. Nahrendorf, K. Musunuru, R.E. Gerszten, J.L. Rinn, C.A. Cowan, Programming human pluripotent stem cells into white and brown adipocytes, Nat. Cell Biol. 14 (2012) 209–219. https://doi.org/10.1038/ncb2411.
[335] M. Oka, N. Kobayashi, K. Matsumura, M. Nishio, K. Saeki, Exogenous Cytokine-Free Differentiation of Human Pluripotent Stem Cells into Classical Brown Adipocytes, Cells. 8 (2019) 373. https://doi.org/10.3390/cells8040373.
[336] R. Xue, M.D. Lynes, J.M. Dreyfuss, F. Shamsi, T.J. Schulz, H. Zhang, T.L. Huang, K.L. Townsend, Y. Li, H. Takahashi, L.S. Weiner, A.P. White, M.S. Lynes, L.L. Rubin, L.J. Goodyear, A.M. Cypess, Y.-H. Tseng, Clonal analyses and gene profiling identify genetic biomarkers of the thermogenic potential of human brown and white preadipocytes, Nat. Med. 21 (2015) 760–768. https://doi.org/10.1038/nm.3881.
[337] K. Shinoda, I.H.N. Luijten, Y. Hasegawa, H. Hong, S.B. Sonne, M. Kim, R. Xue, M. Chondronikola, A.M. Cypess, Y.-H. Tseng, J. Nedergaard, L.S. Sidossis, S. Kajimura, Genetic and functional characterization of clonally derived adult human brown adipocytes, Nat. Med. 21 (2015) 389–394. https://doi.org/10.1038/nm.3819.
[338] A.-L. Hafner, J. Contet, C. Ravaud, X. Yao, P. Villageois, K. Suknuntha, K. Annab, P. Peraldi, B. Binetruy, I.I. Slukvin, A. Ladoux, C. Dani, Brown-like adipose progenitors derived from human induced pluripotent stem cells: Identification of critical pathways governing their adipogenic capacity, Sci. Rep. 6 (2016) 32490. https://doi.org/10.1038/srep32490.
[339] J.X. Shen, M. Couchet, J. Dufau, T. de Castro Barbosa, M.H. Ulbrich, M. Helmstädter, A.M. Kemas, R. Zandi Shafagh, M. Marques, J.B. Hansen, N. Mejhert, D. Langin, M. Rydén, V.M. Lauschke, 3D Adipose Tissue Culture Links the Organotypic Microenvironment to Improved Adipogenesis, Adv. Sci. 8 (2021) 2100106. https://doi.org/10.1002/advs.202100106.
[340] J. Taylor, J. Sellin, L. Kuerschner, L. Krähl, Y. Majlesain, I. Förster, C. Thiele, H. Weighardt, E. Weber, Generation of immune cell containing adipose organoids for in vitro analysis of immune metabolism, Sci. Rep. 10 (2020) 21104. https://doi.org/10.1038/s41598-020-78015-9.
[341] A.J. Klingelhutz, F.A. Gourronc, A. Chaly, D.A. Wadkins, A.J. Burand, K.R. Markan, S.O. Idiga, M. Wu, M.J. Potthoff, J.A. Ankrum, Scaffold-free generation of uniform adipose spheroids for metabolism research and drug discovery, Sci. Rep. 8 (2018) 523. https://doi.org/10.1038/s41598-017-19024-z.
[342] F.M. Acosta, K. Stojkova, J. Zhang, E.I. Garcia Huitron, J.X. Jiang, C.R. Rathbone, E.M. Brey, Engineering Functional Vascularized Beige Adipose Tissue from Microvascular Fragments of

Models of Healthy and Type II Diabetes Conditions, J. Tissue Eng. 13 (2022) 20417314221109336. https://doi.org/10.1177/20417314221109337.
[343] V. Dani, S. Bruni-Favier, B. Chignon-Sicard, A. Loubat, A. Doglio, C. Dani, Regulation of Adipose Progenitor Cell Expansion in a Novel Micro-Physiological Model of Human Adipose Tissue Mimicking Fibrotic and Pro-Inflammatory Microenvironments, Cells. 11 (2022) 2798. https://doi.org/10.3390/cells11182798.
[344] Y. Liu, W. Fu, K. Seese, A. Yin, H. Yin, Ectopic brown adipose tissue formation within skeletal muscle after brown adipose progenitor cell transplant augments energy expenditure, FASEB J. 33 (2019) 8822–8835. https://doi.org/10.1096/fj.201802162RR.
[345] L. Ferren, Morphological differentiation of implanted brown and white fats, Trans. Kans. Acad. Sci. Kans. Acad. Sci. 69 (1966) 350–353.
[346] W. Sun, H. Dong, M. Balaz, M. Slyper, E. Drokhlyansky, G. Colleluori, A. Giordano, Z. Kovanicova, P. Stefanicka, L. Balazova, L. Ding, A.S. Husted, G. Rudofsky, J. Ukropec, S. Cinti, T.W. Schwartz, A. Regev, C. Wolfrum, snRNA-seq reveals a subpopulation of adipocytes that regulates thermogenesis, Nature. 587 (2020) 98–102. https://doi.org/10.1038/s41586-020-2856-x.
[347] M. Mandl, H.P. Viertler, F.M. Hatzmann, C. Brucker, S. Großmann, P. Waldegger, T. Rauchenwald, M. Mattesich, M. Zwierzina, G. Pierer, W. Zwerschke, An organoid model derived from human adipose stem/progenitor cells to study adipose tissue physiology, Adipocyte. 11 (n.d.) 164–174. https://doi.org/10.1080/21623945.2022.2044601.
[348] A.S. Deshmukh, L. Peijs, J.L. Beaudry, N.Z. Jespersen, C.H. Nielsen, T. Ma, A.D. Brunner, T.J. Larsen, R. Bayarri-Olmos, B.S. Prabhakar, C. Helgstrand, M.C.K. Severinsen, B. Holst, A. Kjaer, M. Tang-Christensen, A. Sanfridson, P. Garred, G.G. Privé, B.K. Pedersen, Z. Gerhart-Hines, S. Nielsen, D.J. Drucker, M. Mann, C. Scheele, Proteomics-Based Comparative Mapping of the Secretomes of Human Brown and White Adipocytes Reveals EPDR1 as a Novel Batokine, Cell Metab. 30 (2019) 963-975.e7. https://doi.org/10.1016/j.cmet.2019.10.001.
[349] A.M. Unser, B. Mooney, D.T. Corr, Y.-H. Tseng, Y. Xie, 3D brown adipogenesis to create "Brown-Fat-in-Microstrands," Biomaterials. 75 (2016) 123–134. https://doi.org/10.1016/j.biomaterials.2015.10.017.
[350] S. Muller, I. Ader, J. Creff, H. Leménager, P. Achard, L. Casteilla, L. Sensebe, A. Carrière, F. Deschaseaux, Human adipose stromal-vascular fraction self-organizes to form vascularized adipose tissue in 3D cultures, Sci. Rep. 9 (2019). https://doi.org/10.1038/s41598-019-43624-6.
[351] B.A. Evans, J. Merlin, T. Bengtsson, D.S. Hutchinson, Adrenoceptors in white, brown, and brite adipocytes, Br. J. Pharmacol. 176 (2019) 2416–2432. https://doi.org/10.1111/bph.14631.
[352] K. Shinoda, I.H.N. Luijten, Y. Hasegawa, H. Hong, S.B. Sonne, M. Kim, R. Xue, M. Chondronikola, A.M. Cypess, Y.-H. Tseng, J. Nedergaard, L.S. Sidossis, S. Kajimura, Genetic and functional characterization of clonally derived adult human brown adipocytes, Nat. Med. 21 (2015) 389–394. https://doi.org/10.1038/nm.3819.
[353] Y. Cheng, L. Jiang, S. Keipert, S. Zhang, A. Hauser, E. Graf, T. Strom, M. Tschöp, M. Jastroch, F. Perocchi, Prediction of Adipose Browning Capacity by Systematic Integration of Transcriptional Profiles, Cell Rep. 23 (2018) 3112–3125. https://doi.org/10.1016/j.celrep.2018.05.021.
[354] A. Moisan, Y.-K. Lee, J.D. Zhang, C.S. Hudak, C.A. Meyer, M. Prummer, S. Zoffmann, H.H. Truong, M. Ebeling, A. Kiialainen, R. Gérard, F. Xia, R.T. Schinzel, K.E. Amrein, C.A. Cowan, White-to-brown metabolic conversion of human adipocytes by JAK inhibition, Nat. Cell Biol. 17 (2015) 57–67. https://doi.org/10.1038/ncb3075.
[355] Y. Li, X. Ping, Y. Zhang, G. Li, T. Zhang, G. Chen, X. Ma, D. Wang, L. Xu, Comparative Transcriptome Profiling of Cold Exposure and β3-AR Agonist CL316,243-Induced Browning of White Fat, Front. Physiol. 12 (2021). https://www.frontiersin.org/articles/10.3389/fphys.2021.667698 (accessed October 4, 2023).
[356] A.B. Di Stefano, F. Grisafi, M. Perez-Alea, M. Castiglia, M. Di Simone, S. Meraviglia, A. Cordova, F. Moschella, F. Toia, Cell quality evaluation with gene expression analysis of spheroids (3D) and adherent (2D) adipose stem cells, Gene. 768 (2021) 145269. https://doi.org/10.1016/j.gene.2020.145269.

[357] B.R. Seo, X. Chen, L. Ling, Y.H. Song, A.A. Shimpi, S. Choi, J. Gonzalez, J. Sapudom, K. Wang, R.C. Andresen Eguiluz, D. Gourdon, V.B. Shenoy, C. Fischbach, Collagen microarchitecture mechanically controls myofibroblast differentiation, Proc. Natl. Acad. Sci. U. S. A. 117 (2020) 11387–11398. https://doi.org/10.1073/pnas.1919394117.

[358] V.D. Desai, H.C. Hsia, J.E. Schwarzbauer, Reversible Modulation of Myofibroblast Differentiation in Adipose-Derived Mesenchymal Stem Cells, PLoS ONE. 9 (2014) e86865. https://doi.org/10.1371/journal.pone.0086865.

[359] J. Ye, Emerging Role of Adipose Tissue Hypoxia in Obesity and Insulin Resistance, Int. J. Obes. 2005. 33 (2009) 54–66. https://doi.org/10.1038/ijo.2008.229.

[360] P. Chansoria, S. Asif, K. Polkoff, J. Chung, J.A. Piedrahita, R.A. Shirwaiker, Characterizing the Effects of Synergistic Thermal and Photo-Cross-Linking during Biofabrication on the Structural and Functional Properties of Gelatin Methacryloyl (GelMA) Hydrogels, ACS Biomater. Sci. Eng. 7 (2021) 5175–5188. https://doi.org/10.1021/acsbiomaterials.1c00635.

[361] I. Pepelanova, K. Kruppa, T. Scheper, A. Lavrentieva, Gelatin-Methacryloyl (GelMA) Hydrogels with Defined Degree of Functionalization as a Versatile Toolkit for 3D Cell Culture and Extrusion Bioprinting, Bioeng. Basel Switz. 5 (2018) 55. https://doi.org/10.3390/bioengineering5030055.

[362] Y. Zhang, Z. Wang, Q. Sun, Q. Li, S. Li, X. Li, Dynamic Hydrogels with Viscoelasticity and Tunable Stiffness for the Regulation of Cell Behavior and Fate, Materials. 16 (2023) 5161. https://doi.org/10.3390/ma16145161.

[363] A. Ferrand, D. Hammel, J. Foncy, L. Malaquin, Microphysiological System and Uses thereof, 21305235, n.d.

[364] H. Liu, T. Lu, G.-J. Kremers, A.L.B. Seynhaeve, T.L.M. Ten Hagen, A microcarrier-based spheroid 3D invasion assay to monitor dynamic cell movement in extracellular matrix, Biol. Proced. Online. 22 (2020) 3. https://doi.org/10.1186/s12575-019-0114-0.

[365] A.K. O'Brien, C.N. Bowman, Impact of Oxygen on Photopolymerization Kinetics and Polymer Structure, Macromolecules. 39 (2006) 2501–2506. https://doi.org/10.1021/ma051863l.

[366] R. Simič, J. Mandal, K. Zhang, N.D. Spencer, Oxygen inhibition of free-radical polymerization is the dominant mechanism behind the "mold effect" on hydrogels, Soft Matter. 17 (2021) 6394–6403. https://doi.org/10.1039/D1SM00395J.

[367] Y.W. Chung, F. Ahmad, Y. Tang, S.C. Hockman, H.J. Kee, K. Berger, E. Guirguis, Y.H. Choi, D.M. Schimel, A.M. Aponte, S. Park, E. Degerman, V.C. Manganiello, White to beige conversion in PDE3B KO adipose tissue through activation of AMPK signaling and mitochondrial function, Sci. Rep. 7 (2017) 40445. https://doi.org/10.1038/srep40445.

[368] J.D. White, R.S. Dewal, K.I. Stanford, The Beneficial Effects of Brown Adipose Tissue Transplantation, Mol. Aspects Med. 68 (2019) 74–81. https://doi.org/10.1016/j.mam.2019.06.004.

[369] A. Skardal, T. Shupe, A. Atala, Organoid-on-a-chip and body-on-a-chip systems for drug screening and disease modeling, Drug Discov. Today. 21 (2016) 1399–1411. https://doi.org/10.1016/j.drudis.2016.07.003.

[370] D. Lagarde, Y. Jeanson, J.-C. Portais, A. Galinier, I. Ader, L. Casteilla, A. Carrière, Lactate Fluxes and Plasticity of Adipose Tissues: A Redox Perspective, Front. Physiol. 12 (2021) 689747. https://doi.org/10.3389/fphys.2021.689747.

[371] W. Zhan, J. Alvarez, R.M. Crooks, A two-channel microfluidic sensor that uses anodic electrogenerated chemiluminescence as a photonic reporter of cathodic redox reactions, Anal. Chem. 75 (2003) 313–318. https://doi.org/10.1021/ac020488h.

[372] A. Krześniak, T. Gabler, M. Janik, M. Koba, M. Jönsson-Niedziółka, M. Śmietana, A microfluidic system for analysis of electrochemical processing using a highly sensitive optical fiber microcavity, Opt. Lasers Eng. 158 (2022) 107173. https://doi.org/10.1016/j.optlaseng.2022.107173.

[373] M. Azimzadeh, P. Khashayar, M. Amereh, N. Tasnim, M. Hoorfar, M. Akbari, Microfluidic-Based Oxygen (O2) Sensors for On-Chip Monitoring of Cell, Tissue and Organ Metabolism, Biosensors. 12 (2021) 6. https://doi.org/10.3390/bios12010006.

[374] Q. Teng, W. Huang, T.W. Collette, D.R. Ekman, C. Tan, A direct cell quenching method for cell-culture based metabolomics, Metabolomics. 5 (2009) 199–208. https://doi.org/10.1007/s11306-008-0137-z.
[375] M. Schot, N. Araújo-Gomes, B. van Loo, T. Kamperman, J. Leijten, Scalable fabrication, compartmentalization and applications of living microtissues, Bioact. Mater. 19 (2023) 392–405. https://doi.org/10.1016/j.bioactmat.2022.04.005.
[376] M. Haack-Sørensen, M. Juhl, B. Follin, R. Harary Søndergaard, M. Kirchhoff, J. Kastrup, A. Ekblond, Development of large-scale manufacturing of adipose-derived stromal cells for clinical applications using bioreactors and human platelet lysate, Scand. J. Clin. Lab. Invest. 78 (2018) 293–300. https://doi.org/10.1080/00365513.2018.1462082.
[377] A. Selich, J. Daudert, R. Hass, F. Philipp, C. von Kaisenberg, G. Paul, K. Cornils, B. Fehse, S. Rittinghausen, A. Schambach, M. Rothe, Massive Clonal Selection and Transiently Contributing Clones During Expansion of Mesenchymal Stem Cell Cultures Revealed by Lentiviral RGB-Barcode Technology, Stem Cells Transl. Med. 5 (2016) 591–601. https://doi.org/10.5966/sctm.2015-0176.
[378] D. Budimir, O. Polašek, A. Marušić, I. Kolčić, T. Zemunik, V. Boraska, A. Jerončić, M. Boban, H. Campbell, I. Rudan, Ethical aspects of human biobanks: a systematic review, Croat. Med. J. 52 (2011) 262–279. https://doi.org/10.3325/cmj.2011.52.262.
[379] B. Ayan, N. Celik, Z. Zhang, K. Zhou, M.H. Kim, D. Banerjee, Y. Wu, F. Costanzo, I.T. Ozbolat, Aspiration-assisted freeform bioprinting of pre-fabricated tissue spheroids in a yield-stress gel, Commun. Phys. 3 (2020) 1–14. https://doi.org/10.1038/s42005-020-00449-4.
[380] R. Thiermann, M. Sandler, G. Ahir, J.T. Sauls, J.W. Schroeder, S.D. Brown, G.L. Treut, F. Si, D. Li, J.D. Wang, S. Jun, Tools and methods for high-throughput single-cell imaging with the mother machine, ELife. 12 (2023). https://doi.org/10.7554/eLife.88463.
[381] W. Wang, D. Douglas, J. Zhang, S. Kumari, M.S. Enuameh, Y. Dai, C.T. Wallace, S.C. Watkins, W. Shu, J. Xing, Live-cell imaging and analysis reveal cell phenotypic transition dynamics inherently missing in snapshot data, Sci. Adv. 6 (2020) eaba9319. https://doi.org/10.1126/sciadv.aba9319.
[382] D. Serra, U. Mayr, A. Boni, I. Lukonin, M. Rempfler, L. Challet Meylan, M.B. Stadler, P. Strnad, P. Papasaikas, D. Vischi, A. Waldt, G. Roma, P. Liberali, Self-organization and symmetry breaking in intestinal organoid development, Nature. 569 (2019) 66–72. https://doi.org/10.1038/s41586-019-1146-y.